Patterns in bioreactive transport in underground storage of hydrogen : impact of natural and induced heterogeneity

Noura Eddaoui

▶ **To cite this version:**

Noura Eddaoui. Patterns in bioreactive transport in underground storage of hydrogen : impact of natural and induced heterogeneity. Mechanics [physics]. Université de Lorraine; Université Hassan II (Casablanca, Maroc), 2021. English. NNT : 2021LORR0244 . tel-03564124

HAL Id: tel-03564124
https://hal.univ-lorraine.fr/tel-03564124

Submitted on 10 Feb 2022

HAL is a multi-disciplinary open access archive for the deposit and dissemination of scientific research documents, whether they are published or not. The documents may come from teaching and research institutions in France or abroad, or from public or private research centers.

L'archive ouverte pluridisciplinaire **HAL**, est destinée au dépôt et à la diffusion de documents scientifiques de niveau recherche, publiés ou non, émanant des établissements d'enseignement et de recherche français ou étrangers, des laboratoires publics ou privés.

AVERTISSEMENT

Ce document est le fruit d'un long travail approuvé par le jury de soutenance et mis à disposition de l'ensemble de la communauté universitaire élargie.

Il est soumis à la propriété intellectuelle de l'auteur. Ceci implique une obligation de citation et de référencement lors de l'utilisation de ce document.

D'autre part, toute contrefaçon, plagiat, reproduction illicite encourt une poursuite pénale.

Contact : ddoc-theses-contact@univ-lorraine.fr

LIENS

Code de la Propriété Intellectuelle. articles L 122. 4
Code de la Propriété Intellectuelle. articles L 335.2- L 335.10
http://www.cfcopies.com/V2/leg/leg_droi.php
http://www.culture.gouv.fr/culture/infos-pratiques/droits/protection.htm

THÈSE

Préparée en cotutelle entre l'université Hassan II et l'université de Lorraine

En vue de l'obtention du

DOCTORAT

Présentée par : Noura EDDAOUI

En Sciences Physiques

Spécialité : Mécanique – Génie Civil

Patterns in bioreactive transport in underground storage of hydrogen: impact of natural and induced heterogeneity

---

Soutenue publiquement, le 10 décembre 2021

A *l'Université de Lorraine* devant le Jury **:**

Jaâfar KHALID NACIRI	Professeur Universitaire, Université Hassan II, Faculté des Sciences Aïn Chock, Casablanca, Maroc	Président
Christophe JOSSERAND	Directeur de recherche, Ecole Polytechnique- LadHyx, Palaiseau-France	Rapporteur
Franck PLOURABOUE	Directeur de recherche, Institut National Polytechnique de Toulouse-IMFT, Toulouse-France	Rapporteur
Jamil ABDELMAJID	Professeur Universitaire, Université Sidi Mohamed Ben Abdellah - École Supérieure de Technologie, Fès, Maroc	Rapporteur
Miloud RAHMOUNE	Professeur Universitaire, Université Sidi Mohamed Ben Abdellah - École Supérieure de Technologie, Fès, Maroc	Examinateur
Anne TANIÈRE	Professeur Universitaire, Université de Lorraine - LEMTA, Nancy-France	Examinatrice
Michel PANFILOV	Professeur Universitaire, Université de Lorraine - IECL, Nancy, France	**Directeur de thèse**
Saïd ANISS	Professeur Universitaire, Université Hassan II, Faculté des Sciences Aïn Chock, Casablanca, Maroc	**Co-directeur de thèse**

PREFACE

All the work presented henceforth was carried out in the Institute of Elie Cartan at the University of Lorraine and in the Laboratory of mechanics of the faculty of science of the University Hassan II.

The research was supported by the German Federal Ministry for Economic Affairs and Energy, grant “HyINTEGER”: Investigations on the integrity of wells and technical components exposed to highly corrosive conditions in geological hydrogen reservoirs, 2016–2019 and the National Center for Scientific and Technical Research (CNRST) of Morocco.

This work would not have been possible without the constant support, guidance, and assistance of my supervisors Pr. Said ANISS and Pr. Michel PANFILOV. Their levels of patience, knowledge, and ingenuity is something I will always keep aspiring to. My deepest gratitude to Pr. Michel PANFILOV for directing me to the amazingly interesting field of underground hydrogen storage and giving me the opportunity to combine the research flexibly with my interdisciplinary studies. I would like to thank you very much for your support and understanding over these past four years. you have been an extremely generous advisor, especially in sending me to conferences around the world. I am very grateful for your permanent support, constant optimism, and encouragement throughout this long walk with all its ups and downs. Without your guidance and constant feedback, this PhD would not have been achievable. My sincere thanks go to my supervisor Pr. Said ANISS for his patient support, availability, and for all of the opportunities I was given to further my research. Your scientific guidance and insightful feedback pushed me to sharpen my thinking. I am thankful for the truly extraordinary experience you provided for me, and without you, I simply would not have been able to get to where I am now.

I am deeply grateful to all members of the jury for agreeing to read the manuscript and to participate in the defense of this thesis. Thank you to the members of the monitoring committee, Pr. Melika HINAJE and Pr. Bruno DOUINE. Your encouraging words and thoughtful, detailed feedback have been very important to me.

Furthermore, I would like to extend my sincere thanks to Pr. Leonard Ganzer and Dr. Birger Hagemann, from the Institute of Subsurface Energy Systems - Technische Universität Clausthal, it was a real pleasure working with you during the project HyInteger 2018-2019.

I am grateful to Pr. Brahim AMAZIANE for sharing his expertise and for his hospitality during my internship on the scientific software DuMu^{X} in the Laboratory of Mathematics and its Applications at Université de Pays de l'Adour.

I would like to acknowledge my Doctoral Schools SIReNA and CEDOC and their administrations. My sincerest thanks are extended to Pr. Ahmed MENAI, director of the center of doctoral studies "Sciences Fondamentales et Appliquées" in the faculty of Sciences Ain Chock, Pr. Elmira ARAB TEHRANY-KAHN, director of SIReNa Doctoral School, Mme Estelle BARRANCO, administrative officer in SIReNa. And Especially, I would like to address a kind thought to Pr. Anne GEGOUT-PETIT, director of Institut Élie Cartan de Lorraine and all the IECL administrative staff: Mme Laurence QUIROT, Mme Elodie CUNAT, Mme Valérie GOBERT and Mme Paola SCHNEIDER, M. Didier GEMMERLE. Thank you for your always kind help and availability.

I would also like to give special thanks to professor El Haj LAAMRI for all the precious advices and encouragement.
I'm indebted to my professors at the University Hassan II. In particular, I wish to record my gratitude to Professor Mohamed OUAZZANI TOUHAMI. He taught me to think critically to scrutinize every angle detail before touching the keyboard. He was the reason why I decided to go to pursue a career in research. His enthusiasm and love for research are contagious.

Thank you to all my colleagues at Université Hassan II and Université de Lorraine, with whom I have shared moments of deep anxiety but also of big excitement. I would especially like to thank my officemates Marwa LTAIFA, Rodolphe LOUBATON, and Philippe MACHNER for making the workdays fruitful.

I also would like to thank my second family in France, ANDRIANTSIZAFY Family and my friends particularly, Chaimaa DENNI, Fatima Ezzahra CHARDAL, Wafaa BENTOTO, Nouha LAHLOU, Ilham NAFII, Ilham KATIR, Hafsa JABER, Maha DAOUD, Christine RATSIMBAZAFY, for their friendship and emotional support through all these last years. I deeply appreciate and thank Abdelkrim EL HANNOUNI for all the patience and unfailing support in this adventure – you were always there with a word of encouragement or listening ear.

Most importantly, none of this could have happened without my family. My parents Thami EDDAOUI and Najate LAAMIMA, my sister Zineb EDDAOUI, this dissertation stands as a testament to your unconditional love and encouragement.

LIST OF PUBLICATIONS

(2021e) **Eddaoui N.**, Panfilov M., Ganzer L., and Hagemann B., Impact of Pore Clogging by Bacteria on Underground Hydrogen Storage. Transp Porous Med 139, 89–108 (2021). https://doi.org/10.1007/s11242-021-01647-6 (Article)

(2021d) **Eddaoui N.**, Panfilov M., Aniss S., Ganzer L., and Hagemann B., New Insights on the Effect of Bio-clogging for Enhancing Underground Biomethanation Technology. (Article submitted to the journal)

(2021f) **Eddaoui N,** Panfilov M., Aniss S., Modelling bio-reactive transport and bio-clogging in underground hydrogen storages. Séminaire de l'Institut de Mécanique des Fluides de Toulouse, Toulouse, **France**. **(Oral presentation)** (Seminar)

(2021c) Panfilov M., **Eddaoui N.,** Reaction-Diffusion Patterns in Underground Storage of Hydrogen. Journées scientifiques du GDR MORPHEA, Nancy, **France**. (Proc.) (Conference)

(2021b) **Eddaoui N.,** Panfilov M., Patterns in a reaction-diffusion double porosity system. InterPore 13th Annual Meeting 2021. (Proc.) (Conference)

(2021a) **Eddaoui N**., Panfilov M., and Aniss S., Optimizing biomethanation efficiency in underground Hydrogen and CO2 Storage. Séminaire de l'Ecole doctorale, Nancy, **France**. **(Oral presentation)** (Seminar)

(2019d) Panfilov M., and **Eddaoui N.** Biochemical patterns and waves in underground storage of hydrogen and CO2. SITRAM19: Advances in the SImulation of reactive flow and TRAnsport in porous Media, Pau, **France**. (International workshop)

(2019c) **Eddaoui N.** and Panfilov M., In situ methanation and underground H2/CO2 storage: physicochemical principles and model. Development of a mathematical and numerical model for the near-wellbore region, Clausthal-Zellerfeld, **Germany**. **(Oral presentation)** (Seminar)

(2019b) Panfilov M., and **Eddaoui N.**, In situ methanation and underground H2/CO2 storage: physicochemical principles and model. Stockage géologique de gaz (CO2-H2- CH4) : processus et monitoring de site, Saint-Emilion, **France**. (Abstract) (Colloque)

(2019a) **Eddaoui N.**, Panfilov M., and Aniss S. Enhancement of hydrogen storage through microbial accumulation: modeling and numerical simulation. ICH2P2019: 10th International Conference on Hydrogen Production, Cluj-Napoca, **Romania**. **(Oral presentation)** (Conference)

(2018) Panfilov M., and **Eddaoui N.**, Microbiological Underground Methanation: Principle, Biochemical & Hydrodynamic Models, and Self-Organization. InterPore 10th Annual Meeting and Jubilee, New Orleans, **USA**. **(Oral presentation)** (Conference)

TABLE OF FIGURES

LIST OF TABLES

NOMENCLATURE

- ϕ - reservoir porosity $[-]$
- ϕ_0 - porosity of clean reservoir without bacteria $[-]$
- $\alpha = w, g$ - phase = water, gas
- k - chemical component (H_2, CO_2, CH_4, H_2O)
- n_d and n_a - volume fractions of mobile and fixed (biofilm) microorganisms $\left[cell / m^3\right]$
- n_c- number of microbial cells needed to clog a pore volume (empirical parameter) $\left[cell / m^3\right]$
- c_α^k - molar fraction of component k in phase α $[-]$
- S_α - phase saturation $[-]$
- V_α - average velocity in phase α $\left[m / s\right]$
- $\mathbf{g}$ - gravity acceleration vector $\left[m / s^2\right]$
- K - absolute permeability $\left[m^2\right]$
- K_0 - permeability of clean medium without bacteria $\left[m^2\right]$
- $k_{r\alpha}$ - relative permeability for phase α $[-]$
- p_α - pressure of phase α $\left[Pa\right]$
- p_c - capillary pressure $\left[Pa\right]$
- ρ_α - phase molar density $\left[mol / m^3\right]$
- $\rho_{\alpha,mass}$ - mass density $\left[kg / m^3\right]$
- μ_α - dynamic viscosity of phase α $\left[Pa.s\right]$
- D_b - bacterial diffusion $\left[m^2 / s\right]$
- D_α^k - molecular diffusion of component k in phase α $\left[m^2 / s\right]$
- R^{gr}, R^{dec}- rates of bacterial growth and decay $\left[s^{-1}\right]$

- ψ^{gr} , ψ^{dec} - rates of bacterial growth and decay per one bacterium [s^{-1}. $Cell^{-1}$]
- ω^{k} - rate of production or disappearance of component *k*
- t^{dec} - characteristic time of decay $[s]$
- t^{gr} - characteristic time of growth $[s]$
- k_a - rate of attachment per one bacterium $\left[s^{-1}\right]$
- k_d - rate of detachment per one bacterium $\left[s^{-1}\right]$
- d_p - pore diameter $[m]$
- d_b - average bacterium diameter $[m]$
- η - efficiency of attachment
- d_T - is the characteristic diameter of a pore $[m]$
- α_{eff} - attachment probability after a collision $[-]$
- k_b - Boltzmann constant $\left[J.K^{-1}\right]$
- T – temperature $[K]$

CONTENTS

ABSTRACT

In the era of energy transition and in connection with the international agreement on the transition to a climate-neutral economy by 2050, intensive research is being carried out around the world on renewable energy sources. Due to the intermittent and unpredictable nature of their functioning, the problem of storing excessively produced energy becomes a highly important problem. We are currently talking about a large capacity for storing large amounts of electricity coming from photovoltaic cells and windmills. Since electricity is mutually converted to hydrogen and vice versa, storing it in geological strata in the form of gas becomes the optimal solution.

The conversion of electricity into H_2 can be done by electrolysis. The process is reversible using fuel cells, where hydrogen is converted into electrical current. We obtain the chain: power - to gas - to power. As a result, there are virtually no greenhouse gases, which can lead to the decarbonization of the transport sector and energy-intensive industries.

In this thesis, we analyze the storage of hydrogen in underground porous media, which can be aquifers, or depleted gas reservoirs, or ex-storages of natural gas.

The subject of this thesis is the hydrodynamic analysis of transport of injected gases in a storage coupled with bacterial dynamics. As shown in previous studies, hydrogen is intensively consumed by various types of bacteria, which transform it into methane, for example. The cross-effects of bioreactions and transport determine the formation of complicated spatial structures called *patterns* that lead to a nonuniform distribution of hydrogen over the domain. Our main attention was focused on the impact of medium heterogeneity on pattern formation. Two types of heterogeneity were analyzed: the double porosity, in terms of the macroscopic Barenblatt's model, and the heterogeneity induced by bacteria, growth of which creates the zones of reduced permeability or even completely clogged pores.

The thesis consists of three chapters.

The first chapter is an introduction to the technology of underground hydrogen storage and bio-methanation. In addition, it presents biochemical effects that were observed in real storages of

hydrogen, including the effect of pattern formation. Additionally, it provides a review of existing classical mathematical models able to generate patterns and explain their origin.

The second chapter is devoted to the analysis of spatiotemporal patterns formation and the conditions of their emergence in underground hydrogen storage. We start with a short introduction to multicomponent two-phase flow in porous media with chemical reactions, and to the theory of patterns in dynamical systems. We examine next homogeneous media and develop the technique of stability analysis of diffusion-reaction systems in application to the transport phenomena in an underground storage of hydrogen. After this, we analyze double porosity media and the impact of the natural reservoir heterogeneity on the criteria of pattern existence. Next, we carry out a numerical simulation to capture the regimes when these criteria are verified.

In the last chapter, we analyze the impact of the medium heterogeneity induced by bacteria on hydrogen transport. A growing population of microorganisms leads to partial or complete pore-clogging, reduction of the medium permeability in the zones of bacterial activity. This induces spatial heterogeneity of the medium, as well as the medium anisotropy since the effect of pore-clogging occurs preferably in the direction of bacteria propagation. We develop the conceptual model of bio-clogging and bio-plugging, which incorporates the effects of attachment of bacteria to pore walls and detachment. Several mechanisms of attachment/detachment are examined. The decrease in permeability has an impact on several parameters of two-phase flow, such as the capillary pressure. We also analyze the impact of bio-clogging on the efficiency of hydrogen conversion into biomethane. The analysis is performed numerically using the simulator $DuMu^X$, open scientific software for flow in porous media, developed at the University of Stuttgart and based on Dune developed by Heidelberg.

KURZFASSUNG

Im Zeitalter der Energiewende und im Bezug auf die internationale Vereinbarung für den Übergang an eine klimaneutrale Wirtschaft bis 2050 wird weltweit intensiv an erneuerbaren Energiequellen geforscht. Da sie unstetig und unvorhersehbar funktionieren, ist das Problem der Speicherung von überschüssig produzierter Energie von Wichtigkeit. Derzeit geht es um eine große Kapazität für die Speicherung großer Mengen von Strom aus Photovoltaikzellen und Windrädern. Da Strom in Wasserstoff umgewandelt wird und umgekehrt, ist die Speicherung in geologischen Schichten in Form von Gas die optimale Lösung. Die Umwandlung von Strom in H2 kann durch Elektrolyse erfolgen. Der Prozess ist mit Hilfe von Brennstoffzellen reversibel, wobei Wasserstoff in elektrischen Strom umgewandelt wird. Wir erhalten die Kette: Strom - zu Gas - zu Strom. Infolgedessen entstehen praktisch keine Treibhausgase, was zur Dekarbonisierung des Verkehrssektors und der energieintensiven Industrien führen kann.

In dieser Arbeit wird die Speicherung von Wasserstoff in unterirdischen porösen Medien untersucht, bei denen es sich um Aquifere, erschöpfte Gasreservoirs oder ehemalige Erdgaslagerstätten handeln kann.

Gegenstand dieser Arbeit ist die hydrodynamische Analyse des Transports von injizierten Gasen in einem Speicher, gekoppelt mit bakterieller Dynamik. Wie in früheren Studien gezeigt wurde, wird Wasserstoff intensiv von verschiedenen Bakterienarten verbraucht, die ihn beispielsweise in Methan umwandeln. Die Kreuzwirkungen von Bioreaktionen und Transport bestimmen die Bildung komplizierter räumlicher Strukturen, die als Muster bezeichnet werden und zu einer ungleichmäßigen Verteilung des Wasserstoffs über die Domäne führen. Unser Hauptaugenmerk lag auf den Auswirkungen der Heterogenität des Mediums auf die Musterbildung. Es wurden zwei Arten von Heterogenität analysiert: die doppelte Porosität im Sinne des makroskopischen Barenblatt-Modells und die durch Bakterien verursachte Heterogenität, deren Wachstum Zonen mit verringerter Permeabilität oder sogar vollständig verstopfte Poren schafft. Die Analyse wird numerisch mit dem Simulator DuMu^{X} durchgeführt, einer offenen wissenschaftlichen Software für die Strömung in porösen Medien, die an der Universität Stuttgart entwickelt wurde und auf dem von Heidelberg entwickelten Dune basiert.

RÉSUMÉ

A l'ère de la transition énergétique et en lien avec l'accord international sur la transition vers une économie climatiquement neutre à l'horizon 2050, des recherches intensives sont menées dans le monde sur les énergies renouvelables. Du fait du caractère intermittent et imprévisible de leur fonctionnement, le problème du stockage de l'énergie produite en excès devient un problème très important. On parle actuellement d'une grande capacité de stockage de grandes quantités d'électricité provenant de cellules photovoltaïques et d'éoliennes. L'électricité étant mutuellement convertie en hydrogène et inversement, son stockage dans les couches géologiques sous forme de gaz devient la solution optimale.

La conversion de l'électricité renouvelable en H_2 peut se faire par électrolyse. Le processus est réversible à l'aide de piles à combustible, où l'hydrogène est converti en courant électrique. On obtient la chaîne : power - to gas - to power. En conséquence, il n'y a pratiquement pas de gaz à effet de serre, ce qui peut conduire à la décarbonation du secteur des transports et des industries énergivores.

Dans cette thèse, nous analysons le stockage de l'hydrogène dans des milieux poreux souterrains, qui peuvent être des aquifères, ou des réservoirs de gaz épuisés, ou des ex-stockages de gaz naturel.

Le sujet de cette thèse est l'analyse hydrodynamique du transport des gaz injectés dans un stockage couplé à la dynamique bactérienne. Comme le montrent les études précédentes, l'hydrogène est consommé de manière intensive par différents types de bactéries, qui le transforment en méthane par exemple. Les effets croisés des bio-réactions et du transport conduisent à la formation de structures spatiales complexes appelées modèles qui conduisent à une distribution non uniforme de l'hydrogène sur le domaine. Notre attention principale s'est concentrée sur l'impact de l'hétérogénéité moyenne sur la formation de motifs. Deux types d'hétérogénéité ont été analysés : la double porosité, selon le modèle macroscopique de Barenblatt, et l'hétérogénéité induite par les bactéries dont la croissance crée la zone de pores réduits voire totalement obstrués.

La thèse se compose de trois chapitres.

Le premier chapitre est une introduction à la technologie du stockage souterrain de l'hydrogène et de la biométhanisation. De plus, il présente des effets biochimiques qui ont été observés dans des stockages réels d'hydrogène, y compris l'effet de formation de motifs. De plus, il fournit un examen du modèle mathématique classique existant capable de générer les modèles observés et d'expliquer leur origine.

Le deuxième chapitre est consacré à l'analyse de la formation des patrons spatio-temporels et des conditions de leur émergence dans les stockages souterrains d'hydrogène. Nous commençons par une brève introduction à l'écoulement diphasique multi-composants en milieu poreux avec réactions chimiques, et à la théorie des motifs dans les systèmes dynamiques. Nous examinons ensuite des milieux homogènes et développons la technique d'analyse de stabilité des systèmes de diffusion-réaction en application aux phénomènes de transport dans un stockage souterrain d'hydrogène. Après cela, nous analysons les milieux à double porosité et l'impact de l'hétérogénéité du réservoir naturel sur les critères d'existence du motif. Ensuite, nous effectuons une simulation numérique pour capturer les régimes lorsque ces critères sont vérifiés.

Dans le dernier chapitre, nous analysons l'impact de l'hétérogénéité du milieu induite par les bactéries sur le transport de l'hydrogène. Une population croissante de micro-organismes entraîne un colmatage partiel ou total des pores, une diminution de la perméabilité du milieu dans les zones d'activité bactérienne. Ceci induit une hétérogénéité spatiale du milieu, ainsi que l'anisotropie du milieu, puisque l'effet de bouchage des pores se produit de préférence dans le sens de propagation des bactéries. Nous développons le modèle conceptuel du bio-colmatage et du bio-bouchage, qui intègre les effets de l'attachement des bactéries aux parois des pores et du détachement. Plusieurs mécanismes d'attachement/détachement sont examinés. La diminution de la perméabilité a un impact sur plusieurs paramètres de l'écoulement diphasique, comme la pression capillaire. Nous analysons également l'impact du biocolmatage sur l'efficacité de la conversion de l'hydrogène en biométhane. L'analyse est réalisée numériquement à l'aide du simulateur DuMu^{X}, un logiciel scientifique ouvert d'écoulement en milieu poreux, développé à l'Université de Stuttgart et basé sur Dune développé par Heidelberg.

RÉSUMÉ ÉLARGI

Les émissions élevées de dioxyde de carbone et d'autres gaz à effet de serre (protoxyde d'azote N2O, hydrofluorocarbures HFC...) dans l'atmosphère ont fortement contribué au réchauffement climatique. La dernière conférence des Nations unies sur le changement climatique à Paris (COP21) s'est fixé un défi urgent de réduire les émissions de carbone de l'Union Européen de moitié d'ici 2030 et à zéro d'ici 2050. Conformément à l'objectif de l'UE, d'atteindre la neutralité climatique d'ici 2050, les secteurs énergétiques se tournent de plus en plus vers l'intégration des énergies électriques renouvelables. Toutefois, les ressources renouvelables sont de nature fluctuante et difficilement prévisible. Leur capacité de production provoque des surplus qui devraient être stockés pour éviter de les perdre. Le déploiement croissant des éoliens et des cellules photovoltaïques sur la surface du sol emmène à des quantités géantes de l'électricité produite excessivement, ce qui demande de grandes capacités de stockage. La conversion de l'électricité excessive en gaz (hydrogène) et son stockage sous forme de gaz dans des cavernes ou des strates géologiques poreux est la meilleure solution pour stocker de grandes quantités d'énergie.

La conversion de l'électricité renouvelable en hydrogène (Power – to Gaz) se fait, en effet, en séparant les molécules d'eau à l'aide d'électricité (électrolyse). Cet hydrogène, produit par la technique de l'électrolyse dépourvue de toute émission de gaz à effet de serre, est appelé « vert ». Le processus est réversible : la reconversion de H_2 en électricité (Power – to Gaz – to Power) se passe dans une pile à combustible, dans laquelle les électrons de H_2 se séparent des protons qui passent à travers une membrane imperméable pour les électrons, et les électrons libres forment un courant électrique capable de produire un travail utile. Ces deux conversions ne produisent pratiquement pas de gaz à effet de serre.

La reconversion de H_2 en électricité n'est pas une seule possibilité. L'hydrogène produit peut également être converti en méthane en le faisant réagir avec le CO_2, le processus connu sous le nom de *méthanation.* On distingue deux types de ce processus. *La méthanation chimique* se passe à haute température (≈300°C) et en présence d'un catalyseur (le coût est ~ 400Euros/kW). La *bio-méthanation* est effectuée par des bactéries méthanogènes qui utilisent H_2 et CO_2 pour leur métabolisme et produisent du CH_4 et de l'eau. Elle se passe à basse température (35°C) et pression (90 bar) et coûte beaucoup moins cher que la méthanation chimique. La bio-méthanation peut

être réalisée dans les strates géologiques (*in situ biomethanation*) où les conditions thermodynamiques sont favorables. Le concept de la biométhanation in situ a été introduit en premier dans [Panfilov 2010], [Panfilov, Reitenbach, Ganzer, 2016].

La biométhanation in situ était observée dans le stockage du gaz de ville à Lobodice, situé dans le bassin de la vallée de Hornomoravsky, en République Tchèque. Outre la variation de la composition du gaz stocké dans le temps, qui était en accord avec la réaction de bio-méthanation, on observait le phénomène de formation des zones spatiales sursaturées en hydrogène, et autres zones sursaturées en méthane. Ces structures représentent des *patterns* qui sont typiques pour des systèmes de réaction-diffusion et sont souvent observées dans les processus accompagnés par une activité de microorganismes.

L'analyse que nous avons effectuée pour les processus de transport bio-réactif dans un stockage souterrain de H_2 démontre l'apparition de plusieurs types de patterns dans un tel système : un pattern stable en espace et stationnaire dans le temps, un pattern uniforme en espace, mais oscillant périodiquement et sans cesse dans le temps, un pattern oscillant dans l'espace et dans le temps simultanément. L'existence de telles structures signifie une hétérogénéité spatiale de l'hydrogène et du méthane, ce qui signifie que la méthanation ne couvre pas régulièrement le volume entier du stockage. Si l'objectif est de produire du méthane, alors la conversion ne sera pas complète. Si l'objectif est de stocker H_2 et le convertir ensuite en électricité, les patterns sont un phénomène plutôt positif si on peut augmenter la taille des zones occupées par H_2.

Ainsi, les critères d'existence de patterns est un problème important pour l'industrie, et pas uniquement purement théorique.

Pour convertir tout l'hydrogène en méthane, le rapport H_2/CO_2 dans la composition du gaz injecté devrait correspondre aux coefficients stœchiométriques de la réaction de méthanation. Un tel rapport devrait être maintenu uniformément dans tout le réservoir. Ce serait le meilleur scénario, qui garantirait une haute qualité du gaz produit. L'apparition de patterns pourrait réduire l'efficacité du processus de méthanation. Afin d'éviter leur apparition, nous avons effectué une analyse mathématique et numérique qui nous a permis de détecter les critères de leur apparition.

Un des problèmes les plus intéressants dans la théorie de patterns est l'existence de patterns spatio-temporels, qui représentent des fluctuations périodiques dans le temps et des mosaïques

périodiques en espace simultanément. Notre recherche était focalisée essentiellement sur ce problème.

Le point central de la thèse était consacré à l'impact de l'hétérogénéité du milieu sur les patterns. Nous avons analysé un milieu de double porosité décrit par un modèle macroscopique dans lequel les fractures et les blocs sont deux continuums coexistant qui s'échangent de masse des fluides et des bactéries. Les échanges étaient décrits par le modèle de Barenblatt. Le paramètre d'échange (*the exchange rate*) joue le rôle d'un paramètre responsable pour l'hétérogénéité du milieu : si le milieu est homogène, ce paramètre s'annule. L'interaction de l'hétérogénéité du milieu est des mosaïques causées par les phénomènes de réaction-diffusion est non triviale et peu étudiée dans la littérature. Nous avons trouvé un effet suivant.

Dans un système de double porosité classique, juste la diffusion sans réactions, son comportement après une perturbation initiale est tel qu'il tend vers un système homogène. Les concentrations dans les fractures et les blocs tendent vers une seule valeur limite. Si on rajoute une bio-réaction, alors il existe plusieurs possibilités. Une d'elles est la création d'un pattern identique ou les deux concentrations ; le système tend donc vers un système homogène, comme dans le cas classique. En même temps, il existe une autre solution qui ne tends plus vers un système homogène. Les concentrations dans les fractures et les blocks forment deux patterns différents. Nous avons trouvé les critères exacts d'existence de toutes ces structures.

Le milieu de double porosité à l'échelle non macroscopique était étudié numériquement. Nous avons montré l'apparition d'autres patterns qui ne peuvent pas être capturés dans le modèle macroscopique : ce sont des flaches de concentration qui apparaissent et disparaissent instantanément en courant à travers tout le domaine de façon très chaotique (*travelling flashes*).

Dans le dernier chapitre, nous avons analysé l'impact d'une hétérogénéité du milieu induite par des bactéries sur le transport de l'hydrogène dans un stockage. Une telle hétérogénéité peut être créée par la croissance de la population microbienne, l'attachement des microbes aux paroi des pores, le colmatage des pores, et la réduction de la porosité et perméabilité du milieu. Cela se passent uniquement dans des zones peuplées par les bactéries, et dans les directions de leur propagation, ce qui provoque aussi une anisotropie induite.

Dans ce contexte, nous avons développé un modèle conceptuel de bio colmatage et son implémentation dans un modèle numérique tridimensionnel conçu pour simuler le transport réactif couplé à la dynamique de bactéries. Ce modèle et ce code peuvent également être appliqués à d'autres formes d'écoulement en milieux poreux. Comme la base de notre code, nous avons utilisé un logiciel scientifique à accès libre destiné à la simulation des écoulements multiphasique et multi-composant en milieux poreux développé à l'Université de Stuttgart.

Nous avons montré que l'hétérogénéité induite par bactéries joue le rôle très positif dans le transport du gaz. En effet, si on injecte un gaz dans un aquifère, ce gaz va vite remonter vers la surface en s'étalant sous forme d'une mince couche au-dessus de la structure géologique. Création donc d'un vrai stockage de gaz devient problématique. Dans le cas avec des bactéries, étant le plus actives le long des lignes de courant ascendantes du gaz, elles créent des bouchons sur les trajets verticaux, en forçant le gaz de se propager horizontalement. Ainsi, la propagation due l'hydrogène dans un réservoir devient plus régulière et couvre toute l'épaisseur du réservoir.

La thèse est divisée en trois chapitres.

Le premier chapitre est une introduction à la technologie du stockage souterrain de l'hydrogène et de la biométhanation. Il présente aussi les effets biochimiques qui se produisent dans un stockage souterrain de l'hydrogène et fournit une revue sur les méthodes mathématiques de détection des patterns.

Dans le deuxième chapitre, nous portons notre intérêt sur la formation de patterns, initialement dans un milieu homogène, ensuite dans un milieu de double porosité. Les patterns spatio-temporels et les conditions de leur existence sont notre objectif majeur. Une simulation numérique à la fin du chapitre a pour objectif de capturer les patterns et voir leur forme dans le domaine de leur existence prédit par l'analyse théorique.

Dans le dernier chapitre, nous nous concentrons sur le développement d'un modèle conceptuel du colmatage des pores dus aux activités microbiennes. Le modèle doit incorporer le transport bioactif, le détachement/piégeage microbien, la croissance bactérienne et le biocolmatage. Le chapitre contient l'implémentation numérique du modèle dans le simulateur DuMuX, un logiciel scientifique open source développée à l'Université de Stuttgart et basé sur Dune développé par Heidelberg.

ملخص

يشهد العالم منذ بداية الثورة الصناعية ظهور العديد من التحديات البيئية، أبرزها الاحتباس الحراري ونضوب مصادر الطاقة التقليدية. في عصر الانتقال الطاقي، وفي ضوء الجهود الدولية المبذولة والرامية إلى اقتصاد محايد مناخيا بحلول عام 2050، أصبح الاعتماد على الطاقات المستدامة (Renewable ressources) مسلكا بديلا لا غنى عنه، وبالتالي مجالا نشطا للبحث الأكاديمي والتعاون الدولي. دول من بينها فرنسا، ألمانيا والمغرب اكدت عزمها على الرفع من سقف مساهمة الطاقات المتجددة في قطاعاتها الاقتصادية، لكونها طاقات نظيفة لا تنضب وقابلة للتجديد، غير أن مسألة تخزين الكهرباء التي تولدها المصادر المتجددة صارت تشكل أحد اهم التحديات القائمة، نظرا لتقلباتها وعدم استقرارها، خاصة الطاقة الكهربائية التي تولدها الرياح والطاقة الشمسية، نظرا لارتباطهما بالطقس.

مؤخرا ظهر مفهوم حديث لتخزين الطاقة وهو (Power to Gas) والذي يتمثل في تحويل الكهرباء إلى غاز عن طريق التحليل الكهربائي لجزيئات الماء بفصله إلى هيدروجين واوكسجين. فيعد الهيدروجين وسيلة مثالية لتخزين الكهرباء النظيفة لفترات طويلة من الوقت ويمكن إعادة تحويله بدوره إلى كهرباء نظيفة (Power to Gas to Power) .

الاطروحة تقدم دراسة نظرية وتحليل عددي (Numerical analysis) لإشكالية تخزين الهيدروجين تحت سطح الأرض (في حقول الغاز، مناجم الملح أو النفط المنضب)، وذلك إلى جانب ديناميكية البكتيريا المنتجة للميثان (الغاز الطبيعي) المسمات بالميثانوجينيات (Methanogenic bacteria)، فكما هو مبين في دراسات سابقة، هاته الأنواع من البكتيريا تعيش في باطن الأرض، تستهلك غاز الهيدروجين بشكل مكثف وتحوله إلى غاز الميثان.

التأثير المركب و المتقاطع لديناميكية الغاز و أنشطة البكتيريا المتباينة يؤدي الى تكون أنماط معقدة (Patterns) على مستوى توزيع غاز الهيدروجين داخل الخزان، الشيء الذي من شانه ان يؤثر على مدى جودة او سوء مخزون الغاز. من بين التأثيرات الأخرى التي قد وجدناها وهي انسداد المسامات (Pore-clogging) نتيجة لنمو و انتشار البكتيريا في الوسط، الشيء الذي بدوره يؤثر علي نفاذية الخزان و ديناميكية الغاز داخله.

CHAPTER I UNDERGROUND HYDROGEN: STORAGE OR METHANATION

Contents

1.1. INTRODUCTION

This chapter provides a general introduction to to the technology of underground hydrogen storage and biomethanation. In addition, it presents biochemical effects that were observed in real storages of hydrogen, including the effect of pattern formation.

In the first section, we describe the energetic stakes of hydrogen storage and the general physics of natural hydrogen reservoirs is described. In particular, we explain the instabilities present in these reservoirs, coming from bacteria that transform the reservoir into a bioreactor. We show that the complex dynamics correspond to those obtained for known reaction-diffusion equations which lead in particular to the formation of concentration patterns and temporal oscillations. We discuss in the second part of this chapter the different spatio-temporal bifurcations that allow to describe the physical mechanisms and the formation of these patterns.

1.2. TYPES OF HYDROGEN STORAGES

The production of electricity from renewable sources has fluctuant nature and is frequently produced in excess. This requires a large amount of storage capacity to store the energy (electricity) excessively produced. The conversion of this electricity into a gas (H_2) and underground storage of this gas in geological formations is the best option to store a large amount of energy. The choice of geological structures for underground hydrogen storage should be well detailed to avoid that hydrogen escape beyond the cap rocks (Davood Zivara et al. 2020.). In this context, recent research projects were launched such as **HyINTEGER(2016)**, **Underground Sun Storage (2012)**, **HyUnder (2012)**, **H2STORE(2012)** to investigate the feasibility of the process taking security, capacity, geobiophysicochemical features into account (Birger Haguemann et al. 2017). In this technology, to store hydrogen means to store electricity. After storing, H_2 is extracted and reconverted into electricity in fuel cells.

Another possibility to store hydrogen has the objective to convert it into methane, which is done by methanogenic bacteria inhabiting the porous rocks. In this case, the stored gas is considered as a fuel that will be finally burned for heating and lighting. As the energy potential of methane is higher than that of hydrogen, such a conversion means gas enrichment. To initiate the methanation reaction bacteria also need CO_2, which can be also injected together with hydrogen. In this case, we deal with an in situ methanation reactor.

Three major types of underground gas storage/reactors exist: salt caverns, aquifers, and depleted gas/oil reservoirs

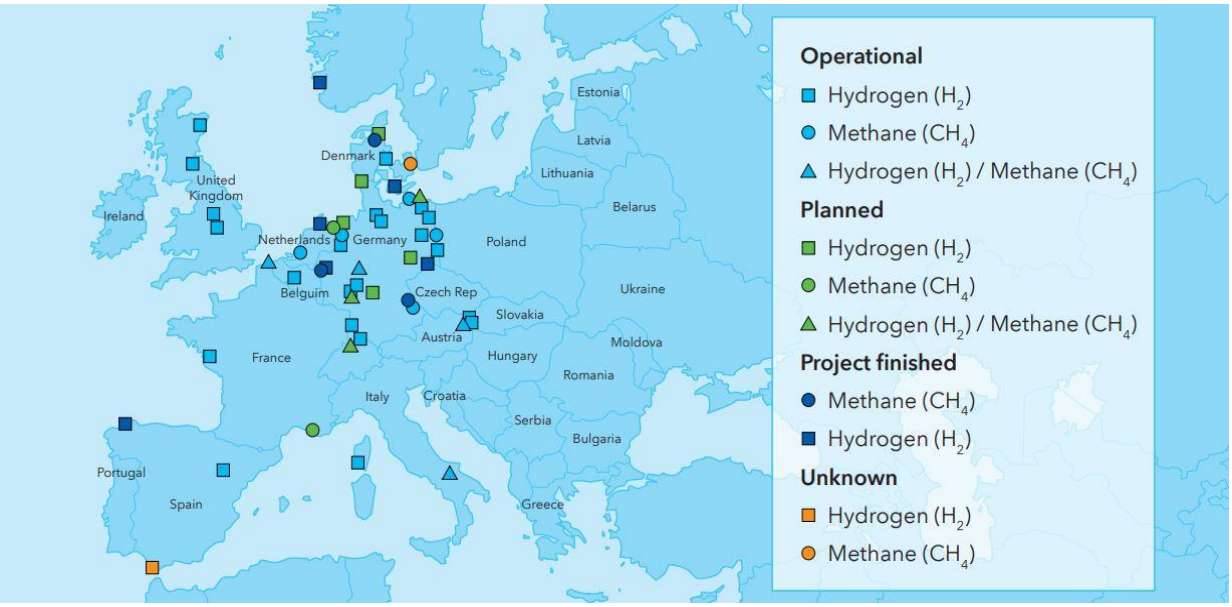

Figure I-1 Map for the implementation of underground hydrogen and methanation storage (European power to gas report)

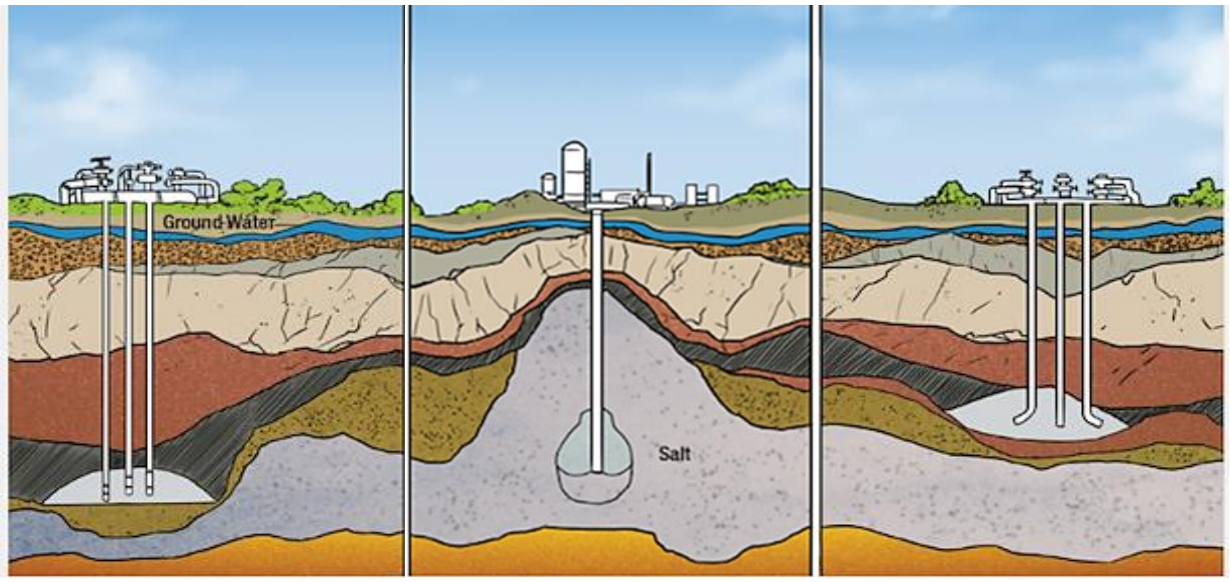

(a) **(b)** **(c)**

Figure I-2 Three major types of underground gas storage: (a) depleted gas/oil reservoirs, (b) salt cavern, and (c) aquifers

Underground gas storage type		
Depleted fields	**Salt caverns**	**Aquifers**
Highly porous and permeable	Very porous and permeable	Porous and permeable
Very high - high storage capacity	High storage capacity	Highest storage capacity
Successfully tested with natural gas mixture	Successfully tested with natural gas mixture	Successfully tested with pure hydrogen and other gases
	Do not react with hydrogen Low bacterial activities because of the higher concentration of brine	High potential of hydrogen's interaction with the rocks, fluids, and microorganism
	Allow higher injection and withdrawal rates Maximum operating pressure: 20 MPa	
Geological settings already well known		

Table 1 Comparison of types of underground gas storage (A. Ebrahimiyekta 2017)

Underground hydrogen storages and biomethanation storage require different geological conditions, which are summarized in the following table:

Technology		
Properties	**Underground hydrogen**	**Underground bio-methanation**
Purpose	storage	Conversion and storage
Gas	H_2 pure	CH_4, H_2 and CO_2
Underground storage type	Porous rock or salt cavern	Porous rock
Depth, m	< 3500	< 2000
Permeability, mD	> 50	
Porosity	> 0.1	

Table 2 Comparison of underground hydrogen storage and underground biomethanation storage(G. Strobel et al. 2020)

Operating site	Storage type	Depth [m]	H_2 [%]	Working Conditions	
Lobodice, **Czech Republic**	Aquifer	430	50	45-59 bar	25-45 °C
Rough gas storage facility, **UK**	DGR*	2743	-	50 - 60 bar	-
Kiel, **Germany**	Salt cavern	-	60	80 - 100 bar	-
Beynes, **France**	Aquifer	439	50	-	-
Underground Sun Storage, **Austria**	DGR*	1000	10	78 bar	40 °C
Mount Simon aquifer, **Canada**	Aquifer	800	-	76 bar	-
Tuz Golu gas storage site, **Turkey**	Salt cavern	1100 - 1400	-	220 bar	-
Lille Thorup, **Denmark**	Salt cavern	1270 - 1690	-	50 – 100 bar	40 – 50 °C
Hychico, **Argentina**	DGR*	600 - 800	Pure	25 bar	-

*Depleted gas reservoir

Table 3 Worldwide hydrogen storage potential sites (D. Zivar et al. 2020)

1.2.1. Hydrogen as the energy carrier. Hydrogen and electricity

Hydrogen and electricity are two sides of the same coin. Hydrogen is expected to become the principal energy carrier by 2050 (Marc A. Rosen et al. 2014). The conversion of renewable electricity into hydrogen H_2 can be done by separating molecules of water using electricity (electrolysis). The process is reversible (i.e., power to make gas to make power), so that the inverse conversion of the electricity into hydrogen occurs in fuel cells. This results in virtually zero greenhouse gas. The produced hydrogen (H_2) is a carbon-free fuel that can lead to the decarbonization of the transport sector and energy-intensive industries. Hydrogen can be used as a clean fuel cell enabling emission-free industrial, commercial, transportation…., could be easily transported in large volume and provide an infinite supply. However, providing hydrogen at a lower cost is still a challenging issue (Office of Energy Efficiency & Renewable Energy of US).

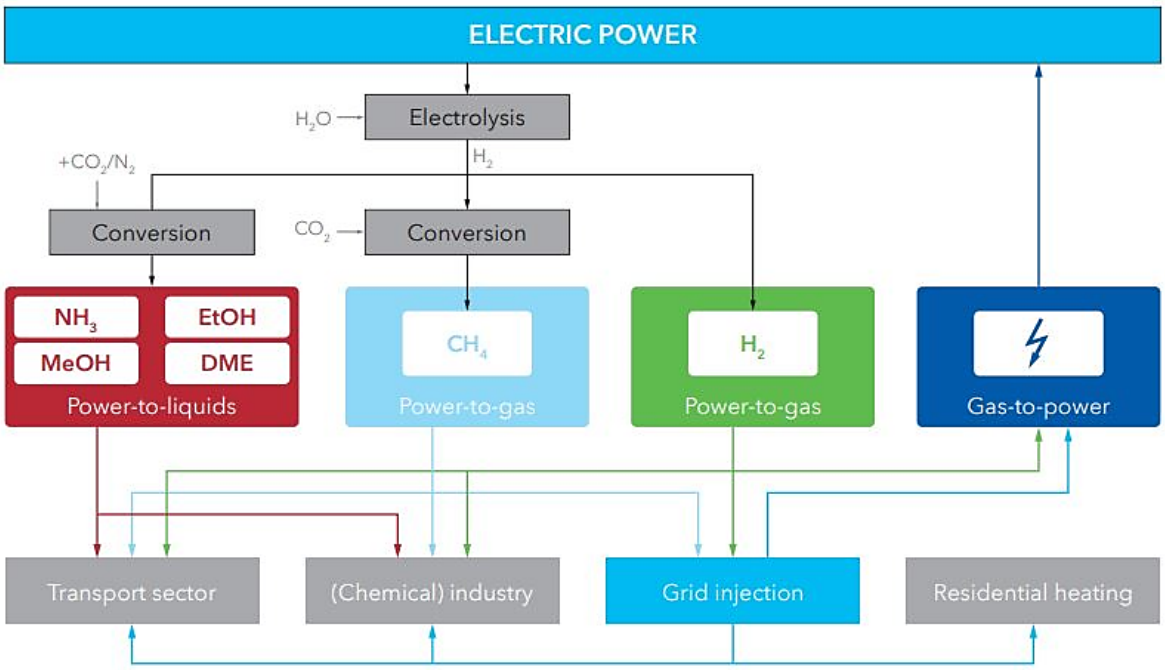

Figure I-3 Power to gas concept (European power to gas report)

1.2.2. Hydrogen as source of methane.

The term methanation refers to the reaction of hydrogenation of Carbone dioxide to generate methane CH_4. The reaction was discovered in 1902 by Paul Sabatier and J.B. Sendersens. In the presence of catalysts, hydrogen and carbon dioxide react at high temperatures and produce methane and water. (Martin Seemann et al. 2019)

The methanation process can be realized in two different manners: synthetically (chemical methanation) at high temperatures (≈ 300°C) and in the presence of an expensive catalyser which can costs ~400Euros/kW_{CH4} or by bacteria (bio methanation) that initiate the chemical reaction and optimize the process and realize it at low temperature (≈ 35°C) and 90 bar. The last manner cost the industry less than the previous one. With the development of renewable electricity and energy storage solutions, biomethanation is becoming more and more considered (Robert A. Dagle et al. 2011). The last United Nations Climate Change Conference in Paris (COP21) fixed an urgent challenge of lowering carbon emissions from electricity supply to nearly zero by 2050 (European Power to gas). The biomethanation provides a realistic way to recycle carbon through

the conversion of CO2 into methane and constitutes a promising solution toward carbon neutrality goals.

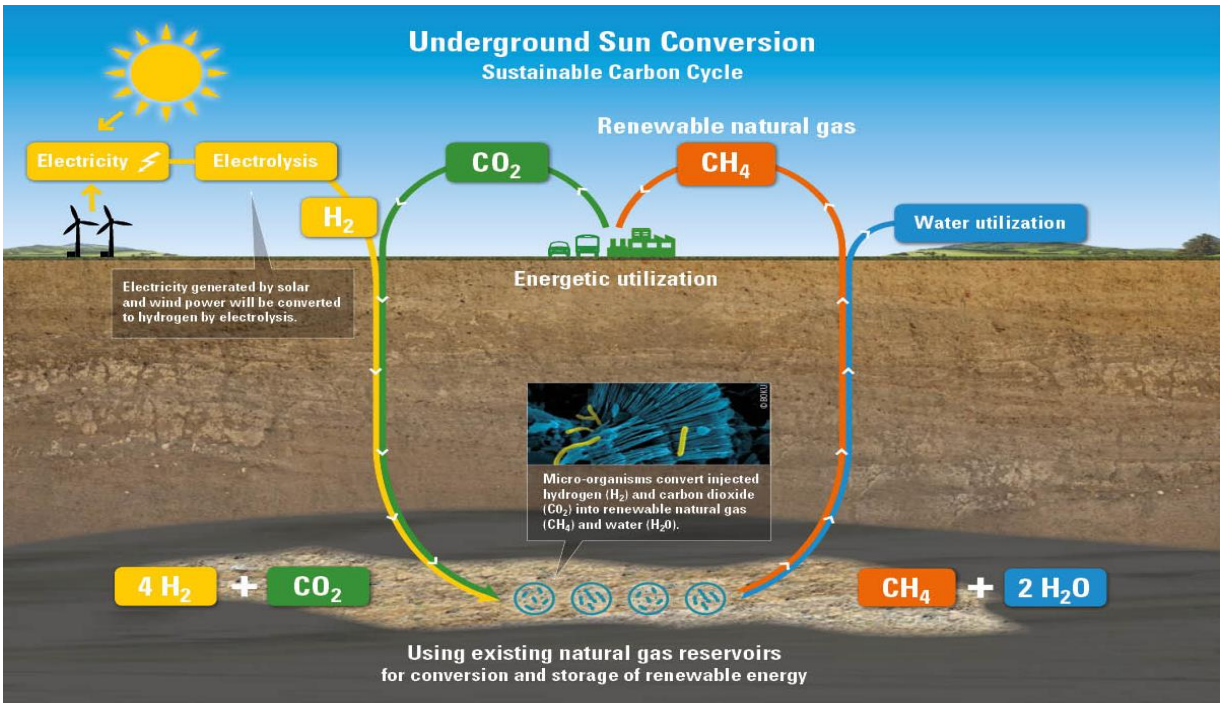

Figure I-4 McPhy project

1.2.3. Hydrogen and methane properties

Generally, hydrogen has a low ignition temperature and a wide flammability range, making leaks a significant hazard for fire and explosion (Portarapillo et al. 2021). Knowledge of the physical properties of Hydrogen and methane allows for safe and successful storage. The energy content of hydrogen is more than 2 times higher than that of methane, making it the fuel with the highest energy content per unit mass. Compared to methane, hydrogen gas is eight times less dense than methane at ambient temperature and pressure which requires a higher pressure (D. Zivar et al. 2020). The lower viscosity of hydrogen induces higher mobility of hydrogen and higher removal efficiency compared to methane. However, this makes Hydrogen very diffusive through the caprocks compared to other gases. At ambient temperature and pressure, methane has a diffusion coefficient three times less than that of hydrogen.

Physical properties at 25°C and 1bar	Hydrogen H_2	Methane CH_4
Heating value, KJ/g	120-142	50-55
Density, kg/m^3	0.0899	0.657
Viscosity, 10^{-5} Pa.s	0.89	1.12
Diffusion coefficient, 10^{-9} m^2/s	5.13	1.85

Table 4 Physical properties of hydrogen and methane (D. Zivar et al. 2020)

1.2.4. Experimental data on underground biomethanation (Lobodice)

The most known project of Underground bio methanation is the Lobodice town gas storage in an aquifer structure near Lobodice, Czech Republic. The underground reservoir was created in water-saturated strata where anaerobic bacteria pressurized with hydrogen / Carbone dioxide mixture (with the ratio 4/1) at the conditions T=25-45°C and P=40 MPa. The initial existing components were H_2=54%, CH_4=21.90%, CO=9%, CO_2=11.67% and N_2=2.5% . The amount of methanogenic microorganisms was about 10^3-10^4 cells per ml. The biomethane production was evaluated before and after.

Within 7 months (Frantisek Buzek et al. 1990) reported a significant variation in the composition of the stored gas (losses of 20% of hydrogen and 2.89% Carbone dioxide). The pressure loss was up to 10% (G. Strobel et al. 2021).

The decrease in pressure can be explained by the transition of part of the gas to the liquid phase, increasing density, and allowing the expansion of the remaining gas phase part. The decrease in pressure was initially attributed to possible gas leaks, however, this explanation did not explain the increase of methane. The only possible explanation for the increase in methane and Hydrogen and carbon dioxide reduction was to assume that the following reactions were happening within the reservoir (D S-K. Ting et al. 2021):

$$4H_{2(l)} + CO_{2(l)} \rightarrow CH_{4(l)} + 2H_2O_{(l)} + \text{energy}$$

However, under the conditions 35°C and 90 bar, this reaction is only possible by methanogenic bacteria. Hydrogen and carbon dioxide are dissolved inside the bacterium cell creating COH+ cation (electron acceptor), while protons separate an electron from the hydrogen. This free

electron reacts with the cations, and after a long Serie of steps, methane, water, and energy which the bacteria consume are produced (Panfilov et al. 2015, D S-K. Ting et al. 2021).

Meanwhile, respiration activates nutrition metabolism, which consists of the consumption of carbon from CO_2 to produce biomass within the cell body (carbon fixation). This increases biomass size and when biomass reaches critical mass, the cell divides in two (Biomass production).

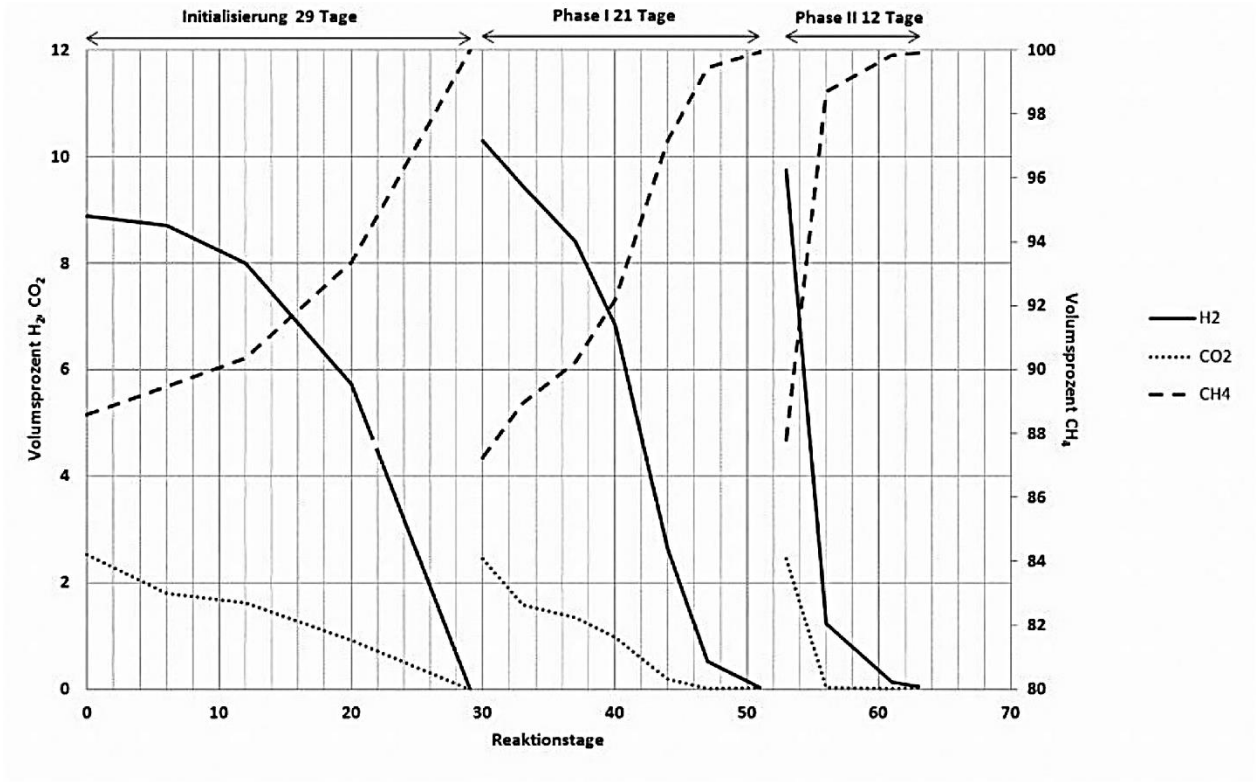

Figure I-5 Methane production from H2 and CO2 (Gion Strobel et al. 2020)

1.2.5. Experimental data on patterns in underground methanation (Lobodice)

Bacterial production alters the gas and liquid flow. Likewise, any flow changes can impact the dynamics of bacterial growth. The coupled effects generate self-organizing phenomena, which arise in the form of large-scale spatial and temporal oscillations of gas concentration (Panfilov

2010). Such phenomenon was observed in Lobodice town storage. (Frantisek Buzek et al. 1990) reported that the distribution of the resulted chemical component within the reservoir was variable in time as in space. Regions were more enriched on H_2 while others were dominated by CH_4. At that time, such effects were less known. The existence of such a problem can significantly affect the technical solutions.

To convert all the injected H_2 and CO_2 into methane, the ratio H_2/CO_2 in the composition of the injected gas should correspond to the stoichiometric coefficients of the Sabatier reaction and such a ratio should be maintained uniformly in the entire reservoir. This would be the best scenario, which would ensure the high quality of the gas produced. However, any non-uniform pattern could reduce the methanation efficiency. In 2010, (Panfilov, 2010) developed a mathematical model for underground hydrogen storage capable to generate the observed patterns and explained their origins.

1.2.6. Microbial reactions

Bacteria are microorganisms that can live in exceptionally harsh environments, like extremely high, low temperatures, or high pH values. They fall into several forms: biofilm, Slimy film of biomass attached to the pore walls, planktonic, tiny organisms floating in the pore-water solution, and/or Neuston attached to the phases interface (Trevor R. Garett et al. 2008). Microbial activities in underground hydrogen storage and their interaction with gases must be thoroughly analyzed as they significantly affect the physico-geo-chemical properties of the reservoir and gas stored purity. Microbial reactions are hard to manipulate due to the miss of data and that depend on the complex behavior of microbes (metabolism) which depend on in turn to its surrounding environment. In underground hydrogen storage, three types of bacterial processes could be considered in the presence of high concentrations of hydrogen:

Methanogenesis:

$$4H_2 + CO_2 \rightarrow CH_4 + 2H_2O$$

The CO_2 can be present in the injected gas or in the carbonaceous rocks in the reservoir.

Acetogenesis:

$$2CO_2 + 4H_2 \rightarrow CH_3COOH + 2H_2O$$

Sulfate-reduction:

$$SO_4^{2-} + 5H_2 \rightarrow H_2S + 4H_2O$$

The sulfate can be present as dissolution in aquifers

Ferric-reduction:

$$3Fe_2^{3+}O_3 + H_2 \rightarrow 2Fe_3^{2+}O_4 + H_2O$$

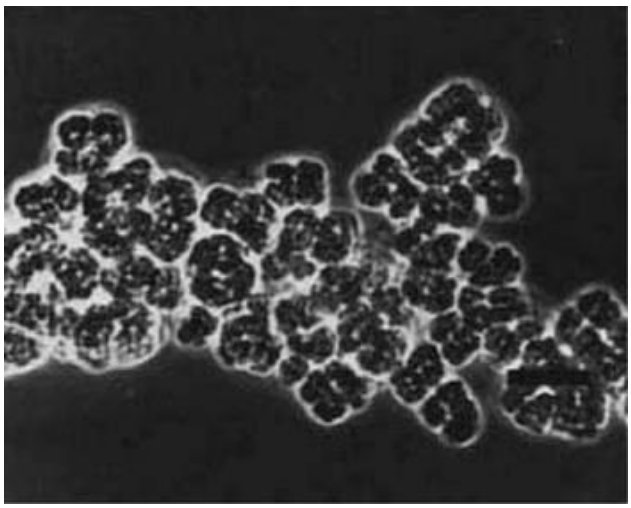

Figure I-6 Electron microscopic image of methanogens (William B. Whitman et al.)

1.3. PATTERNS AND WAVES IN REACTION-DIFFUSION SYSTEMS

1.3.1. Classical diffusion-reaction systems, self-organization, patterns

The first mathematical analysis of patterns was given by the British mathematician and computer scientist A. M. Turing. In 1952, A. M. Turing published his paper entitled: "*The chemical bases of morphogenesis*", in which he demonstrated that the competition between the reaction and the diffusion can generate complex oscillatory solutions (Turing's patterns), a periodic spatial distribution of concentration of morphogenesis which breaks the symmetry of the system. At that

time, this idea aroused little interest due to the fact that was based on an apparent paradox because the diffusion should erase the fluctuations and homogenize the system. Nowadays, there is some qualitative evidence of the capability of Turing models to imitate biological self-organization (V. K. Vanag 2004, Baba Issa Camara et al. 2009). The study of biochemical patterns in reaction-diffusion systems has attracted considerable interest in a large domain of applications but is still less studied in Underground gas storage processes.

The simplest form of reaction-diffusion system is the activator-inhibitor system. The system describes two diffusible components that interact with each other through specific reactions. Turing had already laid the foundation for such a two-component system with linear reaction terms (Turing, 1952)

$$\begin{aligned} \frac{\partial u}{\partial t} &= D_u \Delta u + f(u,v) \\ \frac{\partial v}{\partial t} &= D_v \Delta v + g(u,v) \end{aligned} \qquad \text{Eq I.1.}$$

This model is the base to study the mechanisms leading to morphogenesis and has proved a useful description of phenomena in a large list of fields: Biology, Chemistry, Physics, Ecology, and Economics (Siegfried Roth 2011). The most well-known oscillatory models are Brusselator, Belusov-Zhabotinsky chemical reaction, and Fitzhugh-Nagumo systems (Siegfried Roth 2011).

As mentioned, the interaction between the locally occurring reaction and the transport of species by diffusion allows the formation of various nontrivial phenomena. The classification of different patterns that may exist grows continuously since the reported by (Belousov and Zhabotinskii 1950).

Here, classical types of bifurcations responsible for the appearance of patterns:

- the space independent Hopf bifurcation (at least 2D-reaction diffusion system) (Yifu Wang et al 2007)
- the stationary Turing bifurcation (in 2D-reaction diffusion system) (Shigefumi Hata et al 2014, V. K. Vanag 2004, Baba Issa Camara et al. 2009).
- Wave bifurcations (Standing waves, spiral waves, in 3D-reaction diffusion system or more) (Lingfa Yang et al 2004, Nathaniel Karst et al 2016)

- Other complex patterns exist resulting from the interaction of two types of bifurcations or more (Hopf-Turing instabilities, Hopf-Waves instabilities, Turing waves patterns…) (Lingfa Yang et al 2004, Nathaniel Karst et al 2016)

Bifurcation refers to the qualitative change in the dynamics of the system I.1. At the bifurcation point, the stability of equilibrium states typically changes.

1.3.2. Method of detection of patterns

The patterns correspond to an unstable uniform distribution of the gas concentrations (the plateau solutions). This uniform distribution is the state (u_s, v_s) satisfying the conditions $f(u_s, v_s) = g(u_s, v_s) = 0$ of the system I.1. Stability refers to the capacity of the system to resist small perturbations. There are two different definitions of stability.

Definition 1. ***Stability in the sense of Lyapunov***

The equilibrium state is stable in the sense of Lyapunov if the perturbed system never deviates very far from (u_s, v_s).

Definition 2. ***Stability in the sense of asymptotic stability***

The equilibrium state is asymptotically stable if it satisfies the previous condition and, in addition, the perturbed system tends to return to the original state (u_s, v_s) with time. An asymptotically stable system is also stable in the sense of Lyapunov, but the opposite is not always true. Finally, we say that a state is unstable if it is not stable (R. Murray et al. 1994).

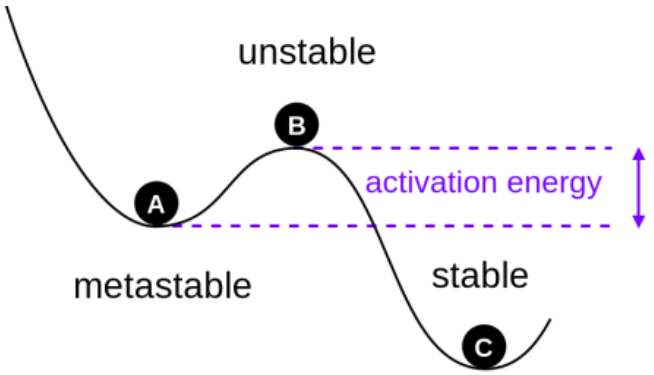

Figure I-7 concepts of equilibrium and stability

A third situation may exist called metastable which refers to the state where a deviation from the equilibrium cannot be observed because the changing is too slow.

Thus, based on the mathematical model, we should perform a linear stability analysis by linearizing the system near to the equilibrium state verifying the plateau solutions. We disturb the homogeneous steady by small-amplitude perturbations. Next, we express the instability conditions for pattern formation in terms of eigenvalues of the linearized system, which depends on the growth rates of the perturbation. We plot the eigenvalues as a function of each of the wavenumber to obtain the dispersion relation. The shape of the dispersive curve provides the nature of the instability (Panfilov 2010). The system is stable if and only if all eigenvalues should be negative in the absence of diffusion.

Eigenvalues, μ	Effect on the homogeneous steady state
All reals and negatives	Driven back the homogeneous steady state
All reals and one or more are positive	Driven away
All reals are negative and there are imaginary parts	Oscillate around the steady-state with decreasing amplitude
One or more have a positive part and there are imaginary parts	Oscillate around the steady-state with increasing amplitude
Imaginary pure	Oscillate around the steady-state with increasing amplitude

Figure I-8 stability evaluation

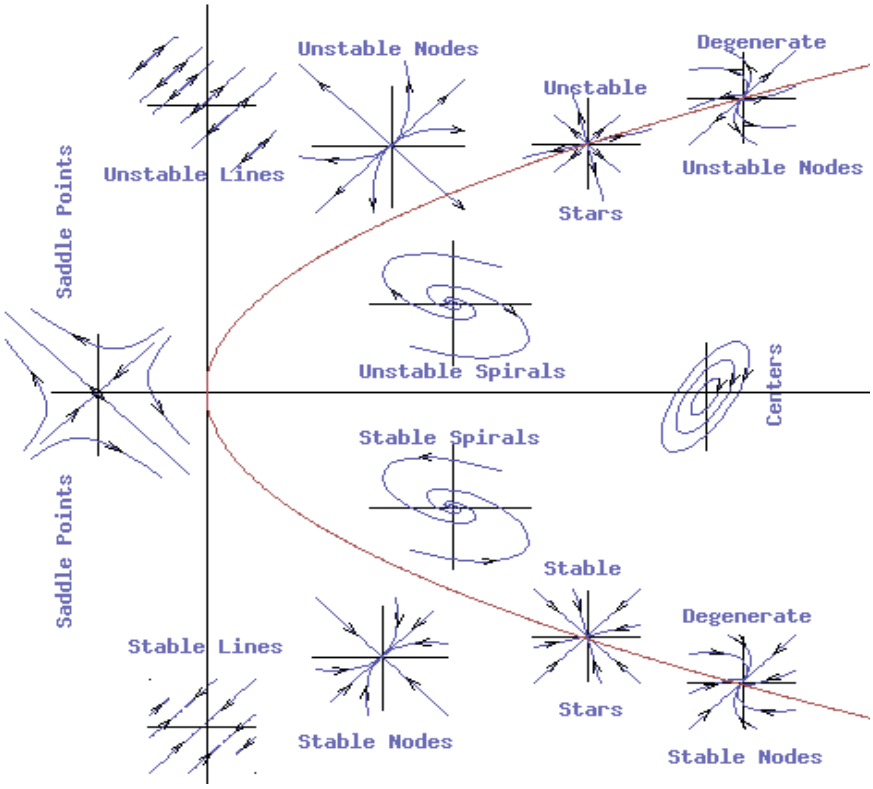

Figure I-9 Types of phase portrait

1.3.3. Turing's instability and stationary patterns

Turing structures correspond to the spatially periodic variations in the concentrations of chemical species. Their characteristics are determined intrinsically and not by external factors. They occur when a spatially uniform steady-state solution stable in the absence of diffusion, becomes unstable when diffusion is present (i.e., the system I.1 self-organizes in the area of the intersection of the stable zone of the dynamical system and the unstable zone of the diffusive system). The stable zone of the diffusionless state corresponds to attenuating oscillations in time, i.e. to a negative real part in the eigenvalues.

Turing patterns appear to have a particular interest not just in biology (Stripes, spots, or reversed spots in two-dimensional Turing systems, H. Shoji et al 2003) and pure/applied chemistry (chlorine dioxide-iodine-malonic acid reaction-diffusion system, D. Feldman et al. 2012; Belousov–Zhabotinsky reaction in liquid marbles, C. Fullarton et al. 2019), but also in geomorphology (Pattern formation in the geosciences, Lucas Goehring 2004), ecology (Dispersal-induced destabilization of metapopulations and oscillatory Turing patterns in

ecological networks, S. Hata et al. 2014), sociology studying phenomenon of crime hotspots using Turing systems (on localized hotspots of an urban crime model, D. J. B. Llyold et al. 2014) and perhaps even a reaction-diffusion mechanism has been suggested as the origin of spiral galaxies in astrophysics).

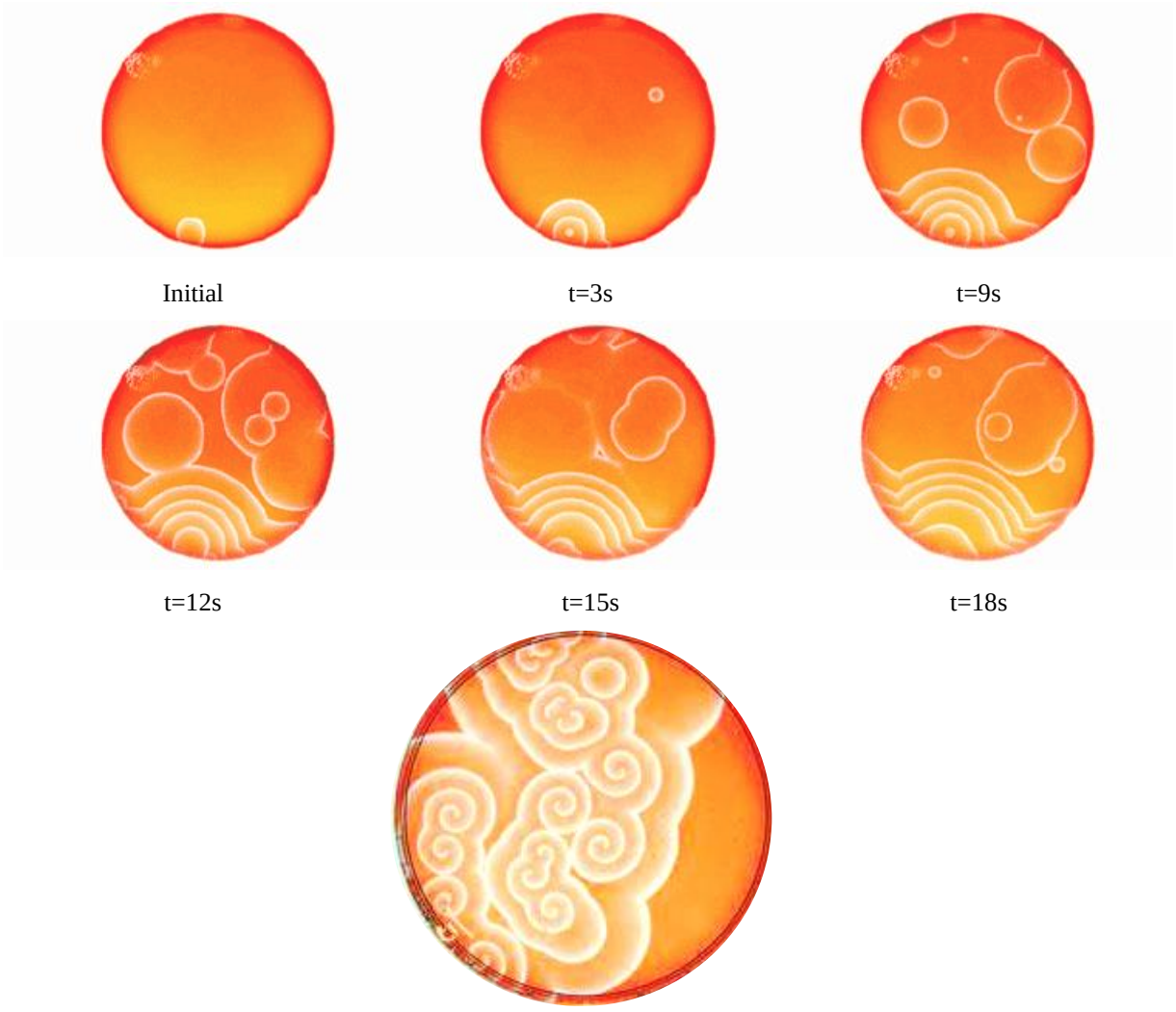

Figure I-10 An experiment of Belousov–Zhabotinskii chemical reactions (X. Yang et al. 2018)

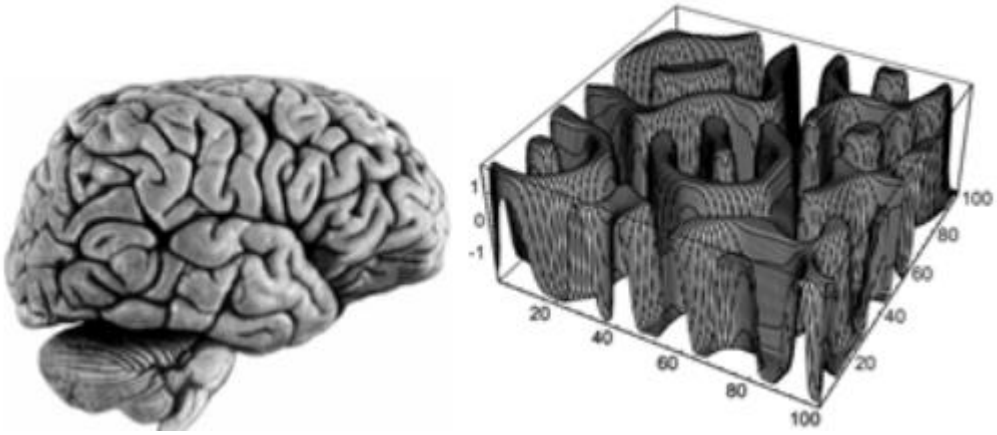

Figure I-11 Labyrinthine Turing pattern formation in the cerebral cortex (J. Cartwright 2002)

Figure I-12 A real jaguar at the left and a Turing Pattern at the right (K. J. Painter 2000)

1.3.4. Hopf-Andronov's bifurcation, instability, and dynamic patterns

The bifurcation of Hopf-Andronov corresponds to a periodic oscillation in time and uniform in space, which attracts other solutions of the system I.1 at $t \to \infty$ to a closed trajectory in the phase space, which attracts other trajectories. Such a structure is called the limit cycle. In the case of two ODE, the limit cycle is a closed two-dimensional curve. In a system of ODEs of higher dimensions, the limit cycle has the form of a multidimensional torus.

CHAPTER II MODELLING OF TWO-PHASE BIO-REACTIVE TRANSPORT IN UNDERGROUND HYDROGEN STORAGE

Contents

2.1. INTRODUCTION

The second chapter is devoted to the analysis of spatiotemporal patterns formation and the conditions of their emergence in underground hydrogen storage. We start with a short introduction to multicomponent two-phase flow in porous media with chemical reactions, and to the theory of patterns in dynamical systems. We examine next homogeneous media and develop the technique of stability analysis of reaction-diffusion systems in application to the transport phenomena in an underground storage of hydrogen. After this, we extend our analysis to heterogeneus media, which is analysed in terms of a macroscopic double porosity model and analyze the impact of the natural reservoir heterogeneity on the criteria of pattern existence. Next, we carry out a numerical simulation to capture the regimes when these criteria are verified.

2.2. MATHEMATICAL MODEL OF TWO-PHASE BIO-REACTIVE TRANSPORT

The modeling of biogeochemical processes in porous media is hard to set up as they result from complex interactive physical, biological, and geochemical processes and occur on different spatial and temporal scales. The first part of this chapter is devoted to the modeling of two-phase bio-reactive transport in underground hydrogen (H_2) and carbon dioxide (CO_2) storage. Modeling two-phase flow coupled to bio-reactive transport requires the consideration of flow processes such as advection, diffusion, biochemical processes being microbial growth and decay, and microbial production/consumption.

Different approaches may be considered depending on the interest scale (Timo Koch et al 2021), ranging from molecular scale [$\sim 10^{-10}$ m] to field scale [$\sim 10^{2}$ m]. In this thesis, our model is based on a macro scale (REV, continuum, or Darcy scale) description which is the most used by large in-situ applications. At the macro scale, the different processes are averaged over an appropriate representative elementary volume (REV) that can give realistic information on the

porous medium (Andreas Bielinski 2007, Johannes Martin Hommel 2016, Birger Hagemann 2017). Due to the averaging procedure, the following scale calls upon a new volume averages variable not known at the micro-scale like the porosity, permeability, and phase saturation.

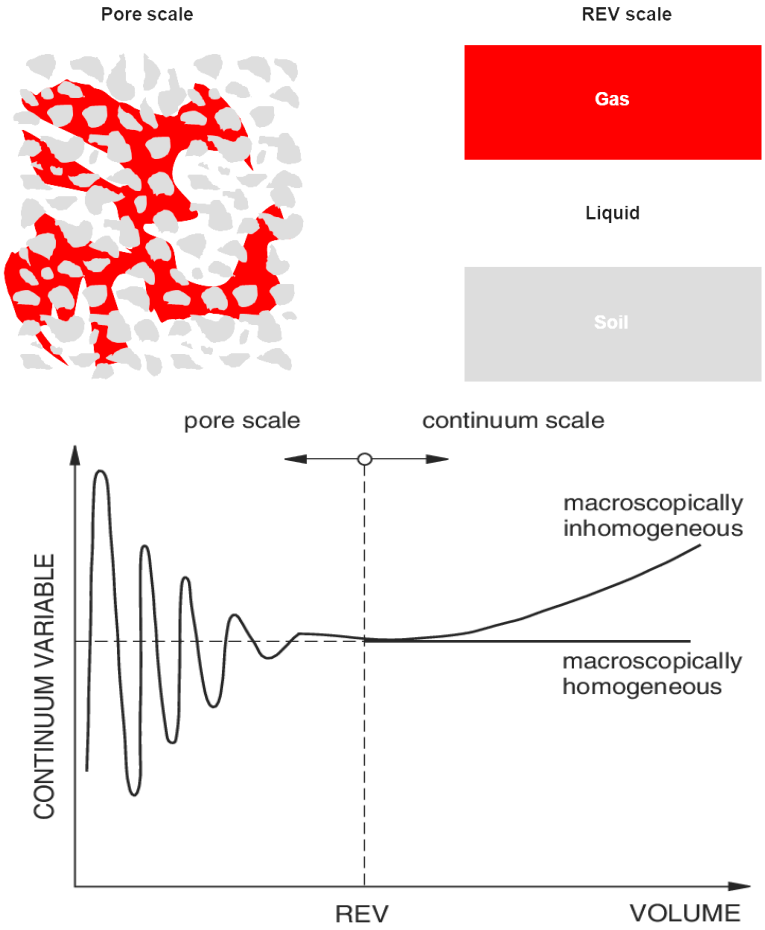

Figure II-1 From pore scale to continuum scale modeling (Andreas Bielinski 2007)

2.2.1. Physical description of the system

Porous medium properties:

- ***Porosity or void fraction*:** a measure of the void volume in a porous medium. It determines the ratio between the volume of the pores and the total volume:

$$\phi = \frac{V_{fluid}}{V_{total}} = 1 - \frac{V_{solid}}{V_{total}} \quad \text{Eq II.1.}$$

- ***The absolute (intrinsic or specific) permeability*** indicates the ability of the rocks to conduct fluid. It is a property characteristic of the porous medium and it is independent of the fluid (Kun Sang Lee 2020).

  The permeability can be obtained from the general Carman-Kozeny formula (Carman-Kozeny 1937):

$$K = \left(\frac{{d_T}^2}{180}\right)\frac{\phi^3}{(1-\phi)^2} \quad \text{Eq II.2.}$$

  d_T is the characteristic diameter of a pore. The unit for permeability used in UGS applications is Darcy or Millidarcy.

Fluid properties:

- ***Density*** **:** defined as mass per volume (mass density) or the number of moles per volume (molar density). The density of a substance changes with pressure and temperature.

- ***Viscosity:*** measures the resistance of the fluid to flow. For Newtonian fluids, it's defined as a proportionality factor which relates the fluid's shear tension τ to the velocity gradient:

$$\tau = \mu\left(\frac{\partial V_{\alpha,x}}{\partial y}\right) \quad \text{Eq II.3.}$$

Phases and components:

- ***Mole and mass fraction:*** *they* describe the composition of a phase**.** Mole fractions c_α^k are defined as the number of moles of a component k divided by the total number of moles in the system within phase α :

$$c_\alpha^k = \frac{x_\alpha^k}{\sum_k x_\alpha^k} \quad \text{Eq II.4.}$$

While the mass fraction C_α^k is defined by:

$$C_\alpha^k = \frac{m_\alpha^k}{\sum_k m_\alpha^k} \quad \text{Eq II.5.}$$

Consequently, the sum of the mole fractions and mass fractions of components *k* in phase α is:

$$\sum_k c_\alpha^k = \sum_k C_\alpha^k = 1 \quad \text{Eq II.6.}$$

Fluid phase interactions in porous media:

For multiphase systems, fluids are interacting with each other which demands the introduction of additional properties.

- ***Fluid saturation:*** a measure of the percent of the pores filled with a fluid phase (gas or water). This property is expressed by the ratio between the volume of the pores filled with phase α and the total pore volume:

$$S_\alpha = \frac{V_\alpha}{V_{pores}} \quad \text{Eq II.7.}$$

By definition, the sum of phase saturations $\sum_\alpha S_\alpha = 1$ is equal to the unity.

- ***Capillary pressure****:* evaluates the pressure difference across the interface creating between two immiscible fluids in contact (Gas and water in our case). The expression of P_c on the continuum scale should be defined based on averaged variables of that scale. The *Brooks and Corey's and Van-Genuchten's models* are the *most used* empirical functions in Reservoir engineering :

  - *Brooks and Corey's* model (1964):

$$p_c = p_g - p_w = P_e \left(\frac{Sw - Swr}{1 - Swr - Snr} \right)^{-\frac{1}{\lambda}} \quad \text{Eq II.8.}$$

- *Van-Genuchten's* model (1980):

$$p_c = p_g - p_w = \frac{1}{\delta}\left(\left(\frac{Sw - Swr}{1 - Swr - Snr}\right)^{-\frac{1}{m}} - 1\right)^{(1-m)} \qquad \text{Eq II.9.}$$

P_e is the entry capillary pressure. S_{wr} is the residual wetting phase saturation that cannot be displaced by the non-wetting fluid phase and remains in the porous medium. Both models are empirical, consequently, the parameters for these relationships (λ, m) can be found experimentally depending on the pore size distribution.

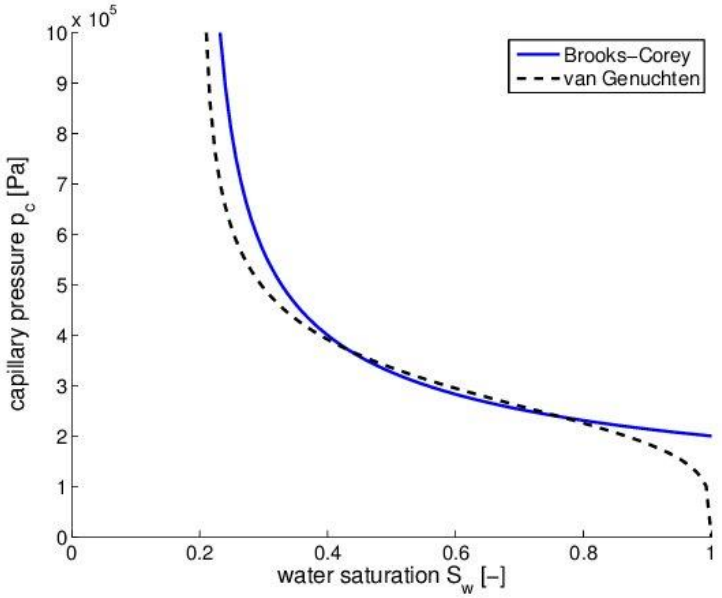

Figure II-2 Capillary pressure after Brooks & Corey (1964) and van Genuchten (1980) (Henrik Büsing et al. 2014).

- ***Relative permeability:*** The relative permeability appears when the flow of phase α is disturbed by the other phase because the pore space where the fluid phase α can flow through is partially or totally occupied by the other fluid phase. $k_{r\alpha}(S_w) \in [0,1]$ and depends on the saturation, a phase α becomes more mobile as the saturation of this phase increase in the porous medium.

The most commonly used empirical models for calculating $k_{r\alpha}(S_w)$ are:

- the *Brooks-Corey's* model (1964):

$$k_{rw} = \left(\frac{S_w - S_{wr}}{1 - S_{wr} - S_{gr}} \right)^{\frac{2+3\lambda}{\lambda}},$$

$$k_{rg} = \left[1 - \left(\frac{S_w - S_{wr}}{1 - S_{wr} - S_{gr}} \right) \right]^2 \left[1 - \left(\frac{S_w - S_{wr}}{1 - S_{wr} - S_{gr}} \right)^{\frac{2+\lambda}{\lambda}} \right], \quad \text{Eq II.10.}$$

- and *Van Genuchten's* model (1980):

$$k_{rw} = \left(\frac{S_w - S_{wr}}{1 - S_{wr} - S_{gr}} \right)^{\gamma} \left[1 - \left(1 - \left(\frac{S_w - S_{wr}}{1 - S_{wr} - S_{gr}} \right)^{\frac{1}{m}} \right)^m \right]^2,$$

$$k_{rg} = \left(1 - \left(\frac{S_w - S_{wr}}{1 - S_{wr} - S_{gr}} \right) \right)^{\xi} \left[1 - \left(\frac{S_l - S_{wr}}{1 - S_{wr} - S_{gr}} \right)^{\frac{1}{m}} \right]^{2m}. \quad \text{Eq II.11.}$$

(λ, m) are the same from *Brooks and Corey's* and *Van-Genuchten's* $k_{r\alpha} - S_w$ correlations. The remaining parameters γ and ξ describe the connectivity of the pores. The often-used values are $\left(\gamma = \frac{1}{2}, \xi = \frac{1}{3} \right)$.

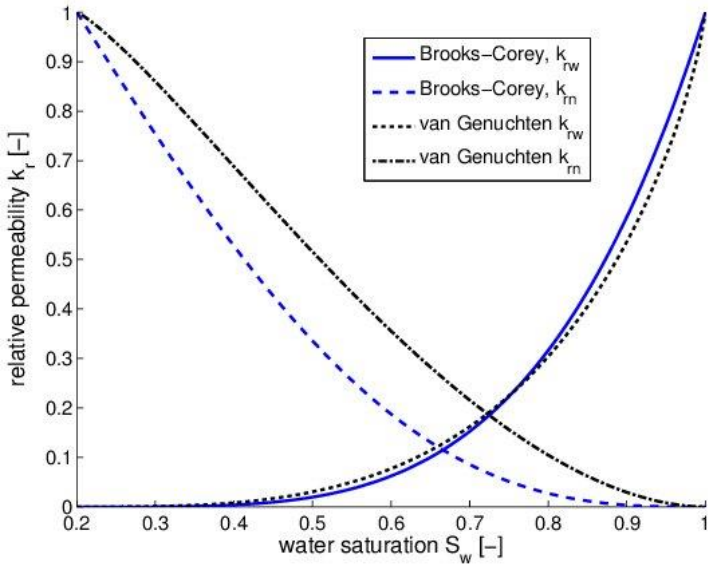

Figure II-3 Relative permeability-saturation relations after Brooks & Corey (1964) and van Genuchten (1980) (Henrik Büsing et al. 2014).

- ***Thermodynamic equilibrium:*** The mass exchange between the phases takes place at a very fast rate w.r.t the other biochemical processes, therefore the composition of both phases is assumed to be in thermodynamic equilibrium. The assumption is widely used in Geochemical processes and petroleum simulations (Birger Hagemann 2017). The condition of thermodynamic equilibrium between the two phases can be expressed with the equality of fugacities:

$$f_g^k = f_w^k \text{ where } f_\alpha^k = P_\alpha \varphi_\alpha^k c_\alpha^k \qquad \text{Eq II.12.}$$

Transport processes in porous media:

- ***Advection:*** Forced horizontal motion due to pressure gradient created by the injection well. On the macro-scale models of two-phase flow, the momentum balance equation is reduced to Darcy's law, which represents the dependence of average velocities V_α on the phase pressures P_α and gravitational forces.

$$\mathbf{V}_\alpha = -\frac{k_{r\alpha}(S_\alpha)}{\mu_\alpha}\mathbf{K}\ \nabla P_\alpha - \rho_{mass,\alpha}\mathbf{g} \qquad \text{Eq II.13.}$$

K is the absolute permeability; μ_α is the dynamic viscosity of the phase α; $\mathbf{g}$ is the gravity acceleration vector. The ratios $\lambda_\alpha = k_{r\alpha}(S_w)/\mu_\alpha$ represent the mobility of the phase α, $\alpha = \{w, g\}$ The sum $\lambda_w + \lambda_g$ is the total mobility.

- ***Diffusion:*** refers to the net motion of chemical component from the region of high concentration to other of lower. The driving force here is the concentrations gradient. The diffusive transport is described in our model by Fick's law:

$$J_\alpha^k = \rho\phi D_\alpha^k \nabla c_\alpha^k \qquad \text{Eq II.14.}$$

The molecular diffusion coefficient of component k depends on the binary diffusion coefficients $\tilde{D}_w^k$ and $\tilde{D}_g^{ij}$.

$$D_w^k = S_w \tau \tilde{D}_w^k$$
$$D_g^k = S_g \tau \left(\sum_{j=1 \neq i}^{n} \frac{c_g^j}{\tilde{D}_g^{ij}} \right)^{-1} \quad \text{Eq II.15.}$$

The actual trajectories that individual fluid particles follow in any porous medium are tortuous. Consequently, *Fick*'s law is usually corrected by introducing a tortuosity factor. Values for τ were suggested by Millington and Quirk (1961), where $\tau = \phi^{\frac{1}{3}} S_\alpha^{\frac{7}{3}}$.

2.2.2. Mass and momentum balance of chemical components and phases

The transport of chemical components *k* in a two-phase flow is governed by a reaction-advection-diffusion equation described by the following system:

$$\sum_{\alpha=w,g} \left[\frac{\partial}{\partial t} \left(\phi \left(\rho_\alpha S_\alpha c_\alpha^k \right) \right) + \underbrace{\nabla \cdot \left(\rho_\alpha c_\alpha^k V_\alpha \right)}_{\text{advection}} - \underbrace{\nabla \cdot \left(\rho_\alpha \mathbf{D}_\alpha^k \phi \nabla c_\alpha^k \right)}_{\text{diffusion}} \right] = \underbrace{\phi S_w \omega^k}_{\substack{\text{rate of the biochemical} \\ \text{reaction caused by bacteria}}} \quad \text{Eq II.16.}$$

where ϕ is the porosity, ρ is the molar density, c is the molar fraction, S is the saturation. The superscript k refers to the chemical component, and the indexes g and w denote the gas and water phase.

The rate of the biochemical reaction ω^k represents the production/consumption term of the component *k*; It is proportional to the growth rate:

$$\omega^k = \pm \frac{1}{Y} \gamma^k R^{gr} \quad \text{Eq II.17.}$$

Where γ^k represents the stoichiometric coefficient of component k in Sabatier reaction equation: $\gamma^{CO_2} = -1$, $\gamma^{H_2} = -4$, $\gamma^{CH_4} = 1$ and $\gamma^{H_2O} = 2$. Y is microbial yield coefficient.

2.2.3. Bacterial transport: model of population dynamics

Bacteria dynamic is described by a reaction-advection-diffusion equation as well. The reaction term consists of a positive part, R^{gr}, responsible for the microbial production or growth and a negative part caused by bacterial decay, R^{dec} (Rittmann et al. 1987, Panfilov 2010, Anozie Ebigbo et al. 2010, Birger Hagemann 2017).

$$\frac{\partial}{\partial t}\left(\phi\left(\rho_w S_w n\right)\right)+\underbrace{\nabla\cdot\left(\rho_w n\mathbf{V}_w\right)}_{\text{advection}}-\underbrace{\nabla\cdot\left(\phi\rho_w S_w D_b\nabla n\right)}_{\text{diffusion}}=\phi S_w\left[R^{gr}-R^{dec}\right] \qquad \text{Eq II.18.}$$

The diffusive term describes the random movement of microorganisms in different directions from the area of high concentration of bacteria to that of low. n represents the number of bacteria per unit volume of porous space, D_b is the bacterial diffusion coefficient. The bacterial population dynamic equation introduces two kinetics functions R^{gr} and R^{dec}, where R^{gr} corresponds to the microbial growth rate in [s−1]and R^{dec} is the decay function in [s−1].

2.2.4. Kinetic functions

Microbial growth and decay are fundamental processes to model microbial transport in porous media. In our study, bacteria use hydrogen and Carbon dioxide for their respiratory metabolism. The mechanism of such respiration consists of splitting an electron from hydrogen atoms and using it to activate the oxidation reaction with CO2 in the body of the cell, which releases energy (Panfilov, 2019). Bacteria consume neither hydrogen atoms nor the reaction products, but only the energy released from the reaction:

$$4H_{2_{(l)}}+CO_{2_{(l)}}\rightarrow CH_{4_{(l)}}+2H_2O_{(l)}+\text{energy} \qquad \text{Eq II.19.}$$

The well-known model describing biomass growth in literature is that of Monod called double Monod model (Monod 1949, Taylor and Jaffe 1990):

$$R^{gr}=\psi^{gr}n=\frac{\rho_w}{t_{gr}}\frac{c_w^{H_2}}{\left(\alpha^{H_2}+c_w^{H_2}\right)}\frac{c_w^{CO_2}}{\left(\alpha^{CO_2}+c_w^{CO_2}\right)}n \qquad \text{Eq II.20.}$$

As it turns out in (Panfilov 2019), the individual growth rate, in turn, can depend on the number of bacteria. A corrective form of the previous model was proposed by the same work in which an additional term (+) was added to take account of this effect:

$$R^{gr} = \psi^{gr} n = \frac{\rho_w}{t_{gr}} \frac{c_w^{H_2}}{\left(\alpha^{H_2} + c_w^{H_2}\right)} \frac{c_w^{CO_2}}{\left(\alpha^{CO_2} + c_w^{CO_2}\right)} n \underbrace{\left(1 - e^{-\delta n^{\alpha}}\right)}_{(+)} \quad \text{Eq II.21.}$$

Microbial decay is assumed to be caused only by microorganisms-predators. It is independent of nutrients, the prof is that bacteria do not die in the absence of nutrients but temporarily stop their activity (Panfilov, 2018)

$$R^{dec} = \psi^{dec} n = \frac{\rho_w}{t^{dec}} n^{\beta} \quad \text{Eq II.22.}$$

$c_w^{H_2}$ and $c_w^{CO_2}$ are the mole fractions of H_2 and CO_2 in water, α^{H_2} and α^{CO_2} are the half-velocities constants, t^{gr} and t^{dec} are respectively the characteristic time of growth and the characteristic time of decay.

2.2.5. Dissolution of species in phases

Dissolution is the mass transfer between different phases. To calculate the amount of dissolved H_2 and CO_2, (Panfilov, 2019) in his book "*Physicochemical Fluid Dynamics in Porous Media*" suggested the use of Henry's law, which expresses the relation between the gas-phase mole fraction of the components k and their mole fraction in the wetting phase.

$$c_w^k = \tilde{H}^k c_g^k P_g, \quad k = H_2, CO_2 \quad \text{Eq II.23.}$$

$\tilde{H}^k$ is the Henry solubility coefficient and P_g is the gas pressure.

As mentioned in (Panfilov, 2019), to transform the maximum of the gas into CH4, the proportion between H_2 and CO_2 in the injected gas should verify the stoichiometric ratios of the Sabatier reaction. Which provides:

$$\tilde{H}^{H_2} c_g^{H_2} P_g = 4\tilde{H}^{CO_2} c_g^{CO_2} P_g, \quad \text{Eq II.24.}$$

and,

$$c_g^{H_2} = \frac{4\tilde{H}^{CO_2}}{\tilde{H}^{H_2}} c_g^{CO_2} = 43.71 c_g^{CO_2} \quad \text{Eq II.25.}$$

Consequently,

$$c_g^{H_2} = \frac{43.71}{44.71} \approx 0.9776 \text{ and } x_g^{H_2} \approx 0.0224.$$

This means that the gas phase is a diluted solution containing 98% of H_2 and 2% of CO_2.

2.2.6. Simplified model of two or three diffusion-reaction equations

Combining the different processes, the full model can be written as follow:

$$\sum_{\alpha=w,g} \left[\frac{\partial}{\partial t} \left(\phi \left(\rho_w \left(1 - S_g\right) c_w^k + \rho_g S_g c_g^k \right) \right) + \nabla \cdot \left(\rho_w c_w^k V_w + \rho_g c_g^k V_g \right) \right] = \pm \frac{\gamma^k \phi \rho_w S_w c_w^{H_2} c_w^{CO_2} n}{t^{gr} Y \left(\alpha^{H_2} + c_w^{H_2} \right) \left(\alpha^{CO_2} + c_w^{CO_2} \right)} \quad \text{Eq II.26.}$$

$$\frac{\partial}{\partial t} \left(\phi \left(\rho_w S_w n \right) \right) + \nabla \cdot \left(\rho_w n \mathbf{V}_w \right) - \nabla \cdot \left(\phi \rho_w S_w D_b \nabla n \right) = \frac{\phi \rho_w S_w c_w^{H_2} c_w^{CO_2} n}{t^{gr} \left(\alpha^{H_2} + c_w^{H_2} \right) \left(\alpha^{CO_2} + c_w^{CO_2} \right)} - \frac{\phi \rho_w S_w n^{\beta}}{t^{dec}} \quad \text{Eq II.27.}$$

To carry out a qualitative stability analysis of the current developed system, we first need to reduce our model to a minimum number of variables, to overcome the complexity of the bio-physiochemical problem. To reduce the model to a system of two ODE (Dimensionless form), we introduce the following assumptions (Panfilov, 2019):

1. The flow takes place in uniform porous media.
2. The gravity and capillary pressure are neglected.

3. The diffusion of chemical components H_2 and H_2O is neglected.
4. The liquid phase is consisted essentially of H_2O, while the gas phase contains ≈98% of H_2. Indeed for H_2O and H_2 we assume that $\rho_g \approx \rho^{H_2}$ and $\rho_w \approx \rho^{H_2O}$,
5. The mixing of components k in both phases is ideal (i.e., no volume change on mixing).
6. The phases are incompressible (i.e., densities still constants and $\nabla \cdot V_\alpha = 0$).
7. Constant injection velocity $V_\alpha = V_\alpha(t)$.
8. The mass exchange between the phases is assumed instantaneously (The Henry Law is valid in this case).
9. Isothermal process as reservoir variation in temperature are minimal (Sidsel Marie Nielsen 2010).
10. The variation of pressure is negligible for thermodynamics functions.
11. Bacteria exist as flowing suspension in the liquid phase.

$$H_2 \text{ and } H_2O: \ \phi \frac{\partial S_g}{\partial t} + V.\nabla F = 0, \qquad \text{Eq II.28.}$$

$$\frac{\partial}{\partial t}\left(\left(\tilde{H}^{CO_2} P_g (1-S_g) + S_g\right) c_g^{CO_2}\right) + \nabla \cdot \left(\left(\tilde{H}^{CO_2} P_g (1-FV) + FV\right) c_g^{CO_2}\right)$$
$$-\nabla \cdot \left(\left(\tilde{\mathbf{D}}_w^{CO_2} (1-S_g) \tilde{H}^{CO_2} P_g + \tilde{\mathbf{D}}_g^{CO_2} S_g\right) \nabla c_g^{CO_2}\right) = -\frac{(1-S_g)\omega^{CO_2}}{\rho^{CO2}}, \qquad \text{Eq II.29.}$$

$$\frac{\partial}{\partial t}\left(\left(\tilde{H}^{CH_4} P_g (1-S_g) + S_g\right) c_g^{CH_4}\right) + \nabla \cdot \left(\left(\tilde{H}^{CH_4} P_g (1-FV) + FV\right) c_g^{CH_4}\right)$$
$$-\nabla \cdot \left(\left(\tilde{\mathbf{D}}_w^{CH_4} (1-S_g) \tilde{H}^{CH_4} P_g + \tilde{\mathbf{D}}_g^{CH_4} S_g\right) \nabla c_g^{CH_4}\right) = 0, \qquad \text{Eq II.30.}$$

$$\frac{\partial}{\partial t}\left((1-S_g)n\right) + \mathbf{V} \cdot \nabla\left(n(1-F)\right) - D_b (1-S_g) \Delta n = \frac{(1-S_g)}{\rho^{H_2O}}\left[R^{gr} - R^{dec}\right] \qquad \text{Eq II.31.}$$

$FV = V_g$; $F = \dfrac{k_{rg}\mu_w}{k_{rg}\mu_w + k_{rw}\mu_g}$; $V = V_w + V_g$ is the total Darcy velocity;

$$c_w^k = \tilde{H}^k c_g^k P_g, \quad k = H_2, CO_2 \ ,$$

To simplify the mathematical analysis, we keep the convective term in the average value.

$$\frac{\partial S_g}{\partial t} + Q^k = 0,\ k = H_2\ ,\ H_2\mathrm{O} \qquad \text{Eq II.32.}$$

$$\frac{\partial}{\partial t}\left(\left(\tilde{H}^{CO_2} P_g \left(1-S_g\right) + S_g\right) c_g^{CO_2}\ \right) + Q^{CO_2}$$
$$-\nabla\cdot\left(\left(\tilde{\mathbf{D}}_w^{CO_2}\left(1-S_g\right)\tilde{H}^{CO_2}P_g + \tilde{\mathbf{D}}_g^{CO_2}S_g\right)\nabla c_g^k\right) = -\frac{\left(1-S_g\right)\omega^{CO_2}}{\rho^{CO2}}, \qquad \text{Eq II.33.}$$

$$\frac{\partial}{\partial t}\left(\left(\tilde{H}^{CH_4} P_g \left(1-S_g\right) + S_g\right) c_g^{CH_4}\ \right) + Q^{CH_4} - \nabla\cdot\left(\left(\tilde{\mathbf{D}}_w^{CH_4}\left(1-S_g\right)\tilde{H}^{CH_4}P_g + \tilde{\mathbf{D}}_g^{CH_4}S_g\right)\nabla c_g^{CH_4}\right) = 0, \qquad \text{Eq II.34.}$$

$$\frac{\partial}{\partial t}\left(\left(1-S_g\right)n\right) + Q^b - D_b\left(1-S_g\right)\Delta n = \frac{\left(1-S_g\right)}{\rho^{H_2O}}\left[R^{gr} - R^{dec}\right] \qquad \text{Eq II.35.}$$

Both components, H_2 and H_2O, dominate in their phase, thus $Q^{H_2} = 0$ and $Q^{H_2O} = 0$.

Consequently, the saturation is invariable in time. We admit that it's invariable also in space.

$$\frac{\partial c_g^{CO_2}}{\partial t} + \frac{Q^{CO_2}}{\left(\tilde{H}^{CO_2}P_g\left(1-S_g\right)+S_g\right)} - \frac{\left(\tilde{\mathbf{D}}_w^{CO_2}\left(1-S_g\right)\tilde{H}^{CO_2}P_g + \tilde{\mathbf{D}}_g^{CO_2}S_g\right)}{\left(\tilde{H}^{CO_2}P_g\left(1-S_g\right)+S_g\right)}\Delta c_g^{CO_2}$$
$$= -\frac{\gamma^{CO_2}\rho^w\left(1-S_g\right)\delta\tilde{H}^{H_2}\tilde{H}^{CO_2}P_g}{\rho^{CO2}t^{gr}Y\left(\tilde{H}^{CO_2}P_g\left(1-S_g\right)+S_g\right)}n^{\alpha+1}c_g^{CO_2}, \qquad \text{Eq II.36.}$$

$$\frac{\partial}{\partial t}\left(\left(\tilde{H}^{CH_4} P_g \left(1-S_g\right) + S_g\right) c_g^{CH_4}\ \right) + Q^{CH_4} - \nabla\cdot\left(\left(\tilde{\mathbf{D}}_w^{CH_4}\left(1-S_g\right)\tilde{H}^{CH_4}P_g + \tilde{\mathbf{D}}_g^{CH_4}S_g\right)\nabla c_g^{CH_4}\right) = 0, \qquad \text{Eq II.37.}$$

$$\frac{\partial n}{\partial t} + \frac{Q^b}{\left(1-S_g\right)} - D_b\Delta n = \frac{\rho_w\delta\tilde{H}^{H_2}\tilde{H}^{CO_2}P_g^{\ 2}}{\rho^{H_2O}t^{gr}}n^{\alpha+1}c_g^{CO_2} - \frac{\rho_w}{\rho^{H_2O}t^{dec}}n^{\beta} \qquad \text{Eq II.38.}$$

To obtain a dimensionless formulation, we introduce the following dimensionless parameters :

$$t^* = \frac{\delta \tilde{H}^{H_2} \tilde{H}^{CO_2} P_g^{\,2} t}{t_{gr}},\ x^* = \frac{x}{\sqrt{D^{CO_2} t^*}},$$

thus,

$$\frac{\partial c_g^{CO_2}}{\partial t^*} + \underbrace{\frac{Q^{CO_2} t^{gr}}{\left(\tilde{H}^{CO_2} P_g \left(1-S_g\right)+S_g\right)\delta \tilde{H}^{H_2} \tilde{H}^{CO_2} P_g^{\,2}}}_{q^{CO_2}} - \underbrace{\frac{\left(\tilde{\mathbf{D}}_w^{CO_2}\left(1-S_g\right)\tilde{H}^{CO_2} P_g + \tilde{\mathbf{D}}_g^{CO_2} S_g\right)}{\left(\tilde{H}^{CO_2} P_g \left(1-S_g\right)+S_g\right) t^* D^{CO_2}}}_{\text{unity}} \Delta_* c_g^{CO_2}$$

$$= \underbrace{-\frac{\rho_w \gamma^{CO_2}\left(1-S_g\right)}{\rho^{CO_2} Y\left(\tilde{H}^{CO_2} P_g \left(1-S_g\right)+S_g\right)}}_{\lambda_1} n^{\alpha+1} c_g^{CO_2}, \qquad \text{Eq II.39.}$$

Eq II.40.

$$\frac{\partial n}{\partial t^*} + \underbrace{\frac{Q^b}{\left(1-S_g\right)} \frac{t^{gr}}{\delta \tilde{H}^{H_2} \tilde{H}^{CO_2} P_g^{\,2}}}_{q^b \ll} - \underbrace{\frac{D_b}{t^* D^{CO_2}}}_{\xi} \left(\Delta\right)^* n = n^{\alpha+1} c_g^{CO_2} - \underbrace{\frac{t^{gr}}{\delta \tilde{H}^{H_2} \tilde{H}^{CO_2} P_g^{\,2} t^{dec}}}_{\lambda_2} n^{\beta} \qquad \text{Eq II.41.}$$

The resulting dimensionless system is as follows:

$$\frac{\partial c_g^{CO_2}}{\partial t} = \Delta c_g^{CO_2} + q^{CO_2} - \lambda_1 n^{\alpha+1} c_g^{CO_2} \qquad \text{Eq II.42.}$$

$$\frac{\partial n}{\partial t} = \xi \Delta n + n^{\alpha+1} c_g^{CO_2} - \lambda_2 n^{\beta} \qquad \text{Eq II.43.}$$

where,

$$q^{CO_2} = \frac{Q_{inj}^{CO_2} t_{gr}}{\delta \tilde{H}^{H_2} \tilde{H}^{CO_2} P_g^{\,2}\left(S_g + \tilde{H}^{CO_2} P_g \left(1-S_g\right)\right)},\ \lambda_1 = \frac{\rho_w \gamma^{CO_2}\left(1-S_g\right)}{\rho^{CO_2} Y\left(S_g + \tilde{H}^{CO_2} P_g \left(1-S_g\right)\right)},$$

$$\lambda_2 = \frac{t_{gr}}{\delta \tilde{H}^{CO_2} \tilde{H}^{H_2} P_g^{\,2} t_{dec}},\ D^{CO_2} = \frac{\left(\tilde{\mathbf{D}}_w^{CO_2}\left(1-S_g\right)\tilde{H}^{CO_2} P_g + \tilde{\mathbf{D}}_g^{CO_2} S_g\right)}{\left(\tilde{H}^{CO_2} P_g \left(1-S_g\right)+S_g\right) t^*} \text{ and } \xi = \frac{D_b}{t^* D_{CO_2}}$$

The resulted physico-biochemical problem is governed by a reaction-diffusion system.

2.2.7. Expected scenarios of the evolution

The first works modeling the theory of self-organization phenomena in underground hydrogen storage were developed by Mikhail Panfilov (Panfilov 2010). The process was described by the last two diffusion-reaction differential equations. The model was able to predict patterns founded in Lobodice storage and expects the possible formation of other types of complex structures in underground hydrogen storage.

Compared to other known patterns in dynamic systems, the property of the resulting patterns is that are determined by processes intrinsic, not external to the system.

It can be expected that the current system we study can generate such complex patterns as well which can explain some in-situ observations on gas patterns in underground methanation (e.g., Lobodice site).

Among the expected effects to obtain: a nontrivial behavior with the creation of new forms of patterns within the reservoir, or new conditions of pattern formation.

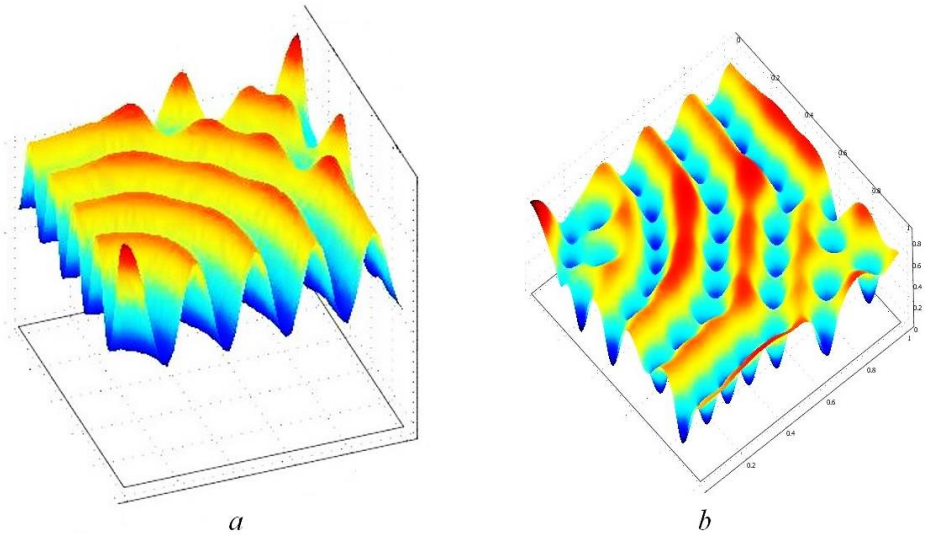

Figure II-4 Stationary patterns as the first type of self-organization in UHS in terms of the hydrogen concentration in space at large times: (a) a single-scale pattern and (b) a two-scale pattern (Panfilov 2010)

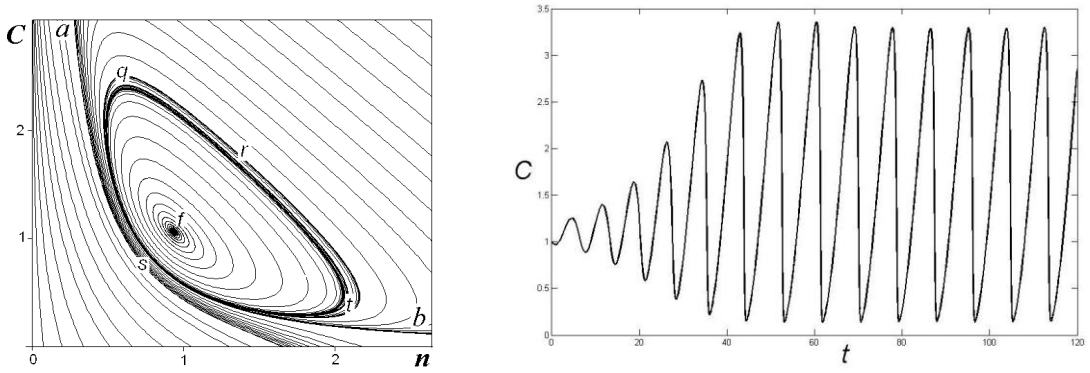

Figure II-5 Oscillatory behavior of CO2 concentration in time (Panfilov 2010)

2.3. PATTERNS IN THE HYDROGEN TRANSPORT MODEL

2.3.1. Physical description of the system

The idea is to convert the maximum of hydrogen H_2 and carbon dioxide CO_2 into methane CH_4 and the composition of the gas should be maintained uniformly in the entire reservoir. The existence of patterns (the spatial alternation of the areas saturated preferably by hydrogen or methane founded in Lobodice reservoir) can significantly influence the technical solutions. Any oscillatory pattern is not spatially uniform which reduces the methanation efficiency (Panfilov 2010). For this purpose, we perform a qualitative mathematical analysis that will allow us to detect the different criteria of the appearance of the pattern regime. The criteria of the creation of structures correspond to criteria of Turing stability.

The classical types of instabilities responsible for the appearance of spatiotemporal patterns are the:

- space independent Hopf instability (at least 2D-reaction diffusion system) (Yifu Wang et al 2007)
- stationary Turing instability (in 2D-reaction diffusion system) (Shigefumi Hata et al 2014, V. K. Vanag 2004, Baba Issa Camara et al. 2009).

- wave instabilities (Standing waves, spiral waves, in 3D-reaction diffusion system or more) (Lingfa Yang et al 2004, Nathaniel Karst et al 2016)
- other complex patterns exist resulting from the interaction of two types of instabilities or more (Hopf-Turing instabilities, Hopf-Waves instabilities, Turing waves patterns,…) (Lingfa Yang et al 2004, Nathaniel Karst et al 2016)

We focus our interest on spatiotemporal patterns formation and the conditions of their emergence in underground hydrogen storage. We analyze how diffusion and reactions induce the instability of an equilibrium state. Next, we carry out a numerical simulation to capture the regimes when these conditions are verified.

2.3.2. Simplified dynamic system, stability analysis

This part of the thesis aims to establish the conditions of Turing and Hopf instability in homogeneous porous media. The mathematical model we consider consists of two-dimensional reaction-diffusion equations which express the conservation of chemical species and bacteria density. It has the following form,

$$\begin{cases} \dfrac{dC}{dt} - d_c \Delta C = q - \lambda_1 N^{\alpha+1} \mathrm{C} \\ \dfrac{dN}{dt} - d_b \Delta N = N^{\alpha+1} C - \lambda_2 N^{\beta} \end{cases} \qquad \text{Eq II.44.}$$

with, $C = c_g^{CO_2}$ and $N = n$.

N represents the number of bacteria, C is the concentrations of nutrients Δ is the Laplacian operator; q denotes the injection rate; λ_1 is the characteristic time of eating and λ_2 is the characteristic time of bacterial decay (λ_1 , λ_2 , α and β are constants)

We can see that system (Eq. II.44.) has a unique non-trivial steady-state solution $E_* = (C_*, N_*)$, with

$$E_* = (C_*, N_*) = \left(\frac{q}{\lambda_1} \left(\frac{\lambda_1 \lambda_2}{q} \right)^{\frac{\alpha+1}{\beta}}, \left(\frac{q}{\lambda_1 \lambda_2} \right)^{\frac{1}{\beta}} \right) \quad \text{Eq II.45.}$$

The destabilization of the steady-state of the system can generate three types of symmetry-breaking bifurcations for the emergence of spatiotemporal patterns in the gas reservoir: the one is the space-independent Hopf bifurcation that breaks the temporal symmetry of the system and leads to oscillations, the second is the Turing bifurcation that breaks the spatial symmetry and gives rise to self-organization patterns and the third type is the Hopf-Turing bifurcation which is the coupling between these two bifurcations that produces spatiotemporal patterns.

2.3.3. Patterns oscillatory in time: limit cycle, Hopf-Andronov bifurcation

In this section, we study the conditions of the appearance of Hopf-Andronov bifurcation for the system (Eq. II.44.) at the equilibrium state E_* by choosing q as bifurcation parameter.

The steady-state solutions and the Hopf periodic solutions are spatially uniform, therefore the Hopf stability analysis of the system (Eq. II.44.) is independent on d_b and d_c, and can be performed using the subsystem

$$\begin{cases} \dfrac{dC}{dt} = q - \lambda_1 N^{\alpha+1} \mathrm{C} \\ \dfrac{dN}{dt} = N^{\alpha+1} C - \lambda_2 N^{\beta} \end{cases}. \quad \text{Eq II.46.}$$

The eigenvalues of the linearized system are calculated by solving the following characteristic equation:

$$P(q) = \Lambda^2 - \Theta(q)\Lambda + \Delta(q) = 0, \quad \text{Eq II.47.}$$

where,

$$\Theta(q) = \text{trace } J = -\lambda_1\left(\frac{q}{\lambda_1\lambda_2}\right)^{\frac{\alpha+1}{\beta}} + (\alpha+1-\beta)\lambda_2\left(\frac{q}{\lambda_1\lambda_2}\right)^{\frac{\beta-1}{\beta}} \quad \text{and}$$

$$\Delta(q) = \det\ J = \lambda_1\lambda_2\beta\left(\frac{q}{\lambda_1\lambda_2}\right)^{\frac{\alpha+\beta}{\beta}}.$$

The Jacobian matrix admits two eigenvalues, which can be formulated as follows:

$$\Lambda_{1,2} = \frac{1}{2}\left(-\lambda_1\left(\frac{q}{\lambda_1\lambda_2}\right)^{\frac{\alpha+1}{\beta}} + (\alpha+1-\beta)\lambda_2\left(\frac{q}{\lambda_1\lambda_2}\right)^{\frac{\beta-1}{\beta}}\right) \pm \frac{1}{2}\sqrt{\left(-\lambda_1\left(\frac{q}{\lambda_1\lambda_2}\right)^{\frac{\alpha+1}{\beta}} + (\alpha+1-\beta)\lambda_2\left(\frac{q}{\lambda_1\lambda_2}\right)^{\frac{\beta-1}{\beta}}\right)^2 - 4\lambda_1\lambda_2\beta\left(\frac{q}{\lambda_1\lambda_2}\right)^{\frac{\alpha+\beta}{\beta}}}. \quad \text{Eq II.48.}$$

The equilibrium point E_* of the subsystem (Eq. II.46.) is unstable when at least one root has a positive real part.

Thus, the equilibrium $E_* = (C_*, N_*)$ is asymptotically stable if and only if $\lambda_1\lambda_2\beta\left(\frac{q}{\lambda_1\lambda_2}\right)^{\frac{\alpha+\beta}{\beta}} > 0$

and $-\lambda_1\left(\frac{q}{\lambda_1\lambda_2}\right)^{\frac{\alpha+1}{\beta}} + (\alpha+1-\beta)\lambda_2\left(\frac{q}{\lambda_1\lambda_2}\right)^{\frac{\beta-1}{\beta}} < 0$.

We can check easily that the Jacobian matrix of the ODE system has a pair of purely complex imaginary eigenvalues at $q_H = q_c = \left((\alpha+1-\beta)\frac{\lambda_2}{\lambda_1}\right)^{\frac{\beta}{\alpha-\beta+2}}\lambda_1\lambda_2$.

For $\lambda_1 = 1,\ \lambda_2 = 1,\ \alpha = 1$ and $\beta = 1$:

$$J_{[C_*,N_*]} = \begin{bmatrix} -q^2 & -2 \\ q^2 & 1 \end{bmatrix},\ \Theta(q) = 1-q^2,\ \Delta(q) = q^2 \text{ and } \Lambda_{1,2} = \frac{1}{2}\left(1-q^2 \pm \sqrt{q^4-6q^2+1}\right),\ q_c = 1$$

Thus,

(i) when $q^4 - 6q^2 + 1 < 0$, the eigenvalues of $J_{[C_*, N_*]}$ have the form $p(q) \pm i\omega(q)$, with $p(q_c) = 0$ and $\omega(q_c) = 1 \neq 0$.

(ii) $\left.\frac{d\alpha(q)}{dq}\right|_{q=q_c} = -2q_c \neq 0$, which means that the eigenvalues cross the imaginary axis with non-null speed, therefore the transversality condition is verified.

It follows that, from the Poincaré-Andronov-Hopf bifurcation theorem:

(i) The homogeneous steady state is asymptotically stable when $q > q_c$ and unstable when $q < q_c$.

(ii) The diffusionless system undergoes the called Hopf bifurcation at the equilibrium point when q crosses through q_c and the bifurcating periodic solutions exist for $q_c - \varepsilon < q < q_c$ .Figure II.6-7. shows the behavior of the subsystem for $q > q_c$. As expected, the equilibrium point is a stable focus. In this region, all the solutions converge to the steady-state solution. If we choose a value of q just a bit below q_c, we get a limit cycle surrounding the steady-state solution. We calculated the result for high t, to eliminate the transient behavior of the limit cycle that arises.

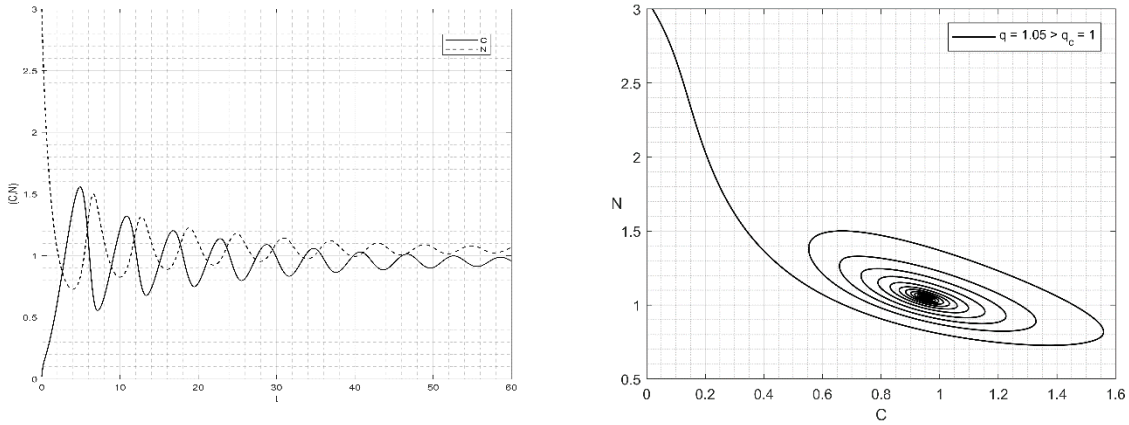

(a) **(b)**

Figure II-6 The behavior of the subsystem (Eq. II.46.), for $q > q_c$

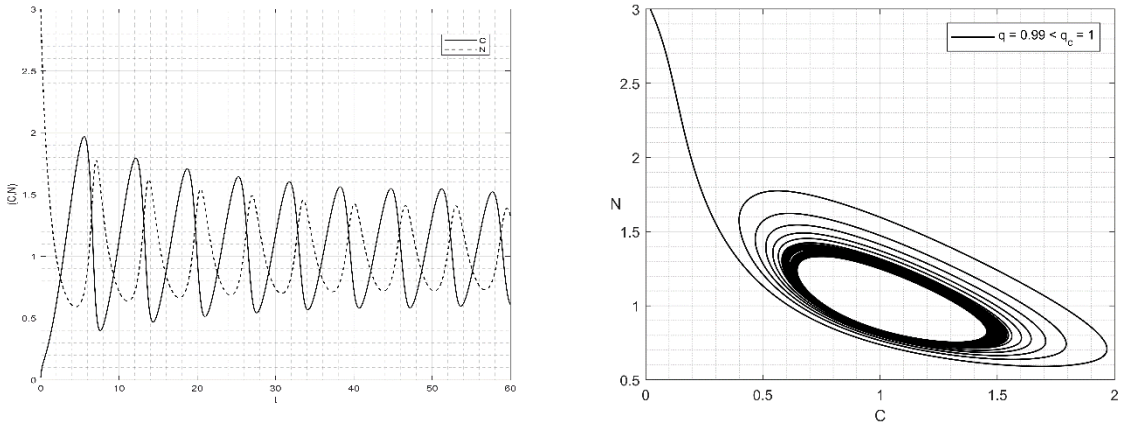

(a) **(b)**

Figure II-7 The behavior of the subsystem (Eq. II.46.), for $q < q_c$

Stability of the limit cycles induced by Hopf bifurcation:

Now, let study the stability of the periodic solutions (limit cycles) arising through Hopf-Andronov bifurcation. For this, we translate the equilibrium $E_* = (C_*, N_*)$ to the origin by considering the following change of variables:

$$u = C - C_*,\ v = N - N_* \qquad \text{Eq II.49.}$$

Thus, the steady-state solution of the subsystem (Eq. II.46.) is transformed into the zero equilibrium of the system (Eq. II.50.).

$$\begin{cases} \dfrac{du}{dt} = q - \lambda_1 (v + N_*)^2 (u + C_*) \\ \dfrac{dv}{dt} = (v + N_*)^2 (u + C_*) - \lambda_2 (v + N_*) \end{cases} \qquad \text{Eq II.50.}$$

Simplifying we obtain,

$$\begin{cases} \dfrac{du}{dt} = -\dfrac{q^3 u + 2q^2 uv + quv^2 + 2qv + v^2}{q} \\ \dfrac{dv}{dt} = \dfrac{q^3 u + 2q^2 uv + quv^2 + qv + v^2}{q} \end{cases} \qquad \text{Eq II.51.}$$

Rewrite system (Eq. II.51.) as

$$\begin{pmatrix} \frac{du}{dt} \\ \frac{dv}{dt} \end{pmatrix} = J_{[0,0]} \begin{pmatrix} u \\ v \end{pmatrix} + \begin{pmatrix} f(u,v,q) \\ g(u,v,q) \end{pmatrix} \quad \text{Eq II.52.}$$

The Jacobian matrix may be written in Jordan normal form at $q = q_c$,

$$\mathrm{H}(q) = TJT^{-1} = \begin{pmatrix} \Re(\Lambda(q)) & -\Im(\Lambda(q)) \\ \Im(\Lambda(q)) & \Re(\Lambda(q)) \end{pmatrix} \quad \text{Eq II.53.}$$

$$\mathrm{H}(q = q_H) = \begin{pmatrix} 0 & -\omega(q_H) \\ \omega(q_H) & 0 \end{pmatrix} \quad \text{Eq II.54.}$$

With $\omega(q_H) = \Im\left(\Lambda_{1,2}\right) = \sqrt{\Delta(q_H)}$, is the frequency of the periodic bifurcated solutions.

we adopt that:

$$T(q) = \begin{pmatrix} \sigma(q) & 1 \\ \eta(q) & 0 \end{pmatrix} \text{ and } T^{-1}(q) = \begin{pmatrix} 0 & \frac{1}{\eta(q)} \\ 1 & -\frac{\sigma(q)}{\eta(q)} \end{pmatrix},$$

with

$$\sigma(q) = \frac{1}{2}\frac{q^2+1}{\Im\left(\Lambda(q)\right)} \text{ and } \eta(q) = -\frac{q^2}{\Im\left(\Lambda(q)\right)}.$$

The considered linear transformation is not unique (Guckenheimer and Holmes, 1983). Thus, by applying the following linear coordinate change:

$$\begin{pmatrix} u \\ v \end{pmatrix} = T \begin{pmatrix} x \\ y \end{pmatrix}, \quad \text{Eq II.55.}$$

we obtain

$$\begin{cases} x = \dfrac{1}{\eta(q)} v \\ y = u - \dfrac{\sigma(q)}{\eta(q)} v \end{cases}, \qquad \text{Eq II.56.}$$

the system becomes,

$$T^{-1}\begin{pmatrix} \dfrac{du}{dt} \\ \dfrac{dv}{dt} \end{pmatrix} = T^{-1} J_{[0,0]} T T^{-1} \begin{pmatrix} u \\ v \end{pmatrix} + T^{-1} \begin{pmatrix} f(u,v,q) \\ g(u,v,q) \end{pmatrix} \qquad \text{Eq II.57.}$$

Thus, we look at:

$$\begin{pmatrix} \dfrac{dx}{dt} \\ \dfrac{dy}{dt} \end{pmatrix} = H(q) \begin{pmatrix} x \\ y \end{pmatrix} + \begin{pmatrix} f(x,y,q) \\ g(x,y,q) \end{pmatrix} \qquad \text{Eq II.58.}$$

Then,

$$\begin{cases} \dfrac{dx}{dt} = \Re\big(\Lambda(q)\big) x - \Im\big(\Lambda(q)\big) y + f(x,y,q) \\ \dfrac{dy}{dt} = \Im\big(\Lambda(q)\big) x + \Re\big(\Lambda(q)\big) y + g(x,y,q) \end{cases} \qquad \text{Eq II.59.}$$

$$\begin{aligned} f(x,y,q) &= \frac{1}{\eta(q)} g(\sigma(q)x + y, \eta(q)x, q) \\ g(x,y,q) &= f(\sigma(q)x + y, \eta(q)x, q) - \frac{\sigma(q)}{\eta(q)} g(\sigma(q)x + y, \eta(q)x, q) \end{aligned} \qquad \text{Eq II.60.}$$

$$\begin{cases} f(x,y,q) = \dfrac{qx}{2\omega(q)^2}(-q^3x^2 + 2\omega(q)q^2x - 2\omega(q)qxy + 4\omega(q)^2 y - qx^2) \\ g(x,y,q) = \dfrac{qx}{4\omega(q)^3}(-q^3x^2 + 2\omega(q)q^2x - 2\omega(q)qxy + 4\omega(q)^2 y - qx^2)(q^2 - 1) \end{cases} \qquad \text{Eq II.61.}$$

The stability of the limit cycle induced by Andronov-Hopf bifurcation is determined by the sign of $l(q)$, which is the sign of the first Lyapunov coefficient.

According to (Guckenheimer and Holmes, 1983), the Lyapunov coefficient formula is given by:

$$\ell(q)=\frac{1}{16}\left(\frac{\partial^3 f}{\partial x^3}+\frac{\partial^3 f}{\partial x\partial y^2}+\frac{\partial^3 g}{\partial y\partial x^2}+\frac{\partial^3 g}{\partial y^3}\right)_{[0,0,q]} + \frac{1}{16\omega(q)}\left(\frac{\partial^2 f}{\partial x\partial y}\left(\frac{\partial^2 f}{\partial x^2}+\frac{\partial^2 f}{\partial y^2}\right)-\frac{\partial^2 g}{\partial x\partial y}\left(\frac{\partial^2 g}{\partial x^2}+\frac{\partial^2 g}{\partial y^2}\right)-\left(\frac{\partial^2 f}{\partial x^2}\frac{\partial^2 g}{\partial x^2}\right)+\left(\frac{\partial^2 f}{\partial y^2}\frac{\partial^2 g}{\partial y^2}\right)\right)_{[0,0,q]} \quad \text{Eq II.62.}$$

(i) if $\ell(q)>0$, then the direction of Hopf bifurcation is subcritical and the bifurcating periodic solutions are asymptotically unstable.

(ii) if $\ell(q)<0$, then the direction of Hopf bifurcation is supercritical and the bifurcating periodic solutions are stable.

We can calculate that,

$$\left(\frac{\partial^3 f}{\partial x^3}+\frac{\partial^3 f}{\partial x\partial y^2}+\frac{\partial^3 g}{\partial y\partial x^2}+\frac{\partial^3 g}{\partial y^3}\right)=-\frac{2q^2\left(2q^2+1\right)}{\omega(q)^2} \quad \text{Eq II.63.}$$

$$\left(\frac{\partial^2 f}{\partial x\partial y}\left(\frac{\partial^2 f}{\partial x^2}+\frac{\partial^2 f}{\partial y^2}\right)-\frac{\partial^2 g}{\partial x\partial y}\left(\frac{\partial^2 g}{\partial x^2}+\frac{\partial^2 g}{\partial y^2}\right)-\left(\frac{\partial^2 f}{\partial x^2}\frac{\partial^2 g}{\partial x^2}\right)+\left(\frac{\partial^2 f}{\partial y^2}\frac{\partial^2 g}{\partial y^2}\right)\right)=\frac{1}{2\omega(q)^4}\hbar(q)\Upsilon(q) \quad \text{Eq II.64.}$$

with,

$$\hbar(q)=q^3(-3q^2x+2\omega(q)q-2\omega(q)y-3x)$$

$$\Upsilon(q)=\left(4q^5x-3\omega(q)q^4+2\omega(q)q^3y-4\omega(q)^2qx-2q^3x+4\omega(q)^3-2\omega(q)qy-2qx-\omega(q)\right)$$

Thus, we obtain

$$\ell(q)_{[x=0,y=0]}=-\frac{1}{2}\frac{q^2(6q^6-9q^4+8q^2-1)}{(q^4-6q^2+1)}, \text{ and } \ell(q_c)=-\frac{1}{8}<0 \quad \text{Eq II.65.}$$

Consequently, the direction of the Hopf bifurcation is supercritical and the induced limit cycles (periodic solutions) are asymptotically stable.

Remark: We can determine the stability of the bifurcation, if it is supercritical (stable) or subcritical (unstable), numerically by examining how the system behaves near the bifurcation. As it's known, in a supercritical Andronov-Hopf bifurcation, the limit cycle grows out of the equilibrium point. In other words, right at the parameters of the Hopf-Andronov bifurcation (region where $q > q_H = q_c$), the limit cycle has zero amplitude, and this amplitude grows like $\sqrt{|q-q|_c}$ as the parameters move further into the limit-cycle regime where $q < q_c$. Figure II.8 shows clearly that the limit cycle grows as we move away from the bifurcation point. Based on this, we can conclude that the Andronov-Hopf bifurcation is supercritical.

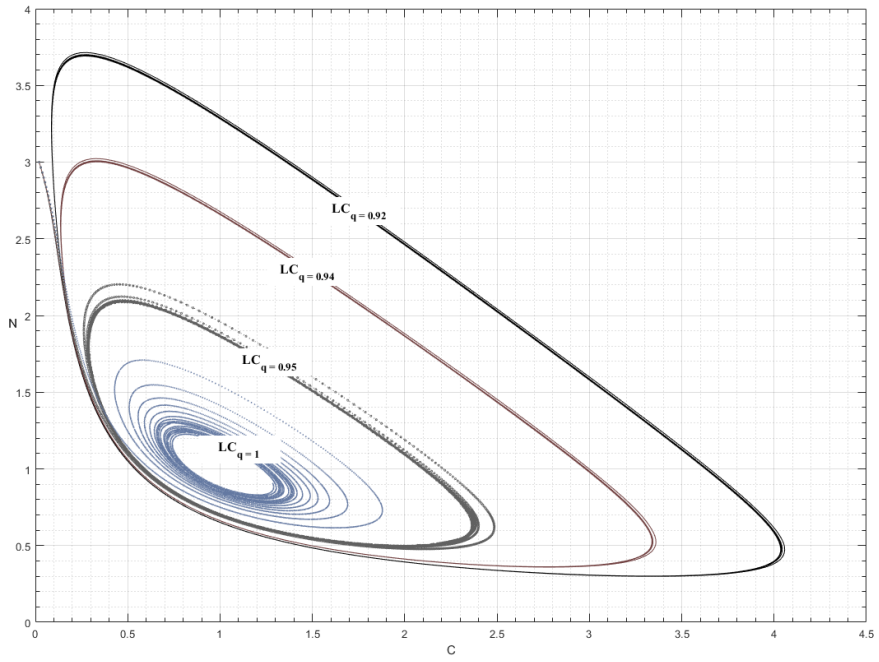

Figure II-8 Limit cycles obtained for $\lambda_1 = 1,\ \lambda_2 = 1,\ \alpha = 1, \beta = 1$

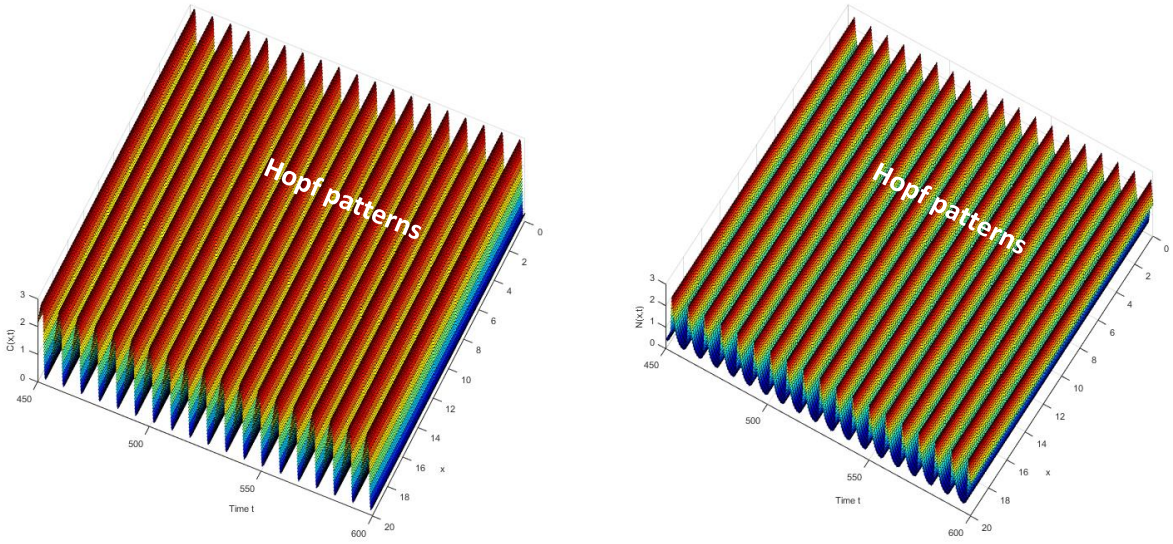

Figure II 9 Numerical simulations of Hopf Patterns: C(x,t) and N(x,t) for $q = 0.97,\ \alpha=\beta=\lambda_1=\lambda_2=1$

2.3.4. Diffusion-reaction system: Stability analysis

To perform linear stability analysis, we introduce a perturbation of the following form:

$$\begin{pmatrix} C \\ N \end{pmatrix} = \underbrace{\begin{pmatrix} C_* \\ N_* \end{pmatrix}}_{\text{equilibrium state}} + \underbrace{\varepsilon \begin{pmatrix} C' \\ N' \end{pmatrix} e^{\Lambda t + ikx}}_{\text{perturbation with small density}} + \mathrm{O}(\varepsilon^2) \qquad \text{Eq II.66.}$$

The linearized system is given as follow,

$$\begin{pmatrix} \dfrac{\partial C'}{\partial t} \\ \dfrac{\partial N'}{\partial t} \end{pmatrix} = \left(J_0 + D\frac{\partial^2}{\partial x^2} \right) \begin{pmatrix} C' \\ N' \end{pmatrix} = J_k \begin{pmatrix} C' \\ N' \end{pmatrix} \qquad \text{Eq II.67.}$$

The Jacobian matrix around the equilibrium point E_* is defined as follow:

$$J_k = \underbrace{\begin{pmatrix} -\lambda_1\left(\frac{q}{\lambda_1\lambda_2}\right)^{\frac{\alpha+1}{\beta}} & -(\alpha+1)\lambda_1\lambda_2\left(\frac{q}{\lambda_1\lambda_2}\right)^{\frac{\beta-1}{\beta}} \\ \left(\frac{q}{\lambda_1\lambda_2}\right)^{\frac{\alpha+1}{\beta}} & (\alpha+1-\beta)\lambda_2\left(\frac{q}{\lambda_1\lambda_2}\right)^{\frac{\beta-1}{\beta}} \end{pmatrix}}_{J_{0,[C_*,N_*]}} - k^2\begin{pmatrix} d_c & 0 \\ 0 & d_b \end{pmatrix} = \begin{pmatrix} J_{11} & J_{12} \\ J_{21} & J_{22} \end{pmatrix} - k^2\begin{pmatrix} d_c & 0 \\ 0 & d_b \end{pmatrix} \quad \text{Eq II.68.}$$

The characteristic equations for the equilibrium E_* are the following quadratic equations:

$$P_k(\Lambda) = \Lambda^2 - \Theta(J_k)\Lambda + \Delta(J_k) = 0 \quad \text{Eq II.69.}$$

Where

$$\Theta(J_k) = J_{11} + J_{22} - k^2\left(d_C + d_B\right) = \Theta(J_0) - k^2\left(d_C + d_B\right) \quad \text{Eq II.70.}$$

$$\Delta(J_k) = d_B d_C k^4 - (d_B J_{11} + d_C J_{22})k^2 + \Delta(J_0) \quad \text{Eq II.71.}$$

The solution of the polynomial equation yields to the following dispersion relation:

$$\Lambda_k = \frac{\Theta(J_k) \pm \sqrt{\left(\Theta(J_k)\right)^2 - 4\Delta(J_k)}}{2} \quad \text{Eq II.72.}$$

For $\lambda_1 = 1,\ \lambda_2 = 1,\ \alpha = 1$ and $\beta = 1$:

$$J_k = J - k^2 D = J_{[C_*,N_*]} = \begin{pmatrix} -q^2 - k^2 d_C & -2 \\ q^2 & 1 - k^2 d_B \end{pmatrix} \quad \text{Eq II.73.}$$

$$\Theta_k(J_k) = 1 - q^2 - k^2\left(d_C + d_B\right) \text{ and } \Delta_k(J_k) = d_B d_C k^4 + (d_B q^2 - d_C)k^2 + q^2 \quad \text{Eq II.74.}$$

While

$$\Lambda_k = \frac{1}{2}\left[1 - q^2 - k^2\left(d_C + d_B\right) \pm \sqrt{\left(1 - q^2 - k^2\left(d_C + d_B\right)\right)^2 - 4\left(d_B d_C k^4 + (d_B q^2 - d_C)k^2 + q^2\right)}\right] \quad \text{Eq II.75.}$$

The growth of the instability is determined by the sign of the real part of Λ_k. The uniform steady state is stable if $\Re(\Lambda_k) < 0$ for all *k*.

The equilibrium $E_* = (C_*, N_*)$ is asymptotically stable if and only if

$$\Theta_k = 1 - q^2 - k^2 (d_C + d_B) = {q_H}^2 - q^2 - k^2 (d_C + d_B) < 0 \quad \text{Eq II.76.}$$

$$\text{and } d_B d_C k^4 + (d_B q^2 - d_C) k^2 + q^2 > 0 \quad \text{Eq II.77.}$$

2.3.5. Turing's stationary patterns

The Turing bifurcation breaks spatial symmetry, leading to the formation of patterns that are stationary in time and oscillatory in space. The Turing instability depends on the reaction rates and bacteria species diffusion ratio and not to the geometry. The bifurcation in a reaction diffusion system occurs when: $\Im(\Lambda_{1,2}) = 0,\ \Re(\Lambda_{1,2}) = 0$ at $k = k^T \neq 0$.

For the sake of convenience, we define

$$\delta(k^2) = \Delta_k = d_B d_C k^4 + (d_B q^2 - d_C) k^2 + q^2 \quad \text{Eq II.78.}$$

which is a quadratic polynomial with respect to k^2.

If $\delta(k^2) < 0$, then $P_k(\Lambda)$ has two roots in which one is positive and another is negative.

When

$$d_B q^2 - d_C < 0 \quad \text{Eq II.79.}$$

$\delta(k^2)$ will take its minimum value, when

$$\frac{d\delta(k^2)}{dk^2} = 2 d_B d_C k^2 + (d_B q^2 - d_C) = 0, \quad \text{Eq II.80.}$$

Then,

$$\delta_{\min} = \delta(k_{\min}{}^2) = -\frac{\left(d_b q^2 - d_c\right)^2}{4 d_b d_c} + q^2 \ , \ k_{\min}{}^2 = -\frac{d_b q^2 - d_c}{2 d_b d_c} \qquad \text{Eq II.81.}$$

We define the ratio $\xi = \frac{d_b}{d_c}$,

$$\delta_{\min} = 0 \qquad \Leftrightarrow \quad -\xi^2 q^4 + 6\xi q^2 - 1 = 0 \qquad \text{Eq II.82.}$$

The discriminant of the quadratic polynomial is

$$d = \left(6q^2\right)^2 - 4q^4 = 32q^4 > 0 \qquad \text{Eq II.83.}$$

Then the equation (3.1) has two positive real roots:

$$\xi_+ = \frac{3 + 2\sqrt{2}}{q^2}, \xi_- = \frac{3 - 2\sqrt{2}}{q^2} \qquad \text{Eq II.84.}$$

where,

$$d_b q^2 - d_c = 0 \qquad \Leftrightarrow \quad \xi = \frac{1}{q^2} = \xi_* \qquad \text{Eq II.85.}$$

We can see that,

$$0 < \xi_- < \xi_* < \xi_+ . \qquad \text{Eq II.86.}$$

Both conditions $\delta_{\min} < 0$ and $(d_B q^2 - d_C) < 0$ must be satisfied. Therefore, the condition $\xi < \xi_-$ is considered. Then, we have the following results:

(i) The equilibrium is asymptotically stable for $\xi > \xi_-$, with $q > q_H$.

(ii) The critical line of Turing instabilities is $\xi = \frac{3 - 2\sqrt{2}}{q^2}$

(iii)When $\xi < \frac{3 - 2\sqrt{2}}{q^2} = \xi_c^T$, the equilibrium is unstable and Turing destabilization occurs.

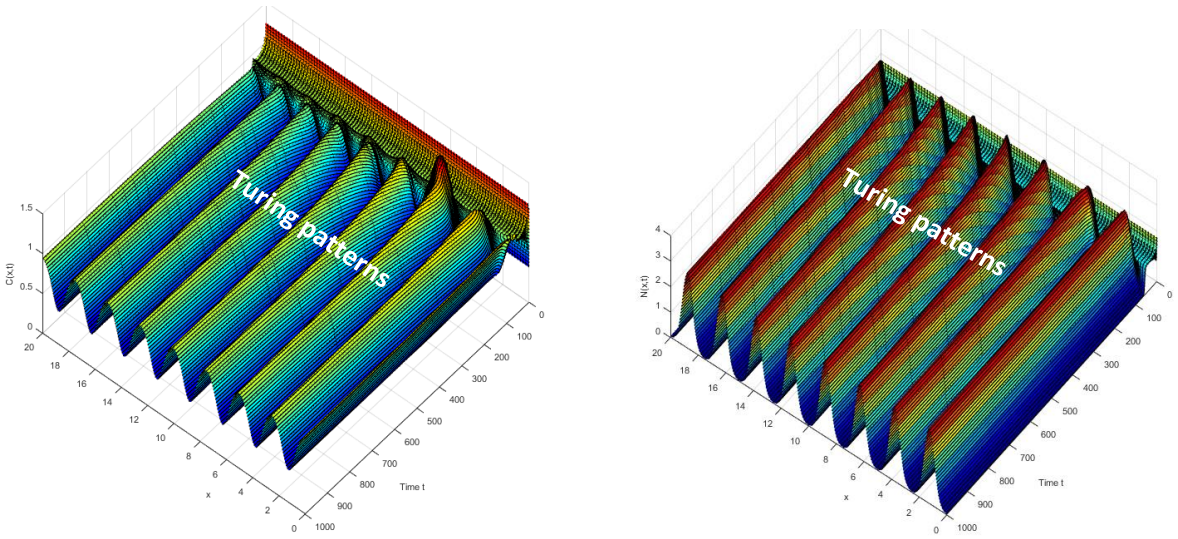

(a) **(b)**

Figure II-10 Numerical simulation for Turing patterns: C(x,t) and N(x,t) for $q=1.1,\ \xi=0.031,\ \alpha=\beta=\lambda_1=\lambda_2=1$

2.3.6. Diagram of patterns

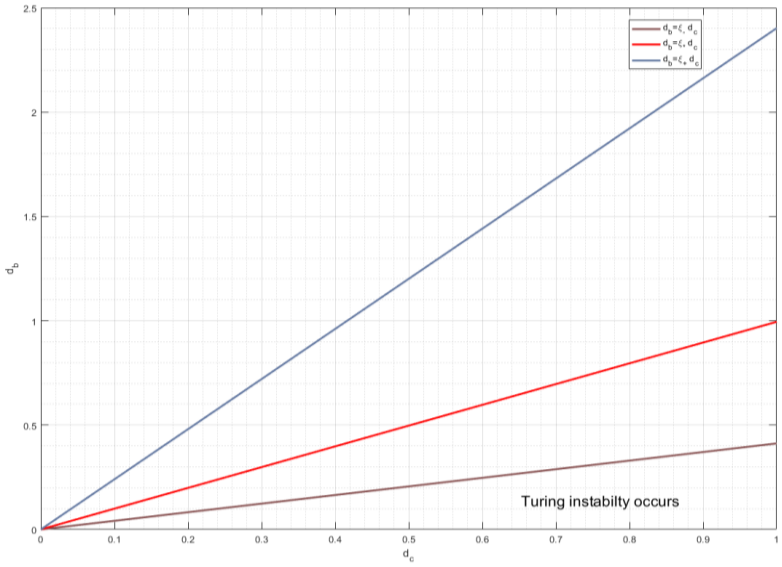

Figure II-11 Bifurcation diagram for Turing instability in parameter space (d_b, d_c) for $q=1.01$. The unstable region is the area between the curve $d_b = \xi_- d_c$ and the d_c axis.

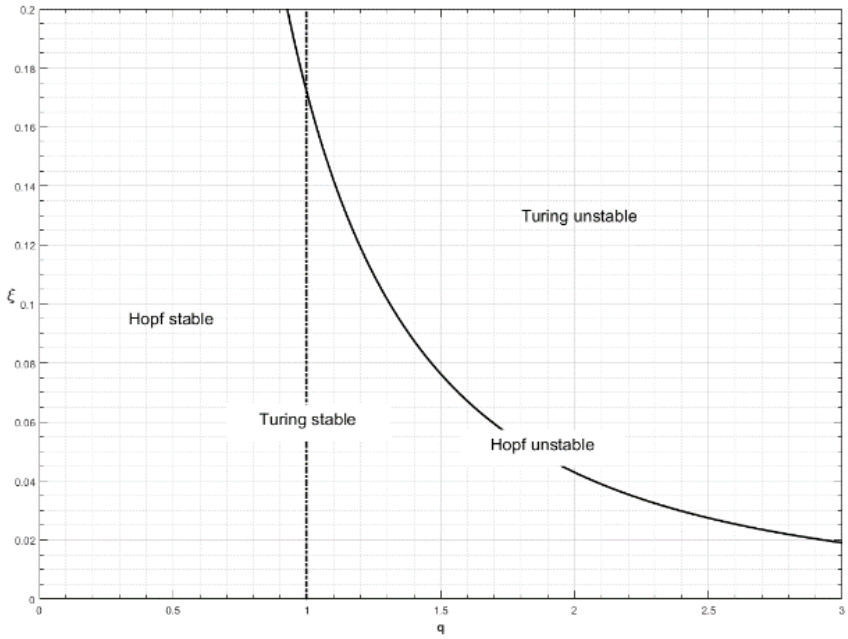

Figure II-12 Bifurcation diagram for Turing instability in parameter space (ξ, q)

2.4. COEXISTENCE OF SPATIAL AND TEMPORARY PATTERNS IN THE HYDROGEN TRANSPORT MODEL

2.4.1. Possible co-existence of Turing's and Hopf-Andronov's patterns (twice patterns)

The general system undergoes Hopf-Turing bifurcation at:

$$q_T = \sqrt{\frac{3-2\sqrt{2}}{\xi_{HT}}} = q_H \qquad \text{Eq II.87.}$$

This condition is satisfied for the following critical value of ξ:

$$\xi_{HT} = 3-2\sqrt{2} = 0.1716 \qquad \text{Eq II.88.}$$

(i) If $\xi < \xi_{HT}$ then $q^T > q^H$. With increasing q, the Hopf threshold is the first to be crossed and thus the Hopf bifurcation will be the first to occur near to the critically.

(ii) If $\xi > \xi_{HT}$, the first bifurcation will occur toward Turing pattern.

2.4.2. Numerical analysis of twice oscillations

We distinguish four different domains. The domain of pure Turing instabilities that are spatially inhomogeneous but stable in time and for which $\xi < \xi^-$ and $q > q^H$. Above, the domain of pure Hopf instabilities that are homogeneous in space but oscillate in time, which is situated at ($\xi > \xi^-$, $q < q^H$). In the domain located under the two bifurcation curves, both Hof and Turing instability may co-exist and compete which gives rise to complex spatiotemporal patterns near to $P_{HT} = (\xi_{HT}, q_{HT})$, the point of intersection. The fourth region is the stable where the steady-state is the only solution of the global system.

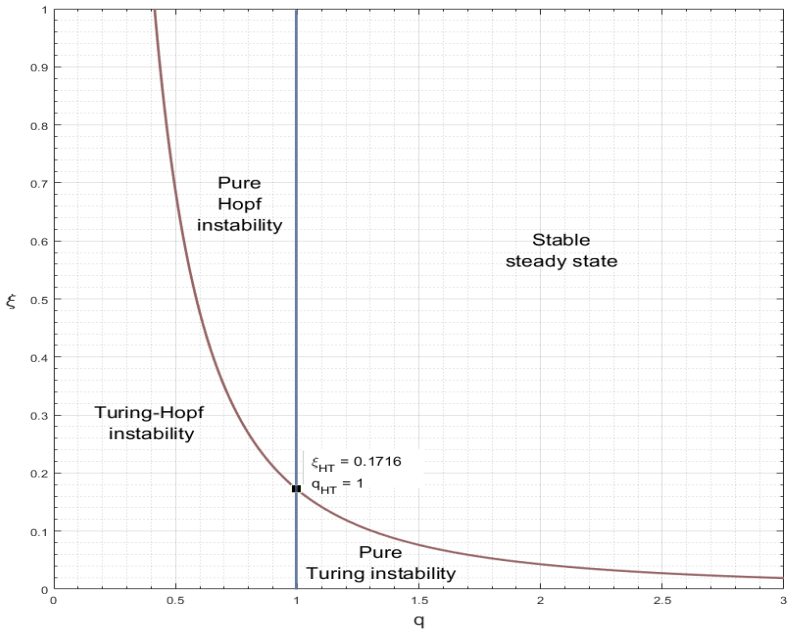

Figure II-13 Bifurcation diagram for system reaction-diffusion system in the (ξ, q) parameter space. The blue line is the Hopf bifurcation curve, and the red line denotes Turing bifurcation.

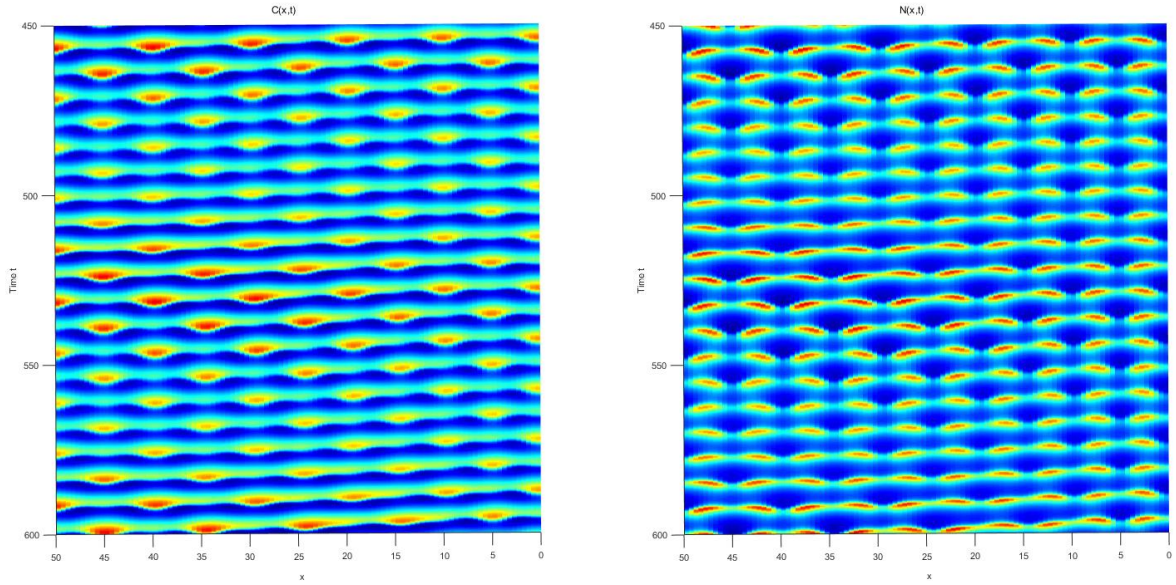

Figure II-14 Numerical simulations of Hopf-Turing structure: C(x,t) and N(x,t) near to the intersection point $P_{HT}=\left(\xi_{HT},q_{HT}\right)$ with $\left(q=0.93,\xi=0.2,\ \alpha{=}\beta{=}\lambda_1{=}\lambda_2{=}1\right)$

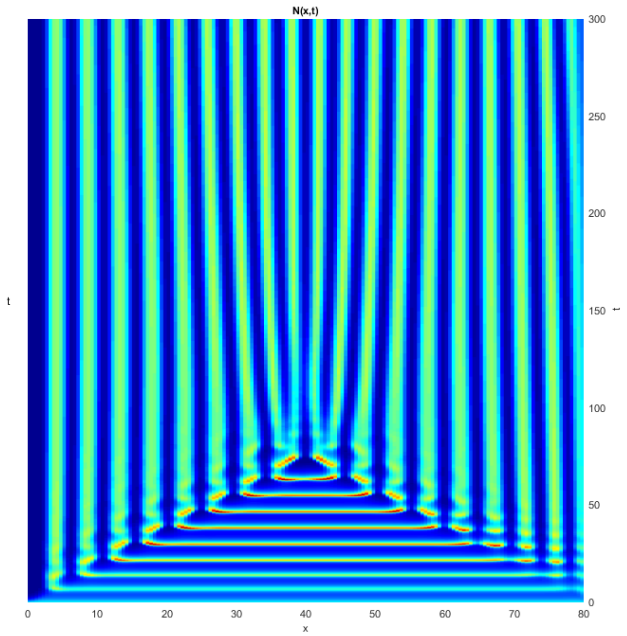

Figure II-15 Numerical simulations of the coexistence Hopf and Turing structures: C(x,t) and N(x,t) far from the intersection point $P_{HT}=\left(\xi_{HT},q_{HT}\right)$.

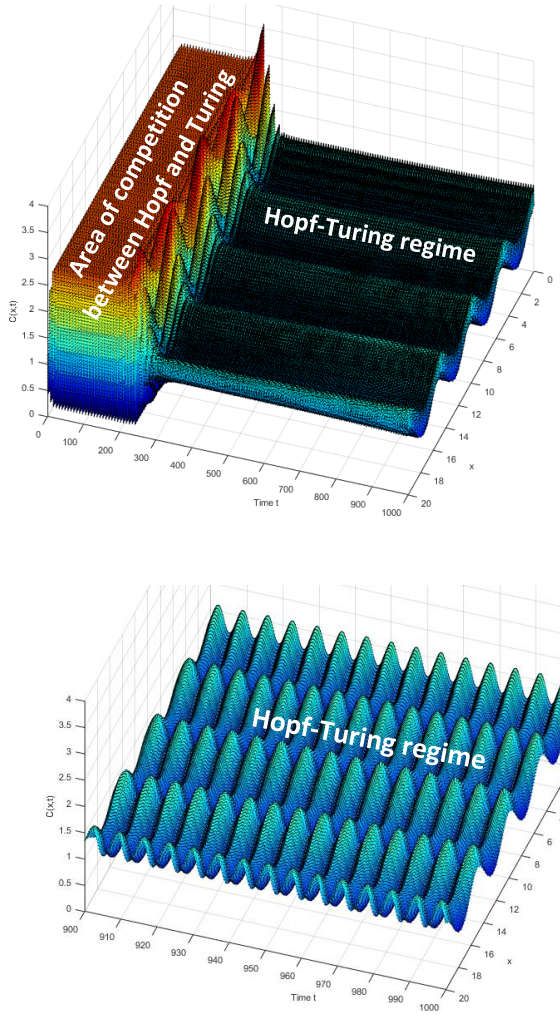

Figure II-16 C(x,t): Numerical simulations of Hopf–Turing patterns near to the intersection point $P_{HT} = (\xi_{HT}, q_{HT})$

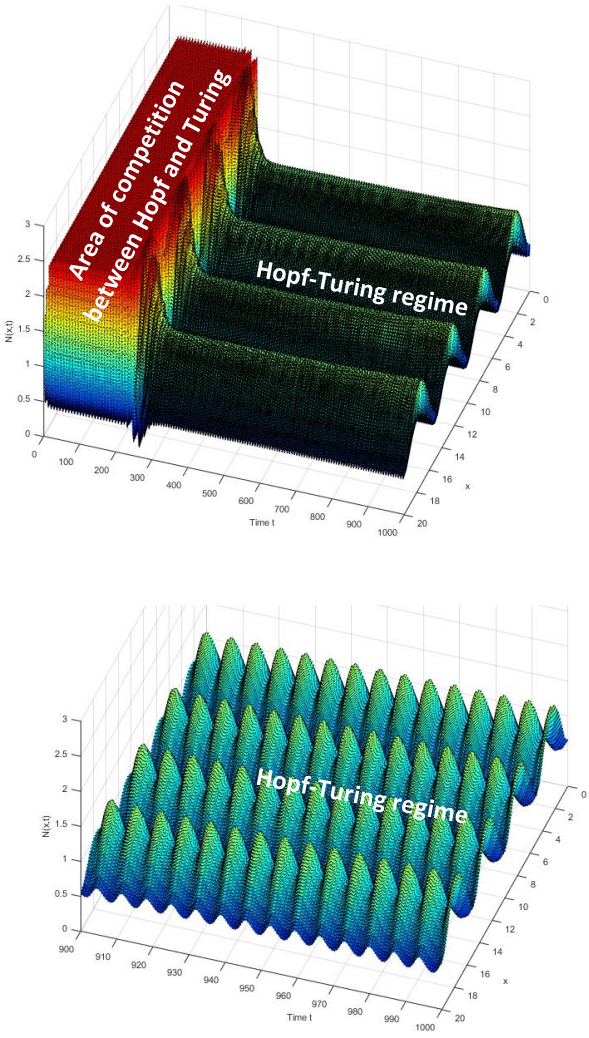

Figure II-17 N(x,t): Numerical simulations of Hopf–Turing patterns near to the intersection point $P_{HT} = (\xi_{HT}, q_{HT})$

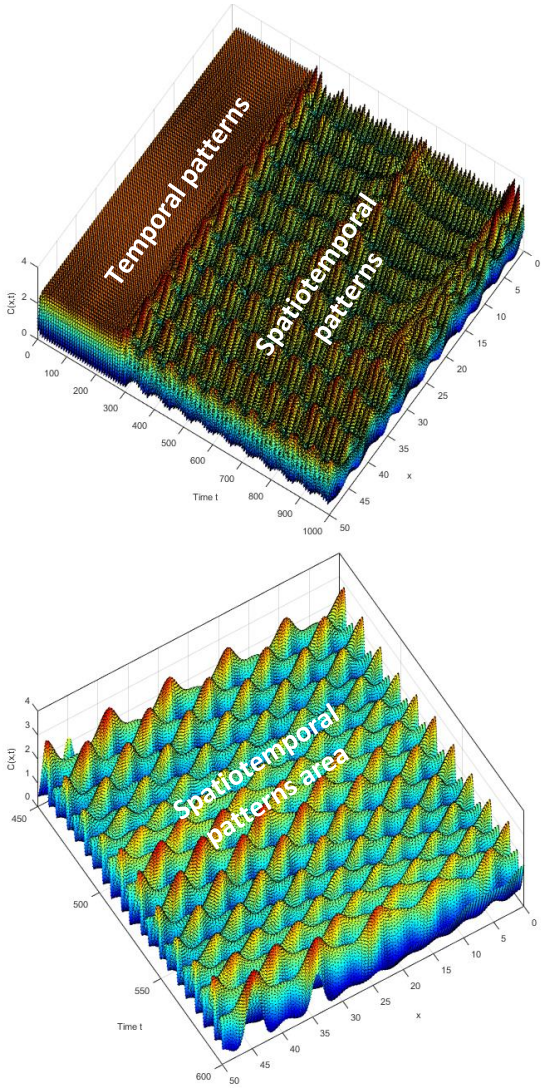

Figure II-18 C(x,t): Numerical simulations of Hopf-Turing structure in another point near to intersection point $P_{HT} = (\xi_{HT}, q_{HT})$

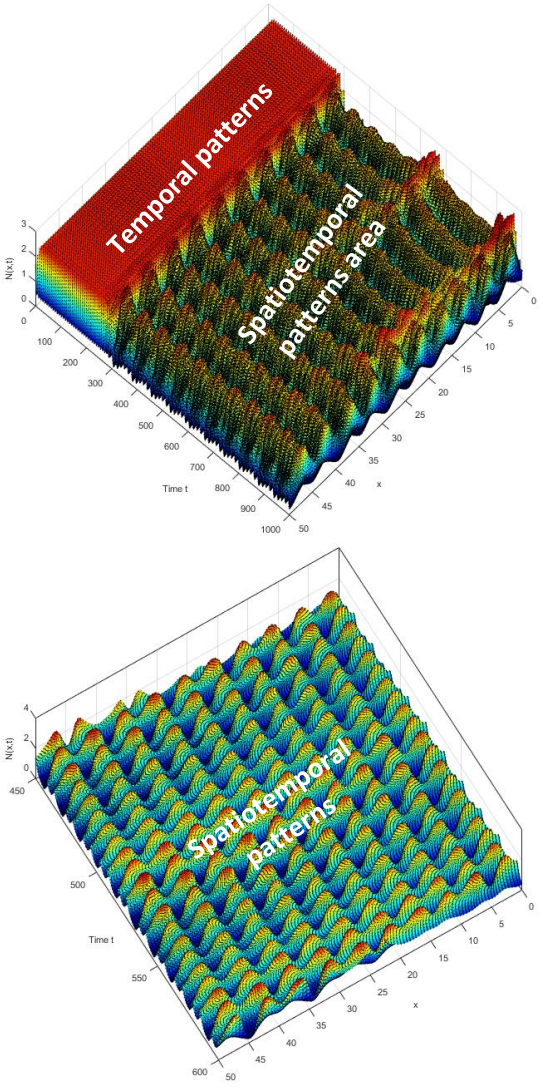

Figure II-19 N(x,t): Numerical simulations of Hopf-Turing structure in another point near to intersection point $P_{HT} = (\xi_{HT}, q_{HT})$

2.5. PATTERNS IN DOUBLE POROSITY REACTION-DIFFUSION SYSTEM

Many books and publications are devoted to the patterns in homogeneous media, whereas the irregularity of the medium may have a quantitative and/or qualitative impact on the pattern formation. Our study show that the heterogeneity can provoke considerable changes on criteria of the appearance of some instabilities in reaction-diffusion systems.

2.5.1. Extension of the model of bio-reactive transport on double porosity media

- We consider a more complicated system of reaction-diffusion equations, which corresponds to simultaneous bacteria and nutrient transport in a double porosity medium. It consists of two interpenetrating continua (fractures and blocks) which exchange the nutrients with each other. The fractures have high permeability (or a high diffusion parameter), while the blocks are low permeable. The term of flow in the equation for blocks can be neglected so that the mass of nutrients in blocks changes only due to the exchange with fractures. We assume that bacteria exist only in the fractures, i.e. they cannot penetrate too narrow pores of the blocks. The model is then:

$$\underbrace{\phi_F \frac{\partial C_F}{\partial t}}_{\text{Gas accumulation}} = \underbrace{\nabla.\left(D_{C_F} \nabla C_F\right)}_{\text{Diffusion}} + \underbrace{q(t)}_{\text{Advection}} - \underbrace{\lambda_1 \left(N_F\right)^{\alpha+1} C_F}_{\text{Consumption rate}} - \underbrace{\omega\left(C_F - C_B\right)}_{\text{Inter domain exchange rate}}$$

$$\underbrace{\phi_F \frac{\partial N_F}{\partial t}}_{\text{Bacteria accumulation}} = \underbrace{\nabla.\left(D_{N_F} \nabla N_F\right)}_{\text{Diffusion}} + \underbrace{\left(N_F\right)^{\alpha+1} C_F}_{\text{Growth rate}} - \underbrace{\lambda_2 \left(N_F\right)^{\beta}}_{\text{Decay rate}} \qquad \text{Eq II.89.}$$

$$\underbrace{\phi_B \frac{\partial C_B}{\partial t}}_{\text{Gas accumulation}} = \underbrace{\omega\left(C_F - C_B\right)}_{\text{Inter-domain exchange rate}}$$

here the first and the third equations describe the transport of nutrients in the fractures and blocks, while the second equation describes bacteria.

The subscripts B and F refer to the block and fracture region, N_F represents the number of bacteria living in the fractures, C_F and C_B are the concentrations of nutrients existing in the fractures and the blocks respectively, ϕ_F and ϕ_B is the internal porosity of fractures and blocks, and ω is the rate of exchange between fractures and blocks; ∇ is the Hamilton operator; q denotes the injection rate; λ_1 is the characteristic time of eating and λ_2 is the characteristic time of bacterial decay (λ_1 , λ_2 , α and β are constants)

The model assumes that the advective transport is neglecting.

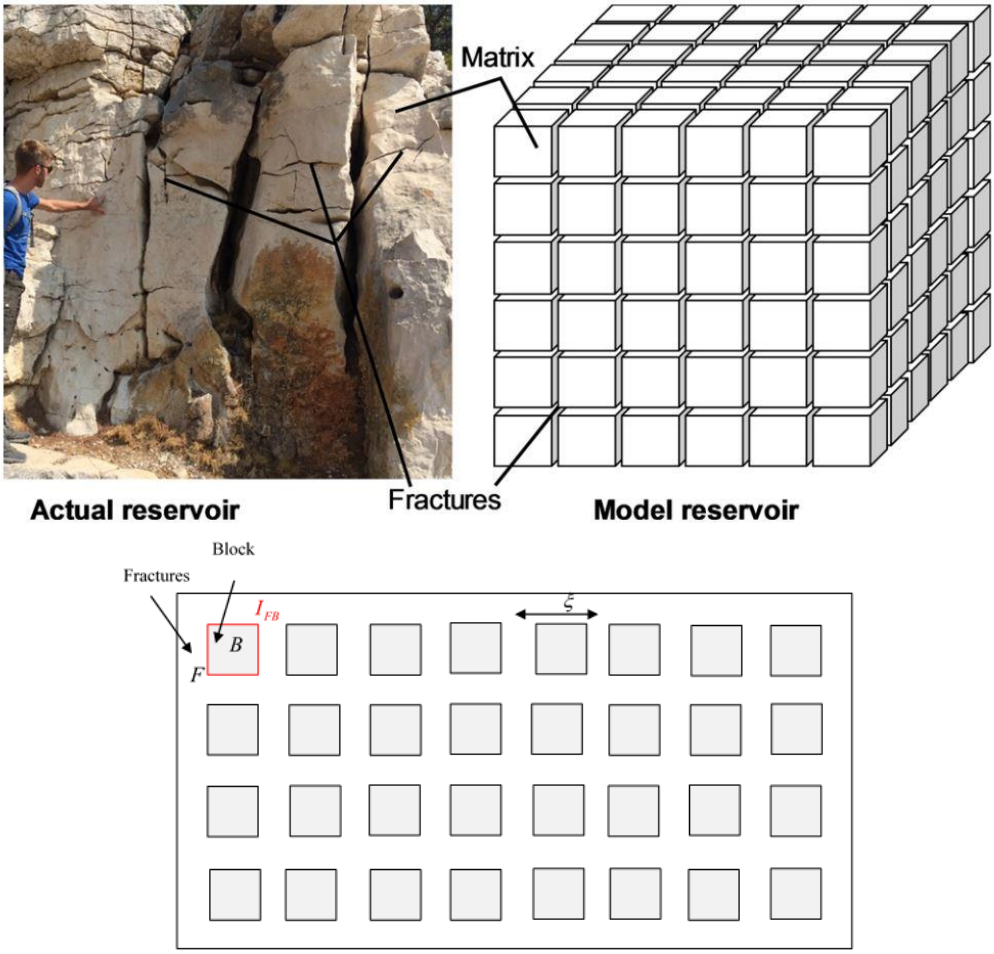

Figure II-20 Schematic of the dual-porous model "**sugar cube fractures**". I_{FB} is the fractures-block interface; ξ is the ratio of the length of a period of heterogeneity to the length of the entire domain, which is $\xi \ll 1$ (D. O. Egya et al. 2019)

At the interface between fractures and blocks sub-domains, the continuity of fluxes and concentrations must be ensured such that:

$$C_F = C_B \text{ at } I_{FB} \quad \text{Eq II.90.}$$

$$\mathbf{n}_{FB}.\left(\mathbf{D}_{\mathbf{C_F}}.\nabla C_F\right) = \underbrace{\mathbf{n}_{FB}.\left(\mathbf{D}_{\mathbf{C_B}}.\nabla C_B\right)}_{=0} \text{ at } I_{FB} \quad \text{Eq II.91.}$$

$\nabla N_F = 0$: Impermeable boundary in all the fracture domain $\sim \mathbf{n}_{FB}.\left(\mathbf{D}_{N_\mathbf{F}}.\nabla N_F\right) = 0$ Eq II.92.

The objective is to analyze the stability of such a system, or, more exactly, the impact of the exchange process on:

- the system stability;
- post-unstable patterns, i.e. the stable patterns that occur after the development of instability and its stabilization.

2.5.2. Stability analysis of the system

In matrix form, the system of equations can be described as follows:

$$\frac{\partial}{\partial t}\mathbf{u} = \mathbf{D}\Delta\mathbf{u} + \mathbf{F}(\mathbf{u}) \quad \text{Eq II.93.}$$

where we denote

$$\mathbf{u} = \begin{pmatrix} C_F \\ N_F \\ C_B \end{pmatrix},\ \mathbf{F}(\mathbf{u}) = \begin{bmatrix} f_1(C_F, N_F, C_B) \\ f_2(C_F, N_F, C_B) \\ f_3(C_F, N_F, C_B) \end{bmatrix} = \begin{bmatrix} q - \lambda_1 \left(N_F\right)^{\alpha+1} C_F - \omega\left(C_F - C_B\right) \\ \left(N_F\right)^{\alpha+1} C_F - \lambda_2 \left(N_F\right)^{\beta} \\ \omega\left(C_F - C_B\right) \end{bmatrix}, \text{ and}$$

$$\mathbf{D} = \begin{bmatrix} D_{C_F} & 0 & 0 \\ 0 & D_{N_F} & 0 \\ 0 & 0 & 0 \end{bmatrix}$$

As seen, such a system consists of:

- Two reaction-diffusion equations and one ordinary differential equation, which places it between the systems of two and three reaction-diffusion equations;

- Two equations of this system are coupled by means of an exchange term, which is a new element of the theory whose impact was not analyzed before.

The objective of the thesis is to find patterns, which are defined as limit (at $t \to \infty$) solutions in the form of stable periodic non-attenuating oscillatory waves, which attract other solutions. The keywords for a pattern are then: limit, periodic, attractor. In other words, a pattern corresponds to a closed trajectory in the phase space, which attracts other trajectories.

If a solution is non-periodic and stable at any time, then it remains non-periodic at $t \to \infty$, therefore this is not a pattern. If a stable solution is periodic at any time, then its phase portrait is a center or a set of centers. A center is not an attractor, i.e. any other solution is not attracted to it. Thus, it is not a pattern. We conclude that a pattern can occur only from an unstable behavior. Consequently, stability analysis becomes the main tool for studying patterns.

As in previous chapters, we can imagine three main types of patterns: steady-state patterns periodically oscillating in space (Turing's patterns), temporal patterns periodically oscillating in time and uniform in space (Hopf-Andronov's patterns), and simultaneous spatio-temporal patterns which oscillate periodically both in space and in time.

The class of simultaneous patterns periodically oscillating in space and time can be very large. A typical example is a standing wave, which exists in a system of three reaction-diffusion equations, but it does not exist in the case of two equations.

We can also expect that another subclass of simultaneous patterns exists, which has no relation to standing waves but occurs near the Hopf-Andronov bifurcation.

Our expectations are thus as follows:

- The number of equations enables us to expect that this system has solutions in the form of standing waves and Hopf-Turing oscillations. At the same time, we have no idea about the probable impact of the exchange term.

The objective is thus to analyze the impact of the exchange terms and the number of equations (three) on patterns that can arise at $t \to \infty$.

The stability analysis for a system of several differential equations can be performed in a standard way by the method of perturbation, or one can use the general theorem of stability, which is

known as Routh – Hurwitz theorem. To formulate it, we need to introduce some intermediate concepts.

Let $\mathbf{u}_{ss}(x) = \left(C_F|_{ss}, N_F|_{ss}, C_B|_{ss}\right)^T$ be the steady-state solution of (Eq II.89.) constant in space. Such a solution must satisfy the condition: $\mathbf{F}(\mathbf{u}_{ss}) = \mathbf{0}$. Let us assume that such function has been perturbed by an arbitrary perturbation of small amplitude ε. Let $\mathbf{u}' = \left(C_F', N_F', C_B'\right)^T$ be the response of the system (Eq II.89.) on such a perturbation, so that the solution has the form: $\mathbf{u} = \mathbf{u}_{ss} + \varepsilon\mathbf{u}'$. Substituting this expression in the system (Eq II.89.), and neglecting higher-order terms, we obtain the following linearized system:

$$\frac{\partial}{\partial t}\mathbf{u}' = \mathbf{D}\Delta\mathbf{u}' + \mathbf{J}(\mathbf{u}_{ss})\mathbf{u}' \qquad \text{Eq II.94.}$$

where $\mathbf{J}(\mathbf{u}) = \begin{bmatrix} \partial f_{1,C_F} & \partial f_{1,N_F} & \partial f_{1,C_B} \\ \partial f_{2,C_F} & \partial f_{2,N_F} & \partial f_{2,C_B} \\ \partial f_{3,C_F} & \partial f_{3,N_F} & \partial f_{3,C_B} \end{bmatrix}$, $\partial f_{1,C_F} \equiv \frac{\partial f_1}{\partial C_F}$, *etc.* is the Jacobian matrix, which occurs from the Taylor expansion of $\mathbf{F}(\mathbf{u})$.

We analyze the perturbation in the form

$$\mathbf{u}' = \mathbf{A}e^{i\mathbf{k}\mathbf{x}+\mu t} \qquad \text{Eq II.95.}$$

where $i = \sqrt{-1}$, **A** is a constant vector, **k** is the wavenumber, and μ is the wave increment. Substituting (Eq II.95.) in (Eq II.94.), we obtain the linear algebraic system

$$\left(\mathbf{J}(\mathbf{u}_{ss}) - \xi\mathbf{D} - \mu\mathbf{I}\right)\mathbf{A} = \mathbf{0}, \qquad \xi \equiv |\mathbf{k}|^2 \qquad \text{Eq II.96.}$$

As **A** is nonzero, we require that $\det\left(\mathbf{J}(\mathbf{u}_{ss}) - \xi\mathbf{D} - \mu\mathbf{I}\right) = 0$, which yields a cubic equation with respect to μ:

$$P(\mu)=0, \quad \text{where} \quad P(\mu)\equiv -\det\left(\mathbf{J}(\mathbf{u}_{ss})-\xi\mathbf{D}-\mu\mathbf{I}_{3,3}\right)=\mu^3+c_1^{\xi}\mu^2+c_2^{\xi}\mu+c_3^{\xi}$$

vector $c^{\xi}=\left(c_1^{\xi},c_2^{\xi},c_3^{\xi}\right)^T$ is:

$$c^{\xi}=\begin{pmatrix} -\text{trace}\left(\mathbf{J}(\mathbf{u}_{ss})-\xi\mathbf{D}\right) \\ -\det\begin{bmatrix} \partial f_{1,C_F}\big|_{ss}-\xi D_{C_F} & \partial f_{1,N_F}\big|_{ss} \\ \partial f_{2,C_F}\big|_{ss} & \partial f_{2,N_F}\big|_{ss}-\xi D_{N_F}\end{bmatrix}-\det\begin{bmatrix} \partial f_{2,N_F}\big|_{ss}-\xi D_{N_F} & \partial f_{2,C_B}\big|_{ss} \\ \partial f_{3,N_F}\big|_{ss} & \partial f_{3,C_B}\big|_{ss}\end{bmatrix}-\det\begin{bmatrix} \partial f_{1,C_F}\big|_{ss}-\xi D_{C_F} & \partial f_{1,C_B}\big|_{ss} \\ \partial f_{3,C_F}\big|_{ss} & \partial f_{3,C_B}\big|_{ss}\end{bmatrix} \\ -\det\left(\mathbf{J}(\mathbf{u}_{ss})-\xi\mathbf{D}\right)\end{pmatrix}$$

To formulate the Routh - Hurwitz stability theorem, it remains to introduce the concept of the Hurwitz matrix $\mathcal{H}$, which is defined as follows, for the system of three differential equations:

$$\mathcal{H}\equiv\begin{pmatrix} c_1^{\xi} & c_3^{\xi} & 0 \\ 1 & c_2^{\xi} & 0 \\ 0 & c_1^{\xi} & c_3^{\xi}\end{pmatrix} \qquad \text{Eq II.97.}$$

2.5.3. Analysis of the characteristic equation: Routh - Hurwitz stability criterion

Definition:

System (Eq II.94.) is called to be stable if $P(\mu)=0$ has only the roots with negative real parts.

Indeed, in this case, any perturbations (Eq II.95.) are vanishing at $t\to\infty$.

Theorem:

System (Eq II.94.) is stable if and only if the following two conditions are fulfilled:

(1) All coefficients of the characteristic polynomial $P(\mu)$ are strictly positive:

$$c_1^{\xi} > 0, \quad c_2^{\xi} > 0, \quad c_3^{\xi} > 0 \qquad \text{Eq II.98.}$$

(2) All determinants of principal minors $\Delta_{(i,i)}^{\xi}$ of the Hurwitz matrix $\mathcal{H}$ (i=1,2,…,n-1) are positive:

$$\Delta_{(1,1)}^{\xi} = c_1^{\xi} > 0, \qquad \Delta_{(2,2)}^{\xi} = \begin{vmatrix} c_1^{\xi} & c_3^{\xi} \\ 1 & c_2^{\xi} \end{vmatrix} = c_1^{\xi} c_2^{\xi} - c_3^{\xi} > 0 \qquad \text{Eq II.99.}$$

2.5.4. Hopf-Andronov's and Turing's patterns

Such a pattern represents a periodic oscillation in time and uniform in space. So, the diffusion term disappears. The analysis of the instability becomes simpler in the case of a diffusionless system, in which the space derivatives disappear, and such a system transforms into a system of ODEs in time.

For diffusionless case, (Eq II.89.) give the system of ODE (Eq II.100.)

$$\begin{aligned} \phi_F \frac{\partial C_F}{\partial t} &= q - \lambda_1 \left(N_F\right)^{\alpha+1} C_F - \omega\left(C_F - C_B\right) \\ \phi_F \frac{\partial N_F}{\partial t} &= \left(N_F\right)^{\alpha+1} C_F - \lambda_2 \left(N_F\right)^{\beta} \\ \phi_B \frac{\partial C_B}{\partial t} &= \omega\left(C_F - C_B\right) \end{aligned} \qquad \text{Eq II.100.}$$

In the absence of diffusion, the space variable disappears, and then ξ=0.

To analyze patterns, we will need to use the criteria of instability, since the concept of a pattern is closely related to the concept of instability. According to Routh - Hurwitz stability criterion, system (Eq II.100.) is stable if and only if, simultaneously:

$$c_1^{\xi=0} > 0, \qquad c_2^{\xi=0} > \frac{c_3^{\xi=0}}{c_1^{\xi=0}}, \qquad c_3^{\xi=0} > 0 \qquad \text{Eq II.101.}$$

The critical values q leading the appearance instabilities depends explicitly on ω. The case ω=0 corresponds to a homogeneous medium (and two ODEs). As seen, the variation of ω has some impact on the instability domain. Heterogeneity will help to develop and strengthen instabilities

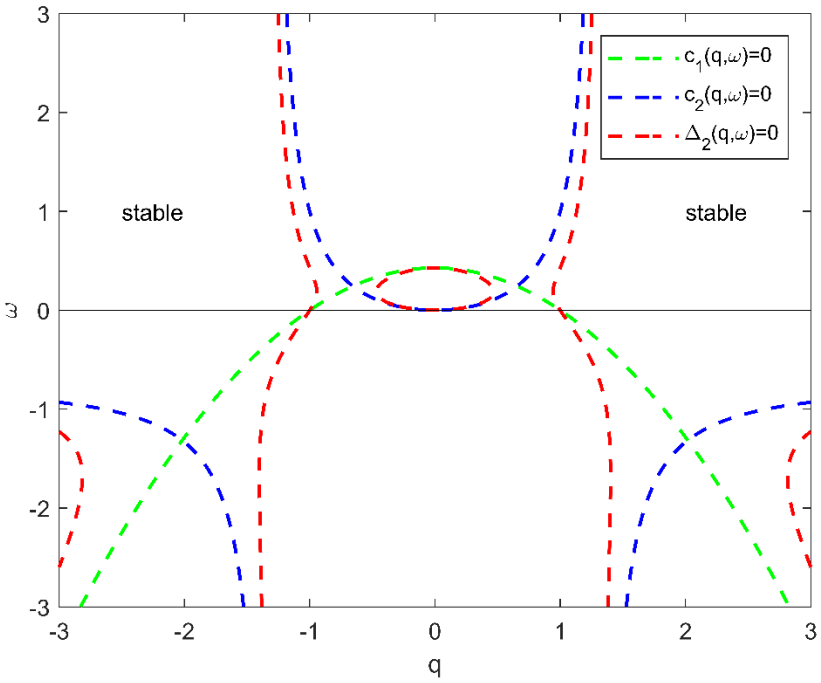

Figure II-21 Plots of the boundary $c_1(q,\omega)=0$, $c_2(q,\omega)=0$ and $\Delta_2(q,\omega)=0$ of the ODE system considering $\lambda_1=\lambda_2=\alpha=\beta=1, \phi_F=0.2, \phi_B=0.15.$

Hopf-Andronov's bifurcation:

The concept of a bifurcation of a dynamical system describes the behavior of its solutions in the vicinity of a singular point with respect to continuous and monotonic variation of a parameter, which is called "control parameter" or "bifurcation parameter".

A periodic oscillation in time and uniform in space, which attracts other solutions at $t\to\infty$ corresponds to a closed trajectory in the phase space, which attracts other trajectories. Such a structure is called the limit cycle. In the case of two ODE, the limit cycle is a closed two-

dimensional curve. In a system of ODEs of higher dimensions, the limit cycle has the form of a multidimensional torus.

A limit cycle is closely related to the concept of the Hopf-Andronov bifurcation. The bifurcation of a dynamical system means a qualitative change in the behavior of its solutions (transition between stable and unstable behavior, or between two different stable states) in the vicinity of a singular point with respect to continuous and monotonic variation of a parameter, which is called "control parameter" or "bifurcation parameter". We will denote it by ρ. In the case of the system (Eq II.89.), the control parameters are q and ω. Parameter q is the rate of nutrient injection in the medium and determines the impact of the external force. Parameter ω is the rate of mass exchange by the nutrients between fractures and blocks and determines the impact of the medium heterogeneity.

The bifurcation of Hopf-Andronov corresponds to the loss of stability of the singular point "focus" under a monotonic and continuous variation of ρ. This necessarily leads to the occurrence of a limit cycle around the focus. Therefore, the Hopf-Andronov bifurcation is related to a limit cycle and to instability. This is not the single type of instability that can arise in a dynamical system, but this is a single type of instability that develops to periodic oscillatory solutions, i.e. leads to patterns.

The critical value of the control parameter ρ at which the system undergoes the Hopf-Andronov bifurcation will be denoted as $\rho_{H.}$

The value ρ_H determines only one boundary of the area of the existence of the limit cycle. Near this point, the limit cycle has a very small effective radius. When ρ moves away from ρ_H, the radius of the limit cycle grows, up to become infinite at point ρ_{H2}, which is the second boundary of the domain of existence of the limit cycle. The value ρ_{H2} can be calculated only numerically.

For a non-attenuating and non-growing time-oscillating mode, it is necessary that $\Im m(\mu) \neq 0$ and $\Re e(\mu) = 0$. More exactly, the necessary and sufficient conditions for the system (Eq II.100.) undergoes a Hopf-Andronov bifurcation at point ρ_H are:

(1) The characteristic equation (Eq II.100.):

$$\det\left(\mathbf{J}(\mathbf{u}_{ss})-\mu\mathbf{I}\right)=\mathbf{0}, \qquad \text{or} \qquad \mu^3+c_1^{\xi=0}\mu^2+c_2^{\xi=0}\mu+c_3^{\xi=0}=0$$

has a pair of pure imaginary roots (μ_1,μ_2) at point ρ_H with $\mu_2=-\mu_1$, and the third root μ_3 is real negative.

(2) $$\left.\frac{d\Re e\left(\mu_{1,2}(\rho)\right)}{d\rho}\right|_{\rho=\rho_H}\neq 0.$$

For n=3, conditions **(1)** and **(2)** are equivalent to the following conditions (Liu, 1992) at $\rho=\rho_H$:

(1') $$c_1^{\xi=0}>0, \qquad c_3^{\xi=0}>0, \qquad \Delta_{(2,2)}\equiv c_1^{\xi=0}c_2^{\xi=0}-c_3^{\xi=0}=0$$

(2') $$\left.\frac{d\Delta_{(2,2)}(\rho)}{d\rho}\right|_{\rho=\rho_H}\neq 0,$$

Therefore a solution oscillating around an equilibrium state u_{ss} means that the selected parameters are in the plan $c_1^{\zeta=0}>0, c_2^{\zeta=0}>0$, and close to the Hopf branch $\Delta_2^{\zeta=0}=c_1^{\zeta=0}c_2^{\zeta=0}-c_3^{\zeta=0}=0$, with $\omega>0$.

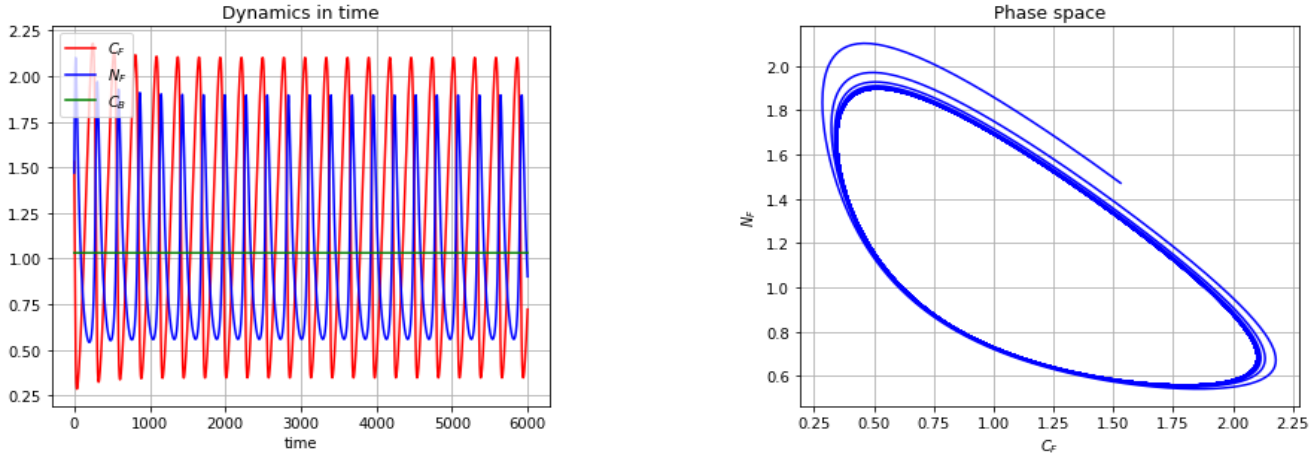

Figure I-22 The behavior of the ODE system for $\lambda_1=1,\ \lambda_2=1,\ \alpha=1,\beta=1,$ $\omega=0,\ q=0.97,\ \phi_F=0.2,\phi_B=0.15$

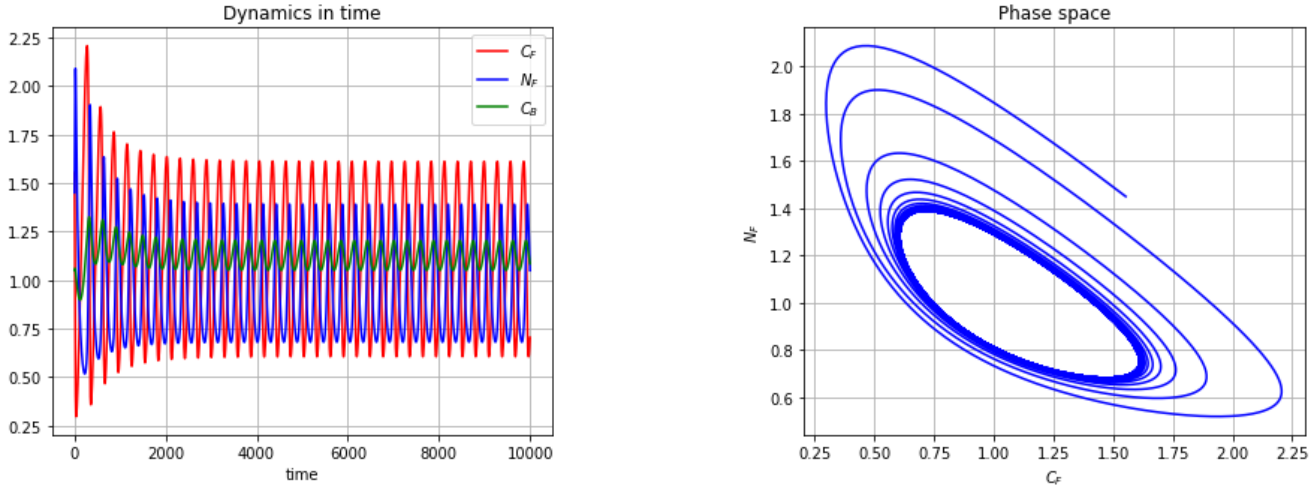

Figure II-23 The behavior of the ODE system $\lambda_1 = 1,\ \lambda_2 = 1,\ \alpha = 1, \beta = 1$,

$\omega = 0.1,\ q = 0.95,\ \phi_F = 0.2, \phi_B = 0.15$

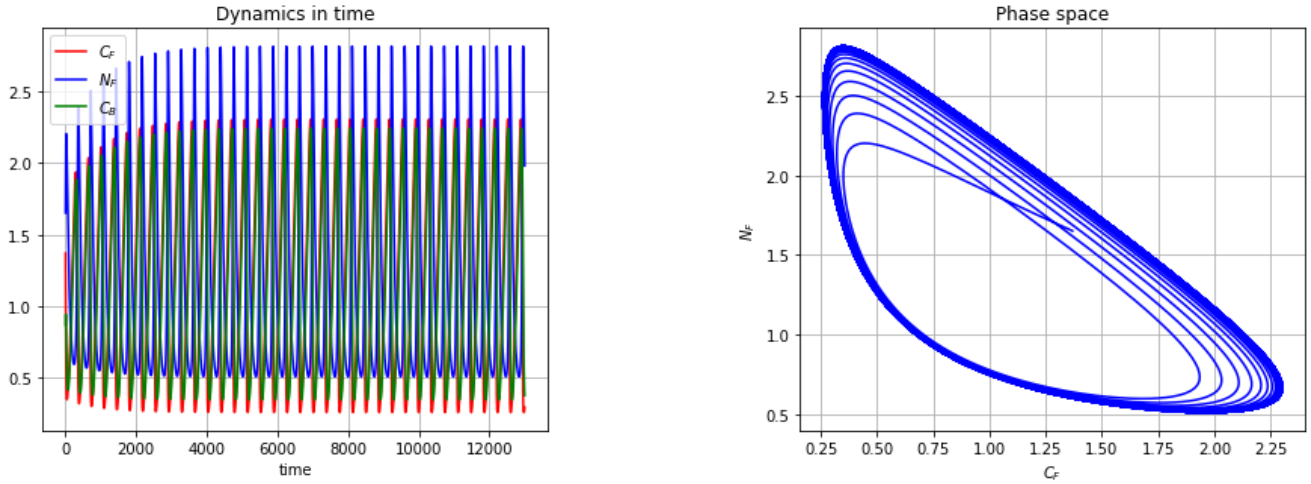

Figure II-24 The behavior of the ODE system for $\lambda_1 = 1,\ \lambda_2 = 1,\ \alpha = 1, \beta = 1$,

$\omega = 1.4,\ q = 1.15,\ \phi_F = 0.2, \phi_B = 0.15$

We can see that the concentration of carbon dioxide increases with increasing exchange term.

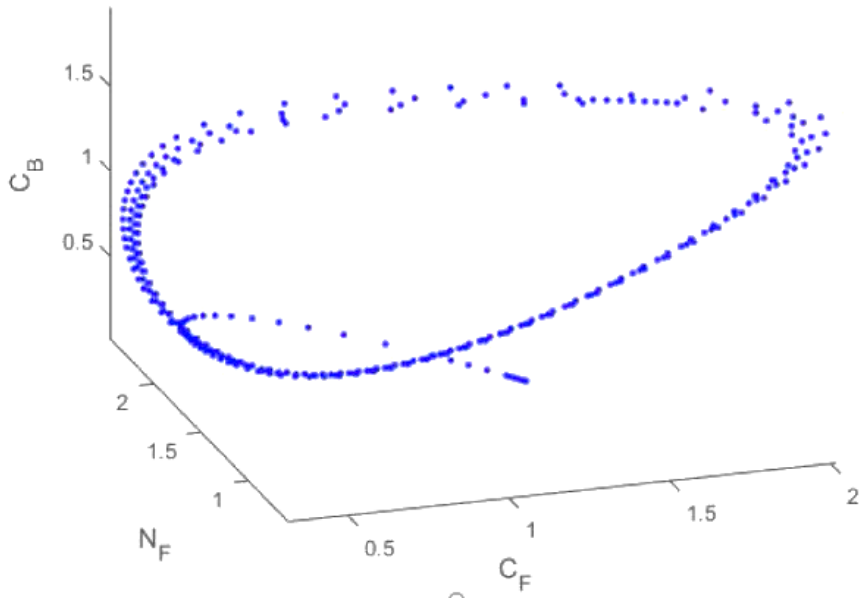

Figure II- 25 3D visualization of the behavior of the ODE system

Turing's patterns:

Turing's pattern is a limit at $t \to \infty$, stationary solution of a reaction-diffusion system periodically oscillating in space and attracting other solutions. it occurs when a spatially uniform steady-state solution u_{ss}, stable in the absence of diffusion, becomes unstable when diffusion is present. Then, Turing's instability occurs in the area of the intersection of the stable zone of the dynamical system (Eq II.100.) and the unstable zone of the PDE system (Eq II.89.). The stable zone of the subsystem (Eq II.100.) corresponds to attenuating oscillations in time, i.e. to $\Re e\left(\mu(0)\right) < 0$. The unstable area is determined by the theorem of Routh-Hurwitz. Then we obtain the conditions of Turing's instability:

$$\begin{cases} c_1^{\zeta=0} > 0, \quad c_1^{\zeta=0} c_2^{\zeta=0} > c_3^{\zeta=0}, \quad c_3^{\zeta=0} > 0 \\ Outside\left\{ c_1^{\zeta} < 0, \quad c_1^{\zeta} c_2^{\zeta} < c_3^{\zeta} \quad or \quad c_3^{\zeta} < 0 \right\}, \quad \text{at} \quad \zeta \neq 0 \end{cases} \qquad \text{Eq II.102.}$$

At the threshold of the Turing instability, we would have $c_3^{\zeta} = 0$.

To achieve the Turing instability, we seek ζ which satisfy

$$\frac{d}{dK}c_3^{\zeta=\zeta_{\min}}==0 \text{ with } \zeta_{\min}>0, \text{ and } -c_3^{\zeta=\zeta_{\min}}=\det\left(\mathbf{J}(\zeta_{\min})\right)>0.$$

Note that

$$c_3^{\zeta}=-\det\left(\mathbf{J}(\zeta)\right)=\frac{\omega}{\phi_B{\phi_F}^2}\left(D_C^F D_N^F {\phi_F}^2\zeta^2+\left(D_C^F\phi_F\left(1-\frac{(\alpha+1)q}{\lambda_1}\left(\frac{q}{\lambda_1\lambda_2}\right)^{\frac{-1}{\beta}}\right)+D_N^F\phi_F\lambda_1\left(\frac{q}{\lambda_1\lambda_2}\right)^{\frac{\alpha+1}{\beta}}\right)\zeta+\lambda_1\left(\frac{q}{\lambda_1\lambda_2}\right)^{\frac{\alpha+1}{\beta}}\right). \quad \text{Eq II.103.}$$

Then, $\det\left(\mathbf{J}(\mathrm{K})\right)$ will take its minimum value, when

$$\frac{d}{d\zeta}c_3^{\zeta}=-\frac{d}{d\zeta}\det\left(\mathbf{J}(\zeta)\right)=\frac{\omega}{\phi_B{\phi_F}^2}\left(2D_C^F D_N^F{\phi_F}^2\zeta+\left(D_C^F\phi_F\left(1-\frac{(\alpha+1)q}{\lambda_1}\left(\frac{q}{\lambda_1\lambda_2}\right)^{\frac{-1}{\beta}}\right)+D_N^F\phi_F\lambda_1\left(\frac{q}{\lambda_1\lambda_2}\right)^{\frac{\alpha+1}{\beta}}\right)\right)=0 \quad \text{Eq II.104.}$$

Solving $\frac{d}{d\zeta}\det\left(\mathbf{J}(\zeta)\right)=0$, we obtain the formula for K in terms of D_C^F and D_N^F, which is given by

$$\zeta\left(D_C^F,D_C^F\right)=\zeta_{\min}\left(D_C^F,D_C^F\right)=-\frac{\left(D_C^F\left(1-\frac{(\alpha+1)q}{\lambda_1}\left(\frac{q}{\lambda_1\lambda_2}\right)^{\frac{-1}{\beta}}\right)+D_N^F\lambda_1\left(\frac{q}{\lambda_1\lambda_2}\right)^{\frac{\alpha+1}{\beta}}\right)}{2D_C^F D_N^F\phi_F} \quad \text{Eq II.105.}$$

To ensure $\zeta_{\min}>0$, we require $\left(D_C^F\left(1-\frac{(\alpha+1)q}{\lambda_1}\left(\frac{q}{\lambda_1\lambda_2}\right)^{\frac{-1}{\beta}}\right)+D_N^F\lambda_1\left(\frac{q}{\lambda_1\lambda_2}\right)^{\frac{\alpha+1}{\beta}}\right)<0$

We define the ratio $\xi=\frac{D_N^F}{D_C^F}$, $0<\xi=\frac{D_N^F}{D_C^F}<-\frac{\left(1-\frac{(\alpha+1)q}{\lambda_1}\left(\frac{q}{\lambda_1\lambda_2}\right)^{\frac{-1}{\beta}}\right)}{\lambda_1\left(\frac{q}{\lambda_1\lambda_2}\right)^{\frac{\alpha+1}{\beta}}}$

Then

$$4\delta_{\min} = \underbrace{-(\lambda_1)^2\left(\frac{q}{\lambda_1\lambda_2}\right)^{\frac{2(\alpha+1)}{\beta}}}_{A(q)}\xi^2 + \underbrace{2\lambda_1\left(1+\frac{(\alpha+1)q}{\lambda_1}\left(\frac{q}{\lambda_1\lambda_2}\right)^{\frac{-1}{\beta}}\right)\left(\frac{q}{\lambda_1\lambda_2}\right)^{\frac{(\alpha+1)}{\beta}}}_{B(q)}\xi - \underbrace{\left(1-\frac{(\alpha+1)q}{\lambda_1}\left(\frac{q}{\lambda_1\lambda_2}\right)^{\frac{-1}{\beta}}\right)^2}_{C(q)} = 0 \quad \text{Eq II.106.}$$

Resolving this equation which is a quadratic polynomial with respect to ξ, we obtain :

$$\xi_{\pm} = \frac{1+\frac{(\alpha+1)q}{\lambda_1}\left(\frac{q}{\lambda_1\lambda_2}\right)^{\frac{-1}{\beta}} \pm 2\sqrt{\frac{(\alpha+1)q}{\lambda_1}\left(\frac{q}{\lambda_1\lambda_2}\right)^{\frac{-1}{\beta}}}}{(\lambda_1)\left(\frac{q}{\lambda_1\lambda_2}\right)^{\frac{(\alpha+1)}{\beta}}} \quad \text{Eq II.107.}$$

We can see that

$$0 < \xi_- = \frac{1+\frac{(\alpha+1)q}{\lambda_1}\left(\frac{q}{\lambda_1\lambda_2}\right)^{\frac{-1}{\beta}} - 2\sqrt{\frac{(\alpha+1)q}{\lambda_1}\left(\frac{q}{\lambda_1\lambda_2}\right)^{\frac{-1}{\beta}}}}{(\lambda_1)\left(\frac{q}{\lambda_1\lambda_2}\right)^{\frac{(\alpha+1)}{\beta}}} < \xi_* = -\frac{\left(1-\frac{(\alpha+1)q}{\lambda_1}\left(\frac{q}{\lambda_1\lambda_2}\right)^{\frac{-1}{\beta}}\right)}{\lambda_1\left(\frac{q}{\lambda_1\lambda_2}\right)^{\frac{\alpha+1}{\beta}}} < \xi_+ = \frac{1+\frac{(\alpha+1)q}{\lambda_1}\left(\frac{q}{\lambda_1\lambda_2}\right)^{\frac{-1}{\beta}} + 2\sqrt{\frac{(\alpha+1)q}{\lambda_1}\left(\frac{q}{\lambda_1\lambda_2}\right)^{\frac{-1}{\beta}}}}{(\lambda_1)\left(\frac{q}{\lambda_1\lambda_2}\right)^{\frac{(\alpha+1)}{\beta}}} \quad \text{Eq II.108.}$$

Both of conditions $\delta_{\min}$ and $\left(D_C^F\left(1-\frac{(\alpha+1)q}{\lambda_1}\left(\frac{q}{\lambda_1\lambda_2}\right)^{\frac{-1}{\beta}}\right)+D_N^F\lambda_1\left(\frac{q}{\lambda_1\lambda_2}\right)^{\frac{\alpha+1}{\beta}}\right)<0$ must be satisfied.

Therefore, the conditions $\xi < \xi_-$ are considered.

Then, we have the following results:

(1) The equilibrium is asymptotically stable for $\xi > \xi_-$.

(2) The critical line of Turing instabilities is $\xi = \dfrac{1+\frac{(\alpha+1)q}{\lambda_1}\left(\frac{q}{\lambda_1\lambda_2}\right)^{\frac{-1}{\beta}} - 2\sqrt{\frac{(\alpha+1)q}{\lambda_1}\left(\frac{q}{\lambda_1\lambda_2}\right)^{\frac{-1}{\beta}}}}{(\lambda_1)\left(\frac{q}{\lambda_1\lambda_2}\right)^{\frac{(\alpha+1)}{\beta}}}$

(3) When , $\xi < \dfrac{1+\frac{(\alpha+1)q}{\lambda_1}\left(\frac{q}{\lambda_1\lambda_2}\right)^{\frac{-1}{\beta}} - 2\sqrt{\frac{(\alpha+1)q}{\lambda_1}\left(\frac{q}{\lambda_1\lambda_2}\right)^{\frac{-1}{\beta}}}}{(\lambda_1)\left(\frac{q}{\lambda_1\lambda_2}\right)^{\frac{(\alpha+1)}{\beta}}} = \xi_{Tc}$ the equilibrium is unstable

and Turing destabilization occurs.

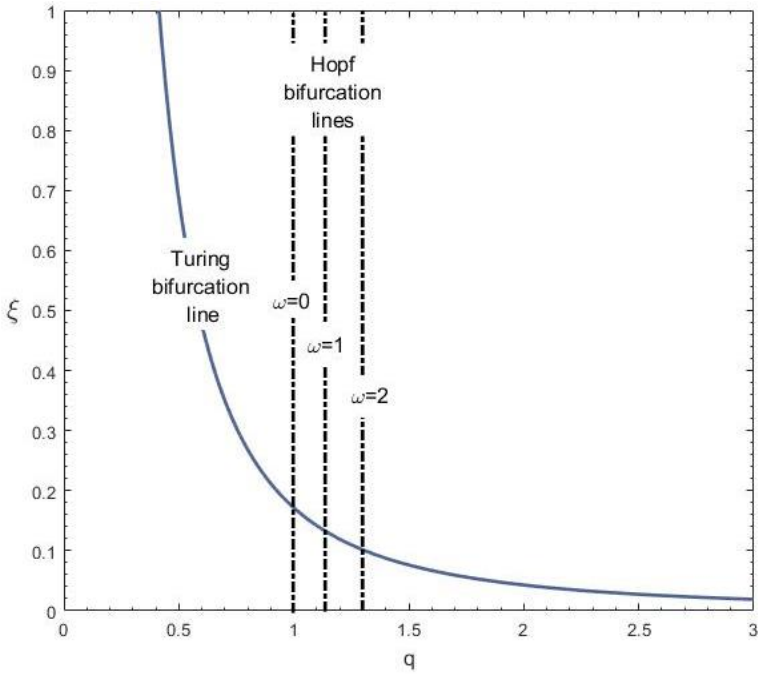

Figure II-26 Bifurcation diagram for Turing instability in parameter space (q,ξ) for $\lambda_1=1,\ \lambda_2=1,\ \alpha=1,\beta=1$, $\phi_F=0.2,\phi_B=0.15$.

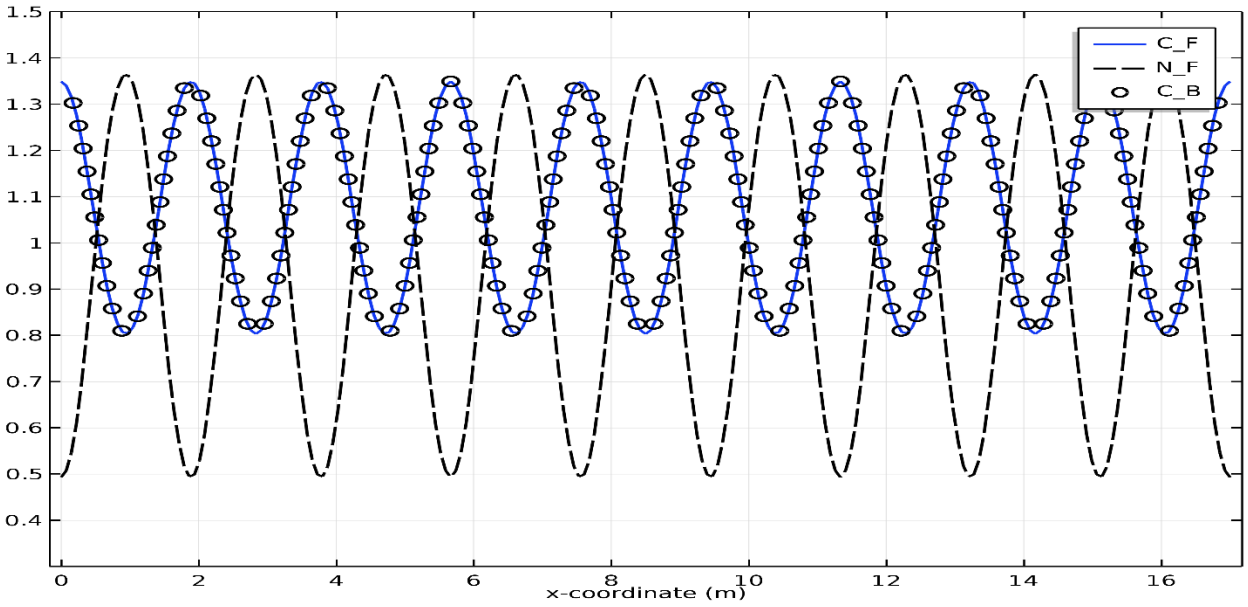

Figure II-27 Numerical simulation for Turing patterns of the average concentration C_F, C_B and the bacterial population N_F in the dual porous model with $\lambda_1=1,\ \lambda_2=1,\ \alpha=1,\beta=1,$ $\omega=0.1,\ q=0.94,\ \phi_F=0.2,\phi_B=0.15, D_{C^F}=1, D_{N^F}=0.17$ at t=1000s.

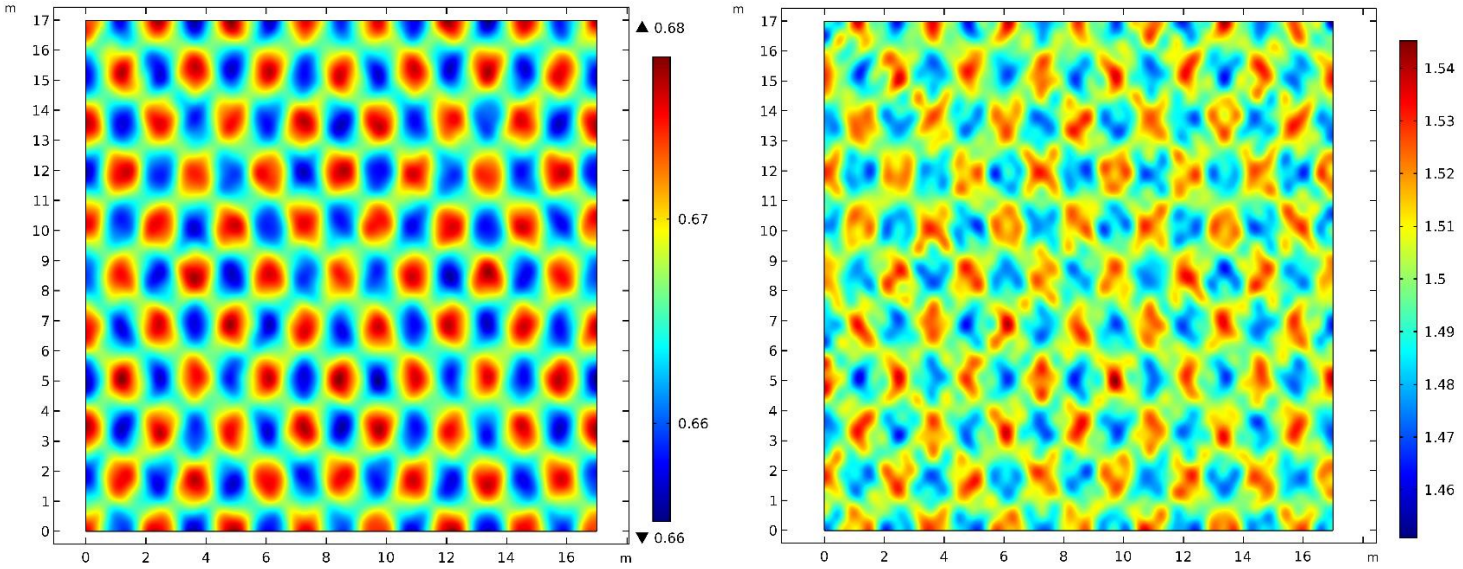

Figure II-28 Spatial patterns of the average concentration C_F, C_B and the bacterial population N_F in the dual porous model with, $\omega = 1,\ q = 1.5,\ \phi_F = 0.2, \phi_B = 0.15, D_{C^F} = 1.5, D_{N^F} = 10^{-6}\ \ \lambda_1 = 1,\ \lambda_2 = 1,\ \alpha = 1, \beta = 1$ at t =500s. The domain is taken to be $\Omega = [17, 17]$.

The key factor inducing the Turing instability is diffusion. The instability region implies that a Turing instability might occur if $D_{C^F} >> D_{N^F}$, which means that spatial patterns may form if the dispersal rate of the gas is far greater than that of a bacterium. The difference in the diffusion rates is a necessary, but not a sufficient condition.

The distribution of the concentration of nutrients in the blocks and in the fractures is exactly the same because the patterns of Turing are stationary. This verifies the third equation of the system $\left.\frac{dC_B}{dt}\right|_{Turing} = 0 = \omega\left(C_F|_{Turing} - C_B|_{Turing}\right).$

2.5.5. Wave's instability: Hopf-Turing instability:

It was concluded that the more complex patterns and instabilities can be founded in the neighborhood of the intersection between Turing and Hopf bifurcation lines. In this intersection the instability is generated by the oscillations of the stable limit cycle and the formation of

diffusive instabilities; the conditions lead to a coupled behavior and then a spatiotemporal pattern. In double porous media, this instability is less well studied though not of lesser importance.

Indeed, we were able to capture these spatio-temporal structures numerically in the point of coordinates $\left(\omega = 0.01, q = 0.93, \phi_B = 0.15, D_{C^F} = 1, D_{N^F} = 0.2\right)$

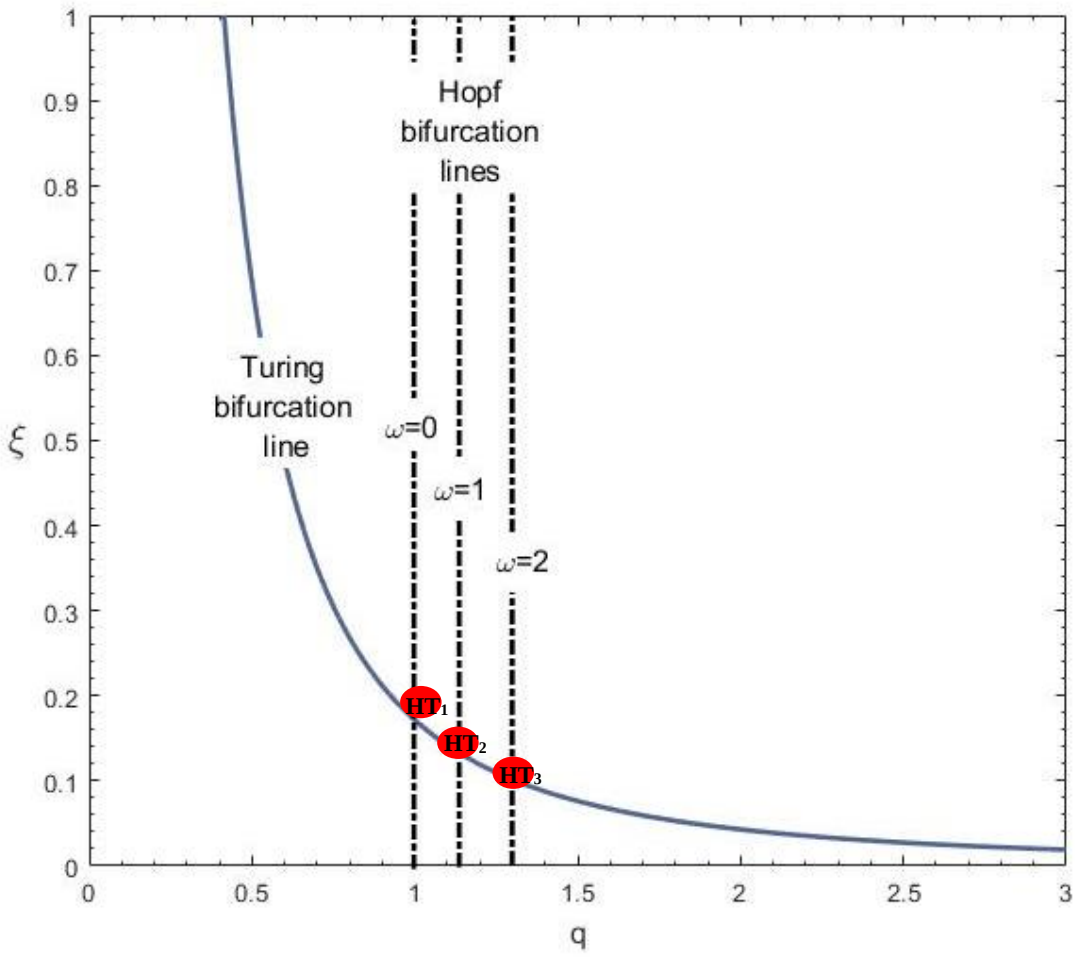

Figure II 29 Hopf Turing coexistence points

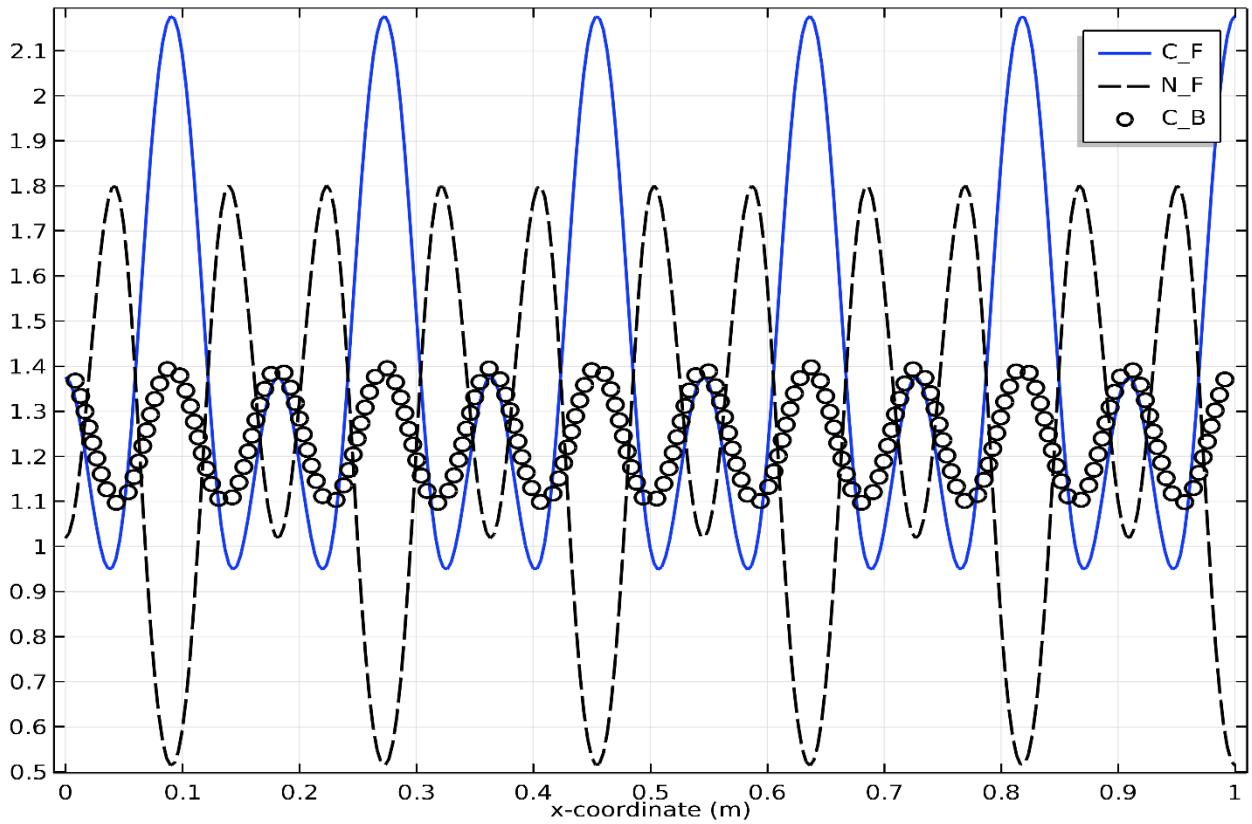

Figure II-30 Numerical simulation for Hopf-Turing patterns of the average concentration C_F, C_B and the bacterial population N_F in the dual porous model with $\lambda_1 = 1,\ \lambda_2 = 1,\ \alpha = 1, \beta = 1,$ $\phi_B = 0.2, \omega = 0.01, q = 0.93, \phi_B = 0.15,\ D_{C^F} = 1, D_{N^F} = 0.2$ .at t=1910

2.5.6. Numerical analysis of patterns in non-homogenized double porosity model:

The homogenized double porous medium can give a qualitative description of patterns may exist but are still less close to the realistic scenarios expected to occur in a heterogeneous system due to the set of simplifications considered and that cost us the loss of considerable effects like memory and delay effects.

The non-homogenized double porosity model can give arise to more complex regimes of pattern. Here pattern regimes are analyzed numerically in a periodic double porous medium. In the case of the non-homogenized double porosity model, other classes of patterns may exist:

Synchronous patterns, similar regime of patterns appear both in blocks and fractures, but with different wavelengths depending on the system size, as shown in the following figure:

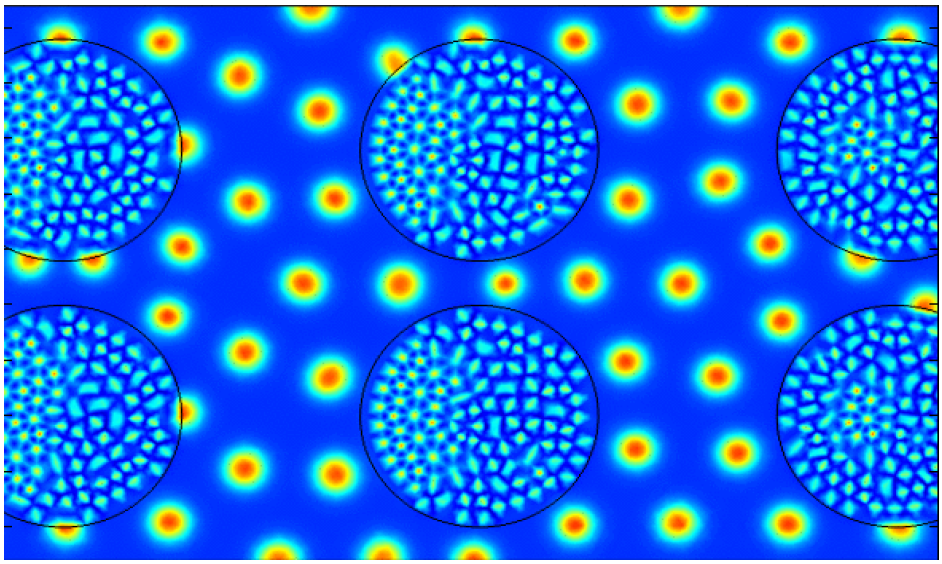

Figure II-31 Synchronous Turing pattern in the non-homogenized double porous medium

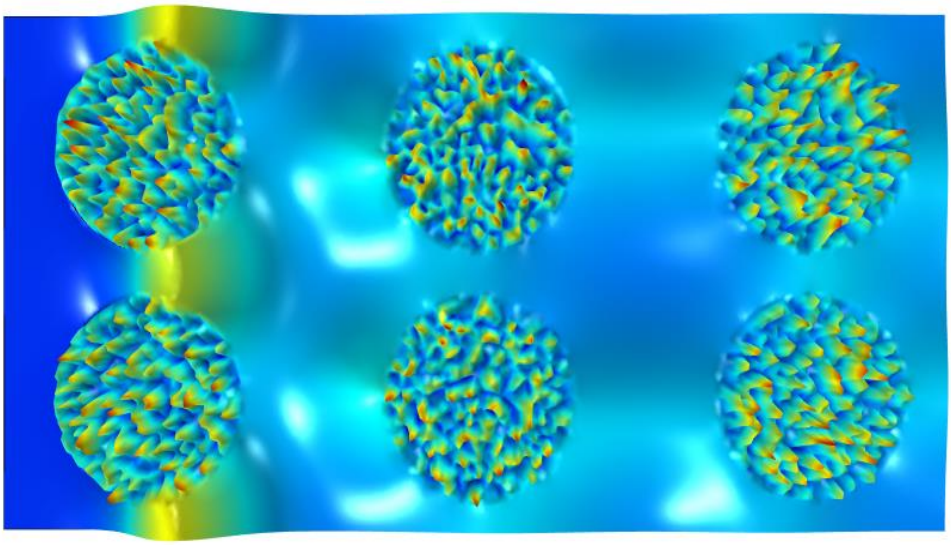

Figure II- 32 Synchronous Jumping waves pattern in the non-homogenized double porous medium.

Due to a delay effect, *asynchronous patterns arise*, creating different regimes in each structure (Fractures, blocks). Fluctuating solutions in time in the block system in the form of a “flash” that

travels between the blocks in a chaotic way combined with Turing patterns in the fractures was obtained as an example of asynchronous patterns.

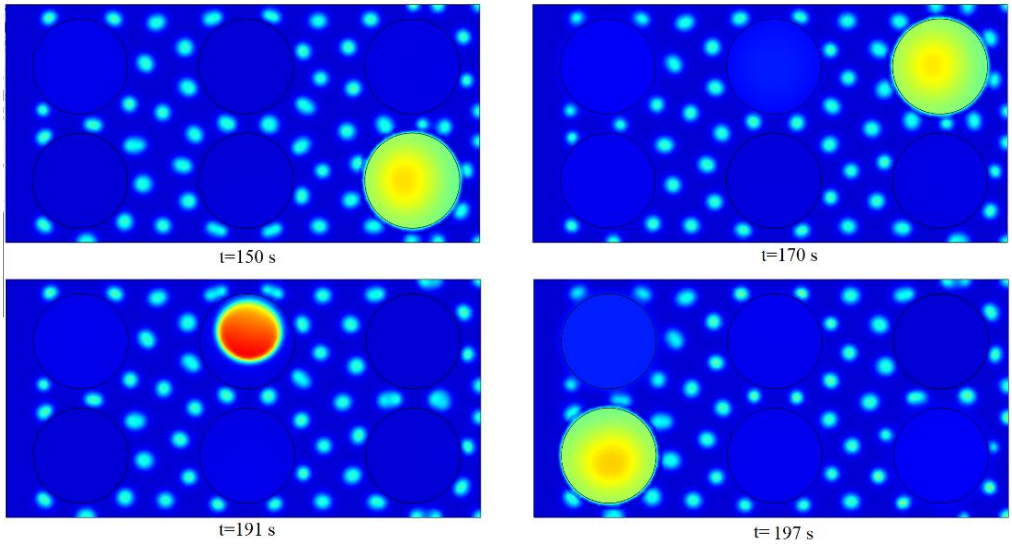

Figure II-33 Asynchronous pattern: traveling flashes / Turing

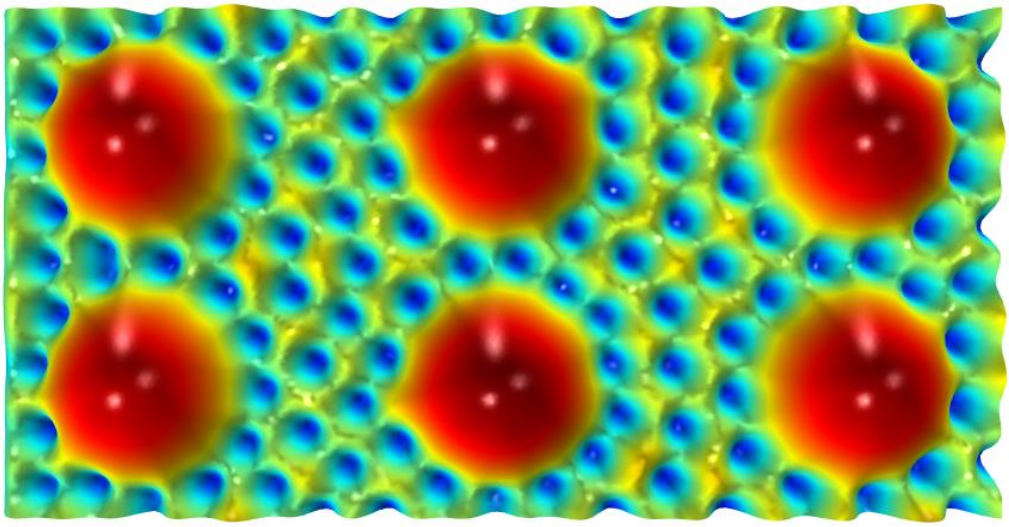

Figure II-34 Asynchronous pattern: Turing in the fractures and stable regime in the blocks

2.6. CONCLUSION

In this chapter, we have analyzed the general conditions of the occurrence of patterns in homogeneous media. In particular, we have shown that a new pattern exists in the case of only two diffusion-reaction equations, which is nonstationary and behaves as *jumping waves*.

After this we have extended our analysis to heterogeneous media, which were analysed in terms of the macroscopic double porosity model. We have shown, in first, that the double porosity displaces the criteria of pattern formation. We have shown that for stationary patterns, the concentration in fractures and in blocks are identical, which corresponds to classical behaviour of the solutions of the double porosity equations. In addition, we have revealed the existence of patterns, in which the concentrations in fractures and blocks are distinct. They undergo spatial and temporal oscillations, which have distinct amplitude, frequency, and phase. This is possible only for wavy patterns, non-stationary. This was confirmed by our numerical tests.

CHAPTER III NUMERICAL ANALYSIS OF THE MODEL OF GAS TRANSPORT WITH BIOREACTIONS AND BIOCLOGGING OF PORES

Contents

3.1. INTRODUCTION

This chapter aims to develop a conceptual model of bio-clogging and bio-plugging and its implementation into a three-dimensional numerical model designed to simulate reactive transport coupled with the dynamics of bacteria. The main purpose of such a model is underground storage of H_2 / CO_2, but it can also be applied to other forms of flow and transport in porous media.

The development of the model of bio-contamination was focused on:

1. Developing mathematical description to various mechanisms of microbial detachment, as erosion (the loss of single microbes), sloughing (the loss of clusters of microbes), abrasion, grazing predators, dispersion (Tufenkji et al. 2007, S. Aggarwal et al. 2019).
2. Finding the dependence of the detachment rate on the flow velocity: indeed, at sufficiently high flow velocity above a threshold value, immobile biomass may be detached and transported by the surrounding fluid, especially in the near-wellbore region where the flow velocity is maximum.
3. Finding the relationship for permeability as the function of the bio-contamination rate and the flow velocity
4. Explore how the potential of microbial accumulation could control the direction of the subsurface hydraulic flow and enhance bioconversion of hydrogen and show how pore-clogging can affect the biomethanation of hydrogen.

Regarding the numerical model, we used the simulator DuMu^X, open scientific software for simulating Multiphase multicomponent flow and transport processes in porous media, developed at the University of Stuttgart and based on the mathematical platform Duma developed by Heidelberg (Timo Koch et al. 2021).

3.2. REVIEW OF PORE CLOGGING BY BACTEIA

Predicting the impact of pore clogging by bacteria on porous media requires a comprehensive mathematical model that could describe all the mechanisms of bacteria' attachement, detcahment and pore plugging (N .Eddaoui al. 2021). Bacterial attachement, detachment and bioclogging are reviewed in section 3.2..

The impact of bacteria on porosity and permeability of porous media was studied in (S.Botteroa et al. 2013; T. Martin et al. 2002; P. Thomas et al. 2011; M. Thullner and W. Kinzelbach 2002). Due to the comparable size of bacteria and pores, a few cells are sufcient to completely plug up a pore channel. The formation of a bio-plug starts in narrow pores in stagnant zones, but then spreads to neighboring active large pores due to the growth of already stuck bacteria, as well as due to the capture of new bacteria into the plug. As a result, this changes fow pathways and

reduces the permeability up to two or even four order of magnitude. A. Brovelli et al. 2009 believe that clogging is caused just by the fltration of dead cells and mobile microbes from liquid and their attachment to pore walls, but not by the biomass growth. Y.J. Ham et al. 2007 demonstrated that the permeability is infuenced by both biomass growth and the detachment and reattachment of bacteria to surfaces. The impact of biomass attachment/detachment on the permeability and porosity, which can lead to partial clogging, has been also shown in T. Garretta et al. 2008.

Constitutive relationships for the dependence of the porosity on the concentration of bacteria have been developed in (A. Brovelli et al. 2009; M. Thullner and W. Kinzelbach 2002), by exploring experimental data.

3.3. BACTERIUM ATTACHMENT, DETACHMENT AND PORE CLOGGING

Bacteria inhabiting in porous rocks can exist in two main forms: freely floating plankton and slimy biomass film attached to the pore walls (biofilms) (Trevor R. Garett et al. 2008). These two forms transit to each other, bacteria attach to and continuously detach from the walls. Not only individual bacteria can detach, but whole biofilm fragments. Biofilm represents the privileged form ensuring a protected and safe habitat for bacterial growth (Trevor R. Garett et al. 2008), but in most situations above a flow velocity threshold biofilm may detach from the solid surface by the surrounding fluid and be transported by it, especially in the near-wellbore region where the most drastic changes in velocity and pressure are expected to occur. Nevertheless, bacteria flowing in suspension may be removed from the fluid and be blocked in the pore walls by one of the following mechanisms: gravity, diffusion, or interception (Timothy D. Scheibe et al. 2006; Trevor R. Garett et al. 2008; A. Brovelli et al. 2009). The adhesion of bacteria to the pore walls has been found to be dependent on a large number of parameters, including flow velocity, fluid density, physical properties of microbial microorganisms (e.g., bacterium size and density), and hydrodynamic properties of the porous medium. The commonly approach used for modeling microbial trapping in porous media is the classical colloid filtration theory (Cunningham 1991; Tufenkji 2005; Mitchell 2010). The conversion of attached biomass to detached and vice versa, due to attachment and detachment is assumed to be a reversible process.

Biomass attachment/detachment modify local pore space and the effective properties of porous media (Soares et al. 1991, Wu et al. 1997, Thullner et al 2001, Mitchell et al 2005, Brovelli et al. 2009). Immobile biomass is able to plug pores and reduce porosity and permeability (Trevor R. Garett et al. 2008).

3.3.1. Physical description

– **Bacterial attachment:**

The attachment process offers bacteria many protective advantages to sustain survival in a favorable environmental host. Surface attachment facilitates nutrient capture and stimulates bacterial reproduction. Some bacteria obtain their necessary metabolites directly from the surfaces to which they adhere (Olga E. Petrova et al. 2012). The surface itself provides bacteria an advantage over the liquid above it. Compared to detached bacteria, attached microorganisms are better resistant to nutrient deficient, changing hydrogeochemical conditions and antimicrobial species (Wimpenny et al. 2000; Trevor R. Garett et al. 2008; Olga E. Petrova et al. 2012). Bacteria within biofilms are notably resistant to their predators as well.

Experiments show that attached microorganisms can play a key role in dioxide carbon leakage mitigation strategies, due to their ability to penetrate small fracture apertures. Attached bacteria can significantly increase the resistance of leakage pathway to flow to set up a hydraulic bio-barrier and plug it (Anozie Ebigbo et al., Mitchell et al. 2010, Adrienne J. Phillips et al. 2013).

Bacterial adhesion to surfaces also has several disadvantages, many industries suffer ill-effects of bacterium-surfaces interactions (Adrienne J. Phillips et al. 2013). Immobile bacteria exhibit different behaviors than free-moving bacteria. Attached microorganisms forming biofilms are a consortium of microorganisms working synergistically (Torben LundSkovhus et al 2017). The presence or activities (or both) of attached bacteria forming biofilm may lead to changes in surface chemistry which could result in microbially influenced/induced corrosion phenomena (MIC). Attached microorganisms can accelerate rates of partial reactions in corrosion through their metabolic processes such as cathodic depolarization through hydrogen utilization, sulfate

reduction, iron oxidation, and sulfur oxidation (Weimin Zhao et al 2018). In the underground gas storage and oil reservoir industry, this causes serious damage to pipelines and process materials and is estimated to cost millions of dollars per year, in failures and on pipeline repairing costs. Biocorrosion constitutes over 25% of the failures experienced in the oil and gas industry (Kermani and Harrop 1996).

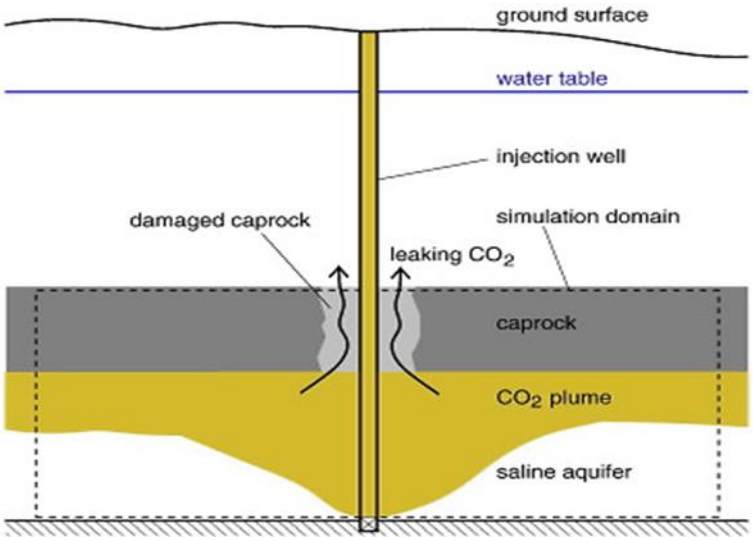

Figure III-1 Sketch of leakage scenario. The caprock near the injection well is damaged and serves as a leakage pathway for CO2. The simulation domain comprises the caprock and the saline aquifer in which the CO2 is stored (Anozie Ebigbo et al. 2010).

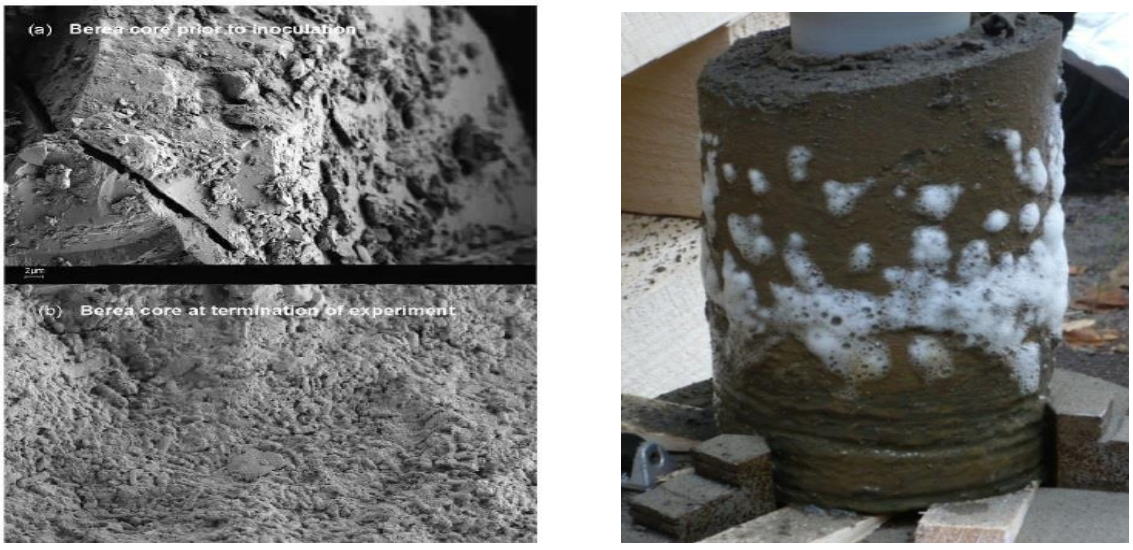

Figure III-2 FESEM images of (a) Berea sandstone core prior to inoculation showing the microorganism-free mineral surfaces of the quartz grains which make up the sandstone, and (b) at the termination of the experiment showing an assemblage of microorganisms attached to the mineral surfaces (Andrew C. Mitchell et al. 2009).

The commonly approach used for modeling microbial trapping in porous media is the classical colloid filtration theory (Cunningham et al., 1991; Tufenkji et al., 2005; Mitchell et al., 2010, Sukumar Roy et al 2018). The microbe is treated as a spherical particle moving through a spherical grain called trapper. When a free bacterium touches a pore wall, it can collide with the wall releasing a sticky fluid. The probability of attachment is very high, as bacteria have a sticky surface. Thus, in the general case, one can introduce a probability of attachment which is defined as the ratio of a number of successfully attached cells to a total number of cells contacting to the pore walls. If one assumes that any collision between a bacterium and the pore walls leads to the attachment, then this probability is equal to 1. Taking the simplest case of bacterium/trapper mediated attachment, bacteria flowing in suspension may be removed from the pore fluid and blocked in the pore walls by three mechanisms: ***(1) diffusion mechanism of deviation,*** the finer microorganisms are usually retained by diffusion. The diffusion of a bacterium is a chaotic motion superposed over the advection. Bacteria cannot strictly follow the streamlines, move randomly (i.e., Brownian movement) until they collide with the pore walls. As seen in Figure III-3, the streamline does not touch the solid, but the bacterium can touch it due to the chaotic diffusive motion around the streamline; ***(2) interception mechanism,*** even if a bacterium moves strictly along a streamline, it can collide with the pore wall, if the streamline passes near the wall, due to finite size of the bacterium; ***(3) inertial mechanism,*** If the streamlines are curvilinear, but the transport velocity is high, bacteria deviate from the curved trajectory and tends to travel along a straight path due to the inertia force Bruce (G. Miller et al. 2017, Rachel M Wheatley et al 2018)

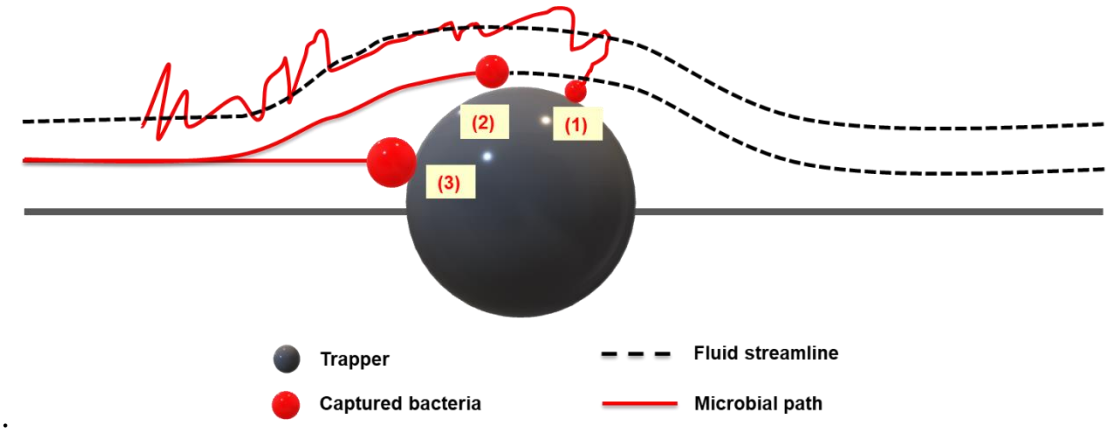

Figure III-3 Schematic representation of a microbial particle collision and attachment interaction in classical colloid filtration theory

In general, bacterial adhesion depends on multiple factors, intrinsic (density, bacterial dimension...) and extrinsic (viscosity and velocity of flowing fluid, drag force created by the moving fluid...) of attached-surface bacterium. The dominant factor here is flow conditions that strongly impact the number of attached-surface bacteria in porous media and break bonds between bacterium and pore walls. The higher the shear rates the stronger the detachment forces. The rate at which the microbial cell detach is reported to be a function of the adhesive forces between the biofilm and the surface to which it is attached (Stoodley et al. 2001).

– **Microbial detachment:**

Microbial detachment process is instead less well understood. Detachment of bacteria from a pore wall can occur in different forms (e.g., erosion, loss of single microbe, loss of clusters of microbes…). Erosion is reported to be the most significant mechanism among them. Mobile biomass can be transported by fluid flow and can also be actively moving in response of a chemical gradient (chemotaxis) (Tufenkji et al. 2007).

The individual bacteria attached to the pore walls can be detached if the flow velocity of the surrounding water is sufficiently high. For a well-developed biofilm, the force of its adhesion is very high, so that its detachment can occur only at very high flow velocities, which are impossible to reach in natural underground reservoirs. However, the creation of a biofilm in narrow pores of geological media seems to be very low probable, therefore we focus our attention on the detachment of individual cells but not a large biofilm. The detachment of a single cell can occur at sufficiently low flow velocity, comparable with those of gas-water flow in underground storage of hydrogen.

The detachment of microorganisms from microbial biofilms has been studied in flowing systems where the dominant mechanisms were perceived to have been local shear forces (Katherine E. Fish et al 2016). Unlike some conventional materials like solids, which can be tested by simple mechanical tests (compression, elongation...), or fluids, for which we perform rheological measurements with rheometry, adhesive forces of bacteria attached to surfaces are difficult to test mechanically. Traditional methods for measuring microbial detachment rate exist,

including but are not limited to, counting the number of cells before and after the detachment event (adhesion number), or measuring the critical force during a detachment test.

An experimental investigation of detachment in bacterial biofilms demonstrates the influence of shear stress on biofilm detachment and relates the mechanical properties of biofilm to the mechanism of adhesive failure (Stoodley et al. 2001). The experience consists in growing biofilms in square glass capillary flow cells under fluid shears ranging Re=17-3600, from periods of between 5 and 31 days. They subject biofilms to variations in shear by adjusting in flow rate. Using a time-lapse epifluorescence microscope they enumerate the suspended bacteria and quantify biofilm deformation in response to fluid shear by measuring the resulting strain in the longitudinal direction. The experiment reported that the detachment of bacteria depends on the preceding conditions during the period of their attachment.

Let us consider a freely moving bacterium in water that begins to attach to a solid surface and V_{bg} be the flow velocity of water in course of the bacterium attachment. This velocity determines the shear stress (or the adhesion force) between the attached bacterium and the solid surface. It is clear that the shear stress is higher for high V_{bg}. After the complete fixation of the bacterium on the solid surface, we increase the flow velocity of water up to a critical value V_c at which the bacterium detaches. It is then expected that V_c depends on V_{bg}, which was confirmed by experiments published by Stoodley et al. If the flow during the attachment was laminar, then V_c is sufficiently low. If, in contrast, the flow was turbulent in course of the attachment, then V_c is very high. Although, the experiments conducted by Stoodley et al. demonstrate that cells detachment occurs sometimes at shear stress approximately twice the stress at which attached bacterial was growing (Stoodley et al. 2002). The corresponding experimental data borrowed from Stoodley's studies are shown in Figure III-4.

Bacteria in an underground gas reservoir, which exist at very low flow velocity, are weakly attached to pore walls, and can be easily detached at a weak shear.

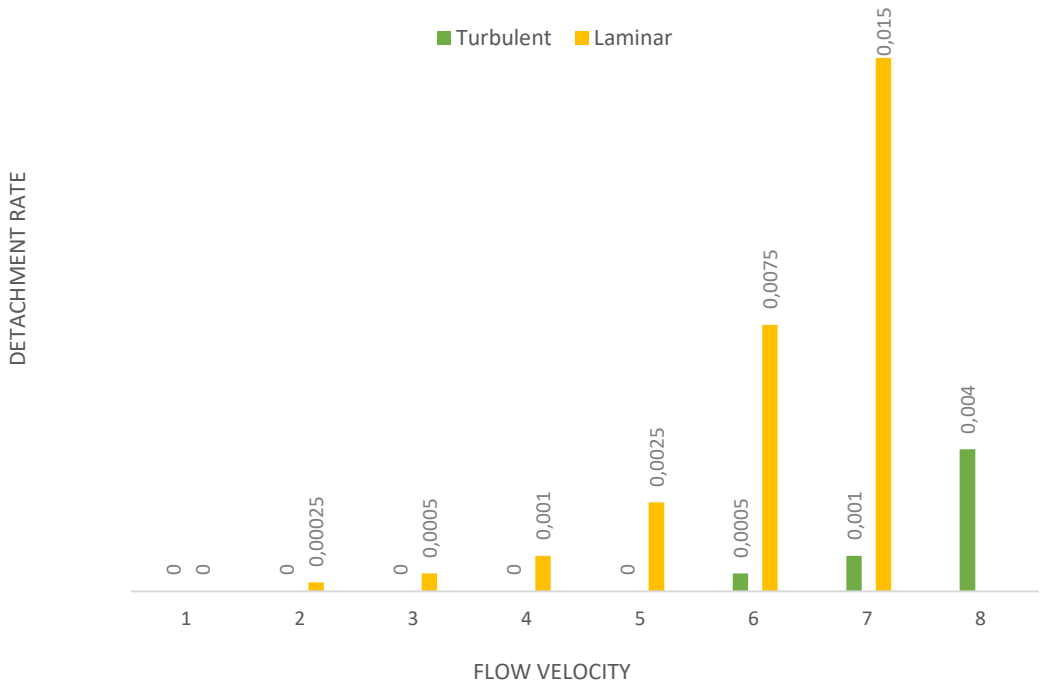

Figure III-4 Shear-induced detachment of attached microorganisms (Stoodley et al.2002).

Detachment of microbial cells is likely to be followed by attachment of cells as long as the attachment conditions permit, so the transition of attached bacteria to detached and vice versa is a continuous process.

– **Bioclogging:**

Hydrodynamic properties of porous media such as porosity and permeability can change significantly over time due to the microbial activities (Soares et al. 1991, Wu et al. 1997, Thullner et al 2001, Mitchell et al 2005, Brovelli et al. 2009). The shape of the permeability–porosity curve is dependent on both the properties of the porous medium and of the biofilm. The growing bacterial population can plug the small pores and reduce porosity and permeability (Trevor R. Garett et al. 2008), which is called "*bioclogging*". Bioclogging is a complex phenomenon resulting from the interaction of many different processes.

According to the reviews (Baveye et al. 1998, Yang et al. 2021), pore-clogging can be divided into three categories according to their causes: physical clogging, chemical clogging, and bio-clogging. Physical clogging is caused mainly by the suspended solids in water; chemical clogging is caused mainly by chemical precipitation. Bio-clogging is due mainly to clogging problems caused by microorganism growth and trapping in narrow pores (filtration). Bio-clogging was observed visually and imposed a lot of technical problems in various fields of geosciences, for instance groundwater extraction, or various techniques of artificial groundwater recharge: injection of water into the subsurface through injection wells, redirection of water across the land surface through channels, infiltration basins, ponds, creation of irrigation furrows or sprinkler systems. In another practical technology, namely, the microbiological enhanced oil recovery, bacteria are injected with water to create artificial bio-plugs in porous media, to redirect the preference pathways of flow and displace oil from stagnant zones (Amnudsen 2015, Sidsel 2010, Updegraff et al. 1983). Microbiological pore clogging is important in another engineering application related to CO2 entrapment in subterranean formations. Bacterial plugs prevent CO2 leaks (Adrienne et al. 2013).

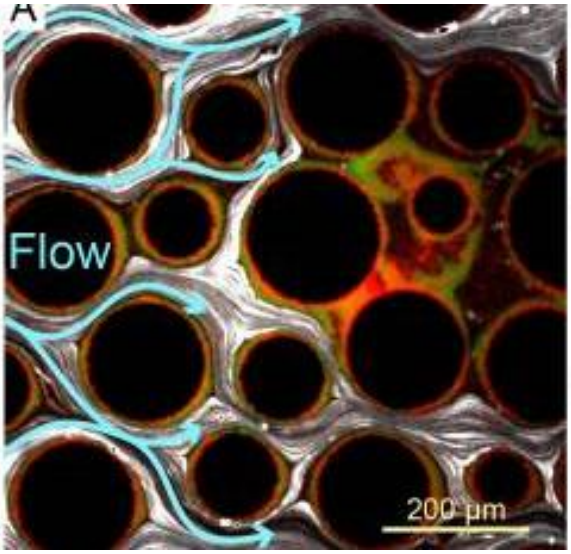

Figure III-5 Microscale experiments conducted by (Carey D Nadel et al. 2017) describe changes on flow paths due to the local clogging in pore spaces by Wild-type (green) and ΔpelA (red) P. aeruginosa bacteria

(Ham et al. 2007) reported that the increase or the decrease can occur not only due to microbial growth and/or microbial decay but also due to some microbial processes such as the detachment from and (re)attachment of bacteria to the surfaces.

(Thullner et al. 2002) investigated the influence of microbial growth on the porosity and permeability of porous media. (Thullner et al. 2002) have shown that microbial growth may reduce the hydrodynamic properties of porous media up to two orders of magnitude and lead to bioclogging. In addition to that, microbial activities can change the flow pattern in the narrow porous. (Thullner et al. 2002) suppose that the bioclogging happens meanly near the inlet or injecting nutrients ports (wellbore zone in our case

(Brovelli et al. 2008) have considered that the porosity and permeability changes are linked to the filtration of colloids suspended in the pore fluid (e.g. dead cells and detached microbes. (Ham et al. 2007) demonstrated that the permeability and porosity of porous media can be affected by biomass growth and attachment on the solid matrix.

Studies correlated biomass growth with hydraulic conductivity reduction (Wu et al., 1997); other studies linked the biofilm thickness with the permeability and porosity of porous media (Cunningham et al., 1991), and biomass density with the reduction of hydraulic conductivity (Taylor and Jaffé, 1990a).

3.3.2. Mathematical model of attachment, detachment, and bioclogging

Good overviews of microbial adhesion are given in (Timothy D. Scheibe et al. 2006, Nathalie Tufenkji et al. 2006, Ian L. Molnar et al. 2015). In this thesis, we focus on a basic description of adhesion that is coherent in most bio-colloids filtration concepts. We calculate the microbe attachment rate coefficient with an extended relation derived from (Nathalie Tufenkji et al. 2006):

$$k_a = \frac{3}{2}\frac{(1-\phi)|V_w|}{d_T}\alpha_{eff}\left(\eta_{\text{diffusion}} + \eta_{\text{interception}} + \eta_{\text{inertia}}\right) \quad \text{Eq III.1.}$$

where,

$$\eta_{\text{diffusion}} = 0.9\left(\frac{k_b T}{\mu_w d_b d_T |V_w|}\right)^{\frac{2}{3}}, \eta_{\text{interception}} = 1.5\left(\frac{d_b}{d_T}\right)^2 \text{ and } \eta_{\text{inertia}} = \frac{(\rho_b - \rho_w) g d_b^{\,2}}{18\mu_w |V_w|} \quad \text{Eq III.2.}$$

$\eta_{\text{dif}}, \eta_{\text{int}}, \eta_{\text{iner}}$ are the probabilities of a collision by three mechanisms described in section (3.1.1) ; α is the attachment probability after a collision; ϕ is the porosity; d_p is the pore diameter; V_w is the flow velocity (the absolute value). The dependence of k_a on the flow velocity is obvious, as nothing is trapped if nothing flows. Similarly, for the pore diameter and the porosity: nothing is trapped if the pore volume is too large.

The probability α depends on the pore size, but can be assumed to be equal to 1 (Kuan-Mu et al. 1971) because a single contact between a cell and the solid wall is enough to attach the cell.

The probability of a collision $\eta = \eta_{\text{dif}} + \eta_{\text{int}} + \eta_{\text{iner}}$ is the main parameter to determine. To determine three components that correspond to three mechanisms of collision mentioned above, let us introduce the following notations: D_b is the coefficient of cell diffusion; d_b is the diameter of a bacterial cell; μ_w is the dynamic viscosity of water; k_B is the Boltzmann constant; T is the temperature; ρ_b and ρ_w are the bacterium and water density, respectively.

The probability of collision due to stochastic fluctuations η_{dif} is all the higher as the diffusion velocity of bacteria D_b / d_p is high compared to the convective velocity V_w. In other words, η_{dif} is inversely proportional to the Peclet number $\text{Pe} = V_w d_p / D$. In turn, the diffusion parameter D_b can be estimated from various semi-empirical formulae developed for diffusion in liquids, which are based on the Stokes-Einstein formula: $D_b = k_B T / (6\pi\mu_w d_b)$. The more developed formulae contain several empirical coefficients and exponents.

The probability of the geometrical interception η_{int} is proportional to the ratio of the bacterial and pore cross-sections $(d_b / d_p)^2$. More precisely, it can be calculated as the probability that a

small circle that occurs randomly inside a large circle will touch the borders of the large circle, which will lead to the appearance of a numerical coefficient in front of $\left(d_b / d_p\right)^2$.

The term of inertial deviation η_{iner} is proportional to the difference of bacterial and water densities and then it can be neglected since the density of bacteria, which consist of nearly 70% of water, is practically identical to that of water.

Collecting these results we obtain definitely the following expression:

$$\eta_{\text{dif}} + \eta_{\text{int}} + \eta_{\text{iner}} = 0.9\left(\frac{k_b T}{\mu_w d_b d_p V_w}\right) + 1.5\left(\frac{d_b}{d_p}\right)^2 \qquad \text{Eq III.3.}$$

Biofilm detachment from the solid surface could be determined by the relationship between the adhesive force and the shear stress caused by the tangential flow of surrounding fluid (Stoodley et al. 2001, Rittmann 1982)**.** Here, the microbial detachment rate coefficient is an exponential function of the magnitude of the water-phase flow $|V_w|$, as reported by (Stoodley et al.2002):

$$k_{\text{det}} = \begin{cases} k_d^{\max} e^{-\frac{w^2}{1-w^2}} & ,V_w > V_c \quad ,\text{w}=\dfrac{V_w - V_m}{V_c - V_m} \\ 0, \quad V_w \le V_c \end{cases} \qquad \text{Eq III.4.}$$

The model contains three empirical parameters, the critical velocity of detachment (below which the detachment is impossible) V_c; the maximal velocity V_m at which the detachment rate stabilizes and the maximal detachment rate $k_d^{\max}$ that corresponds to V_m. The critical velocity depends on the initial velocity of the bacterium attachment V_{bg}, as explained in the previous section.

Experimental data show that the critical shear stress of detachment τ_c is approximately twice as large as the initial shear stress τ_{bg} (under which the bacterium has been attached):

$$\tau_c = 2.3\tau_{bg} \qquad \text{Eq III.5.}$$

This implies that:

$$V_c = \sqrt{2.3} V_{bg} \qquad \text{Eq III.6.}$$

Another semi-empirical model was proposed by (Rittmann 1982) based on the physical characteristics, shear stress, media porosity, and specific surface area. (Gerald E. Speitel et al. 1987) proposed that in addition to the physical characteristic, the biological effect should be as well accounted for biofilm detachment; this is through bacterial growth rate. Experiments proved that high growth rates (i.e., fast-growing biofilm) make the biofilm much more susceptible to detach compared with slow-growing biofilm. (Gerald E. Speitel et al. 1987) proposed the following two-term model for biofilm detachment rate:

$$k_d = \bar{k}_{d1} \left[\frac{(1-\phi)^3}{{d_p}^2 \phi^3 A} \mu_w |V_w| \right]^{\bar{k}_{d2}} + \bar{k}_{d3} \psi^{gr} \qquad \text{Eq III.7.}$$

The first term account for the external shear stress exerted by the flow on the biofilm surface and the second term is an internal force exerted by microorganisms themselves on the biofilm surface. k_d is the detachment rate, $\bar{k}_{d1}$, $\bar{k}_{d2}$ and $\bar{k}_{d3}$ are empirical parameters dependent of the microbial substrate. The coefficients $\bar{k}_{d1}$ and $\bar{k}_{d2}$ can be taken from (Rittmann 1982) experimental data, set to be 2.29×10^{-6} and 0.58 (resp.). (Gerald E. Speitel et al. 1987) obtained value for $\bar{k}_{d3}$ ranging from 0.042 to 0.089 by performing a linear regression analysis. ψ^{gr} is the growth rate.

As mentioned in the last section, the growth of the bacterial population can lead to large accumulations of bacterial cells that clog the pores, which causes a reduction of medium porosity and permeability. Several models exist that relate the porosity to biomass growth with monotonically decreasing functions (Civan et al. 2005; Kirk E. Nelson et al. 2011). However, permeability and porosity reduction can be defined as a non-linear function of bacterial accumulation (Brovelli et al. 2009). This is independent of the state of bacteria: attached or detached.

Instead to consider a linear dependency of the porosity on the biomass accumulation, we can consider the following nonlinear semi-empirical relationship:

$$\phi(n_a, n_d) = \frac{\phi_0}{1 + \left(\frac{n_a + n_d}{n_c} \right)^2} \qquad \text{Eq III.8.}$$

where n_c is the number of bacteria needed to get a maximal bioclogging effect, which is an empirical parameter, ϕ_0 is the porosity of the clean reservoir without bacteria.

The variation of permeability can be obtained from the general Carman-Kozeny formula. The magnitude of permeability reduction depends on the third power of porosity (Carman-Kozeny 1937):

$$K(n_a, n_d) = \left(\frac{{d_T}^2}{180} \right) \frac{\phi(n_a, n_d)^3}{\left(1 - \phi(n_a, n_d)\right)^2} \qquad \text{Eq III.9.}$$

3.3.3. Full model of two-phase transport with bioreactions and bioclogging

The coupled model that describes the flow of two phases (gas and water), transport of four chemical components (H_2O, H_2, CH_4, CO_2), dynamics of two classes of bacteria: attached (immobile) and detached (transported); bacterial attachment and detachment kinetics, and pore-clogging is based on the following main assumptions:

- The mass exchange in chemical species between two phases is instantaneous, which means that the phase concentrations are governed by the local phase equilibrium. This is justified by a fine dispersed structure of phases in porous medium and the large surface of contact between them
- The detachment and attachment of bacteria means the transition of one class of bacteria to another one
- Bacteria do not attach to each other, as they have physiological mechanism (flagella) that prevents them from mutual collisions
- The mechanisms of transport are advection, molecular diffusion, and buoyancy

- The porous medium is nondeformable

The mass balance of detached and attached bacteria has the form:

$$\frac{\partial}{\partial t}\left(\phi S_w n_d\right)+\nabla\cdot\left(n_d\mathbf{V}_w\right)-\nabla\cdot\left(D_b S_w\nabla n_d\right)=\underbrace{\psi^{gr}S_w n_d}_{\text{I}}-\underbrace{\psi^{dec}S_w n_d}_{\text{II}}-\underbrace{k_a S_w n_d}_{\text{III}}+\underbrace{k_d S_w n_a}_{\text{IV}} \qquad \text{Eq III.10.}$$

$$\frac{\partial}{\partial t}\left(\phi S_w n_a\right)=\underbrace{\psi^{gr}S_w n_a}_{\text{V}}-\underbrace{\psi^{dec}S_w n_a}_{\text{VI}}+\underbrace{k_a S_w n_d}_{\text{III}}-\underbrace{k_d S_w n_a}_{\text{IV}} \qquad \text{Eq III.11.}$$

The mass balance of chemical species is:

$$\sum_{\alpha=w,g}\left\{\frac{\partial}{\partial t}\left(\phi\rho_\alpha S_\alpha c_\alpha^k\right)+\nabla\cdot\left(\rho_\alpha c_\alpha^k\mathbf{V}_\alpha\right)-\nabla\cdot\left(\rho_\alpha D_\alpha^k\phi\nabla c_\alpha^k\right)\right\}=\underbrace{\phi\rho_w S\omega^k}_{\text{VII}}, \quad k=H_2,\ CO_2,\ CH_4,\ H_2O \qquad \text{Eq III.12.}$$

The momentum balance of two phases:

$$\mathbf{V}_w=-\frac{K\,k_{rw}(S_w)}{\mu_w}\,\nabla P_w-\rho_w^*\mathbf{g}\ , \qquad \mathbf{V}_g=-\frac{K\,k_{rg}(S_w)}{\mu_g}\,\nabla P_g-\rho_g^*\mathbf{g} \qquad \text{Eq III.13.}$$

$$p_g=p_w+p_c(S_w) \qquad \text{Eq III.14.}$$

where S_w is the water saturation; c_α^k is the mole fraction of component k in phase α; ρ_α is the molar density [mol/m^3]; V_α is the Darcy velocity; P_α is the phase pressure; ρ_α^* is the mass density [kg/m^3]; μ_α is the dynamic viscosity; $\mathbf{g}$ is the gravity acceleration vector; K is the absolute permeability; $\lambda_\alpha=k_{r\alpha}(S_w)/\mu_\alpha$ is the phase mobility; $k_{r\alpha}(S_w)$ is the relative permeability; ϕ is the medium porosity; ψ_j^{gr} and ψ_j^{dec} are the rates of bacterial growth and decay per one bacterium; ω^k is the production/decay rate of component *k* due to the bio-activity; $p_c(S_w)$ is the capillary pressure.

Herein the terms I – VII are the rates of:

I and V: the growth of the mobile and fixed populations, respectively;

II and VI: the population decay;

III: the attachment of bacteria to the pore walls;

IV: the detachment of bacteria;

VII: the rate of production or disappearance of component k (the bio-reactions occur in water, this is why only the water density and saturation enter in this formula).

The density of the gas is assumed to be linear with respect to pressure as for the ideal gas. The liquid density was calculated as that of an ideal solution.

The function of population growth ψ^{gr} is a fundamental characteristic of bacterial dynamics that characterizes the individual physiological property of the population. For the methanogenic bacteria we are studying in this work, population growth is directly dependent on the consumption of carbon contained in CO_2 (in addition to this, nitrogen, phosphorus, sulfur, and other elements are also consumed, but in significantly smaller quantities). In addition, bacteria consume CO_2 and H_2 for respiration, which is a redox process that brings energy to bacteria. The respiration act can be summarized in the form of the following chemical reaction:

$$4H_2 + CO_2 \rightarrow CH_4 + 2H_2O + \text{energy} \qquad \text{Eq III.15.}$$

The emitted energy is consumed by bacteria.

Although respiration does not directly lead to an increase in the biomass, it slows down or accelerates it, since, without sources of respiration, any activity of bacteria dies out (they go into hibernation).

Consequently, the nutrition rate can be considered proportional to the respiration rate (synchronization hypothesis, (Panfilov 2019), and thus it is proportional to the concentrations of CO_2 and H_2 in the surrounding water. If we take into account that the growth rate stabilizes with an abundance in CO_2 and H_2, then we obtain the multiplicative Monod's law:

$$\psi^{gr} = \frac{1}{t^{gr}} \frac{c_w^{H_2}}{\left(\alpha^{H_2} + c_w^{H_2}\right)} \frac{c_w^{CO_2}}{\left(\alpha^{CO_2} + c_w^{CO_2}\right)} \qquad \text{Eq III.16.}$$

where α^{H_2} and α^{CO_2} are the half-velocities constants, t^{gr} is the characteristic time of growth under the conditions of excess in nutrients.

Along with growing, a population can decay, which is mainly caused by microorganisms-predators. Then the decay depends on the concentration of predators, which, in turn, increases due to the presence of prey. Consequently, the decay rate is a function of the concentration of methanogenic bacteria (Panfilov 2019)

$$\psi_j^{dec} = \frac{1}{t^{dec}} n_j^{\beta-1} \qquad \text{Eq III.17.}$$

where t^{dec} is the characteristic time of decay; j=a, d for attached and detached cells, respectively; β is an empirical parameter. According to (Murray 1993), we accept the linear approximation between the total decay rate and the number of bacteria, that is β=1. The data for t^{dec} can be found in (Panfilov 2019).

The rate of the disappearance of H_2, as well as the rate of production of CH_4 and H_2O is proportional to the rate of microbe respiration, in accordance with the methanation reaction, so that

$$\omega^k = \frac{\gamma^k \psi^{gr}}{Y}\left(n_a + n_d\right), \qquad k = H_2,\ CH_4,\ H_2O \qquad \text{Eq III.18.}$$

where γ^k is the stochiometric coefficient $\gamma^{CO_2} = -1$, $\gamma^{H_2} = -4$, $\gamma^{CH_4} = 1$ and $\gamma^{H_2O} = 2$; Y is the reaction yield: the ratio between the biomass growth and nutrient consumption. If all nutrients were transformed into energy and biomass, then $\omega^k = \gamma^k \psi^{gr}\left(n_a + n_d\right)$. In reality, only a part of nutrients is transformed, so that $Y \le 1$. This parameter is empirical and cannot be estimated without experiment. Several data on Y can be found in the literature (Panfilov 2019, Murray 1993).

For petrophysical functions as relative permeability and capillary pressure, we used polynomial approximations.

Brooks-Corey's model (1964):

$$\begin{cases} k_{rw} = \left(\dfrac{S_w - S_{wr}}{1 - S_{wr} - S_{gr}} \right)^{\frac{2+3\lambda}{\lambda}}, \\ k_{rg} = \left[1 - \left(\dfrac{S_w - S_{wr}}{1 - S_{wr} - S_{gr}} \right) \right]^2 \left[1 - \left(\dfrac{S_w - S_{wr}}{1 - S_{wr} - S_{gr}} \right)^{\frac{2+\lambda}{\lambda}} \right], \end{cases} \quad \text{Eq III.19.}$$

$$p_c = p_g - p_w = P_c^0 \varepsilon \left(\frac{S_w - S_{wr}}{1 - S_{wr} - S_{gr}} \right)^{-\frac{1}{\lambda}}, \quad P_c^0 = \sigma \cos\theta \sqrt{\frac{\phi_0}{K_0}}, \quad \varepsilon = \sqrt{\frac{K_0 \phi}{\phi_0 K}} \quad \text{Eq III.20.}$$

S_{wr} is the residual wetting phase saturation that cannot be displaced by the non-wetting fluid phase and remains in the porous medium. The parameter λ can be found experimentally depending on the pore size distribution. ϕ_0 and K_0 are the porosity and permeability of the clean medium without bacteria; σ is the surface tension at the interface gas-water, θ is the contact angle for the system gas-water-solid. The parameter ε enables us to take into account the spatial variation of the capillary pressure in a heterogeneous medium.

The molecular diffusion is described in our mathematical model by the Fick's law:

$$\begin{aligned} D_w^k &= S_w \tau \tilde{D}_w^k \\ D_g^k &= S_g \tau \left(\sum_{j=1 \neq i}^{n} \frac{c_g^j}{\tilde{D}_g^{ij}} \right)^{-1} \end{aligned} \quad \text{Eq III.21.}$$

The molecular diffusion coefficient of component k depends on the binary diffusion coefficients $\tilde{D}_w^k$ and $\tilde{D}_g^{ij}$. The actual trajectories that individual fluid particles follow in any porous medium are tortuous. Consequently, ***Fick***'s law is usually corrected by introducing a tortuosity factor.

Values for τ was suggested by *Millington and Quirk* (1961), where

$$\tau = \phi^{\frac{1}{3}} S_\alpha^{\frac{7}{3}} \quad \text{Eq III.22.}$$

The mole fractions of components in gas and liquid are governed by the conditions of phase equilibrium. In fact, a porous medium with its small pores and many branching of pore channels provides a finely dispersed structure of phases (drops or bubbles, or films, etc.) with a large contact surface between them, which makes the establishment of phase equilibrium very fast. In terms of fugacity, the equilibrium is formulated as follows:

$$f_g^k\left(P_g, c_g^1, ..., c_g^n\right) = f_w^k\left(P_w, c_w^1, ..., c_w^n\right) \qquad \text{Eq III.23.}$$

for all components *k*, where the structure of the fugacity is well developed in thermodynamic literature. In the particular case, these equations can be reduced to Henry's law for gaseous components:

$$c_w^k = H^k P_g c_g^k, \qquad k = \mathrm{H_2}, \mathrm{CO_2}, \mathrm{CH_4}; \qquad \sum_k c_\alpha^k = 1, \quad \alpha = \mathrm{g,w} \qquad \text{Eq III.24.}$$

and the condition of the insolubility of water in the gas phase: $c_g^{\mathrm{H_2O}} = 0$. Here H^k is the Henry solubility.

This system of six equations contains nine unknowns: height concentrations c_α^k and pressure P_g. Therefore, two concentrations can be considered as independent (for instance, $c_g^{\mathrm{H_2O}}$ and $c_g^{\mathrm{CO_2}}$), while six other concentrations depend on $c_g^{\mathrm{H_2O}}$, $c_g^{\mathrm{CO_2}}$ and pressure P_g.

The phase composition can be disturbed by a chemical reaction. Unlike phase equilibrium, a chemical reaction is a kinetic process, that is, a nonequilibrium effect. Then the phase equilibrium can also be violated. This difficulty can be circumvented by assuming that the characteristic rate of stabilization of the phase composition is much higher than the rate of the chemical reaction. This assumption is widely used in geochemistry and petroleum engineering (Birger Hagemann 2017).

The molar balance equations are closed by the sum of saturations and concentrations:

$$\sum_k c_\alpha^k = 1 \text{ and } \sum_\alpha S_\alpha = 1 \qquad \text{Eq III.25.}$$

3.4. SOLUTION OF THE PROBLEM

In this section, 3D numerical simulations are carried out to demonstrate the model's capabilities. The model describes the multi-phase multi-component flow coupled with bioreactions, bioclogging processes and takes into account the microbial (re)attachment/detachment mechanisms. For the numerical simulations, we decided to use the numerical simulator DuMu^X. The chosen parameters are assumed to be realistic.

The following targets are proposed:

- evaluate the wellbore bioclogging by the biomass production process in underground hydrogen storage.
- Explore how the potential of microbial accumulation could impact flow pathways.
- Show how pore-clogging can affect the biomethanation reaction.

3.4.1. Description of the solver DuMuX

DuMu^X is the Abr. of **Du**ne for **Mu**lti-{Phase, Component, scale, Physics,…} flow and transport processes in porous media. It is a tool for simulating Multiphase multicomponent flow and transport processes in porous media, developed at the University of Stuttgart in the Department of Hydromechanics and Modelling of Hydrosystems (Timo Koch et al. 2021). DuMu^X is based on DUNE, the Distributed and Unified Numerics Environment, which is an open- scientific numerical software framework written in C++ for solving partial differential equations (PDEs). DuMuX includes several models of multiple complexities: from stationary isothermal single-phase flow to unsteady non-isothermal multiphase compositional complex flow processes and with challenging complex porous media. The software has been successfully applied to simulate a number of geological gas (CO_2, H_2, CH_4, …) storage scenarios, transport of therapeutic agents through biological tissue (Schröder 2014), simulating brain tissue perfusion (Timo Koch et al. 2020), modeling of biofilms and mineral precipitation, modeling root-soil interaction, modeling Oil Recovery Processes (dumux.org). Other available concurrent numerical simulators dealing with non-isothermal multiphase multicomponent transport processes can be found (**e.g.**,

COMSOL Multiphysics, OPM, ECLIPSE, ELSA, FEHM, GEM, GPRS, MoReS, MRST, MUFTE, OpenGeoSys, PFLOTRAN, ROCKFLOW).

DuMu^x software consists of models, each one can be used depending on the problem that needs to be handled. An overview of the currently available models is given in the following table:

coupled fully implicit	decoupled semi-implicit
1p, 1p2c, 2p 2p1c, 2p2c, 2pdfm, 2pminc, 2pnc, 2pncmin, 3p, 3p3c, co2, mpnc, nonisothermal, Richards, 3pwateroil, 2pia, 2p2cia, 2pMINC, linear-elasticity2pDFM, 1p2cDoubleContinuum, 1DPipe3DPorousFlow, …	1p, 2p,2p2c

Table 5 Currently available models within DuMux (p: phase, c: component, ni: non-isothermal, min: mineralization and ia for interfacial area

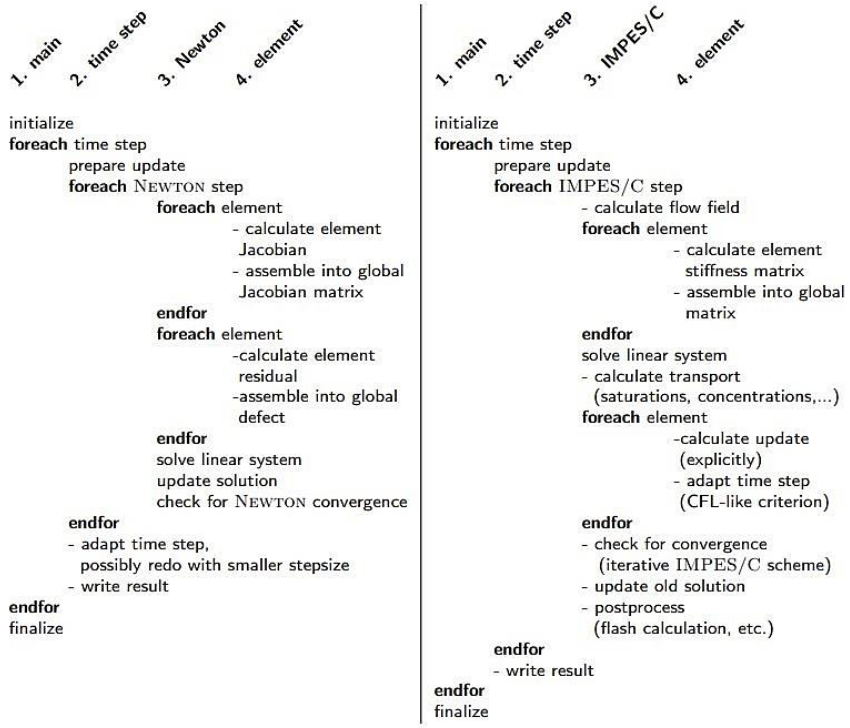

Figure III-6 Structure of a coupled fully-implicit (left) and a decoupled semi-implicit (right) scheme in DuMux.

For the solution of the porous media problems, DuMu^x accords to the user to choose between two existing standard approaches: a coupled fully implicit approach and a decoupled semi-implicit approach. The first discretize the coupled balance equations by an implicit method in time, while in the second, two different discretization methods are used, the pressure equation is solved implicitly, and the transport is solved explicitly.

Euler scheme is implemented for the temporal discretization. the forward or the backward quotient leads to the explicit and implicit Euler method, respectively.

Looking an unknown quantity u in terms of storage term M, flux F, and source S

$$\frac{\partial M\left(u\left(X,t\right)\right)}{\partial t}+\nabla.F\left(u\left(X,t\right),\nabla u\left(X,t\right)\right)=S\left(u\left(X,t\right)\right), \qquad \text{Eq III.26.}$$

in an explicit Euler method, F and S are evaluated in terms of known quantities at the previous time step.

$$\frac{M\left(u\left(X,t^{k+1}\right)\right)-M\left(u\left(X,t^{k}\right)\right)}{\Delta t}+\nabla.F\left(u\left(X,t^{k}\right),\nabla u\left(X,t^{k}\right)\right)=S\left(u\left(X,t^{k}\right)\right), \qquad \text{Eq III.27.}$$

while an implicit formulation the quantities F and S are evaluated as unknown quantities at the new time step k+1,

$$\frac{M\left(u\left(X,t^{k+1}\right)\right)-M\left(u\left(X,t^{k}\right)\right)}{\Delta t}+\nabla.F\left(u\left(X,t^{k+1}\right),\nabla u\left(X,t^{k+1}\right)\right)=S\left(u\left(X,t^{k+1}\right)\right). \qquad \text{Eq III.28.}$$

The implicit Euler scheme is unconditionally stable, while the explicit method is stable only if Δt is low than a certain limit that depends on the problem equations(Helmig 1997).

Our system of partial differential equations should be discretized in space as well. DuMu^X allows the use of three different spatial discretization methods for the different models: (1) the cell-centered finite volume methods; (2) the vertex-centered finite volume methods (the box method); (3) and the standard Galerkin finite element methods. The most widely used methods for modeling thermo-hydro-mechanical-chemical and biological processes in the process of gas

storage are the fully coupled cell-centered finite volume and vertex-centered finite volume methods. For the cell-centered finite volume methods, a finite volume discretization is required. The fluxes are balance over the control volumes and the remain discrete values are determined at the center of the grid cell. However, for the vertex-centered finite volume methods a secondary finite volume mesh, based on a finite element mesh, is constructed by connecting the barycenter of the element with the midpoints of the element edges. The fluxes here are balanced over the sub-control volumes of each element and the discrete values are calculated at the nodes of the elements (Johannes Martin Hommel Thesis 2016).

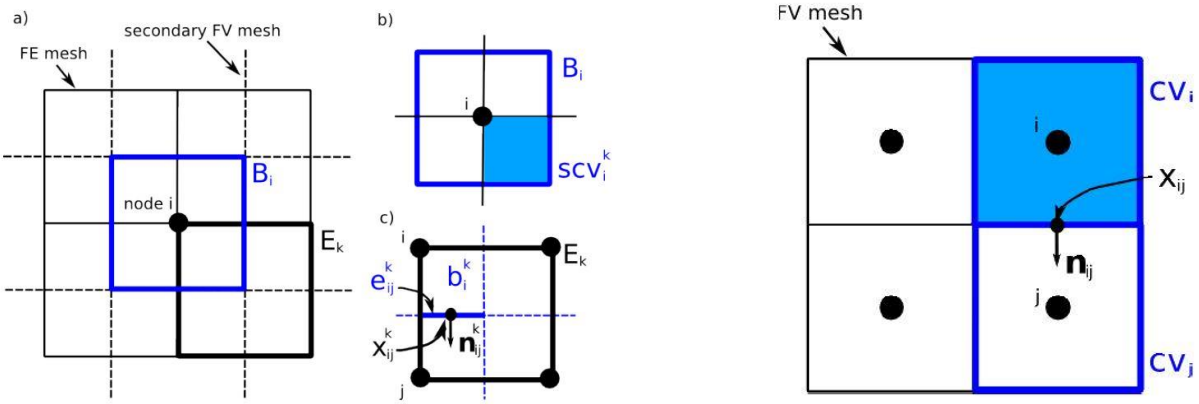

(a) Control volumes of the vertex-centered FVM (b) Control volumes of the cell-centered FVM

Figure III-7 Meshes and control volumes of two FVMs.

The unknowns are associated to black nodes (DuMu^x handbook)

We will consider here a cell-centered implicit Euler scheme; The finite volume method consists in discretizing the integral form of the system of equations on each control volume and assume that the solution everywhere in the control volume is equal to the cell average value. The integral form can be written as follows:

$$\int_{\Omega_i} \frac{M\left(u\left(X,t^{k+1}\right)\right)-M\left(u\left(X,t^{k}\right)\right)}{\Delta t}\, dV_i + \int_{\partial\Omega_i} F\left(u\left(X,t^{k+1}\right),\nabla u\left(X,t^{k+1}\right)\right)\mathbf{n}_{ij}\, d\Gamma_i = \int_{\Omega_i} S\left(u\left(X,t^{k+1}\right)\right) dV_i, \quad \text{Eq III.29.}$$

Ω_i is the interior and $\partial\Omega_i$ is the boundary of the control volume CV_i, Γ_i denotes the (problem dimension -1)-dimension measure of the boundary and $\mathbf{n}_{ij}$ is the unit normal vector to $\partial\Omega_i$ at point outward to CV_i .

$$M_i^{(k+1)} \approx \frac{1}{|V_i|}\int_{\Omega_i} M\left(u\left(X,t^{k+1}\right)\right)dV_i,\ S_i^{(k+1)} = \frac{1}{|V_i|}\int_{CV_i} S\left(u\left(X,t^{k+1}\right)\right)dV_i, \qquad \text{Eq III.30.}$$

The quantities *u* in the control volume CV_i and the neighboring CV_j are needed to calculate the flux integral across the interface γ_{ij}.

$$\int_{\partial\Omega_i} F\left(u\left(X,t^{k+1}\right),\nabla u\left(X,t^{k+1}\right)\right)\mathbf{n}_{ij}d\Gamma_i = \sum_{j=1}^{n}\left|\gamma_{ij}\right|F_{ij,\partial\Omega_i}^{(k+1)} \qquad \text{Eq III.31.}$$

n is the number of neighboring control volumes. For a common face of two control volumes CV_i and CV_j, the normal fluxes satisfy the conservation property:

$$\underset{\text{flux in}}{F_{ij}^{(k+1)}} + \underset{\text{flux out}}{F_{ji}^{(k+1)}} = 0, \text{ since } \mathbf{n_{ij}} + \mathbf{n_{ji}} = 0. \qquad \text{Eq III.32.}$$

The Final discretized system may be written as follow:

$$|V_i|\left(M_i^{(k+1)} - M_i^{(k)}\right) + \Delta t\sum_{j=1}^{n}\left|\gamma_{ij}\right|F_{ij}^{k+1} - \Delta t|V_i|S_i^{(k+1)} = 0 \qquad \text{Eq III.33.}$$

.(3.1)

To solve this system it is necessary to linearize the equations. This is done with the Newton-Raphson method (a root-finding algorithm). The result is a linear equation system that can be written as

$$J\left(Z^{k+1,m}\right)\Delta\left(Z^{k+1}\right) = r\left(Z^{k+1,m+1}\right) \qquad \text{Eq III.34.}$$

where *m* is the iterations counter. Z is the vector of primary variables, $J = \frac{\partial r}{\partial Z}$ is the Jacobian matrix, $\Delta Z = Z^{k+1,m+1} - Z^{k+1,m}$ is the correction of the solution vector, and r is the residual vector.

The new solution is calculated by:

$$Z^{k+1,m+1} = Z^{k+1,m} + \Delta Z \qquad \text{Eq III.35.}$$

The convergence test is done by comparing the primary variables for the same step of calculation before and after an iteration of the solver solutions. If a residual reduction is achieved, the solution is written out and the next iteration step can start. The simulation ends when the final simulation time is reached.

3.4.2. Implementation of the model into DuMu^x

The mathematical model described in section 3.1 was implemented into DuMux. We have used an extended coupled module that incorporates the bio-reactive transport into two-phase multi-component flow module, that we called 2P4C2B (two-phase four-component and two microbial species).

The flow and transport processes taken into account by the model are advection, buoyancy, and diffusion. The fluid system contains four chemical components: H_2O, H_2, CH_4, CO_2. Two additional balance equations are added to the 2pnc model one for attached microorganisms and the second for free bacteria. No interactions between the molecules of the different components, so all phases are ideal mixtures. The gas phase is assumed to be ideal, and the gas density is given by the ideal gas law. The interactions between the fluids and the porous medium are considered using capillary pressures and relative permeabilities as functions of the fluid saturations that are given by Brooks Corey model with parameters $\lambda = 2$, $P_e = 0.1MPa$. Hydrostatic pressure distribution is applied. Adapted set of primary variables: n_a (population of attached bacteria), n_d (population of detached bacteria).

The possible appearance and disappearance of one phase is controlled by the primary variables switch process, we distinguish three different cases:

Phase state	Primary variables	Primary variable switch
Liquid phase only	$p_w, X_w^{H_2}$	$\sum_k X_g^k > \left(X_g^k\right)^{\max}$: gas phase appears and $X_w^{H_2}$ switch to $X_g^{H_2O}$
Gas phase only	$p_w, X_g^{H_2O}$	$\sum_k X_w^k > \left(X_w^k\right)^{\max}$: liquid phase appears and $X_g^{H_2O}$ switch to $X_w^{H_2}$
Both phases	p_l, either S_l or S_g	If $S_l < S^{\min}$: liquid phase disappears and S_l switch to $X_g^{H_2O}$ If $S_g < S^{\min}$: gas phase disappears and S_l switch to $X_w^{H_2}$

Table 6 adequate primary variable choice

The (re) attachment and detachment mechanisms are added as dependent source/sink terms to the two bacteria balance equations. The rock matrix is taken into account via the porosity and permeability of the porous medium. Our code takes into account the bio clogging of the pores as well. The porosity and the permeability values are updated during each Newton iteration.

We analyzed the injection of a mixture of H_2 and CO_2 into an aquifer with a length of 100 m and a height of 80 m and situated at 1700 m below the ground level. The domain of study was a 3D radial sector of a cylinder near the injecting well. The well radius is 0.85 m. The clean-porous domain is assumed to be homogeneous with porosity $\phi_0 = 0.2$ and absolute permeability $K_0 = 5.10^{-12} m^2$. The upper and lower sides are impermeable. Two lateral planes are not crossed by any streamlines, therefore the normal flow velocity through them is zero. The vertical axis is the injecting well. The injection rate of hydrogen is four times greater than that of CO_2. Gas is injected from below (in the left down corner), to avoid the effect of immediate lateral spreading along the reservoir cover. An initial population of methanogenic bacteria was uniformly present in all medium. The initial concentrations are: $n_a^{(0)} = 9.10^6$ and $n_d^{(0)} = 1.10^3$ bacteria in 1 m^3. The reservoir is initially fully saturated with water, thus $S_w\left(X, t=0\right) = 1$. The initial mole fractions are zero except for water $c_w^{H_2O} \approx 1$.

Parameter	Value
Porosity, ϕ_0	0.2
Permeability, K_0	5.10^{-12} m^2
Diffusion coefficient of immobile bacteria, D_b	10^{-7} m2.s^{-1}
Entry capillary pressure, P_e	10^5 Pa
t^{gr}	$6{,}761.10^3$ s
a_{H_2}	$1{,}094.10^{-7}$
a_{CO_2}	$3{,}18810^{-6}$
Yield, Y	$1{,}739.10^{12}$
Boltzmann constant, k_b	$1{,}380649.10^{-23}$ J.k^{-1}
Temperature, T	310 K
Liquid velocity at which the biofilm was grown, V_{bg}	$0{,}66.10^{-8}$ m.s^{-1}
Maximal velocity, V_m	3.10^{-6} m.s^{-1}
Critical bacterium concentration, n_c	7.10^8
Detachment rate, $k_{\text{det}}^{\max}$ (Stoodely model)	0.001 s^{-1}

Table 7 Data used for simulations. (Gion Strobel et al. 2020, Panfilov 2019, Kirk E. Nelson et al. 2010, Maria Auset et al. 2005)

We used nonconforming ALUGRID mesh so that the size of the elements decreases as far as they approach the injection well. The simulations were carried out using three different grids, in order to check the convergence and stability: a coarser mesh with 6720 cells and 13866 points, a medium mesh consisting of 9600 cells and 19602 points, and eventually the finest mesh with 28560 cells and 57838 points. The coarser mesh provided close results for gas and water flow but was unable to capture the impact of bio-clogging on gas transport. The finest mesh has captured this effect, but it costs us a high CPU time. Unlike them, the medium mesh gave good results in less time.

The cell-centered finite volume method was applied for spatial discretization. The coupled fully implicit Euler scheme was used for time discretization. The resulted discretized system of equations was linearized by the Newton-Raphson method with an adaptive time step that was controlled through the number of iterations needed for the convergence of Newton's solver.

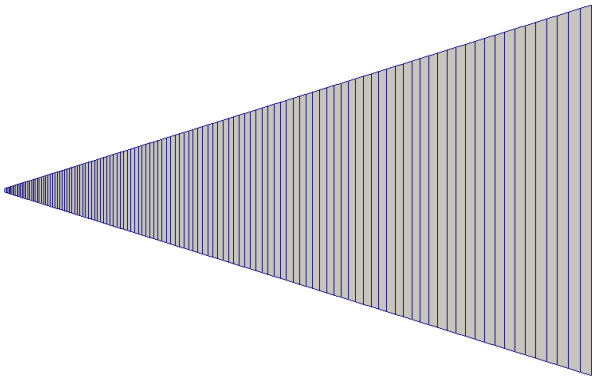

Figure III-8 Mesh mode

3.4.3. Case study I: scenario of H_2/CO_2 storage without bioclogging

In the first test, we consider that the bioclogging is ignored. The obtained results are shown in Figures 9 and 10. We can observe a fast rise of the injected gas to the reservoir cover, with the maximum velocity at the front of the vertical rise. Consequently, we can expect that the detachment of bacteria is more intensive in the vertical direction.

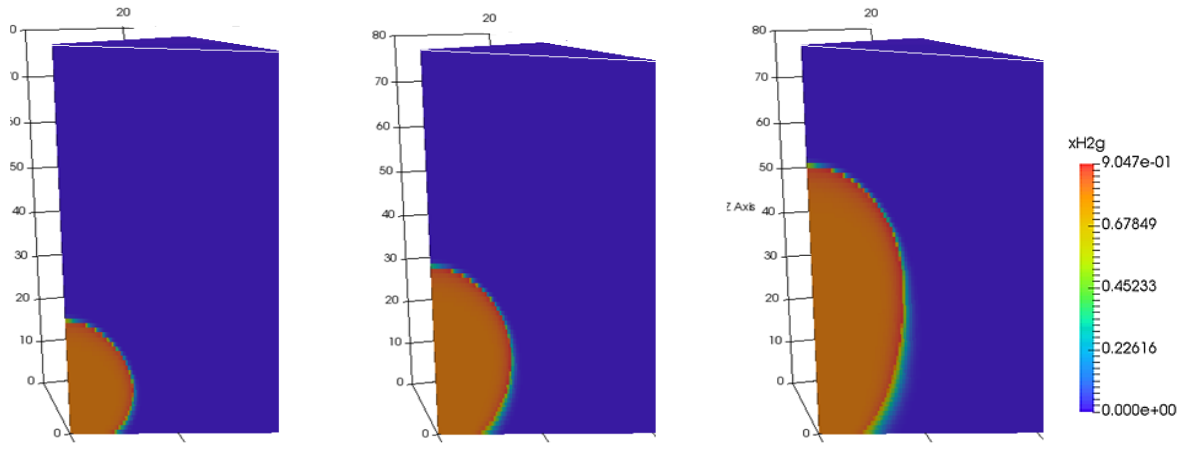

Figure III-9 Hydrogen fraction molar: after 10 days, 22 days, and 42 days of injection at the rate 0.5 kg m^{-2} s^{-1}

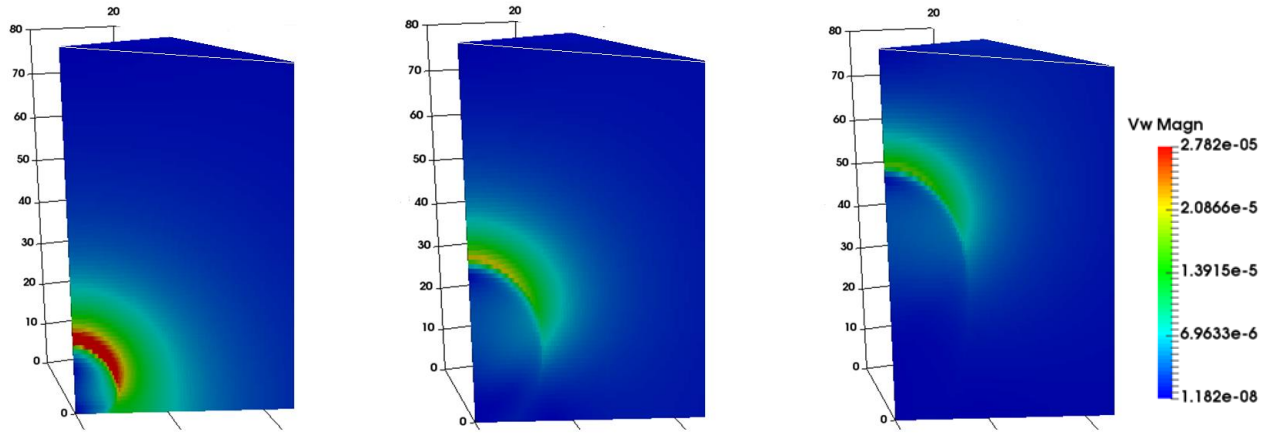

Figure III-10 Flow velocity field near the injecting well: after 10 days, 22 days, and 42 days of injection at the rate 0.5 kg m^{-2} s^{-1}

3.4.4. Case study II: scenario of H_2/CO_2 storage with bioclogging

In the second test we performed, the medium porosity and permeability were variable and dependent on the number of bacteria. As the type of bacteria, attached or detached, has no importance for clogging, we ignored the attachment process, for the sake of simplicity, assuming that the probability of attachment is very low in the reservoir. We also ignored the decay of the bacterial population. Indeed, the decay is mainly caused by various predators, like other microorganisms or fungi, which is an unlikely event in a sparsely populated environment.

– **Evolution of the bacterial population:**

Figures show the evolution of the immobile biomass distribution as a function of time. The biomass concentration increases mainly near the wellbore region, this is not surprising as this is the region with higher flow velocity where the detachment process is privileged. Fig III-12 illustrates the variation of detached bacteria along the radial direction.

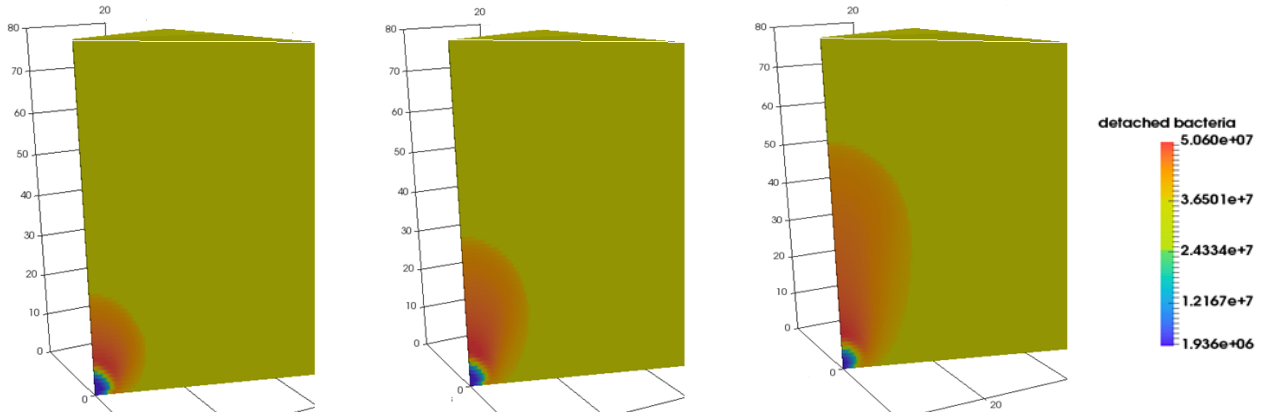

Figure III-11 Evolution of the concentration of detached bacteria near the injecting well: after 10 days, 22 days, and 42 days of injection at the rate 0.5 kg m^{-2} s^{-1} The maximal value is 5.06 10^7 bacteria in 1 m^3 , the minimum is 1.93 10^6.

Fig 12 illustrates the variation of the number of detached bacteria in the radial direction.

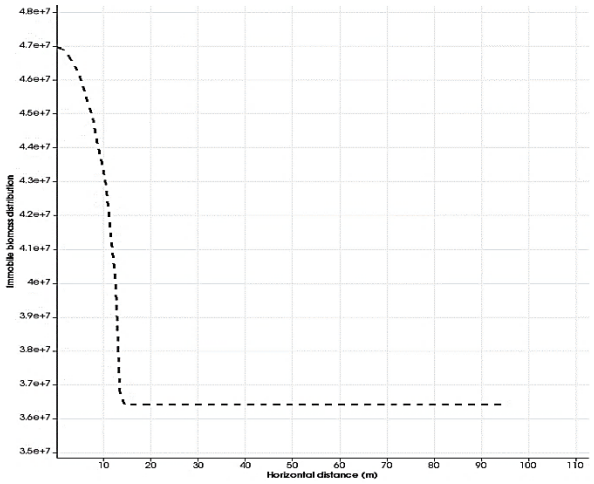

Figure III-12 Distribution of detached bacteria along the horizontal direction from the injector at (x,y=0, z = 20m, t=42 days)

– **Evolution of porosity and permeability caused by bioclogging:**

The spatial variations of permeability and porosity are presented in Figures 13 and 14.

The reduction in the porosity and the permeability is more significant near the injection well. Again, the more critical zone is close to the wellbore region. Overall, the numerical results show a qualitatively a good agreement with experiment results published by (Ham et al., 2007 and Brovelli et al, 2009).

The variation of porosity and permeability is very different in the vertical and horizontal directions. The measured decrease due to bioclogging was more severe in the vertical direction. However, the minimum permeability is 0.058 D in the vertical direction, while in the horizontal the minimum permeability is 0.059 D. The length of the zone where the permeability is reduced is higher in the vertical direction (about 50 m) than in the horizontal direction (15 m). In the horizontal direction, porosity change is minimal with to 0.19695, while decreases in the vertical direction to 0.1961 at a distance of 8 m from the injection well.

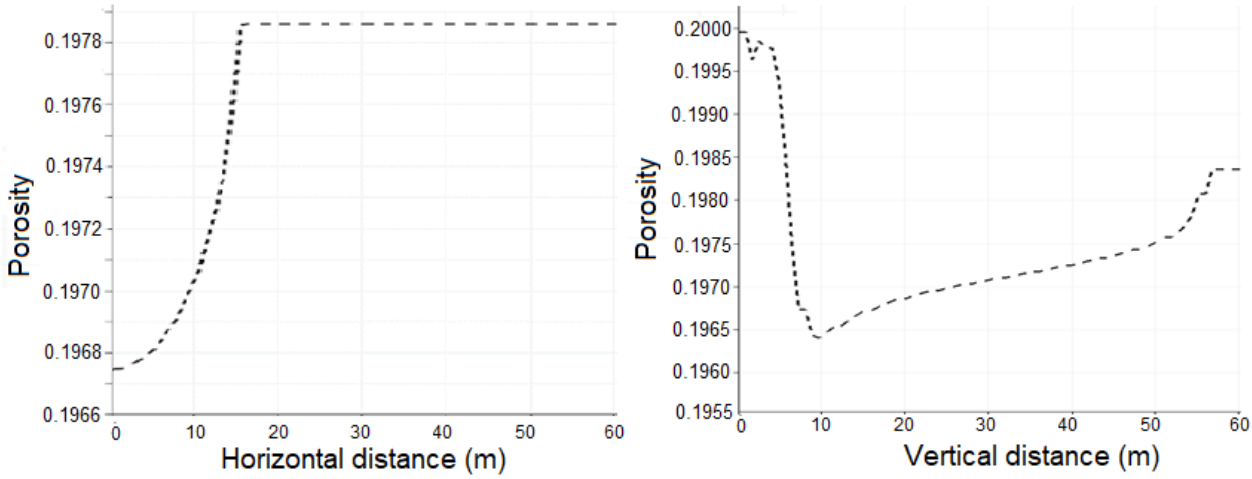

Figure III-13 Variation of the porosity in space in horizontal and vertical direction from the point of injection, for the same moment of time

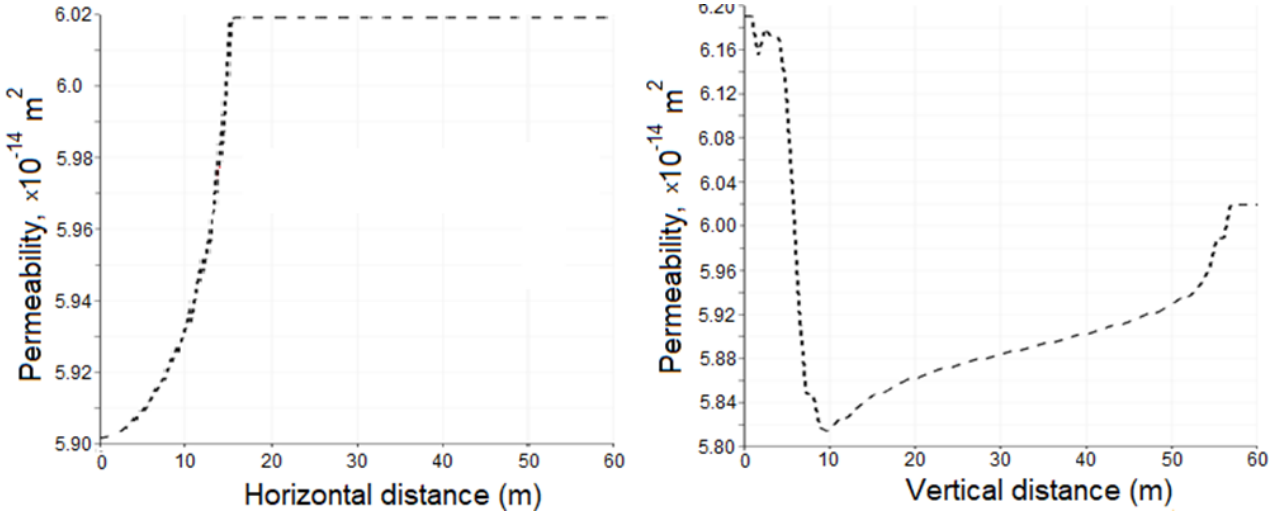

Figure III-14 Variation Variation of the absolute permeability in space in horizontal and vertical direction from the point of injection, for the same moment of time

– **Impact of bioclogging on gas propagation:**

The next step is to quantify the effects of bioclogging on the injected gas transport. Fig. 15 and 16 show the evolution of hydrogen mole fraction and gas saturation in the horizontal and vertical direction of the reservoir in the case with and without bioclogging.

Parameters used for the last simulations were adjusted in order to envision the following effects.

Parameter	*Value*
Porosity, ϕ_0	0.3
$[n_a^{(0)}; n_d^{(0)}]$	$[1.10^4; 8.10^6]$

Table 8 Data used to **investigate th**e effect of bioclogging on gas transport.

According to Fig. 15 - 16, when the medium permeability in the vertical direction decreases, it becomes more difficult for gas to lift up than to propagate horizontally. The bioclogging hinders the vertical rise of gas and leads to the preferred horizontal gas migration. Furthermore, advection transport is becoming increasingly evident, which increases horizontal migration. Thus, bacteria play the role of a regulator that can ensure hydrogen propagation deep into the reservoir and to reduce its vertical rise towards the cover. We can thus imagine the technique of injecting bacteria together with H_2 and CO_2, to intensify this regulatory effect.

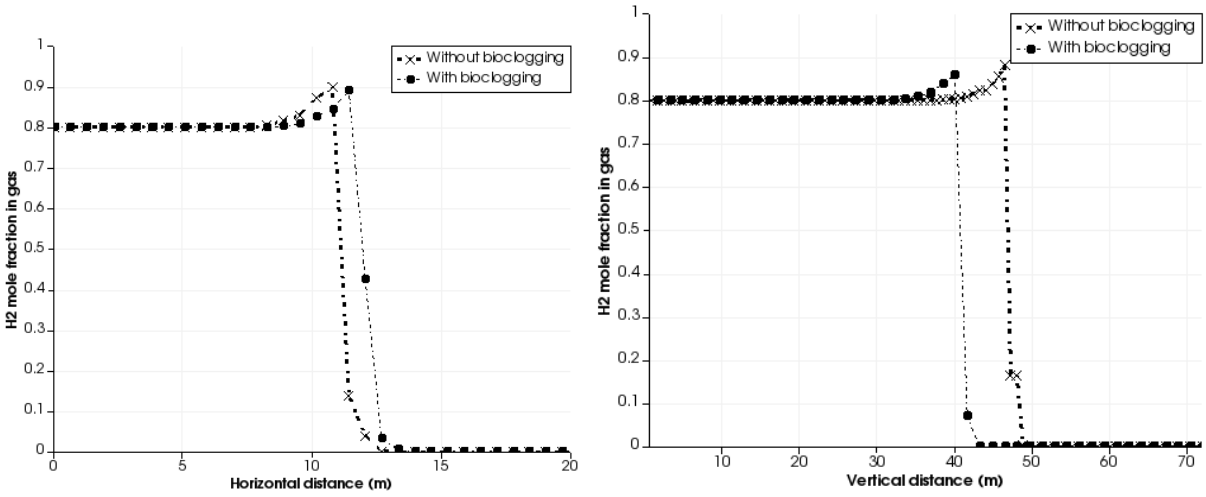

Figure III-15 Hydrogen mole fraction in the horizontal and vertical direction in the case of bioclogging and without it (without bacteria), for 16th day of injection

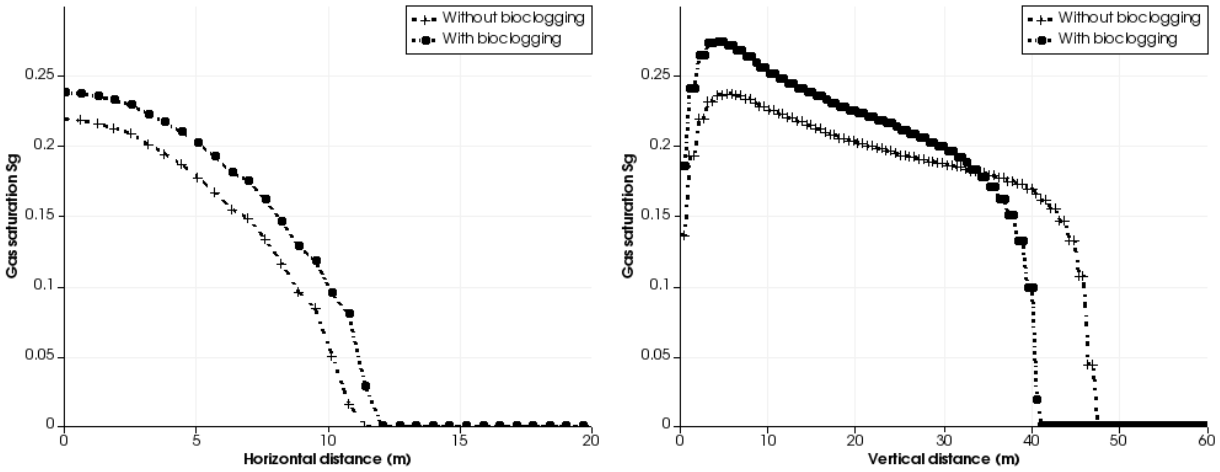

Figure III-16 Gas saturation in the horizontal and vertical direction in the case of bioclogging and without it (without bacteria), for the 16th day of injection

– **Joint capillary-bacterial clogging:**

The classical expected impact of the capillary pressure is twofold: (i) it should destroy sharp fronts of saturation and make them smoother, and (ii) it prevents gas from entering a water-saturated medium if the medium is water-wet (the effect of *capillary entry pressure*). These effects have been well observed in our simulations. At the same time, we revealed an additional important joint impact of the capillary pressure and bio-clogging on gas propagation. We compared the results obtained for two cases of the initial average capillary pressure that correspond to low and strong capillarity, respectively: $\hat{P}_c^0 = 0.1$ MPa and $\hat{P}_c^0 = 10$ MPa, where $\hat{P}_c$ is defined by (3.9). (We kept a small but non-zero capillary pressure in calculations to ensure regularization of numerical schemes and avoid instability in the simulation).

Fig. 17 shows the spatial distribution of gas saturation for these two cases along the vertical and horizontal axes respectively. The case of strong capillarity corresponds to the solid curves. As seen, due to the joint impact of bio-clogging and capillarity, the gas propagation in the vertical direction is even more retarded, while it is enhanced in the horizontal plan. This is caused by the fact that the capillary counteraction to gas penetration increases in the region of bio-clogging, in which the permeability is reduced and then the capillary pressure grows. Consequently, the

barrier action of the long vertical plug formed by bacteria is amplified by the capillary counteraction, which forces the injected gas to propagate horizontally.

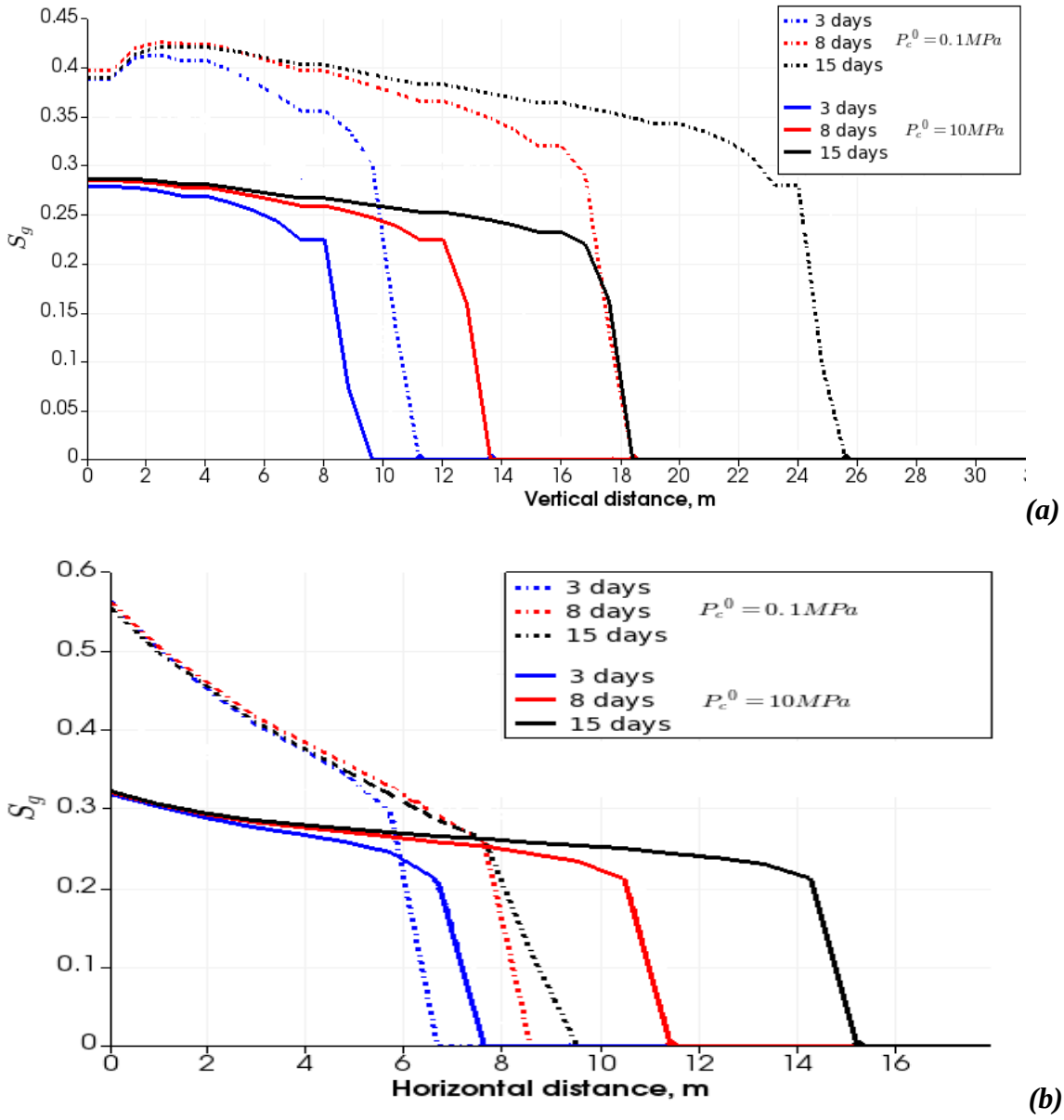

Figure III-17 Gas saturation in the vertical direction (a) and radial direction (b) at high and low capillary pressure (the solid and dotted curves, respectively), for three moments of time

The shape of the gas-saturated zone for the same moment in time is shown in Fig. 18, for three cases: without bacteria, with bacterial clogging but with zero capillarity, and for bio-clogging in the presence of capillarity. As it can be seen, the shape of the area occupied by the gas becomes more and more uniform in all directions.

In order to quantitatively characterize the influence of the investigated effects on gas propagation, we introduced a ***planar speed of gas propagation***, defined as the square of the distance traveled by the gas in time *t*, divided by time *t*. If the gas flow were plane-radial and stationary, then this parameter would be constant, which explains the reason for its choice. Table 6 illustrates how this parameter changes under the action of bio-clogging and joint impact of bio-clogging and capillarity.

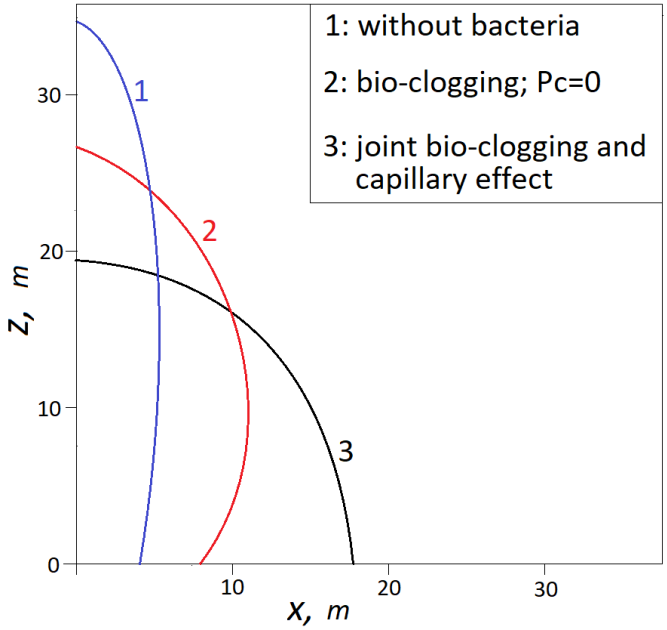

Figure III-18 Shape of the gas-saturated area in three cases: (1) without bio-clogging and P_c=0; (2) with bio-clogging and P_c=0; and (3) with bio-clogging and with non-zero P_c

	Without bacteria and P_c=0	With bio-clogging and P_c=0	Joint capillary-bacterial clogging (P_c=10 MPa)
Vertical propagation rate [m^2/day]	67	42	23
Horizontal propagation rate [m^2/day]	3	10	17

Table 9 Impact of bio-clogging and capillarity of the planar rate of gas propagation

It can be seen that both bio-clogging and capillarity enhance the horizontal rate of propagation and reduce the vertical rate, which makes the gas bubble regular and close to spherical.

– **Impact of capillary-bacterial clogging on reservoir pressure:**

Since the capillarity hampers gas to flow and reduces its saturation, this reduces the population growth and activity. As the result, this reduces the bio-clogged region. Fig. 19 illustrates the effect of permeability reduction caused by bio-clogging at low and high capillary pressure. It is clearly seen that the capillary pressure reduces the clogged region in both directions.

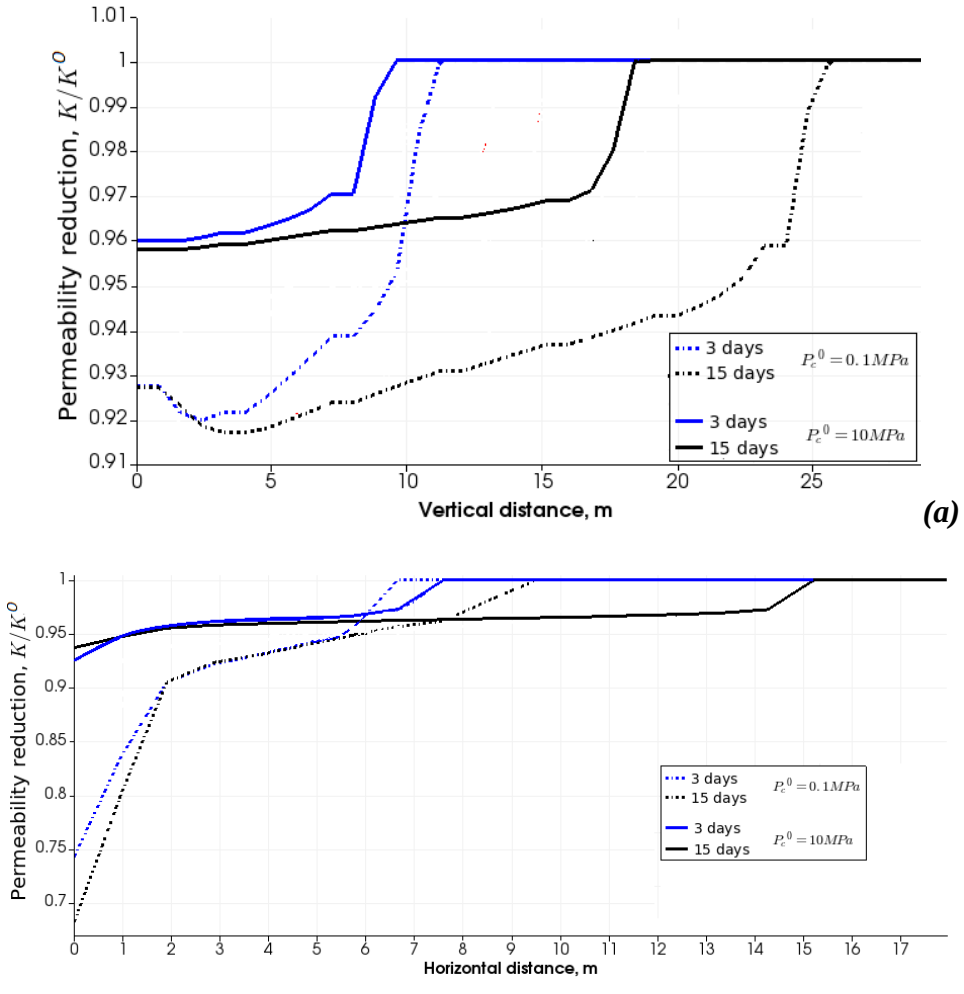

Figure III-19 Permeability reduction in vertical direction (a) and radial direction (b) at high and low capillary pressure (the solid and dotted curves, respectively), for two moments of time

If the volume occupied by gas reduces then the gas pressure must. This was observed in our simulations. Within the area of 30 m around the well and after the stabilization, the gas pressure was about 20 MPa in the case without capillary pressure. For $\hat{P}_c^0 = 10$ MPa, the reservoir pressure increased up to 31 MPa ahead of the gas-saturated zone and 32 MPa behind the front of gas propagation.

In other words, the gas bubble becomes more regular, but smaller and more compressed, due to the joint effect of capillary-bacterial clogging.

– **Impact of bioclogging by biofilms on hydrogen conversion:**

Here, we present the bioclogging problem taking account of microbial attachment and the model of Gerald E. Speitel et al. 1987 for biofilms detachment. We evaluate the pore space reduction due to the attachment of bacteria to the pores. The permeability reduction is higher than that presented in the last test due to microbial filtration. The reduction was severe near the wellbore region. The results are in good agreement with experimental data published by (Anozie Ebigbo et al. 2010). The length of the zone where the permeability is reduced is higher in the vertical distance (about 25 m) than in the radial (about 6 m). After 15 days of injection, in the radial direction, permeability is reduced by 62%, while is reduced by 44% in the vertical direction. Fig. 20 (c) shows that the ratio porosity/permeability grows over time which implies that capillary pressure increases as well and this accelerates bioclogging.

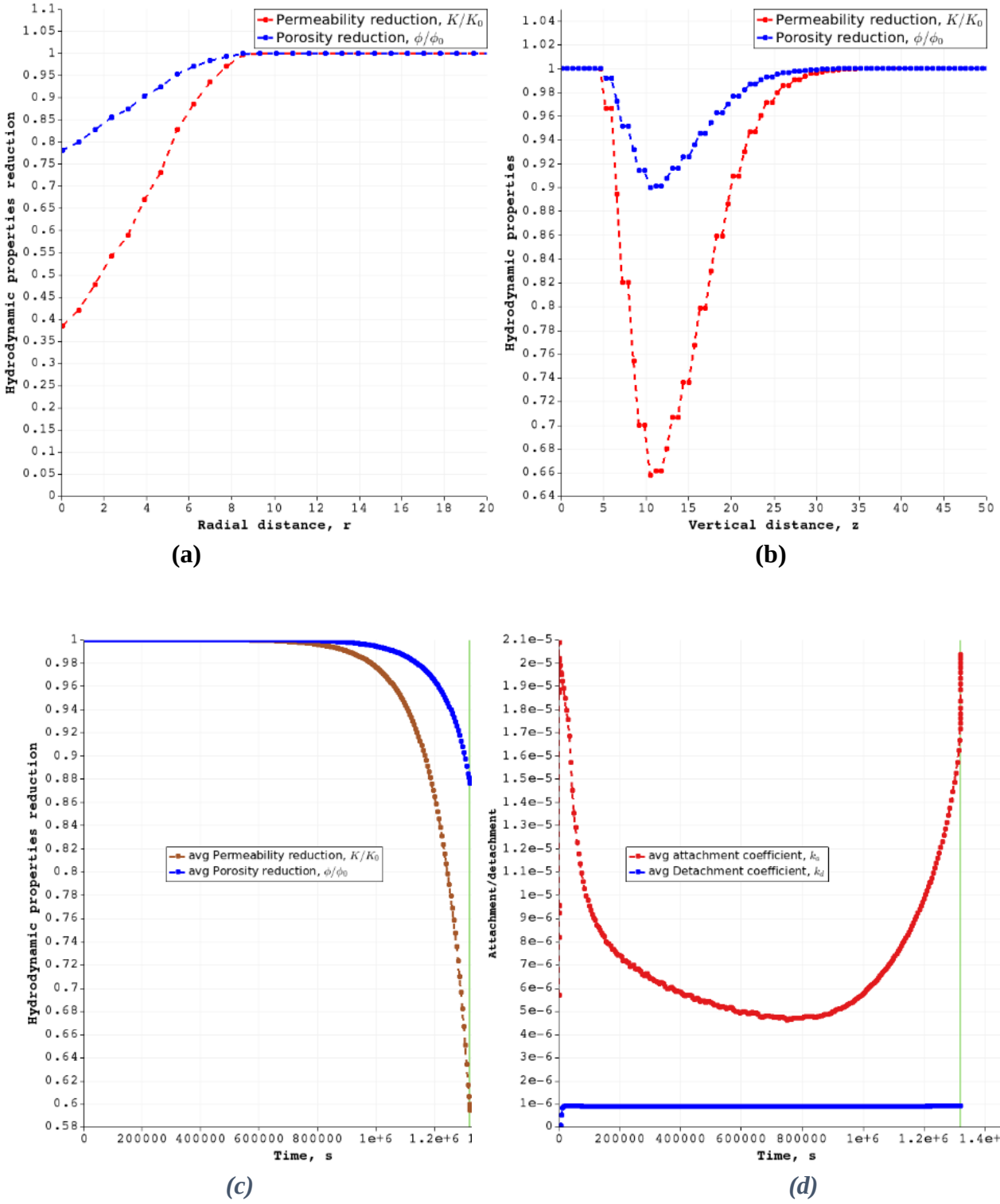

Figure III-20 Variation of porosity and permeability in radial (a) and vertical (b) distance after 15 days and over time (c), and measured attachment and detachment coefficients over time (d).

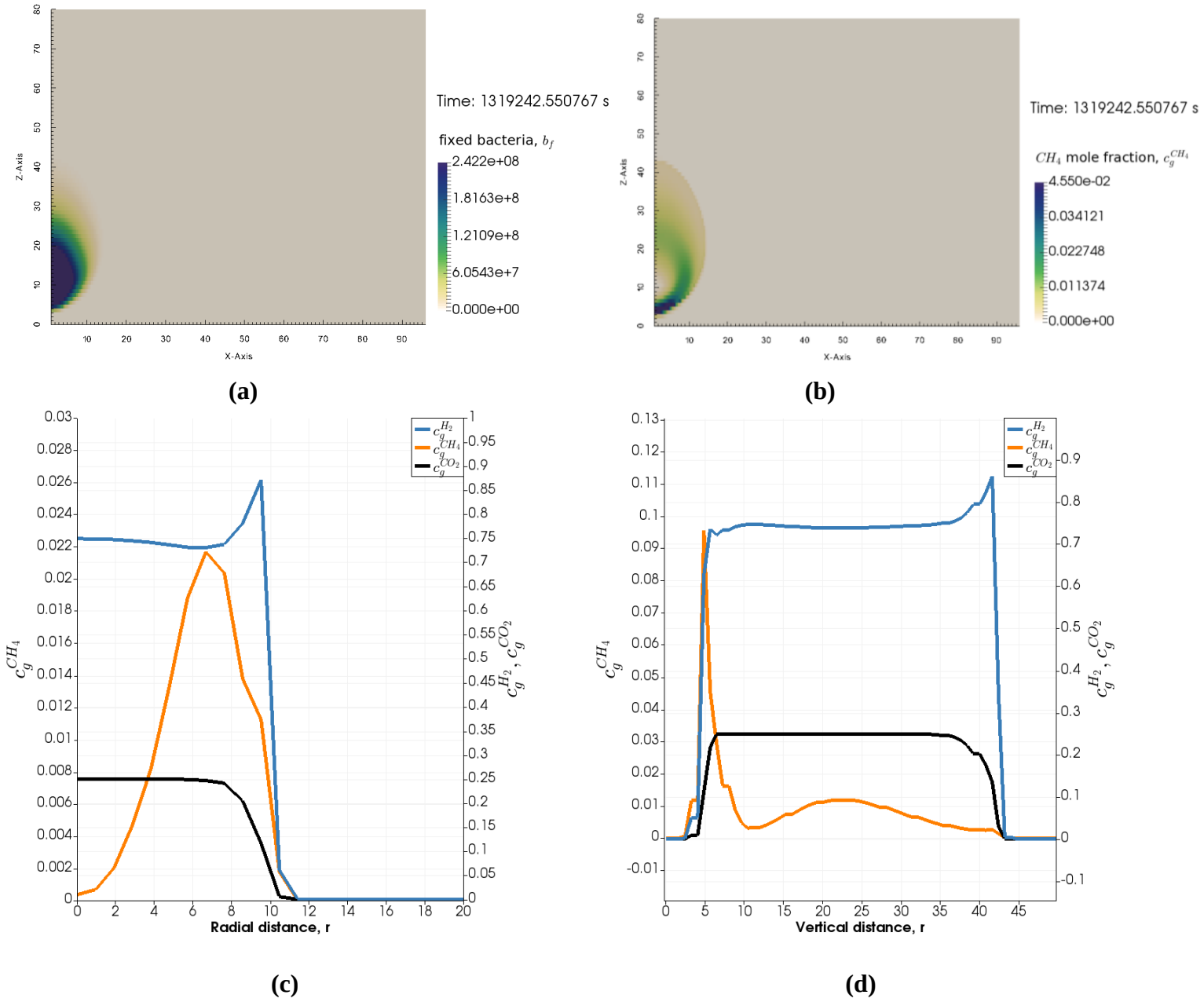

Figure III-21 2D distribution of (a) fixed bacteria, (b) biomethane production within the reservoir and (c-d) hydrogen and carbon dioxide concentration vs. methane bio-production after 15 days

Figure 20 (d) shows the evolution of the measured attachment and detachment coefficients over time. The attachment mechanism dominates which should amplify the concentration of biomass attached to the pore wall and bioclogging as well.

Figure 21 (a) shows the distribution of fixed biomass within the reservoir after 15 days of injection. As soon as the nutrients reach the entry zone, fixed bacteria start growing, in turn producing biomethane. It is observed from figure 21 (a-b) that biomass is more present and reactive near to the injection zone, which is a region rich on nutrients H_2 and CO_2. The results are in good agreement with Brovelli et al. 2009 and Sivasankar et al 2019 studies and reproduce well the fixed biomass distribution observed in the experiments presented in Brovelli et al. 2009. Figure 21 shows also a comparison of the hydrogen, carbon dioxide, and methane distribution in the vertical and horizontal direction. Within only 15 days bacteria due to their activity was able to transform ~ 2% of hydrogen into methane. For the same period, in the underground reservoir of Lobodice town (Czech Republic) and with a density of 10^9 cell/m^3 bacteria has transformed 60% of the quantity we have obtained (Frantisek Buzek et al. 1990) (i.e. *Bioclogging enhance methane production)*

It could be observed that the vertical spreading of hydrogen is faster than that of methane. Compared to methane, hydrogen is eight times less dense than methane and the lower viscosity of hydrogen induces higher mobility of hydrogen. This makes hydrogen very diffusive compared to other gases (figure 21 (c-d)).

The simulations of the microbial biomass concentration and their rate of attachment to the pore walls in the cases with and without bio-clogging are plotted in figure 22. Due to the high concentration of bacteria captured in the clogged zone, bacterial activities in this region grow, and as a consequence their production on biomass increases. Due to the reduction of the pores volume, bioclogging increases the flow velocity and capillary pressure (figure 23). As consequence, this increases the probability that a bacterium collides with a pore surface. It is found that the impact of bioclogging on the attachment mechanism is more important near the injection zone.

The influence of bioclogging on biomethanation efficiency is analyzed in the two last results. Due to bio-clogging, the conversion of H_2/CO_2 into methane by bacteria is improved by two orders of magnitude from 0.0014 to 0.0023. The fixed bacteria in the clogged zones work synergistically to enhance their reactivities and as consequences boost their production of biomethane. Thus, bioclogging improves biomethane conversion efficiency by trapping more bacteria, improving their growth, and accelerating their activities.

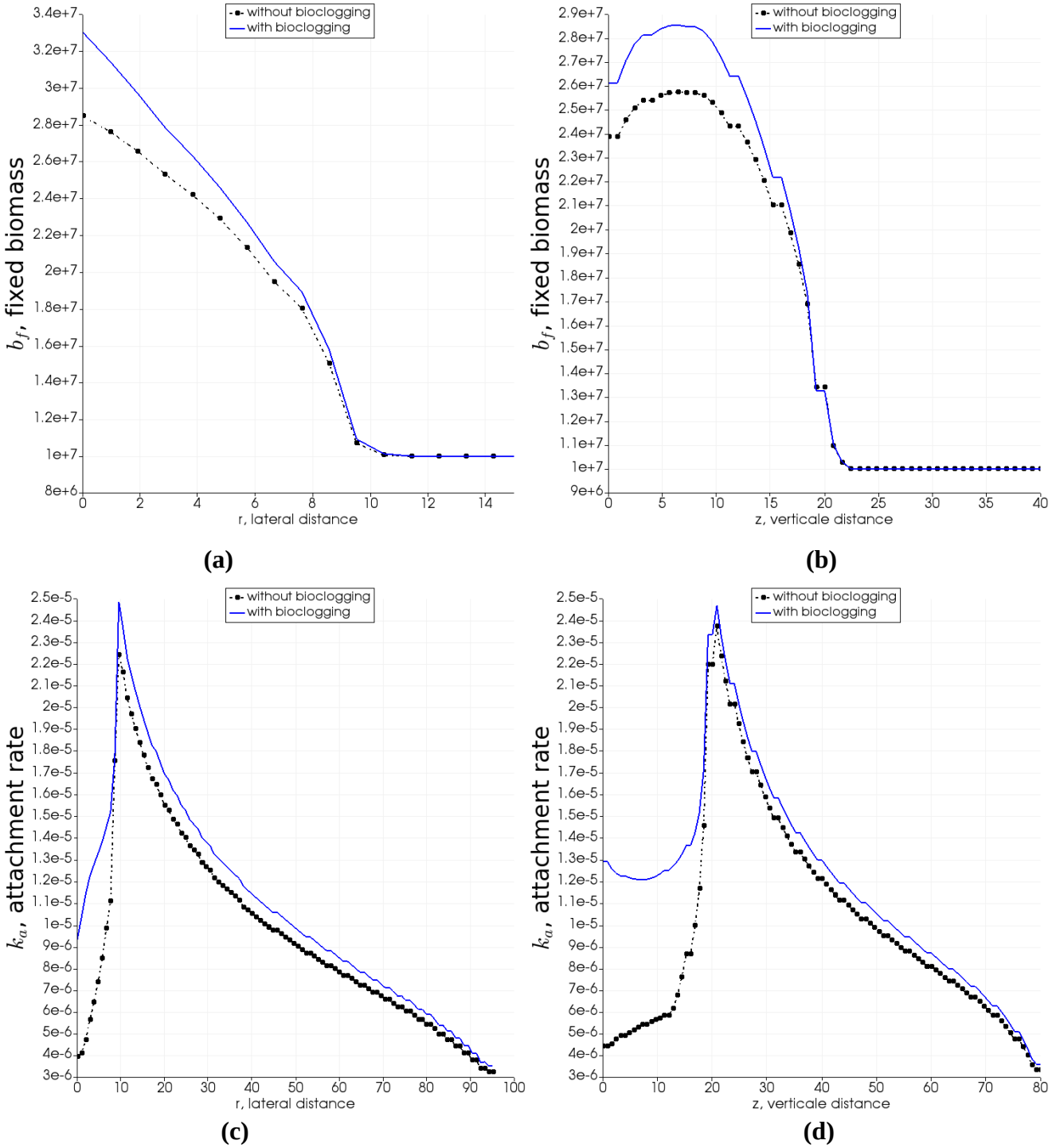

Figure III-1 Influence of bioclogging on (a-b) attached biomass concentration and (c-d) attachment mechanism in radial (left) and vertical (right) directions

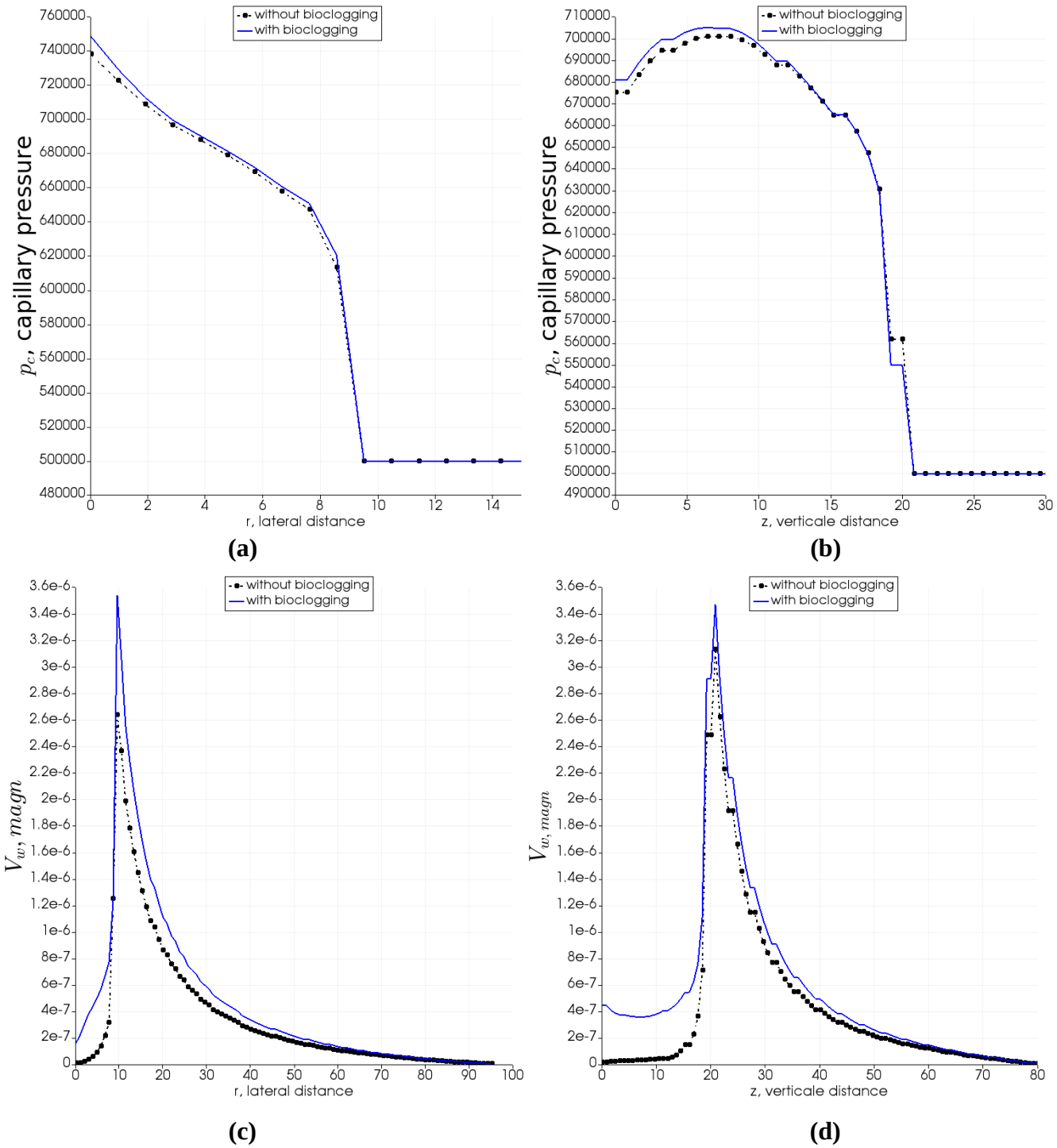

Figure III-23 Impact of bioclogging on flow velocity and capillary pressure

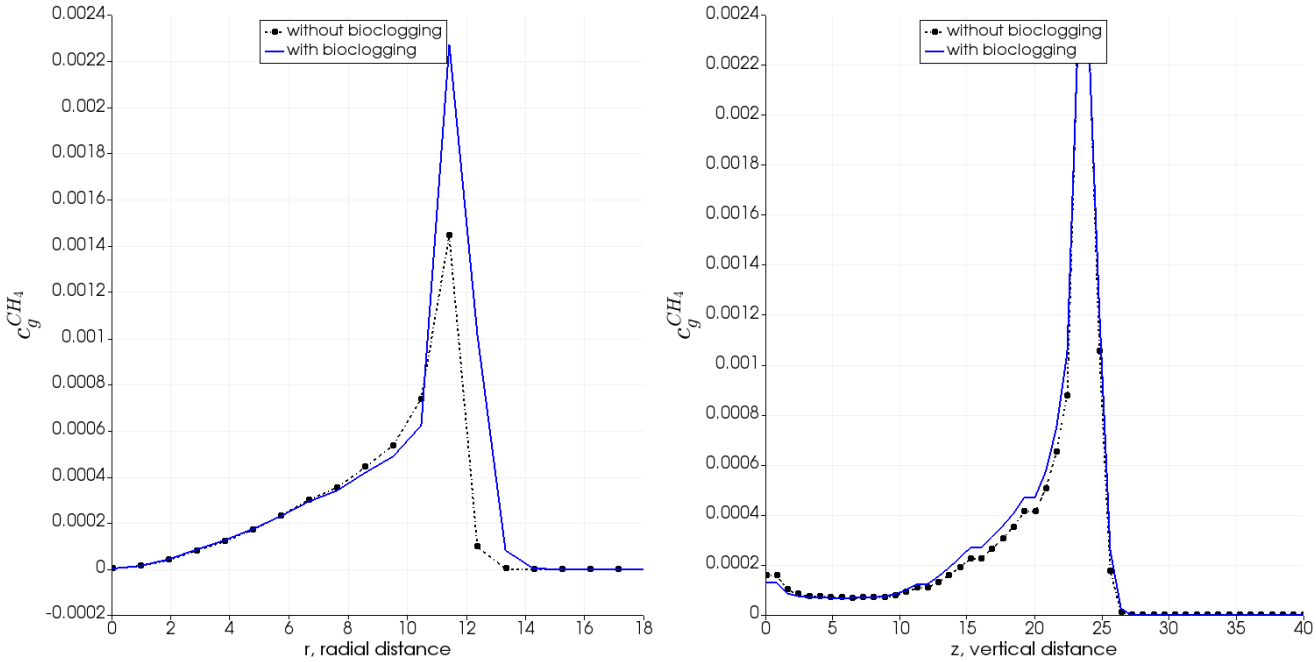

(a) **(b)**

Figure III-24 – Influence of bioclogging on biomethanation process

3.5. CONCLUSION

Accumulation of a sufficient biomass plug pores and reduce their porosity and permeability, leading to "bio-clogging". In this chapter, we modeled and simulated bio-clogging in underground H_2/CO_2 storage. We have developed a mathematical model, describing fluid flow, bio reactive transport, microbial detachment/trapping, bacterial growth, and bio plugging. We have investigated the impact of pore-clogging on the hydrodynamic properties of the reservoir. We have found that bio-clogging induces heterogeneity of the medium in the form of a region of low permeability, which gradually increases as the bacterial population grows. The most clogged region was located near the wellbore region. The measured decrease due to bioclogging was more severe in the vertical direction. Thus, we have investigated the impact of biomass growth on capillary pressure, we find that capillary pressure increases with a high density of biomass. Our research has shown that while bio-congestion is inevitable, it is not so bad and may even be

beneficial. Indeed, accumulating in places of high hydrogen saturation, that is, on the preferential paths of its migration, bacteria force hydrogen to change the way and move in different directions. As a result, instead of a rapid vertical ascent, which is undesirable for us, hydrogen is forced to move horizontally into the depth of the formation, creating an almost ideal gas bubble. We have shown that capillary forces enhance this effect so that the gas bubble tends to become uniform in all directions. Due to the joint effect of bio-clogging and capillarity, the gas bubble becomes more regular, but smaller and more compressed. In this case, bioclogging should boost its effect as well. Furthermore, we found that within only 15 days bacteria due to their activity are able to transform ~ 2% of hydrogen into methane which was three times greater than the result obtained in the experiments realized in the Lobodice reservoir. We have also shown that bioclogging could improve biomethane conversion efficiency by trapping more bacteria, improving their growth, and accelerating their activities. We can conclude that controlled bioclogging can help for efficient performance in underground natural gas reservoir fields to achieve the maximum efficiency of hydrogen conversion into biomethane.

CONCLUSIONS

This thesis is devoted to analyze the behavior of the solutions of the system of equations that describes transport phenomena in an underground storage of hydrogen created in an aquifer or depleted gas reservoir. We know that the behavior of hydrogen is very different from that of natural gas due to the fact that hydrogen is actively used by bacteria inhabiting rocks, which transform it into methane. Such a biotic reaction occurs in presence of CO_2, which is always dissolved in groundwater or can be injected together with hydrogen. Consequently, the mathematical model of the process is a system of transport equations for several chemical species (H_2, CO_2, CH_4, H_2O,…) dissolved in gas and water, and an equation of bacterial dynamics, which includes bacterial growth, probable decay, and movement. The kinetics of the methanation reaction is determined by the metabolic process in the bacterial population, and, finally, is strongly related to the kinetics of population growth.
After storing underground, hydrogen can be used in two main industrial ways.

First of all, it can be reconverted into electricity in fuel cells and used in vehicles, which requires to have very pure hydrogen. However, the losses of hydrogen caused by the methanation reaction make it impossible to store in the pure state. This is why the practical objective of storing would be to minimize biochemical reactions, which would facilitate the subsequent treatment on the surface of the hydrogenous mixture extracted from the storage facility. Note that the main principle, in this case, is to minimize the mixing of hydrogen with other gases.

Secondly, hydrogen can be used as a fuel for heating and lighting buildings. In this case, its partial conversion to methane means the enrichment of the fuel, since the energy potential of 1 m^3 of methane is higher than that of hydrogen. In this case, we should intensify the reaction of methanation in the storage. Such a process of in situ methanation occurs at low temperature, is much less expensive than the high-temperature methanation, and can represent industrial interest. The main principle, in this case, is to maximize the mixing of hydrogen with CO_2 to convert all hydrogen.

However, the mixing in such a system is not so simple to control, as the evolution of the transport phenomena in storage obeys its own physical laws, which do not take into account technological expectations. The main problem that hampers us to regulate mixing are the phenomena of self-organization that occur in a diffusion-reaction system. They lead to the formation of *patterns* – stable spatial or temporal-spatial structures (mosaïques), some kind of fluctuations in space or in time, or both in space and in time simultaneously, which are the solutions of the transport equations at $t \to \infty$. The parameters of patterns are strictly determined by the physics of flow and the kinetics of reactions. Fortunately, the gas injection rate and the composition of the injected gas are also two parameters that can change the geometry of patterns, providing us the possibility to control the process of their formation.

A pattern means the existence of zones with high concentrations of hydrogen and other zones with low concentrations. Therefore, mixing becomes non-uniform in space and non-complete. Patterns reduce the degree of mixing. This can be good for the first goal: to use hydrogen as converted electricity. But this is certainly not good for the second goal to transform hydrogen into methane. Thus, the theoretical problem of finding criteria of the pattern existence obtains a clear practical sense.

In this thesis, we distinguish three types of patterns:

(i) stationary patterns caused by the so-called *Turing's instability*;
(ii) uniform in space but periodically oscillating in time, related to the phenomenon of the Hopf-Andronov bifurcation and the occurrence of a limit cycle;
(iii) and *wavy patterns*, periodically oscillating in space and in time simultaneously and related both to Turing's and Hopf-Andronov instability.

We have analyzed the general conditions of the occurrence of all three types of patterns in homogeneous media. In particular, we have shown that a new pattern exists in the case of only two diffusion-reaction equations, which is nonstationary and behaves as *jumping waves*.

After this we have extended our analysis to heterogeneous media, which were analysed in terms of the macroscopic double porosity model. We have shown, in first, that the double porosity displaces the criteria of pattern formation. We have shown that for stationary patterns, the concentration in fractures and in blocks are identical, which corresponds to classical behaviour

of the solutions of the double porosity equations. Secondly, we have revealed the existence of patterns, in which the concentrations in fractures and blocks are distinct. They undergo spatial and temporal oscillations, which have distinct amplitude, frequency, and phase. This is possible only for wavy patterns, non-stationary. This was confirmed by our numerical tests.

In the last part of the thesis, we analyzed the same transport equations in the case when bacteria induce a medium heterogeneity, by clogging some pores and reducing the permeability, porosity, and capillary pressure between gas and water. For this purpose, we have developed the conceptual model of particle attachment and detachment to pore walls. Several mechanisms of attachment are considered. Experimental data for some phenomenological coefficients were found in the literature. This model has been implemented into a numerical simulator ($DuMu^X$). The subsequent analysis was based on this conceptual model and was performed numerically. We analyzed the injection of hydrogen in an aquifer in three-dimensional domain. We have shown that bio-clogging reduces locally the permeability, and, in addition, induces some anisotropy because the decrease in permeability was higher in the direction of bacteria propagation (in vertical direction). Due to this, the rise of gas to the cover was retarded and even stopped. So that the injected gas had to flow in horizontal direction non clogged by bacteria. Consequently, the propagation of gas becomes more regular, which is favorable to the creation of a gas storage. The induced heterogeneity forces the gas to change the path and to move in other directions. Capillary forces, which increase in clogged areas, enhance this effect, so that the gas tends to propagate uniformly in all directions. Due to the joint effect of bio-clogging and increased capillarity, the gas migration becomes more regular. We found that bacteria are able to transform 2% of hydrogen into methane in course of 15 days, which is three times faster than the result obtained in the experiments realized in Lobodice reservoir. Thus, we conclude that bio-clogging increases bio-methanation efficiency.

PERSPECTIVES

The work presented in this manuscript reveals perspectives for an in-depth analysis of some of certain scientific questions.

- The challenge of studying the possible occurrence of other complex patterns in underground gas storage, as standing waves, spiral waves, twinkling patterns and if so, proving there existence in real gas reservoirs

- Including other bacterial behaviors that can affect microbial activities such as bacterial swimming motility, chemotaxis, cell death by necrosis, autophagic cell death and apoptosis or programmed cells suicide.

- Another problem, is to include the impact of biocorrosion process on microbial activities and gas conversion.

- Geological model of a real gas reservoir has to be considered and implemented in our code. It would be interesting to perform tests on more realistic cases to test the robustness of the numerical code

BIBLIOGRAPHY

- Abu-Al-Saud, M.O., Esmaeilzadeh, S., Riaz, A., Tchelepi, A.: Pore-scale study of water salinity effect on thin-film stability for a moving oil droplet. Journal of colloid and interface science. 569 (1): 366-377 (2020).

- Adrienne, P., Ellen, L., Joachim, E., Richard, E., Mitchell A., Robin, G., Alfred C., Lee, S.: Potential CO2 Leakage Reduction through Biofilm-Induced Calcium Carbonate Precipitation. Environ. Sci. Technol. 47: 142−149 (2013).

- Ahusborde, E., Amaziane, B., El Ossmani, M.: Numerical modeling of coupled two-phase multicomponent flow with reactive geochemical transport in porous media. Procs JEMP2016 Conference. (2016).

- Amundsen, A., Microbial Enhanced Oil Recovery: Modeling and Numerical Simulations (Ph.D. Thesis). Norwegian University of Science and Technology. (2015).

- Baveye, P., Vandevivere, P., Hoyle, B.L., DeLeo, P.C., Sanchez de Lozada, D.: Environmental impact and mechanisms of the biological clogging of saturated soils and aquifer materials. Crit. Rev. Environ. Sci. Technol. 28 (2): 123-191 (1998)

- Botteroa, S., Storcka T., Heimovaarab, J., Loosdrechta, M., Enzienc, M. V., Picioreanua, N.: Biofilm development and the dynamics of preferential flow paths in porous media. Biofouling. 29 (9): 1069-1086 (2013).

- Bourgeat, A., Panfilov, M.: Effective two-phase flow through highly heterogeneous porous media: Capillary nonequilibrium effects. Computational Geosciences. 191–215 (1998).

- Brovelli., A., Malaguerra., F., Barry., D.A.: Bioclogging in porous media: Model development and sensitivity to initial conditions. Environmental Modelling & Software. 24: 611-626 (2009).

- Buzek, F., Onderka, V., Vancura, P., Wolf., I.: Carbon isotope study of methane production in a town gas storage reservoir. Fuel. 73(5):747– 752, (1994).

- Carden, P.O., Paterson, L.: Physical, chemical and energy aspects of underground hydrogen storage. International Journal of Hydrogen Energy. 4(6):559–569, (1979).

- Cartwright, J.: Labyrinthine Turing pattern formation in the cerebral cortex. Journal of theoretical biology. 217 1: 97-103 (2002).

- Chen, Z.: Reservoir Simulation: Mathematical Techniques in Oil Recovery. SIAM. 77 (2007)

- COMSOL Multiphysics. https://www.comsol.de/.

- Cunningham, A. B., Characklis, W. G., Abedeen, F., Crawford, D.: Influence of biofilm accumulation on porous media hydrodynamics. Environ Sci Technol. 25: 1305–1311 (1991)

- Dagle, R. A., Dagle, Vanessa, Bearden, Mark D., Holladay, Jamelyn D., Krause, Theodore R., and Ahmed, Shabbir. An Overview of Natural Gas Conversion Technologies for Co-Production of Hydrogen and Value-Added Solid Carbon Products. United States: N. p., (2017). doi:10.2172/1411934

- Ebigbo, A., Golfier, F., Quintard , M. : A coupled, pore-scale model for methanogenic Microbial activity in underground hydrogen storage. Advances in Water Resources. 61:74–85, 2013.

- Ebrahimiyekta, A.: Characterization of geochemical interactions and migration of hydrogen in sandstone sedimentary formations : application to geological storage(Ph.D. Thesis). Université d'Orléans. (2017).

- Egya, D. O., Geiger, S., P. Corbett, W. M., March, R,., Bisdom, K., Bertotti, G., Bezerra, F. H.: Analysing the limitations of the dual-porosity response during well tests in naturally fractured reservoirs. Petroleum Geoscience. 25 (1): 30–49 (2019).

- Feldmann, F., Hagemann, B., Ganzer, L., Panfilov M.: Numerical simulation of hydrodynamic and gas mixing processes in underground hydrogen storages. Environmental Earth Sciences. 75(16):1165 (2016).

- Garretta, T., Manmohan, B., Zhibing, Z.: Bacterial adhesion and biofilms on surfaces. Progress in Natural Science. 18: 1049–1056 (2008).

- Hagemann, B.: Numerical and analytical modeling of gas mixing and bio-reactive transport during underground hydrogen storage (Ph.D. Thesis). Université de Lorraine and Clausthal University of Technology. (2017).

- Hagemann, B., Rasoulzadeh, M., Panfilov, M., Ganzer, L., and Reitenbach, V. Hydrogenization of underground storage of natural gas: impact of hydrogen on the hydrodynamic and bio-chemical behaviour. Computational Geosciences. (2015).

- Hagemann, B., Rasoulzadeh, M., Panfilov, M., Ganzer, L., Reitenbach, V.: Mathematical modeling of unstable transport in underground hydrogen storage. Environmental Earth Sciences.73 6891–6898 (2015)

- Ham, Y. J., Kim, S. B., Park, S. J.: Numerical Experiments For Bioclogging In Porous Media, Environmental Technology. 28: 1079-1089 (2007).

- Ide Y., Izuhara H., Machida T. Turing instability in Reaction-Diffusion models on complex networks. Physica A: Statistical mechanics and its applications. 457(1): 331 – 347 (2016).

- Kirk, E. N., Timothy, P. G.: New collector efficiency equation for colloid filtration in both natural and engineered flow conditions. Water resources research. 47 (5), (2011)

– Koch, T., Gläser, D., Weishaupt, K., et al.: DuMux 3 – an open-source simulator for solving flow and transport problems in porous media with a focus on model coupling. Computers and Mathematics with Applications. (2020)

– Flemisch, B., Darcis, M., Erbertseder, K., Faigle, B., Lauser, A., Mosthaf, K., Müthing, S., Nuske, P., Tatomir, A., Wolff, M. and R. Helmig: DuMux : DUNE for Multi-{Phase, Component, Scale, Physics, …} Flow and Transport in Porous Media. Advances in Water Resources. (2011)

– Kolmogorov A., Petrovskii I., and Piskunov N. A study of the diffusion equation with increase in the amount of substance, and its application to a biological problem. Moscow Univ Bull.Math-Mech, 1, 1 - 25, (1937).

– Kuan-Mu, Y., Mohammad T. H., Charles, R. O.: Water and Waste Water Filtration: Concepts and Applications. Environmental Science & Technology. 5 (11): 1105-1112 (1971).

– Martin, T., Josef, Z., Wolfgang, K.: Influence of Microbial Growth on Hydraulic Properties of Pore Networks. Transport in Porous Media. 49: 99–122 (2002).

– Murray, J.D.: Mathematical biology. Sringer-Verlag, Berlin Heidelberg. (1993).

– Painter, K.J, Maini, P.K. Othmer, H.G.: Chemotactic response to multiple signaling cues. J. Math. Biol., 41, 285-314 120, (2000) https://link.springer.com/ article/10.1007/ s002850000035

– Panfilov, M.: Physicochemcial fluid dynamics in porous media (Application in geosciences and petroleum engineering). Willey-VCH. (2019).

– Panfilov, M.: Underground storage of hydrogen: in situ self-organisation and methane generation. Transport in Porous Media. 85: 841-865 (2010).

– Panfilov, M.: Theory and Applications of Transport in Porous Media. Kluwer Academic Publishers. (2000).

- Panfilov, M., Reitenbach, V., Ganzer, L.: Self-organization and shock waves in Underground Methanation Reactors and Hydrogen Storages. Environmental Earth Sciences. 75 (4): 1-12 (2016).

- Panfilov, M., Rasoulzadeh, M.: Appearance of the nonlinearity from the nonlocality in diffusion through multiscale fractured porous media. Computational Geosciences. 17:269–286 (2013).

- Panfilov M., Zaleski S., and Josserand Ch. Mechanisms of formation of natural hydrogen reservoirs in thermal aquifers: impact of methanogen bacteria and the non-equilibrium of gas bubble dynamics. Proces. ECMOR XV – 15th European Conference on the Mathematics of Oil Recovery, Amsterdam, (2016).

- Roy, S., Ghosh, S., Bhowmick, N.: Application of Colloidal Filtration Theory on Textile Fibrous Media: Effect of Fiber Orientation on Bacterial Removal Efficiency and Attachment. *Journal of The Institution of Engineers.* (2018)

- Saiers, J. E., Ryan, J. N.: Colloid deposition on non-ideal porous media: The influences of collector shape and roughness on the single-collector efficiency. Geophysicl Research Letters. 32 (21), (2005) https://doi.org/10.1029/2005GL024343.

- Schnakenberg J.: Simple chemical reaction systems with limit cycle behaviour. J. Theor. Biol. 81(3): 389 – 400 (1979).

- Sidsel, M. N.: Microbial plugging: Microbial Enhanced Oil Recovery – Advanced Reservoir Simulation. (Ph.D. Thesis). Technical University of Denmark. (2010).

- Stoodley, P., Cargo, R., Rupp, C. J., Wilson, S., Klapper, L.: Biofilm material properties as related to shear-induced deformation and detachment phenomena. Journal of Industrial Microbiology and Biotechnology. 29: 361–367 (2002).

- Strobel, G., Hagemann, B., Martins, T., Ganzer, L.: Underground bio-methanation: Concept and potential. *Renewable and Sustainable Energy Reviews.* (2020).

- Turing, A.M.: The chemical basis of morphogenesis. Philos.Trans. R. Soc. London, Ser. B, B237: 37 – 72 (1952).

- Thomas, P., Cristian, P., Mark, L., Michael, J.: The effect of biofilm permeability on bioclogging of porous media. Biotechnology and bioengineering. 109: 1031-1042 (2011).

- Thullner, M., Kinzelbach, W.: Influence of microbial growth on hydrailic properties of pore networks. Transport in porous media. 49: 99-122 (2002).

- Toleukhanov, A., Panfilov, M., Kaltayev, A.: Storage of hydrogenous gas mixture in geological formations: self-organisation in presence of chemotaxis. Int. J. Hydrogen Energy. (2015).

- Torkzaban, S., Brdford, S. A.: Critical role of surface roughness on colloid retention and release in porous media. Water Research. 88: 274-284 (2015).

- Tufenkji, N.: Modeling microbial transport in porous media: Traditional approaches and recent developments. Advances in Water Resources. 30:1455-1469 (2007).

- Updegraff, D. M.: "The effect of microorganisms on the permeability and porosity of petroleum reservoir rock," in Microbial Enhanced Oil Recovery, Zajic, J.E., Ed. Penn Well Book, Tulsa. 37–44 (1983).

- Yang, Y., Wu, Y., Lu, Y., Shi, M., Chen, W.: Microorganisms and their metabolic activities affect seepage through porous media in groundwater artificial recharge systems: A review. J. Hydrol. 598: 126-256 (2021).

- Zgang, L., Chao, X., Yaohao, G., Guangpu, Z., Shiyu, C., Wang, X., Jing, W., Sun, H., Yang, Y.,Yao, J.: The Effect of Surface Roughness on Immiscible Displacement Using Pore Scale Simulation. Transport Porous Media. (2021). DOI:10.1007/s11242-020-01526-6.

– Zivar, D., Kumar, S., Foroozesh, J.: Underground hydrogen storage: A comprehensive review. International Journal of Hydrogen Energy. 46(45) (2020).

ANNEXE A

Formation de patterns bio-réactifs dans un stockage souterrain de l'hydrogène : impact de l'hétérogénéité naturelle et induite

CHAPITRE I : Introduction au Stockage souterrain de l'hydrogène et patterns

Les émissions élevées de dioxyde de carbone et d'autres gaz à effet de serre (protoxyde d'azote N2O, hydrofluorocarbures HFC...) dans l'atmosphère ont fortement contribué au réchauffement climatique. La dernière conférence des Nations unies sur le changement climatique à Paris (COP21) s'est fixé un défi urgent de réduire les émissions de carbone de l'Union Européen de moitié d'ici 2030 et à zéro d'ici 2050. Conformément à l'objectif de l'UE, d'atteindre la neutralité climatique d'ici 2050, les secteurs énergétiques se tournent de plus en plus vers l'intégration des énergies électriques renouvelables. Toutefois, les ressources renouvelables sont de nature fluctuante et difficilement prévisible. Leur capacité de production provoque des surplus qui devraient être stockés pour éviter de les perdre. Le déploiement croissant des éoliens et des cellules photovoltaïques sur la surface du sol emmène à des quantités géantes de l'électricité produite excessivement, ce qui demande de grandes capacités de stockage. La conversion de l'électricité excessive en gaz (hydrogène) et son stockage sous forme de gaz dans des cavernes ou des strates géologiques poreux est la meilleure solution pour stocker de grandes quantités d'énergie.

La conversion de l'électricité renouvelable en hydrogène (Power – to Gaz) se fait, en effet, en séparant les molécules d'eau à l'aide d'électricité (électrolyse). Cet hydrogène, produit par la technique de l'électrolyse dépourvue de toute émission de gaz à effet de serre, est appelé « vert ». Le processus est réversible : la reconversion de H_2 en électricité (Power – to Gaz – to Power) se passe dans une pile à combustible, dans laquelle les électrons de H_2 se séparent des protons qui passent à travers une membrane imperméable pour les électrons, et les électrons libres

forment un courant électrique capable de produire un travail utile. Ces deux conversions ne produisent pratiquement pas de gaz à effet de serre.

La reconversion de H_2 en électricité n'est pas une seule possibilité. L'hydrogène produit peut également être converti en méthane en le faisant réagir avec le CO_2, le processus connu sous le nom de *méthanation.* On distingue deux types de ce processus. *La méthanation chimique* se passe à haute température (≈300°C) et en présence d'un catalyseur (le coût est ~ 400Euros/kW). La *bio-méthanation* est effectuée par des bactéries méthanogènes qui utilisent H_2 et CO_2 pour leur métabolisme et produisent du CH_4 et de l'eau. Elle se passe à basse température (35°C) et pression (90 bar) et coûte beaucoup moins cher que la méthanation chimique. La bio-méthanation peut être réalisée dans les strates géologiques (*in situ biomethanation*) où les conditions thermodynamiques sont favorables. Le concept de la biométhanation in situ a été introduit en premier dans (Panfilov 2010, Panfilov et al. 2016).

La biométhanation in situ était observée dans le stockage du gaz de ville à Lobodice, situé dans le bassin de la vallée de Hornomoravsky, en République Tchèque. Outre la variation de la composition du gaz stocké dans le temps, qui était en accord avec la réaction de bio-méthanation, on observait le phénomène de formation des zones spatiales sursaturées en hydrogène, et autres zones sursaturées en méthane. Ces structures représentent des *patterns* qui sont typiques pour des systèmes de réaction-diffusion et sont souvent observées dans les processus accompagnés par une activité de microorganismes.

La première analyse mathématique des patterns biologiques a été réalisée par le mathématicien et informaticien britannique A. M. Turing. En 1952, A. M. Turing a publié son article intitulé : "*The chemical bases of morphogenesis*", dans lequel il démontrait que la compétition entre la réaction et la diffusion peut générer des solutions oscillatoires complexes, une distribution spatiale périodique de la concentration de la morphogenèse qui rompt la symétrie du système. A l'époque, cette idée a suscité peu d'intérêt car elle reposait sur un paradoxe apparent puisque la diffusion devrait effacer les fluctuations et homogénéiser le système. Aujourd'hui, il existe des preuves qualitatives de la capacité des modèles de Turing à imiter l'auto-organisation biologique (V. K. Vanag 2004, Baba Issa Camara et al. 2009).

Les patterns semblent présenter un intérêt particulier non seulement en biologie (Stripes, spots, or reversed spots in two-dimensional Turing systems, H. Shoji et al 2003) et en chimie

pure/appliquée (chlorine dioxide-iodine-malonic acid reaction-diffusion system, D. Feldman et al. 2012 ; Belousov-Zhabotinsky reaction in liquid marbles, C. Fullarton et al. 2019), mais aussi en géomorphologie (Pattern formation in the geosciences, Lucas Goehring 2004), en écologie (Dispersal-induced destabilization of metapopulations and oscillatory Turing patterns in ecological networks, S. Hata et al. 2014), dans la sociologie comme des prédicteurs des points chauds de la criminalité (Dispersal-induced destabilization of metapopulations and oscillatory Turing patterns in ecological networks, S. Hata et al. 2014) et même un mécanisme de réaction-diffusion a été suggéré pour l'étude de l'origine des galaxies spirales en astrophysique.

L'étude des modèles biochimiques dans les systèmes de réaction-diffusion a suscité un intérêt considérable dans un large domaine d'applications, mais elle est encore moins étudiée dans les processus de stockage des gaz souterrains.

CHAPTER II : MODÉLISATION DU TRANSPORT BIPHASIQUE BIO-RÉACTIF DANS UN STOCKAGE SOUTERRAIN DE L'HYDROGÈNE

L'analyse que nous avons effectuée pour les processus de transport bio-réactif dans un stockage souterrain de H_2 démontre l'apparition de plusieurs types de patterns dans un tel système : un pattern stable en espace et stationnaire dans le temps, un pattern uniforme en espace, mais oscillant périodiquement et sans cesse dans le temps, un pattern oscillant dans l'espace et dans le temps simultanément. L'existence de telles structures signifie une hétérogénéité spatiale de l'hydrogène et du méthane, ce qui signifie que la méthanation ne couvre pas régulièrement le volume entier du stockage. Si l'objectif est de produire du méthane, alors la conversion ne sera pas complète. Si l'objectif est de stocker H_2 et le convertir ensuite en électricité, les patterns sont un phénomène plutôt positif si on peut augmenter la taille des zones occupées par H_2.

Ainsi, les critères d'existence de patterns est un problème important pour l'industrie, et pas uniquement purement théorique.

Pour convertir tout l'hydrogène en méthane, le rapport H_2/CO_2 dans la composition du gaz injecté devrait correspondre aux coefficients stœchiométriques de la réaction de méthanation. Un tel rapport devrait être maintenu uniformément dans tout le réservoir. Ce serait le meilleur scénario, qui garantirait une haute qualité du gaz produit. L'apparition de patterns pourrait réduire l'efficacité du processus de méthanation. Afin d'éviter leur apparition, nous avons effectué une analyse mathématique et numérique qui nous a permis de détecter les critères de leur apparition.

Un des problèmes les plus intéressants dans la théorie de patterns est l'existence de patterns spatio-temporels, qui représentent des fluctuations périodiques dans le temps et des mosaïques périodiques en espace simultanément. Notre recherche était focalisée essentiellement sur ce problème.

Le point central de la thèse était consacré à l'impact de l'hétérogénéité du milieu sur les patterns. Nous avons analysé un milieu de double porosité décrit par un modèle macroscopique dans lequel les fractures et les blocs sont deux continuums coexistant qui s'échangent de masse des fluides et des bactéries. Les échanges étaient décrits par le modèle de Barenblatt. Le paramètre d'échange (*the exchange rate*) joue le rôle d'un paramètre responsable pour l'hétérogénéité du milieu : si le milieu est homogène, ce paramètre s'annule. L'interaction de l'hétérogénéité du milieu est des

mosaïques causées par les phénomènes de réaction-diffusion est non triviale et peu étudiée dans la littérature. Nous avons trouvé un effet suivant.

Dans un système de double porosité classique, juste la diffusion sans réactions, son comportement après une perturbation initiale est tel qu'il tend vers un système homogène. Les concentrations dans les fractures et les blocs tendent vers une seule valeur limite. Si on rajoute une bio-réaction, alors il existe plusieurs possibilités. Une d'elles est la création d'un pattern identique ou les deux concentrations ; le système tend donc vers un système homogène, comme dans le cas classique. En même temps, il existe une autre solution qui ne tends plus vers un système homogène. Les concentrations dans les fractures et les blocks forment deux patterns différents. Nous avons trouvé les critères exacts d'existence de toutes ces structures.

Le milieu de double porosité à l'échelle non macroscopique était étudié numériquement. Nous avons montré l'apparition d'autres patterns qui ne peuvent pas être capturés dans le modèle macroscopique : ce sont des flaches de concentration qui apparaissent et disparaissent instantanément en courant à travers tout le domaine de façon très chaotique (*travelling flashes*).

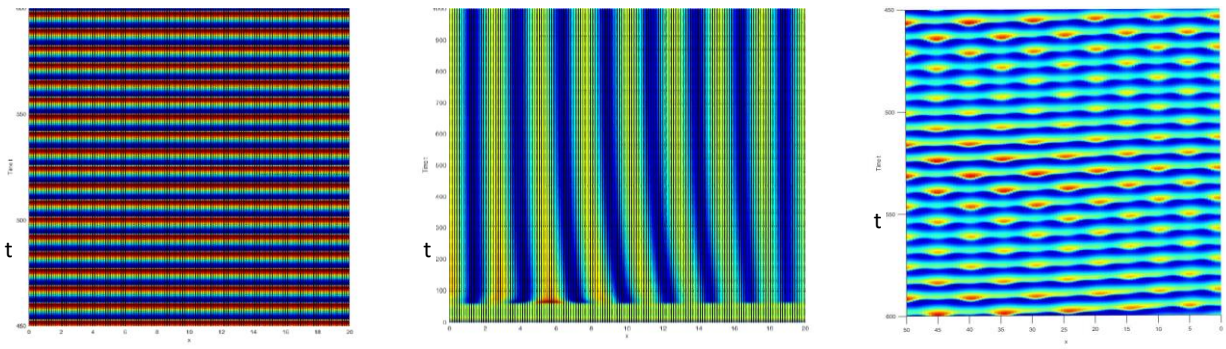

Fig. A.1. Représentation spatio-temporelle des Patterns de Hopf-Andronov (a), Turing (b) et Hopf Turing (c) dans un problème de réaction diffusion (milieu homogène)

x x x

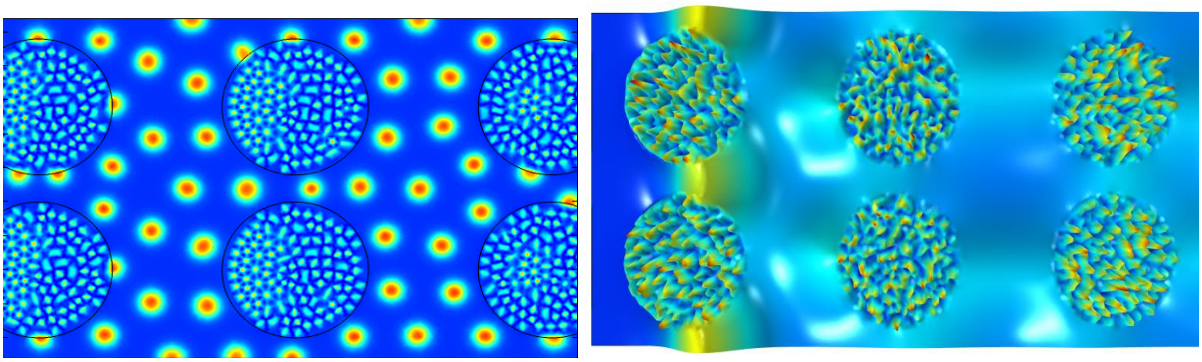

(a) (b)

Figure A.2 Synchronous (a) Turing pattern and (b) Jumping waves pattern in the non-homogenized double porous medium

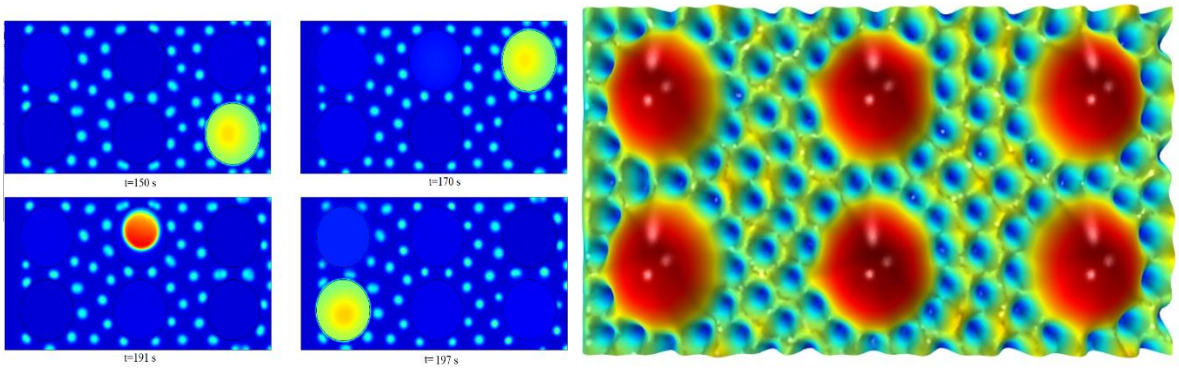

Figure A.3 Asynchronous pattern: (1) traveling flashes / Turing and (b)Turing in the fractures and stable regime in the non-homogenized double porous medium

CHAPITRE III : ANALYSE NUMÉRIQUE DU MODÈLE DE TRANSPORT DE GAZ AVEC BIORÉACTIONS ET BIOCLOGGING DES PORES

Dans ce dernier chapitre, nous avons analysé l'impact d'une hétérogénéité du milieu induite par des bactéries sur le transport de l'hydrogène dans un stockage souterrain d'hydrogène. Une telle hétérogénéité peut être créée par la croissance de la population microbienne, l'attachement des microbes aux paroi des pores, le colmatage des pores, et la réduction de la porosité et perméabilité du milieu. Cela se passent uniquement dans des zones peuplées par les bactéries, et dans les directions de leur propagation, ce qui provoque aussi une anisotropie induite.

Dans ce contexte, nous avons développé un modèle conceptuel de bio colmatage, qui décrit la dynamique des bactéries couplée ou transport hydrodynamique des constituant chimiques participants dans le stockage.

1. Governing equations for in-situ underground biomethanation processes with bio-clogging

Les hypothèses retenues dans la présente étude sont les suivantes : (a) Le réservoir est homogène. (a) Les mécanismes de transport sont l'advection, la diffusion et la gravité.

Introduisons l'ensemble des notations suivantes :

- ϕ - porosité du réservoir $[-]$
- ϕ_0 - porosité du réservoir propre sans bactéries $[-]$
- $\alpha = w, g$ - phase = liquide, gaz
- k - composants chimique (H_2, CO_2, CH_4, H_2O)
- n_d et n_a - fractions volumiques des microorganismes mobiles et fixes (biofilm) $\left[cell / m^3\right]$
- n_c - nombre de cellules microbiennes nécessaires pour boucher $1m^3$ de volume de pores (paramètre empirique) $\left[cell / m^3\right]$
- c_α^k - fraction molaire du composant k dans la phase α $[-]$
- S_α - saturation de phase $[-]$
- V_α - vitesse moyenne dans la phase α $[m / s]$
- $\mathbf{g}$ - vecteur gravité $\left[m / s^2\right]$
- K - permeabilité absolue $\left[m^2\right]$
- K_0 - permeabilité du réservoir propre sans bactéries $\left[m^2\right]$
- $k_{r\alpha}$ - permeability relative de la phase α $[-]$
- p_α - pression de la phase α $[Pa]$
- p_c - pression capillaire $[Pa]$
- ρ_α - densité molaire de la phase α $\left[mol / m^3\right]$
- $\rho_{\alpha,mass}$ - densité massique de la phase α $\left[kg / m^3\right]$
- μ_α - viscosité dynamique de la phase α $[Pa.s]$
- D_b - diffusion des bactéries $\left[m^2 / s\right]$
- D_α^k - diffusion moléculaire du component k dans la phase α $\left[m^2 / s\right]$

- ψ^{gr} , ψ^{dec} - taux de croissance et décès des bactéries par unité d'une bactérie $\left[s^{-1}\right]$
- ω^{k} - taux de production et de consommation du composant k
- t^{dec} - temps caractéristique de décès $[s]$
- t^{gr} - temps caractéristique de croissance $[s]$
- k_a - taux d'attachement par unité de bactérie $\left[s^{-1}\right]$
- k_d - taux de détachement par unité de $\left[s^{-1}\right]$
- d_p - diamètre des pores $[m]$
- d_b - diamètre moyen de bactérie $[m]$
- η - efficacité de l'attachement
- α_{eff} - probabilité d'attachement après une collision $[-]$
- k_b - constante de Boltzmann $\left[J.K^{-1}\right]$
- T – température $[K]$
- γ^{k} - coefficient stœchiométrique du composant k
- Y - rapport entre la croissance de la biomasse et la consommation de nutriments.

Équations de conservation pour le transport bactérien

Les équations de conservation des bactéries fixes et immobiles contiennent la croissance des populations mobiles et fixes (I et V respectivement), la décroissance de la population (II et VI), l'attachement des bactéries aux parois des pores (III) et le détachement des bactéries (IV).

$$\frac{\partial}{\partial t}\left(\phi\left(n_a,n_d\right)S_w n_d\right)+\nabla\cdot\left(n_d\mathbf{V}_w\right)-\nabla\cdot\left(D_b S_w\nabla n_d\right)=\underbrace{\psi^{gr}S_w n_d}_{\text{I}}-\underbrace{\psi^{dec}S_w n_d}_{\text{II}}-\underbrace{k_a S_w n_d}_{\text{III}}+\underbrace{k_d S_w n_a}_{\text{IV}} \quad \text{Eq. A.1}$$

$$\frac{\partial}{\partial t}\left(\phi\left(n_a,n_d\right)S_w n_a\right)=\underbrace{\psi^{gr}S_w n_a}_{\text{V}}-\underbrace{\psi^{dec}S_w n_a}_{\text{VI}}+\underbrace{k_a S_w n_d}_{\text{III}}-\underbrace{k_d S_w n_a}_{\text{IV}} \quad \text{Eq. A.2}$$

Équation de conservation pour le transport des composants dans un écoulement diphasique

Pour le transport de quatre composants chimiques (H_2O, H_2, CH_4, CO_2) dans un écoulement à deux phases (gaz et eau), l'équation de conservation peut être écrite comme suit :

$$\sum_{\alpha=w,g}\left\{\frac{\partial}{\partial t}\left(\phi\left(n_a,n_d\right)\rho_\alpha S_\alpha c_\alpha^k\right)+\nabla\cdot\left(\rho_\alpha c_\alpha^k\mathbf{V}_\alpha\right)-\nabla\cdot\left(\rho_\alpha D_\alpha^k\phi\left(n_a,n_d\right)\nabla c_\alpha^k\right)\right\}=\underbrace{\phi\left(n_a,n_d\right)\rho_w S\omega^k}_{\text{VII}} \quad \text{Eq. A.3}$$

VII correspond au taux de production ou de consommation du composant k.

L'équation du bilan de quantité de mouvement est réduite à la loi de Darcy pour deux phases :

$$\mathbf{V}_w = -\mathbf{K}\ n_a, n_d\ \frac{k_{rw}(S_w)}{\mu_w}\ \nabla P_w - \rho_w^* \mathbf{g}$$
$$\mathbf{V}_g = -\mathbf{K}\ n_a, n_d\ \frac{k_{rg}(S_w)}{\mu_g}\ \nabla P_g - \rho_g^* \mathbf{g} \qquad \text{Eq. A.4}$$

Le modèle empirique le plus utilisé pour le calcul des perméabilités relatives est celui de Brooks Corey (1964) :

$$k_{rw} = \left(\frac{S_w - S_{wr}}{1 - S_{wr} - S_{gr}}\right)^{\frac{2+3\lambda}{\lambda}},\ k_{rg} = \left[1 - \left(\frac{S_w - S_{wr}}{1 - S_{wr} - S_{gr}}\right)\right]^2 \left[1 - \left(\frac{S_w - S_{wr}}{1 - S_{wr} - S_{gr}}\right)^{\frac{2+\lambda}{\lambda}}\right], \qquad \text{Eq. A.5}$$

La perméabilité relative apparaît quand l'écoulement d'une phase devient perturbé par l'autre phase, du fait que l'espace des pores où la phase fluide peut s'écouler est partiellement ou totalement occupé par l'autre phase.

L'expression de P_c tient compte de la variation de la pression capillaire par effet de colmatage des pores.

$$p_c = p_g - p_w = \sigma \cos\theta \sqrt{\frac{\phi(n_a, n_d)}{K(n_a, n_d)}} \left(\frac{S_w - S_{wr}}{1 - S_{wr} - S_{gr}}\right)^{-\frac{1}{\lambda}} \qquad \text{Eq. A.6}$$

où $\lambda, m, P_{end}, S_{wr} \sim S_{gr} \sim 0.2$ sont des paramètres empiriques; σ est la tension superficielle à l'interface gaz-eau, θ est l'angle de contact pour le système gaz-eau-solide (≈ 30°).

L'échange de masse entre les phases est très rapide par rapport aux autres processus biochimiques, donc la composition des deux phases est supposée être en équilibre thermodynamique. Cette hypothèse est largement utilisée dans les processus géochimiques et les simulations pétrolières (Birger Hagemann 2017). La condition d'équilibre thermodynamique entre les deux phases peut être exprimée par l'égalité des fugacités :

$$f_g^k\left(P_g, c_g^1, ..., c_g^n\right) = f_w^k\left(P_w, c_w^1, ..., c_w^n\right) \quad \text{Eq. A.7}$$

croissance et la décroissance

La croissance et la décroissance microbienne sont deux processus fondamentaux dans la modélisation du transport microbien dans les milieux poreux. Pour les bactéries méthanogènes que nous étudions dans ce travail, la croissance de la population dépend directement de la consommation du carbone contenu dans le CO_2 (l'azote, le phosphore, le soufre et d'autres éléments sont également consommés, mais en quantités beaucoup plus faibles). De plus, les bactéries consomment du H_2 pour leur respiration, qui est un processus d'oxydo-réduction qui apporte de l'énergie aux bactéries.

Par conséquent, le taux de nutrition peut être considéré proportionnel aux concentrations de CO_2 et H_2 dans le fluide environnant (Panfilov, 2019). Si l'on tient compte du fait que le taux de croissance se calme avec l'abondance de CO_2 et de H_2, on obtient la loi de Monod multiplicative (Monod 1949, Taylor et Jaffe 1990) :

$$\psi^{gr} = \frac{1}{t^{gr}} \frac{c_w^{H_2}}{\left(\alpha^{H_2} + c_w^{H_2}\right)} \frac{c_w^{CO_2}}{\left(\alpha^{CO_2} + c_w^{CO_2}\right)} \quad \text{Eq. A.8}$$

En parallèle à sa croissance, une population bactérienne peut se dégrader, ce qui est principalement causé par des micro-organismes-prédateurs. La décroissance dépend de la concentration de prédateurs, qui, à son tour, augmente en raison de la présence de proies. Par conséquent, le taux de décès est une fonction de la concentration de bactéries méthanogènes (Panfilov, 2019).

$$\psi_j^{dec} = \frac{1}{t^{dec}} n_j^{\beta-1} \quad \text{Eq. A.9}$$

Fixation des bactéries aux parois des pores

Des revues sur l'adhésion microbienne aux parois des pores sont donnés dans (Timothy D. Scheibe et al. 2006, Nathalie Tufenkji et al. 2006, Ian L. Molnar et al. 2015). Il a été constaté que le principal facteur affectant l'adhésion des bactéries à une surface solide est la vitesse

d'écoulement du fluide environnant, dont l'augmentation peut rompre le lien entre les bactéries et la surface.

Pour construire le modèle du processus d'adhésion des bactéries aux parois des pores, nous avons fait recours à la théorie classique de la filtration des colloïdes (Cunningham et al., 1991 ; Tufenkji et al., 2005 ; Mitchell et al., 2010 ; Sukumar Roy et al., 2018). Une bactérie adhère en deux étapes : d'abord, elle entre en collision ou touche la paroi solide, après la bactérie sécrète un liquide collant lui permettant de se fixer à la surface du pore. La collision avec la paroi serait impossible si les bactéries, transportées par le liquide, se déplaçaient strictement le long d'une ligne de courant, puisque les lignes de courant ne touchent pas les parois.

Mais trois mécanismes différents font dévier les bactéries de la ligne de courant et rendent les collisions possibles :

(1) les fluctuations chaotiques dans le mouvement des bactéries, similaires à la marche brownienne,

(2) l'interception géométrique de la cellule : si la ligne de courant, le long de laquelle la bactérie se déplace, passe très près de la paroi, alors la bactérie peut entrer en collision avec la paroi ;

(3) l'interception inertielle : selon l'effet centrifuge, lorsque la particule est plus lourde que le liquide, la force d'inertie a tendance à l'écarter de la ligne de courant incurvée et la force à se déplacer le long d'une ligne droite, (B.G. Miller et al., 2017, R. M. Wheatley et al., 2018).

Par conséquent, le taux d'attachement [1/s] peut être décrit par les relations suivantes tirées de (Nathalie Tufenkji et al. 2006) :

$$R_a = k_a b_{\mathrm{m}}, \qquad k_a = \frac{3\alpha_{\mathrm{eff}}(1-\phi)|V_w|}{2d_p}\left(0.9\left(\frac{k_b T}{\mu_w d_b d_p |V_w|}\right)^{\frac{2}{3}} + 1.5\left(\frac{d_b}{d_p}\right)^2 + \frac{(\rho_b-\rho_w) g {d_b}^2}{18\mu_w |V_w|}\right) \qquad \text{Eq. A.10}$$

Le terme d'interception due à l'inertie peut être négligé puisque la densité des bactéries, constituées à près de 90% d'eau, est pratiquement identique à celle de l'eau.

Notons que les bactéries ne se fixent pas les unes aux autres, car elles disposent d'un mécanisme physiologique (flagelles) qui les empêche d'entrer en collision les unes avec les autres.

Détachement des bactéries de la surface des pores :

Le détachement du biofilm de la surface solide pourrait être déterminé par la relation entre la force adhésive et la contrainte de cisaillement causée par l'écoulement tangentiel du fluide environnant (Stoodley et al. 2001, Rittmann 1982). Ici, le coefficient de vitesse de détachement microbien est une fonction exponentielle de l'ampleur de l'écoulement de la phase aqueuse, comme indiqué par (Stoodley et al.2002) :

$$k_{\text{det}} = \begin{cases} k_d^{\max} e^{-\frac{w^2}{1-w^2}} & ,V_w > V_c \quad ,\text{w}=\dfrac{V_w - V_m}{V_c - V_m} \\ 0, \quad V_w \le V_c \end{cases} \qquad \text{Eq. A.11}$$

Le modèle contient trois paramètres empiriques, la vitesse critique de détachement (en dessous de laquelle le détachement est impossible) V_c ; la vitesse maximale V_m à laquelle le taux de détachement se stabilise et le taux de détachement maximal $k_d^{\max}$ qui correspond à V_m . La vitesse critique dépend de la vitesse initiale de la fixation de la bactérie. V_{bg} .

Un autre modèle semi-empirique a été proposé par (Rittmann 1982) basé sur les caractéristiques physiques, la contrainte de cisaillement, la porosité du milieu et la surface spécifique. (Gerald E. Speitel et al. 1987) ont proposé qu'en plus des caractéristiques physiques, l'effet biologique soit également pris en compte pour le détachement du biofilm ; ceci par le biais du taux de croissance bactérienne. Des expériences ont prouvé que des taux de croissance élevés (c'est-à-dire un biofilm à croissance rapide) rendent le biofilm beaucoup plus susceptible de se détacher par rapport à un biofilm à croissance lente. (Gerald E. Speitel et al. 1987) ont proposé le modèle à deux termes suivant pour le taux de détachement du biofilm :

$$R_d = k_d b_{\text{f}}, \qquad k_d = k_{d1}\left[\frac{(1-\phi)^3}{{d_p}^2 \phi^3 A}\mu_w |V_w|\right]^{k_{d2}} + k_{d3}\psi^{\text{gr}} \qquad \text{Eq. A.12}$$

Le premier terme à gauche tient compte des forces externes exercées par l'écoulement sur la surface du biofilm, tandis que le second terme prend en compte le détachement dû à la croissance du biofilm.

Les paramètres empiriques k_{d1}, k_{d2} et k_{d3} dépendent du type de nutriments. Dans (Rittmann 1982) il a été obtenu expérimentalement : $k_{d1} = 2.29 \times 10^{-6}$ et $k_{d2} = 0.58$, et dans (Gerald E. Speitel et al. 1987) il a été établi $\bar{k}_{d3} = 0.042 - 0.089$.

Taux de biocontamination

Nous évaluons la réduction de l'espace des pores due à l'accumulation des bactéries aux pores. Les variations de perméabilité et de porosité dépendent de la fraction volumique des bactéries et peuvent être estimés en utilisant la fonction suivante (H. Y. Jeong et a. 2018):

$$\phi = \phi\left(n_a + n_d\right) = \frac{\phi_0}{1 + \left(\frac{n_a + n_d}{n_c}\right)^2} \qquad \text{Eq. A.13}$$

En utilisant la formule de Carman-Kozeny (Carman-Kozeny 1937), nous obtenons pour la perméabilité :

$$\frac{K\left(n_a, n_d\right)}{K_0} = \left(\frac{\phi\left(n_a, n_d\right)}{\phi_0}\right)^3 \left(\frac{1-\phi_0}{1-\phi\left(n_a, n_d\right)}\right)^2 \qquad \text{Eq. A.14}$$

Cette formule détermine la perméabilité relative définie comme le rapport entre la perméabilité modifiée et la perméabilité du milieu propre.

2. Simulations numériques

Le modèle mathématique présenté a été implémenté dans DuMuX. DuMuX est l'Abr. de Dune pour les processus d'écoulement et de transport Multi-{Phase, Component, scale, Physics,...} dans les milieux poreux. Il s'agit d'un outil de simulation des processus d'écoulement et de transport multi phasique et multi composant dans les milieux poreux, développé à l'Université de Stuttgart (Timo Koch et al. 2021). Basé sur DUNE, l'Abr. de Distributed and Unified Numerics Environment, qui est un software scientifique open access écrit en C++ pour la résolution des équations différentielles partielles (EDP). DuMuX comprend plusieurs modèles de complexité multiple : de l'écoulement monophasé isotherme stationnaire aux processus d'écoulement

complexe multiphasique non isotherme instable et avec des milieux poreux complexes déformables.

Nous avons utilisé un modèle d'écoulement multiphasique multi composant appelé 2pnc déjà implémenté dans DuMuX et nous avons développé notre propre module couplé étendu que nous avons appelé 2pnc2b qui incorpore le transport bio-réactif, les processus d'attachment et de détachement, et le biocolmatage.

Les équations de conservation sont modélisées par des équations d'advection-diffusion-réaction qui sont des équations aux dérivées partielles de type parabolique. Les non-linéarités du problème viennent essentiellement des termes de réaction et du terme de colmatage inclus dans la fonction porosité et perméabilité. Pour ce type de problème, la résolution numérique repose le plus souvent sur une méthode entièrement implicite qui consiste à résoudre le problème global à chaque itération en temps. La discrétisation spatiale repose sur une approche volumes finis "Cell-centered". On utilise le maillage non structuré ALUGRID composée de 9600 cellules et 19602 points. Le système non linéaire est résolu par la méthode Newton-Raphson avec un pas de temps adaptatif. Le test de convergence est effectué en comparant les variables primaires du problème pour la même étape de calcul avant et après de chaque itération. Si une réduction résiduelle est obtenue, la solution est écrite et l'étape d'itération suivante peut commencer. La simulation se termine lorsque le temps de simulation final est atteint.
Les mécanismes de (ré)attachement et de détachement, la croissance et le décès des bactéries sont ajoutés comme termes source/puits. Les valeurs de porosité et de perméabilité sont mises à jour lors de chaque itération.

L'apparition et la disparition possibles d'une phase ont été contrôlées par le processus de commutation des variables primaires, nous distinguons trois cas différents :

Le calcul a été effectué sur un PC Intel(R) Core(TM) i7-7600U CPU @ 2.80 GHz, 2901 MHz, 2 cœurs, 4 threads. Le temps CPU était estimé de ~90 h. Le temps de simulation était équivalent à 4 mois.

État de la phase	Variables primaires	commutation des variables
liquide uniquement	$p_w, X_w^{H_2}$	$\sum_k X_g^k > \left(X_g^k\right)^{\max}$: la phase gazeuse apparaît et $X_w^{H_2}$ switch à $X_g^{H_2O}$
gazeuse uniquement	$p_w, X_g^{H_2O}$	$\sum_k X_w^k > \left(X_w^k\right)^{\max}$: la phase liquide apparaît et $X_g^{H_2O}$ switch à $X_w^{H_2}$
Les deux phases existent	p_l, soit S_l ou S_g	If $S_l < S^{\min}$: la phase liquide disparaît S_l switch à $X_g^{H_2O}$ If $S_g < S^{\min}$: la phase liquide disparaît et S_l switch à $X_w^{H_2}$

Table A.1 - commutation des variables aux cours des phénomènes d'apparition et de disparition des phases : choix adéquat de la variable primaire

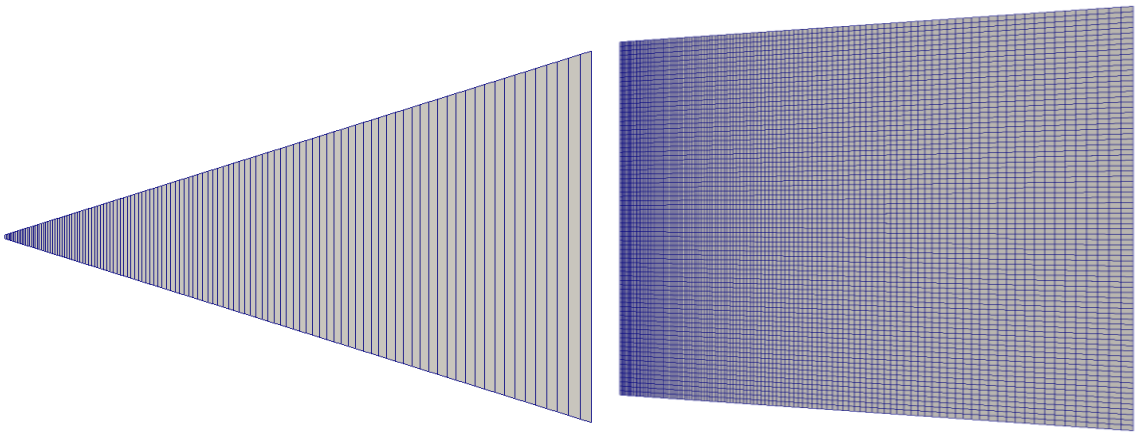

Figure A.4 maillage et domaine du reservoir

L'ensemble des variables primaires est: n_a, n_d, $c_g^{H_2}$, $c_g^{CO_2}$, P_w, et S_g.

Le domaine est un secteur radial 3D d'un cylindre de 100 m de longueur et 80 m de hauteur, représentant un aquifère situé à 1700 m sous le niveau du sol. L'axe vertical est le puits d'injection. Le rayon du puits est de 0,85 m. La température de l'aquifère est constante $T = 310\ °K$. Le domaine propre-poreux est homogène avec une porosité $\phi_0 = 0.34$ et une perméabilité absolue $K_0 = 5.10^{-12}\, m^2$. Les faces supérieure et inférieure sont imperméables. Le taux d'injection de l'hydrogène est quatre fois supérieur à celui du CO_2. Le gaz est injecté par le bas (dans le coin inférieur gauche), pour éviter l'effet de propagation latérale immédiate le long de la couverture du réservoir. Une population initiale de bactéries méthanogènes habite dans le

milieu global à des concentrations : $n_a^{(0)} = 9.10^6$ bactéries dans 1 m^3 et $n_d^{(0)} = 1.10^3$. Le réservoir est initialement entièrement saturé d'eau. Les fractions molaires initiales sont nulles, sauf pour l'eau $c_w^{H_2O} \approx 1$.

Évolution de la porosité et de la perméabilité causée par le bioclogging :

Les variations spatiales de la perméabilité et de la porosité sont présentées sur les Figures A.5-6. La réduction est plus significative près du puits d'injection. La zone la plus critique est proche de la région du puits de forage. Les résultats numériques montrent un bon accord qualitatif avec les résultats expérimentaux publiés par (Ham et al., 2007 et Brovelli et al, 2009). La diminution mesurée due au bioclogging est plus sévère dans la direction verticale. Cependant, la perméabilité minimale est de 0,058 D dans la direction verticale, tandis que dans la direction horizontale la perméabilité minimale est de 0,059 D. La longueur de la zone où la perméabilité est réduite est plus élevée dans la direction verticale (environ 50 m) que dans la direction horizontale (15 m). Dans la direction horizontale, le changement de porosité est minimal avec 0.19695, alors qu'il diminue dans la direction verticale à 0.1961 à une distance de 8 m du puits d'injection.

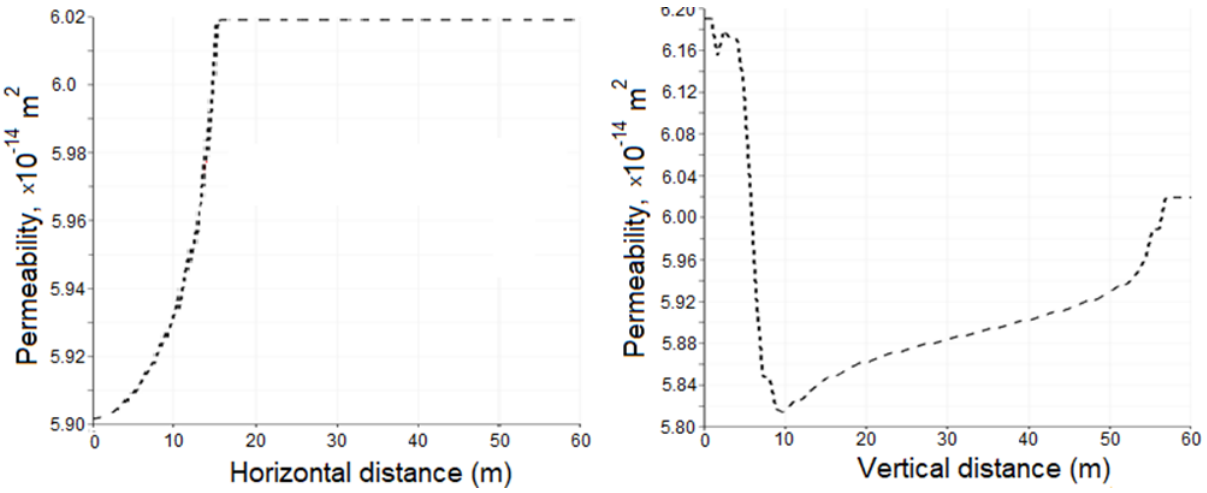

Figure A.5 Variation de la porosité dans l'espace dans les directions horizontale et verticale à partir du point d'injection, pour un même instant.

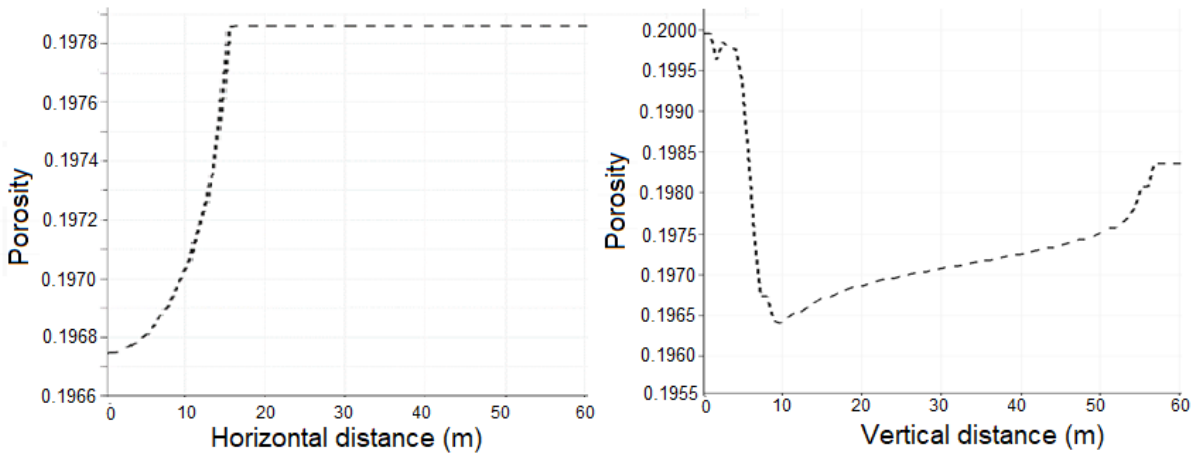

Figure A.6 Variation de la perméabilité absolue dans l'espace dans les directions horizontale et verticale à partir du point d'injection, pour un instant fixe

Impact du bioclogging sur la propagation du gaz :

L'hétérogénéité induite par bactéries joue le rôle très positif dans le transport du gaz. En effet, si on injecte un gaz dans un aquifère, ce gaz va vite remonter vers la surface en s'étalant sous forme d'une mince couche au-dessus de la structure géologique. Création donc d'un vrai stockage de gaz devient problématique. Dans le cas avec des bactéries, étant le plus actives le long des lignes de courant ascendantes du gaz, elles créent des bouchons sur les trajets verticaux, en forçant le gaz de se propager horizontalement. Ainsi, la propagation due l'hydrogène dans un réservoir devient plus régulière et couvre toute l'épaisseur du réservoir

Les Figures A.7-8 montrent l'évolution de la fraction molaire d'hydrogène et de la saturation en gaz dans la direction horizontale et verticale du réservoir dans le cas avec et sans bioclogging. D'après les deux figures, lorsque la perméabilité du milieu dans la direction verticale diminue, il devient plus difficile pour le gaz de remonter que de se propager horizontalement. Le bioclogging entrave la remontée verticale du gaz et conduit à privilégier la migration horizontale du gaz. De plus, le transport par advection est de plus en plus évident, ce qui augmente la migration horizontale. Ainsi, les bactéries jouent le rôle d'un régulateur capable d'assurer la propagation de l'hydrogène en profondeur dans le réservoir et de réduire sa remontée verticale vers la couverture.

On peut donc imaginer la technique d'injection de bactéries conjointement avec du H_2 et du CO_2, pour intensifier cet effet régulateur.

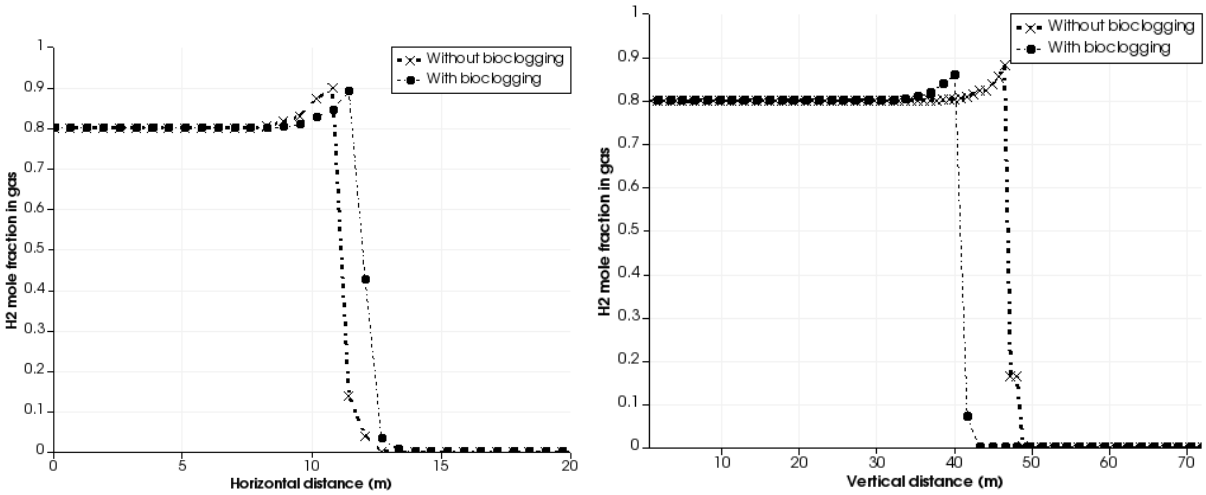

Figure A.7 Fraction molaire d'hydrogène dans la direction horizontale et verticale dans le cas du bioclogging et sans celui-ci (sans bactéries), au 16ème jour d'injection

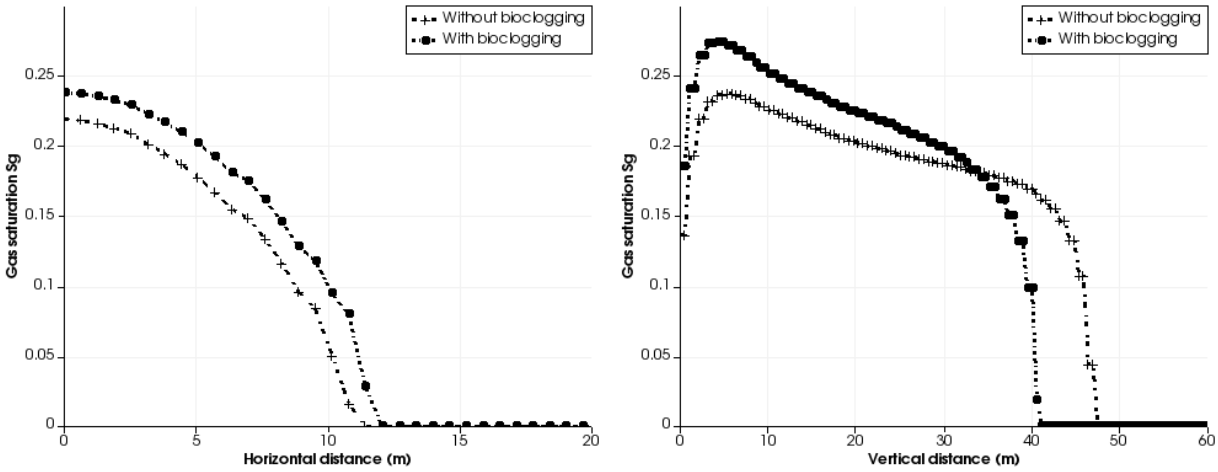

Figure A.8 Saturation en gaz dans la direction horizontale et verticale dans le cas du bioclogging et sans celui-ci (sans bactéries), pour le 16ème jour d'injection.

Colmatage simultané capillaire-bactérien

L'impact classique attendu de la pression capillaire est double : (i) elle devrait détruire les fronts de saturation aigus et les rendre plus lisses, et (ii) elle empêche le gaz de pénétrer dans un milieu saturé en eau si celui-ci est mouillé (effet de la pression d'entrée capillaire). Ces effets ont été bien observés dans nos simulations. En même temps, nous avons révélé un autre impact conjoint

important de la pression capillaire et du biocolmatage sur la propagation du gaz. Nous avons comparé les résultats obtenus pour deux cas de la pression capillaire moyenne initiale qui correspondent à une capillarité faible et forte, respectivement : $\hat{P}_c^0 = 0.1$ MPa et $\hat{P}_c^0 = 10$ MPa.

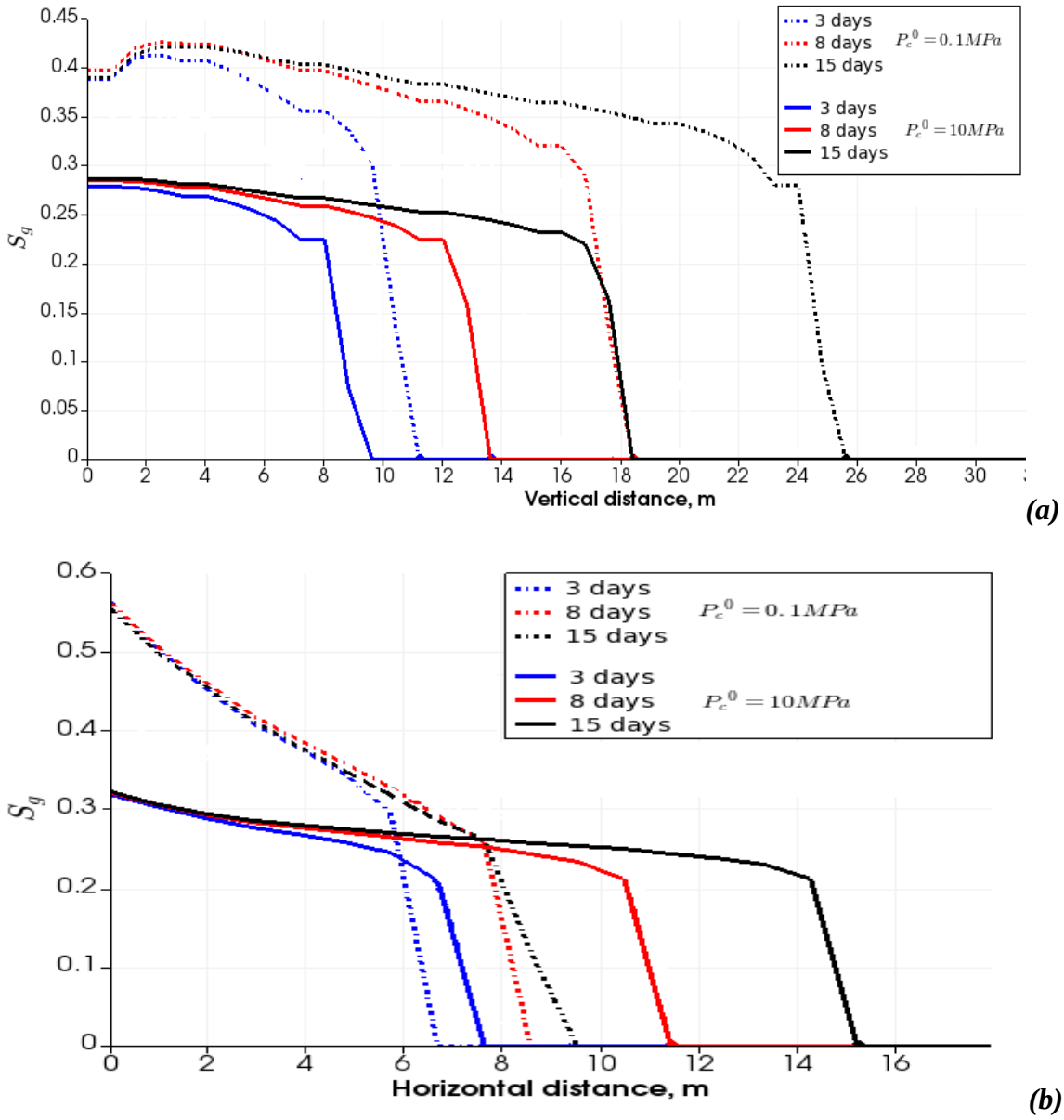

Figure A.9 Saturation en gaz dans la direction verticale (a) et dans la direction radiale (b) à une pression capillaire élevée et faible (les courbes en trait plein et en pointillé, respectivement), pour trois moments de temps

La figure montre la distribution spatiale de la saturation en gaz pour ces deux cas, respectivement le long des axes vertical et horizontal. Le cas de forte capillarité correspond aux courbes pleines. Comme on peut le voir, en raison de l'impact conjoint du bio-colmatage et de la capillarité, la

propagation du gaz dans la direction verticale est encore plus retardée, alors qu'elle est renforcée dans le plan horizontal. Ceci est dû au fait que la contre-action capillaire à la pénétration du gaz augmente dans la région de bio-colmatage, où la perméabilité est réduite et où la pression capillaire augmente. Par conséquent, l'action de barrière du long bouchon vertical formé par les bactéries est amplifiée par la contre-action capillaire, ce qui oblige le gaz injecté à se propager horizontalement. La forme de la zone saturée en gaz pour le même instant est représentée sur la

La figure suivante pour trois cas : sans bactéries, avec colmatage bactérien mais avec capillarité nulle, et pour un colmatage biologique en présence de capillarité. Comme on peut le voir, la forme de la zone occupée par le gaz devient de plus en plus uniforme dans toutes les directions. Afin de caractériser quantitativement l'influence des effets étudiés sur la propagation du gaz, nous avons introduit une vitesse planaire de propagation du gaz, définie comme le carré de la distance parcourue par le gaz au temps t, divisé par le temps t. Si l'écoulement du gaz était plan-radial et stationnaire, alors ce paramètre serait constant, ce qui explique la raison de son choix. Le tableau 6 illustre l'évolution de ce paramètre sous l'action du bio-colmatage et de l'impact conjoint du bio-colmatage et de la capillarité.

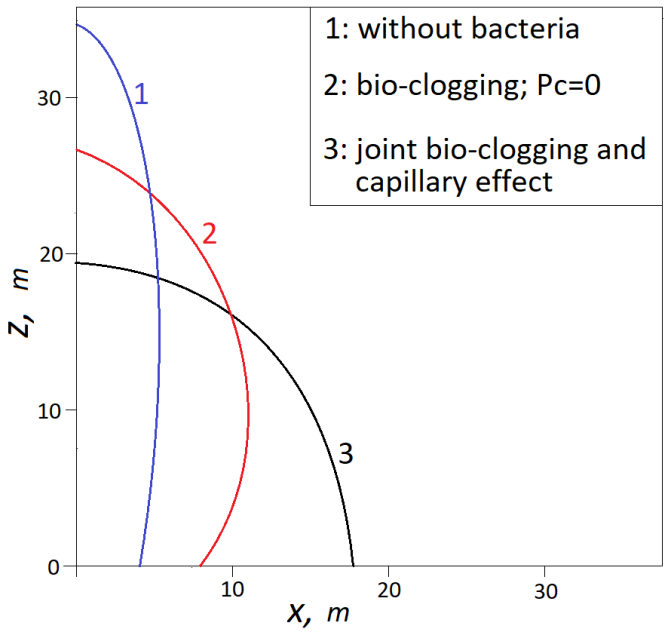

Figure A.10 Forme de la zone saturée en gaz dans trois cas : (1) sans bio-clogging P_c=0; (2) avec le bio-clogging et P_c=0; et (3) avec bio-clogging et avec une valeur non nulle de P_c

Impact du colmatage capillaire-bactérien sur la pression du réservoir :

Comme la capillarité empêche le gaz de circuler et réduit sa saturation, cela réduit la croissance et l'activité de la population. Par conséquent, cela réduit la région de bio-colmatage. La figure illustre l'effet de la réduction de la perméabilité causée par le bio-colmatage à une pression capillaire faible et élevée. On voit clairement que la pression capillaire réduit la région obstruée dans les deux sens. Si le volume occupé par le gaz diminue, la pression du gaz doit diminuer. Ceci a été observé dans nos simulations. Dans la zone de 30 m autour du puits et après la stabilisation, la pression du gaz était d'environ 20 MPa dans le cas sans pression capillaire. Pour MPa, la pression du réservoir a augmenté jusqu'à 31 MPa en avant de la zone saturée en gaz et 32 MPa en arrière du front de propagation du gaz. En d'autres termes, la bulle de gaz devient plus régulière, mais plus petite et plus comprimée, en raison de l'effet conjoint du colmatage capillaire-bactérien.

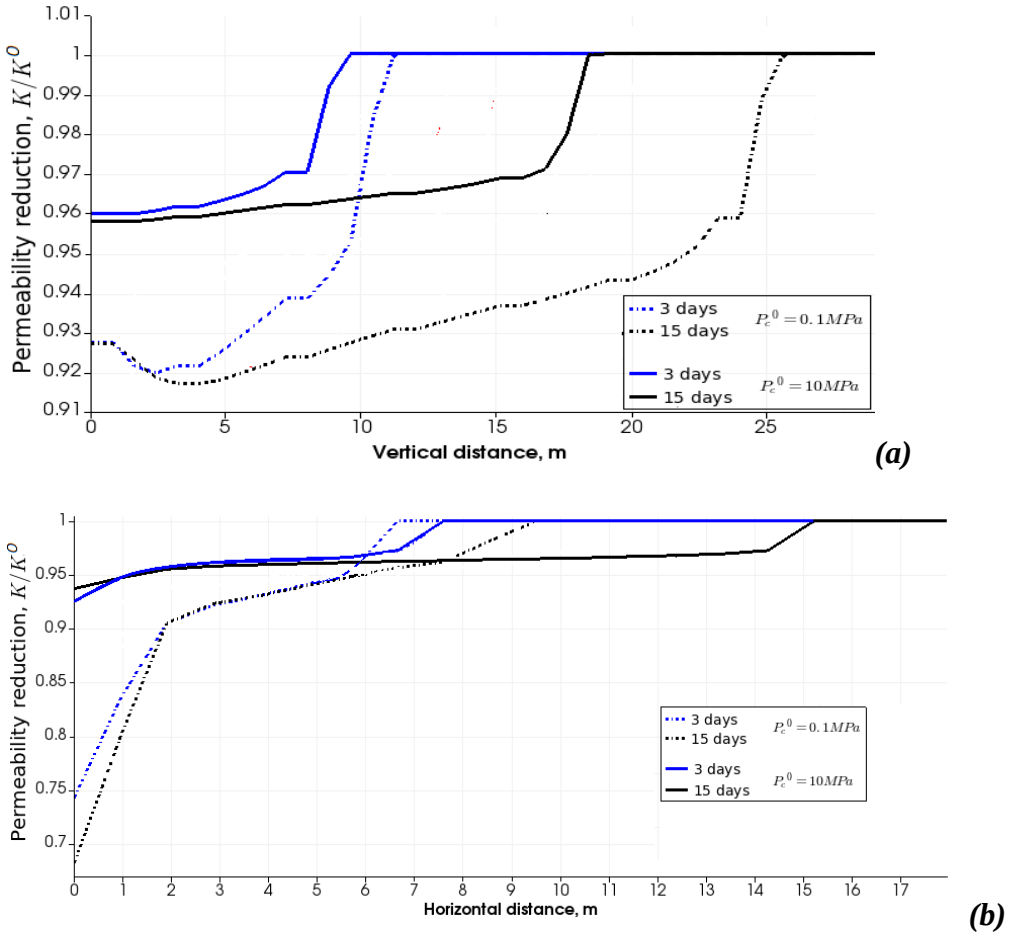

Figure A.11 Réduction de la perméabilité dans la direction verticale (a) et dans la direction radiale (b) à une pression capillaire élevée et faible (les courbes en trait plein et en pointillé, respectivement), pour deux moments de temps

Impact du bioclogging par les biofilms sur la conversion de l'hydrogène :

Ici, nous présentons le problème du bioclogging en tenant compte de l'attachement microbien et du modèle de Gerald E. Speitel et al. 1987 pour le détachement des biofilms. Nous évaluons la réduction de l'espace poreux due à l'attachement des bactéries aux pores.

La réduction de la perméabilité est plus élevée que celle présentée dans le dernier test en raison de la filtration microbienne. La réduction est sévère près de la région du puits de forage. Les résultats sont en bon accord avec les données expérimentales publiées par (Anozie Ebigbo et al. 2010). La longueur de la zone où la perméabilité est réduite est plus élevée dans la distance verticale (environ 25 m) que dans la distance radiale (environ 6 m). Après 15 jours d'injection, dans la direction radiale, la perméabilité est réduite de 62%, tandis qu'elle est réduite de 44% dans la direction verticale. La Figure montre que le rapport porosité/perméabilité augmente avec le temps, ce qui implique que la pression capillaire augmente également et que cela accélère le bioclogging en conséquence.

La figure A .12 (d) montre l'évolution des coefficients d'attachement et de détachement mesurés au cours du temps. Le mécanisme d'attachement domine, ce qui devrait amplifier la concentration de biomasse attachée à la paroi des pores et le bioclogging également. La figure A .13 (a) montre la distribution de la biomasse fixée dans le réservoir après 15 jours d'injection. Il est observé sur la figure A .13 (a-b) que la biomasse est plus présente et réactive près de la zone d'injection, qui est une région riche en nutriments H_2 et CO_2. Les résultats sont en bon accord avec les études de Brovelli et al. 2009 et Sivasankar et al 2019 et reproduisent bien la distribution de biomasse fixe observée dans les expériences présentées dans Brovelli et al. 2009. La figure A .13 montre également une comparaison de la distribution de l'hydrogène, du dioxyde de carbone et du méthane dans la direction verticale et horizontale. En seulement 15 jours, les bactéries, grâce à leur activité, ont été capables de transformer ~ 2% de l'hydrogène en méthane. Pour la même période, dans le réservoir souterrain de la ville de Lobodice (République Tchèque) et avec une densité de 10^9 cellules/m^3 les bactéries ont transformé 60% de la quantité que nous avons obtenue (Frantisek Buzek et al. 1990) , cela montre que le Bioclogging augmente la production de méthane.

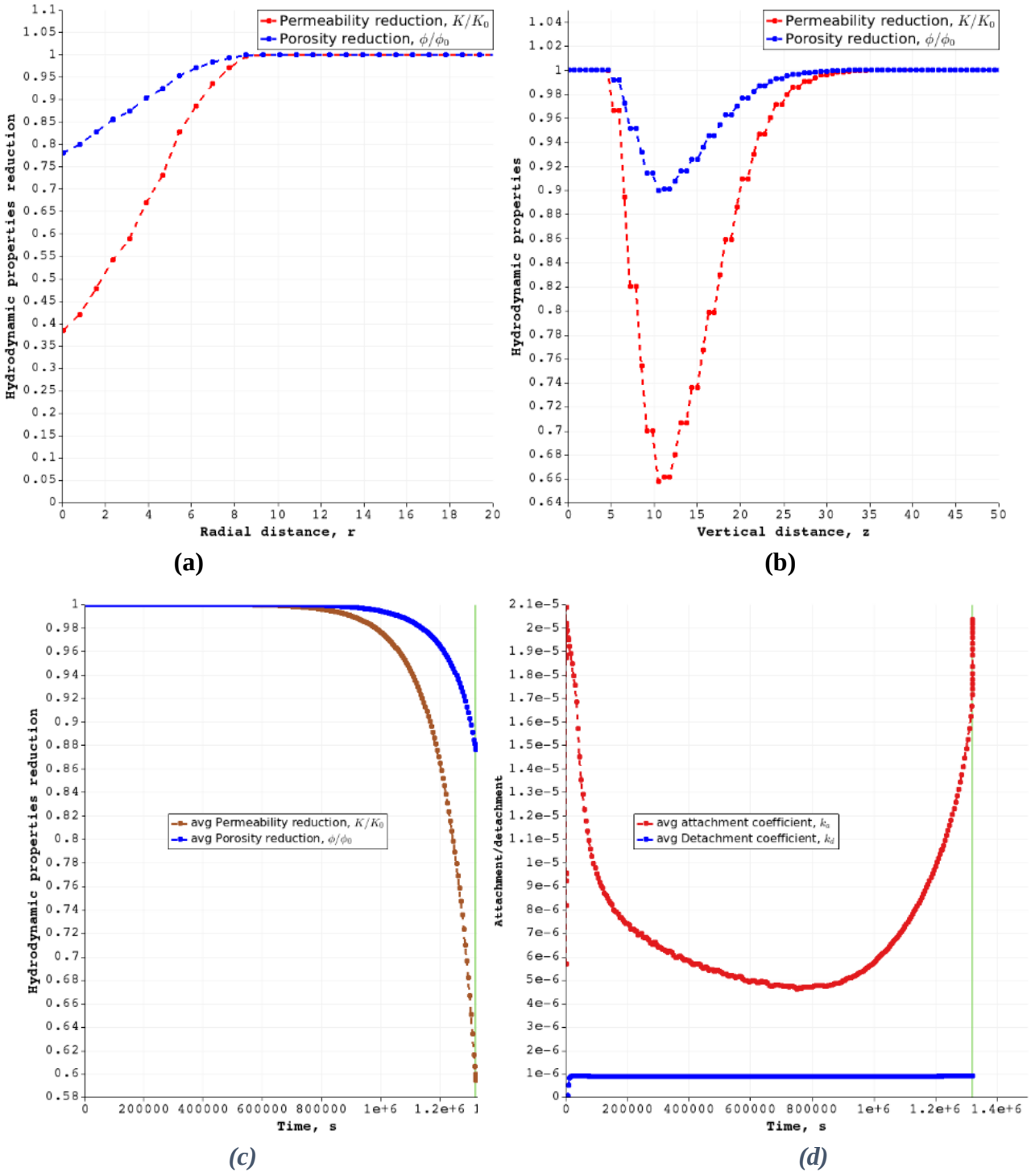

Figure A.12 Variation de la porosité et de la perméabilité en distance radiale (a) et verticale (b) après 15 jours et dans le temps (c), et coefficients d'attachement et de détachement mesurés dans le temps (d).

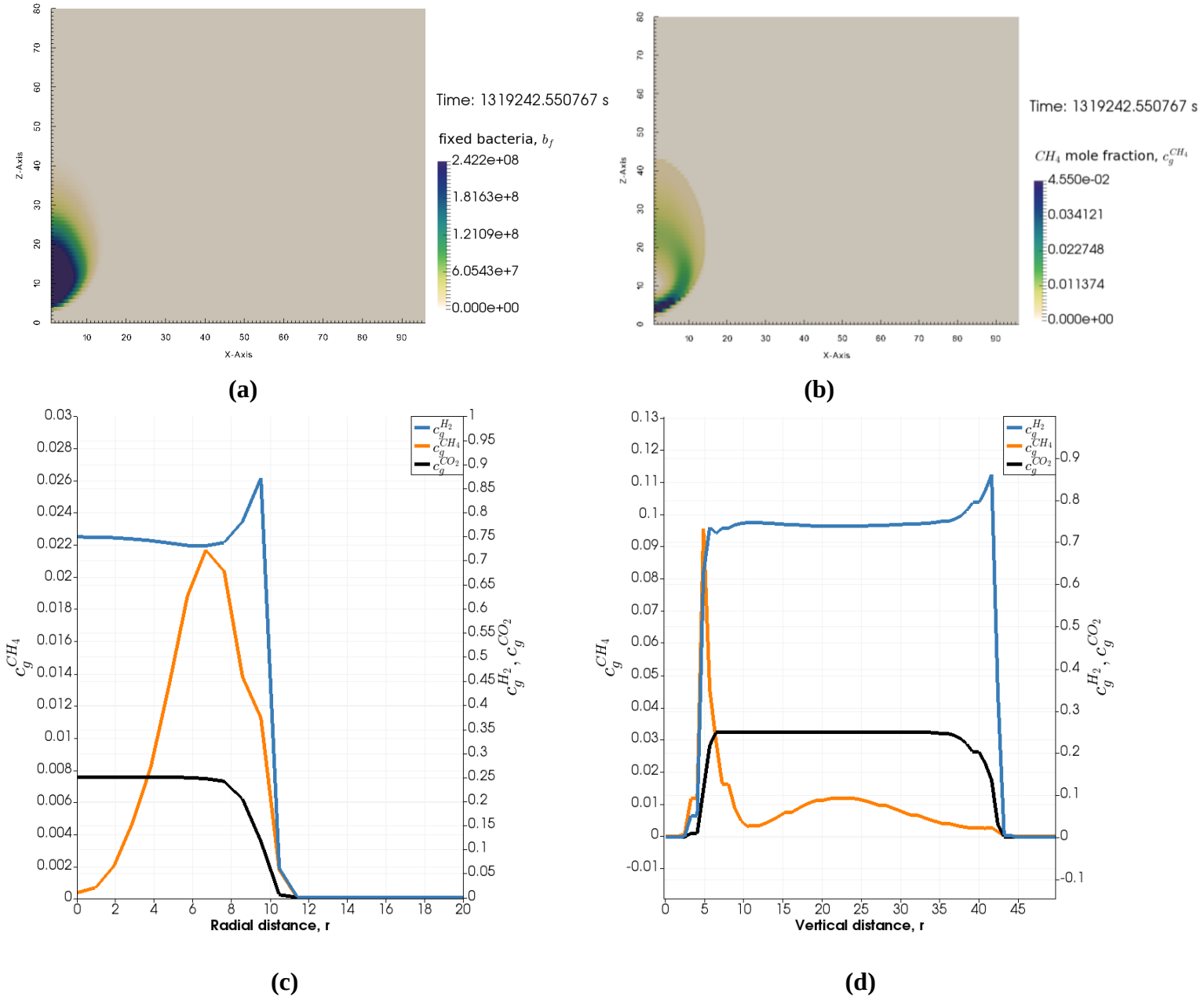

Figure A.13 Distribution 2D de (a) bactéries fixées, (b) production de biométhane au sein du réservoir et (c-d) concentration d'hydrogène et de dioxyde de carbone en fonction de la bio-production de méthane après 15 jours.

On a pu observer également que la propagation verticale de l'hydrogène est plus rapide que celle du méthane. Comparé au méthane, l'hydrogène est huit fois moins dense que le méthane et la faible viscosité de l'hydrogène induit une grande mobilité de l'hydrogène. Cela rend l'hydrogène très diffusif par rapport aux autres gaz (figure A .13 (c-d)).

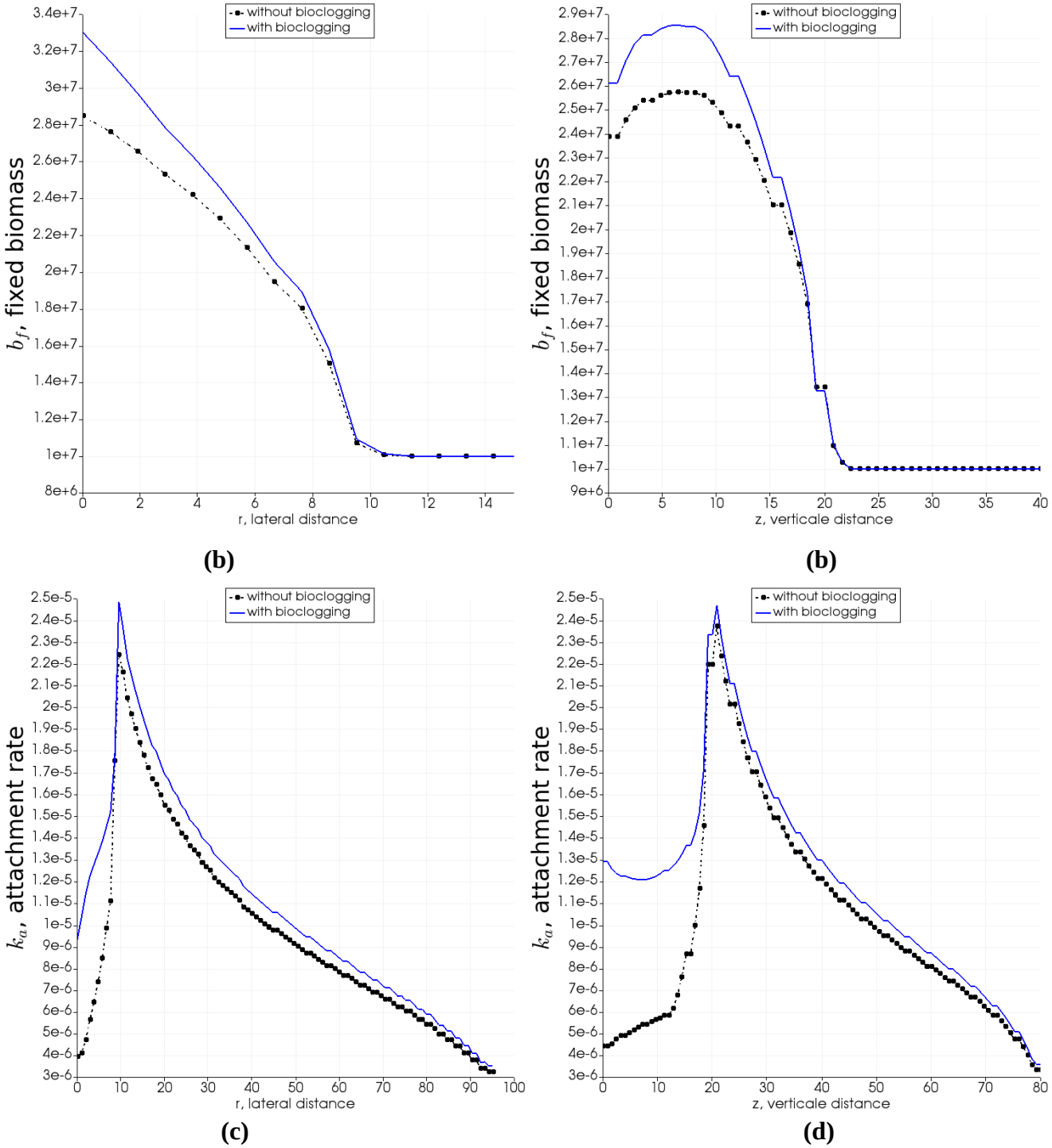

Figure A.14 Influence du bioclogging sur (a-b) la concentration de la biomasse fixée et (c-d) le mécanisme de fixation dans les directions radiale (gauche) et verticale (droite).

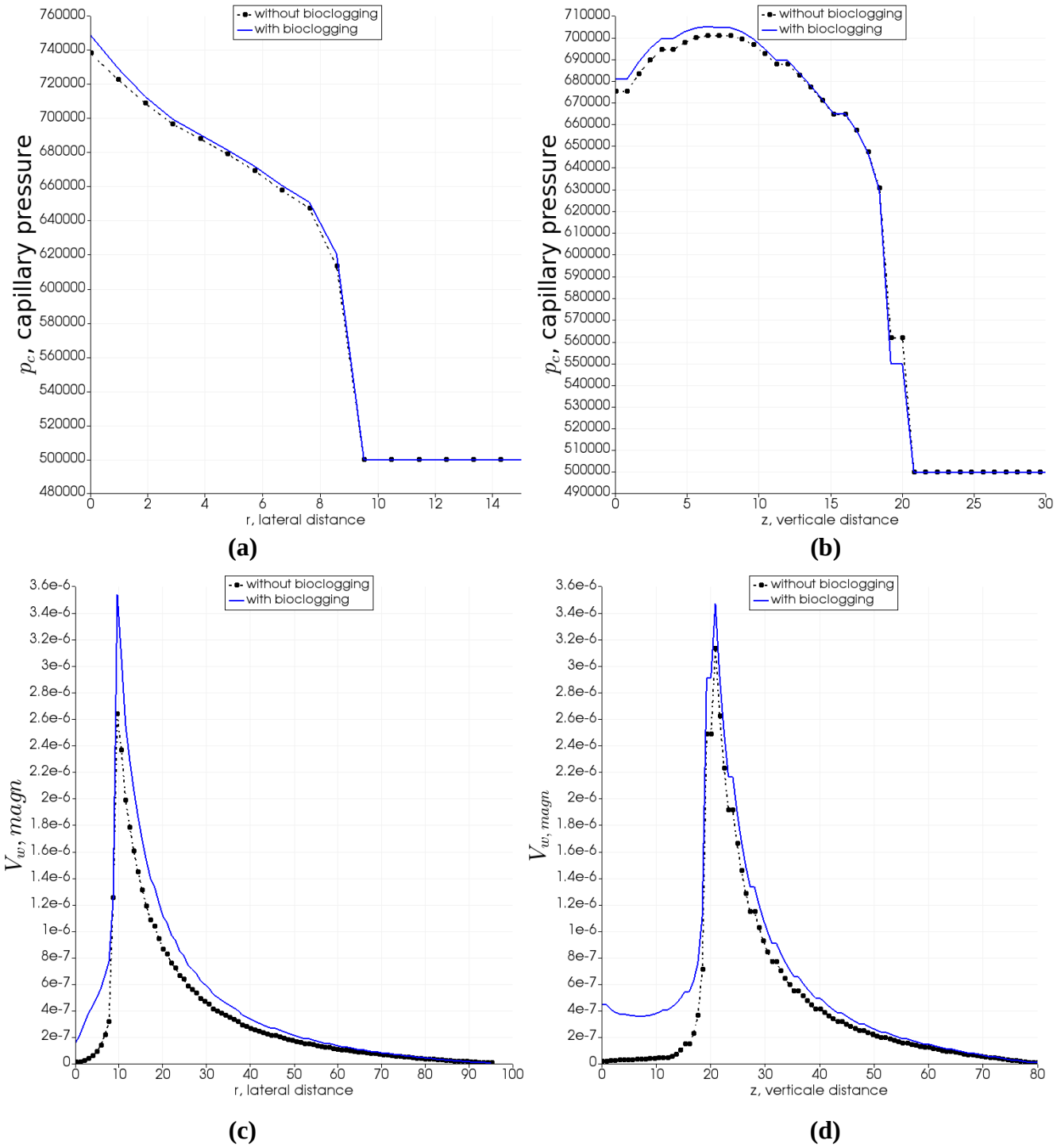

Figure A.15 Impact du bioclogging sur la vitesse d'écoulement et la pression capillaire

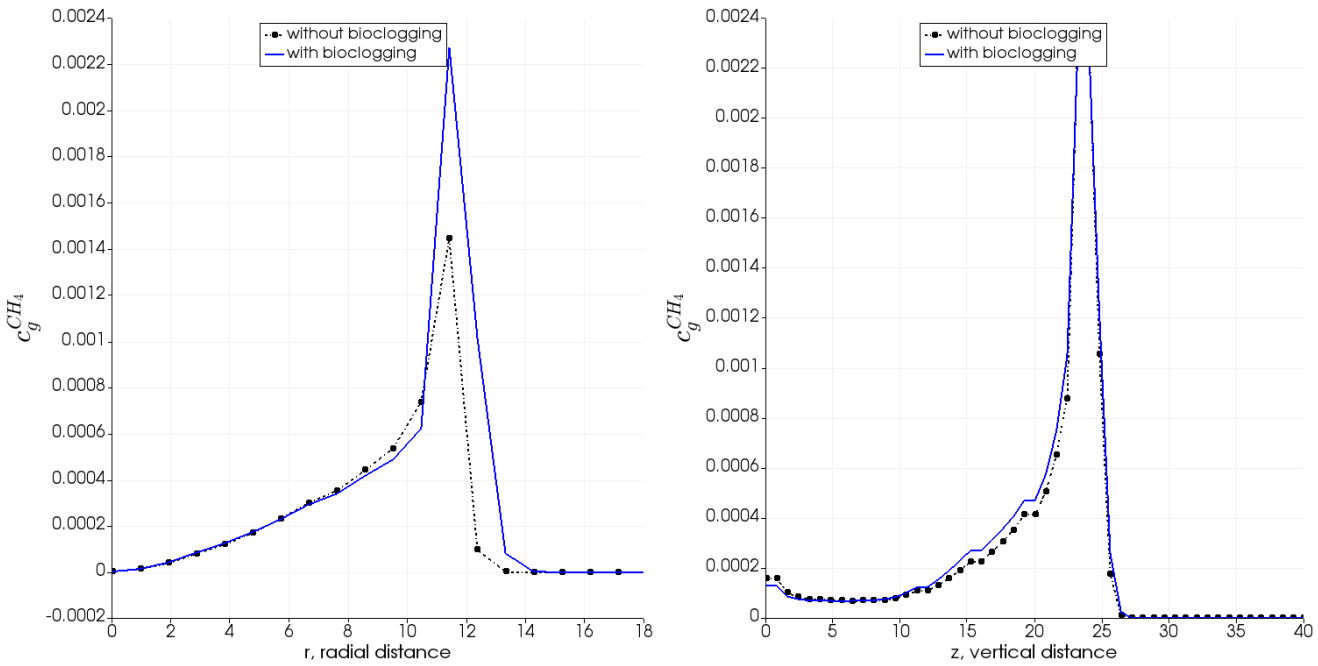

(a) **(b)**

Figure A.16 - Influence du bioclogging sur le processus de biométhanation

Les simulations de la concentration de la biomasse microbienne et de son taux de fixation aux parois des pores dans les cas avec et sans bio-colmatage sont représentées sur la figure A .14. En raison de la forte concentration de bactéries capturées dans la zone de colmatage, les activités bactériennes dans cette région augmentent, et par conséquent leur production de biomasse augmente. En raison de la réduction du volume des pores, le bioclogging augmente la vitesse d'écoulement et la pression capillaire (figure A .15). En conséquence, cela augmente la probabilité qu'une bactérie entre en collision avec la surface d'un pore. On constate que l'impact du bioclogging sur le mécanisme d'attachement est plus important à proximité de la zone d'injection.

L'influence du bioclogging sur l'efficacité de la biométhanisation est analysée dans les deux derniers résultats. Grâce au bioclogging, la conversion de H_2/CO_2 en méthane par les bactéries est améliorée de deux ordres de grandeur, passant de 0,0014 à 0,0023. Les bactéries fixées dans les zones colmatées travaillent en synergie pour améliorer leurs réactivités et par conséquent augmenter leur production de biométhane. Ainsi, le bioclogging améliore le rendement de conversion du biométhane en piégeant davantage de bactéries, en améliorant leur croissance et en accélérant leurs activités.

CONCLUSIONS

Cette thèse est consacrée à l'analyse du comportement des solutions du système d'équations qui décrit les phénomènes de transport dans un stockage souterrain d'hydrogène créé dans un aquifère ou un réservoir de gaz épuisé. Nous savons que le comportement de l'hydrogène est très différent de celui du gaz naturel en raison du fait que l'hydrogène est activement utilisé par les bactéries habitant les roches, qui le transforment en méthane. Une telle réaction biotique se produit en présence de CO_2, qui est dissous dans les eaux souterraines ou peut être injecté en même temps que l'hydrogène. Par conséquent, le modèle mathématique du processus est un système d'équations de transport pour plusieurs espèces chimiques (H_2, CO_2, CH_4, H_2O,...) dissoutes dans le gaz et l'eau, et de dynamique des bactéries, qui comprend la croissance, le décès probable et le mouvement des bactéries. La cinétique de la réaction de méthanisation est déterminée par le processus métabolique de la population bactérienne et est fortement liée à la cinétique de croissance de la population.

Après avoir été stocké sous terre, l'hydrogène peut être utilisé de deux manières principales dans l'industrie.

Tout d'abord, il peut être reconverti en électricité dans des piles à combustible et utilisé dans des véhicules, ce qui nécessite de disposer d'un hydrogène très pur. Or, les pertes d'hydrogène dues à la réaction de méthanisation rendent impossible son stockage à l'état pur. C'est pourquoi l'objectif pratique du stockage serait de minimiser les réactions biochimiques, ce qui faciliterait le traitement ultérieur en surface du mélange hydrogéné extrait de l'installation de stockage. Notez que le principe objet, dans ce cas, est de minimiser le mélange de l'hydrogène avec d'autres gaz.

Deuxièmement, l'hydrogène peut être utilisé comme combustible pour le chauffage et l'éclairage des bâtiments. Dans ce cas, sa conversion partielle en méthane signifie l'enrichissement du combustible, puisque le potentiel énergétique de 1 m3 de méthane est supérieur à celui de l'hydrogène. Dans ce cas, il faut intensifier la réaction de méthanisation dans le stockage. Un tel procédé de méthanation in situ se déroule à basse température, est beaucoup moins coûteux que la méthanation à haute température, et peut représenter un intérêt industriel. L’objet principal,

dans ce cas, est de maximiser le mélange de l'hydrogène avec le CO2 pour convertir tout l'hydrogène.

Cependant, le mélange dans un tel système n'est pas si simple à contrôler, car l'évolution des phénomènes de transport dans le stockage obéit à des lois physiques propres, qui ne tiennent pas compte des attentes technologiques. Le principal problème qui nous empêche de réguler le mélange est le phénomène d'auto-organisation qui se produit dans un système de diffusion-réaction. Ils conduisent à la formation de motifs - des structures stables spatiales ou temporo-spatiales (mosaïques), des sortes de fluctuations dans l'espace ou dans le temps, ou dans l'espace et dans le temps simultanément, qui sont les solutions des équations de transport à $t \to \infty$. Les paramètres des modèles sont strictement déterminés par la physique de l'écoulement et la cinétique des réactions. Heureusement, le taux d'injection de gaz et la composition du gaz injecté sont également deux paramètres qui peuvent modifier la géométrie des patrons, nous offrant la possibilité de contrôler le processus de leur formation.

Un motif signifie l'existence de zones à forte concentration d'hydrogène et d'autres zones à faible concentration. Par conséquent, le mélange devient non uniforme dans l'espace et non complet. Les motifs réduisent le degré de mélange. Cela peut être bon pour le premier objectif : utiliser l'hydrogène comme électricité convertie. Mais ce n'est certainement pas bon pour le second objectif, à savoir transformer l'hydrogène en méthane. Ainsi, le problème théorique de trouver des critères d'existence des modèles prend un sens pratique évident.

Dans cette thèse, nous distinguons trois types de modèles :

(i) les modèles stationnaires causés par l'instabilité dite de Turing ;

(ii) uniformes dans l'espace mais oscillant périodiquement dans le temps, liés au phénomène de la bifurcation de Hopf-Andronov et à l'apparition d'un cycle limite ;

(iii) et des motifs ondulés, oscillant périodiquement dans l'espace et dans le temps simultanément et liés à la fois à l'instabilité de Turing et de Hopf-Andronov.

Nous avons analysé les conditions générales de l'apparition de ces trois types de motifs dans des milieux homogènes. En particulier, nous avons montré qu'un nouveau modèle existe dans le cas de seulement deux équations de diffusion-réaction, qui est non stationnaire et se comporte comme des vagues de saut.

Ensuite, nous avons étendu notre analyse aux milieux hétérogènes, qui ont été analysés en termes de modèle macroscopique de double porosité. Nous avons montré, dans un premier temps, que la double porosité déplace les critères de formation des motifs. Nous avons montré que pour des motifs stationnaires, la concentration dans les fractures et dans les blocs est identique, ce qui correspond au comportement classique des solutions des équations de la double porosité. Deuxièmement, nous avons révélé l'existence de modèles, dans lesquels les concentrations dans les fractures et les blocs sont distinctes. Elles subissent des oscillations spatiales et temporelles, qui ont une amplitude, une fréquence et une phase distinctes. Ceci n'est possible que pour les motifs ondulés, non stationnaires. Ceci a été confirmé par nos tests numériques.

Dans la dernière partie de la thèse, nous avons analysé les mêmes équations de transport dans le cas où les bactéries induisent une hétérogénéité du milieu, en bouchant certains pores et en réduisant la perméabilité, la porosité et la pression capillaire entre le gaz et l'eau. Pour cela, nous avons développé le modèle conceptuel d'attachement et de détachement des particules aux parois des pores. Plusieurs mécanismes d'attachement sont considérés. Des données expérimentales pour certains coefficients phénoménologiques ont été trouvées dans la littérature. Ce modèle a été implémenté dans un simulateur numérique ($DuMu^X$). L'analyse subséquente était basée sur ce modèle conceptuel et a été réalisée numériquement. Nous avons analysé l'injection d'hydrogène dans un aquifère dans un domaine tridimensionnel. Nous avons montré que le biocolmatage réduit localement la perméabilité, et, de plus, induit une certaine anisotropie car la diminution de la perméabilité était plus importante dans la direction de propagation des bactéries (dans le sens vertical). De ce fait, la montée du gaz vers la couverture a été retardée et même stoppée. Ainsi, le gaz injecté a dû s'écouler dans la direction horizontale non obstruée par les bactéries. Par conséquent, la propagation du gaz devient plus régulière, ce qui est favorable à la création d'un stockage de gaz. L'hétérogénéité induite oblige le gaz à changer de trajectoire et à se déplacer dans d'autres directions. Les forces capillaires, qui augmentent dans les zones colmatées, renforcent cet effet, de sorte que le gaz a tendance à se propager uniformément dans toutes les directions. Grâce à l'effet conjoint du bio-colmatage et de la capillarité accrue, la migration du gaz devient plus régulière. Nous avons constaté que les bactéries sont capables de transformer 2% d'hydrogène en méthane en 15 jours, ce qui est trois fois plus rapide que le

résultat obtenu dans les expériences réalisées dans le réservoir de Lobodice. Ainsi, nous concluons que le bio-clogging augmente l'efficacité de la bio-méthanation.

Abstract:

In the era of energy transition and in connection with the international agreement on the transition to a climate-neutral economy by 2050, intensive research is being carried out around the world on renewable energy sources. Due to the intermittent and unpredictable nature of their functioning, the problem of storing excessively produced energy becomes a highly important problem. We are currently talking about a large capacity for storing large amounts of electricity coming from photovoltaic cells and windmills. Since electricity is mutually converted to hydrogen and vice versa, storing it in geological strata in the form of gas becomes the optimal solution. The conversion of electricity into H_2 can be done by electrolysis. The process is reversible using fuel cells, where hydrogen is converted into electrical current. We obtain the chain: power - to gas - to power. As a result, there are virtually no greenhouse gases, which can lead to the decarbonization of the transport sector and energy-intensive industries.
In this thesis, we analyze the storage of hydrogen in underground porous media, which can be aquifers, or depleted gas reservoirs, or ex-storages of natural gas.

The subject of this thesis is the hydrodynamic analysis of transport of injected gases in a storage coupled with bacterial dynamics. As shown in previous studies, hydrogen is intensively consumed by various types of bacteria, which transform it into methane, for example. The cross-effects of bioreactions and transport determine the formation of complicated spatial structures called *patterns* that lead to a nonuniform distribution of hydrogen over the domain. Our main attention was focused on the impact of medium heterogeneity on pattern formation. Two types of heterogeneity were analyzed: the double porosity, in terms of the macroscopic Barenblatt's model, and the heterogeneity induced by bacteria, growth of which creates the zones of reduced permeability or even completely clogged pores. The analysis is performed numerically using the simulator DuMu^X, open scientific software for flow in porous media, developed at the University of Stuttgart and based on Dune developed by Heidelberg.

Keywords:

Patterns; Underground hydrogen; Storage; Population dynamics; Two-phase flow; Reactive transport; Numerical simulation; DuMu^X.